2013

Energy spectra comparisons for matched clinical electron beams on Elekta linear accelerators using a permanent magnet spectrometer

David McLaughlin
Louisiana State University and Agricultural and Mechanical College

ENERGY SPECTRA COMPARISONS FOR MATCHED CLINICAL ELECTRON BEAMS ON ELEKTA LINEAR ACCELERATORS USING A PERMANENT MAGNET SPECTROMETER

A Thesis

Submitted to the Graduate Faculty of the
Louisiana State University and
Agricultural and Mechanical College
in partial fulfillment of the
requirements for the Degree of
Master of Science

in

The Department of Physics and Astronomy

by
David James McLaughlin
B.S., Pennsylvania State University, 2010
December 2013

Acknowledgments

I would like to take this opportunity to thank Mary Bird Perkins Cancer Center for funding my work and providing me access to the facilities, equipment, and personnel needed to complete this project.

I thank my advisor Dr. Kenneth Hogstrom. The idea of using permanent magnets for clinical electron beam energy spectroscopy was his, as were many of the ways of proceeding with the analysis. His decades of experience were essential to the success of this project. I am lucky to have had him as an advisor. I am also grateful to my supervisory committee: Dr. Robert Carver, Dr. John Gibbons, Dr. James Matthews, and Dr. Polad Shikhaliev. Particularly, I thank Dr. Shikhaliev for providing and reading my Computed Radiography strips and Dr. Carver for running Monte Carlo simulations on my behalf. I thank clinical medical physicist Dan Neck for measuring electron percent depth dose curves for me and Elekta service engineer James Payne for assisting by tuning the electron beams and answering my questions about beam tuning. I thank Dr. Joseph Deasy for answering my emails and Elekta engineer Neil McCann for providing documentation and answering my questions.

Thanks also go to Yvonne Thomas, Paige Barcia, Arnell Nelson, and Susan Hammond for their assistance. Countless tasks would have gone uncompleted, or completed inadequately, without their help. I thank my classmates in general for aiding in my academic success and Adam Watts in particular for sharing his apartment with me as I finished my thesis. Additionally, I thank my cubicle mates, John Chapman and Garret Pitcher, for aiding my research progress with their knowledge of radiation transport physics and MATLAB.

Finally, I would like to thank my family and friends, in Baton Rouge and abroad, for their guidance, compassion, and support. Particularly, I thank my parents, Robert and Susan McLaughlin, for their love and support through challenging times. My success is inextricably linked to my community, and I am indebted to them in ways that cannot be repaid.

Table of Contents

List of Tables

List of Figures

Abstract

Purpose: The purpose of this work was to use a permanent magnet electron energy spectrometer to measure and compare electron beam energy spectra from matched electron beams on Elekta radiotherapy accelerators at Mary Bird Perkins Cancer Center.

Methods: Electron beam collimation, X-ray background collimation, and irradiation geometry were developed to produce suitable latent images in computed radiography (CR) strips at the exit side of a 0.5-Tesla permanent magnet spectrometer. An analytical technique transformed CR strip images into energy spectra on central axis at 95-cm source-to-collimator distance. Electron energy spectra at 7, 9, 10, 11, 13, 16, and 20 MeV for four Elekta accelerators, whose beams had been matched to one of two reference accelerators at commissioning, were measured and compared to measured energy spectra of their reference accelerator. Percent depth-dose (%DD) matching criteria of 0.05 cm for R_{50} and 0.1 cm for $R_{80\text{-}20}$ correlated to 0.12 MeV and 2.0 MeV for the modified incident peak mean energy ($\langle E \rangle^*_{m,o}$) and full-width-at-half-maximum (FWHM) of the energy spectra, respectively.

Results: For 19 of the 28 matched beams, $\langle E \rangle^*_{m,o}$ did not match $\langle E \rangle^*_{m,o}$ of their reference accelerator to within 0.12 MeV, showing shifts likely due to inadequate beam tuning subsequent to commissioning and energy drifting of the accelerator within quality assurance (QA) limits ($\pm$0.2 cm of R_{50}). However, FWHM of all 28 matched beams matched FWHM of their reference accelerator despite having considerably different spectral shapes. By correlating %DD metrics with energy spectra metrics, it was determined that R_{50} had a linear relationship with $\langle E \rangle^*_{m,o}$, whereas R_{80-20} depended primarily on $\langle E \rangle^*_{m,o}$ and secondarily on FWHM.

Conclusions: First, this study demonstrated that not all MBPCC electron beam energy spectra were matched. Second, electron beams with matched %DD metrics do not necessarily have matched energy spectra, which are more sensitive for comparing beams than %DD curves. Third, the instrument, methods, and analytical analysis developed in this study offer the potential for an inexpensive, lightweight, real-time electron energy spectrometer which could be useful for beam tuning and matching, QA, and determination of X-ray and electron beam energy spectra for radiation transport calculations.

Chapter 1 - Introduction

1.1. Background and significance

1.1.1. History and clinical use of electron beam therapy

Electron beams have long played an important role in radiation oncology. Treatments first developed in the 1930s and 1940s with Van de Graff generators demonstrating the clinical utility of electron beams. These treatments have matured, with conventional electron beam therapy being delivered with microwave-powered linear accelerators.

Electron beams are a radiotherapy modality useful for treating superficial planning target volumes (PTVs) located within 6.0 cm of an external surface of a patient (Hogstrom, 2003). This is due to the finite ranges and sharp distal falloffs of electron beams' central-axis percent depth-dose (%DD) curves, which are apparent in the %DD curves measured at Mary Bird Perkins Cancer Center (MBPCC) in Figure 1.1.

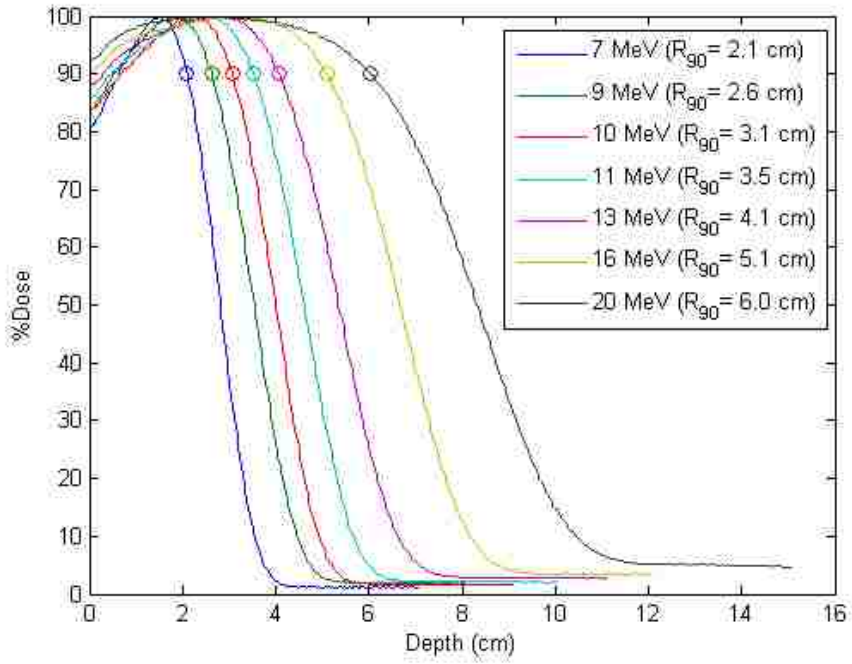

Figure 1.1. Electron central-axis %DD curves. Electron %DD curves measured on MBPCC's Baton Rouge Elekta Infinity accelerator on Jan/14/2013 by clinical MBPCC staff. All beam energies shown are nominal energies. The distal 90% dose points are indicated by the open circles.

Electron beam %DD curves have a fairly uniform dose plateau from the surface to the distal depth of 90% of the maximum dose, R_{90}. Also, they have a sharp falloff between the depths of the 90% and 10% dose, R_{90-10}. The distal region of the %DD curve where this sharp falloff happens is known as the dose falloff region. This falloff allows radiation oncologists to irradiate a PTV between the patient surface and 6.0 cm depth, keeping the PTV completely inside a 90% isodose surface while sparing normal tissue distal to the PTV. Above 20 MeV however, lateral penumbra and bremsstrahlung production increase rapidly with energy, while the gradient of the dose falloff region decreases, deteriorating the clinically desirable properties of electron beams. Additionally, electron beams below about 6 MeV have too low of a surface dose to be clinically useful. Thus, manufacturers currently provide electron beam energies typically limited to incident peak energies, $E_{p,o}$, between 6 MeV and 20 MeV.

Due to these unique properties, electron beams are useful for several clinical sites. For example, a significant portion of post-mastectomy chest wall, post-lumpectomy breasts, parotid gland, nose, and ear PTVs can be treated completely or partially with electron beams (Tapley 1976, Hogstrom 1991). The sharp distal dose falloff of electron beams allows them to be used while sparing distal tissue, such as the lung for chest wall treatments, and the brain, spinal cord, eyes and optic chiasm for head and neck treatments. In conjunction with bolus material, electron beams can be used to treat skin lesions. They are also ideal for total skin and total scalp treatments, as the deeper structures can be spared while maintaining a fairly uniform dose to the skin. Beyond this, electrons have been proven for several less common cases such as retinoblastoma patients, where there is a chance for preserving vision in the afflicted eye, or for use in craniospinal irradiation of pediatric patients, where reducing integral dose is important (Gerbi *et al* 2009).

1.1.2. Basic properties of electron beam %DD curves

Various range definitions, given to different aspects of electron beam %DD curves, are illustrated in Figure 1.2. R_{100} is the depth of maximum dose (D_m). The region between the surface and R_{100} is known as the buildup region. R_{90} or R_t is the therapeutic range, marking the depth of the distal edge of the 90% isodose surface. This range parameter is sometimes called the therapeutic range because radiation oncologists require that R_{90} exceeds the maximum PTV depth, and they often prescribe the dose to the 90% isodose line. R_{50} is the depth where the dose is half the maximum and is correlated to the mean energy (ICRU 35 1984). R_p is the practical range, so named because it marks the depth beyond which the electron dose is practically negligible. More exactly, it is the point where the tangent of the steepest point on the descending portion of the depth dose curve (i.e. the dose falloff region) intersects the extrapolated bremsstrahlung background (ICRU 35 1984). R_p is correlated to the most probably energy incident upon a water phantom (ICRU 35 1984). D_s is the dose at the surface of the water phantom. D_x is the bremsstrahlung dose tail that exists beyond R_p.

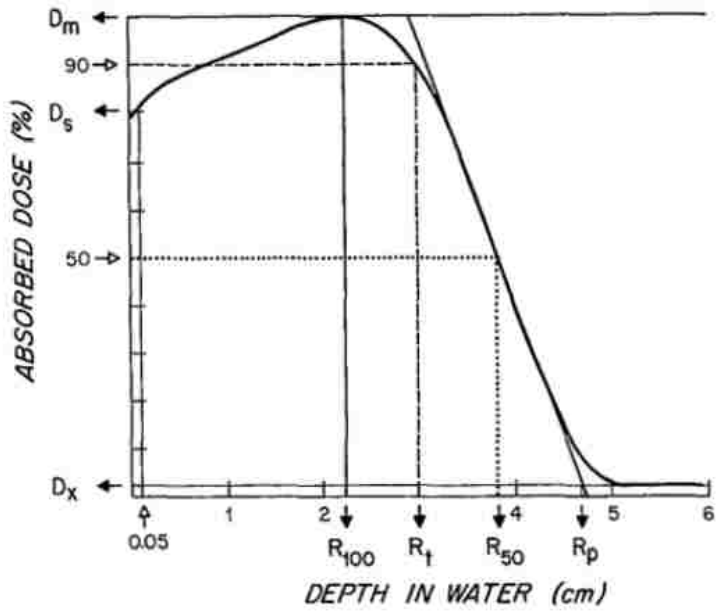

Figure 1.2. Nomenclature for clinical electron beam %DD curve parameters. Illustrated are the surface dose, D_s, maximum dose, D_m, depth of maximum dose, R_{100}, depth of 90% dose, R_{90}, depth of 50% dose, R_{50}, and the practical range, R_p (from Brahme and Svensson 1976).

1.1.3. Basic properties of electron beam energy spectra

The kinetic energy, E, distribution of the electrons that compose a therapeutic electron beam is referred to as the electron beam's energy spectrum. The energy spectrum, illustrated in Figure 1.3, has units of energy on the x-axis and units of relative planar fluence (or probability) per unit energy, the latter being a type of probability density, on the y-axis.

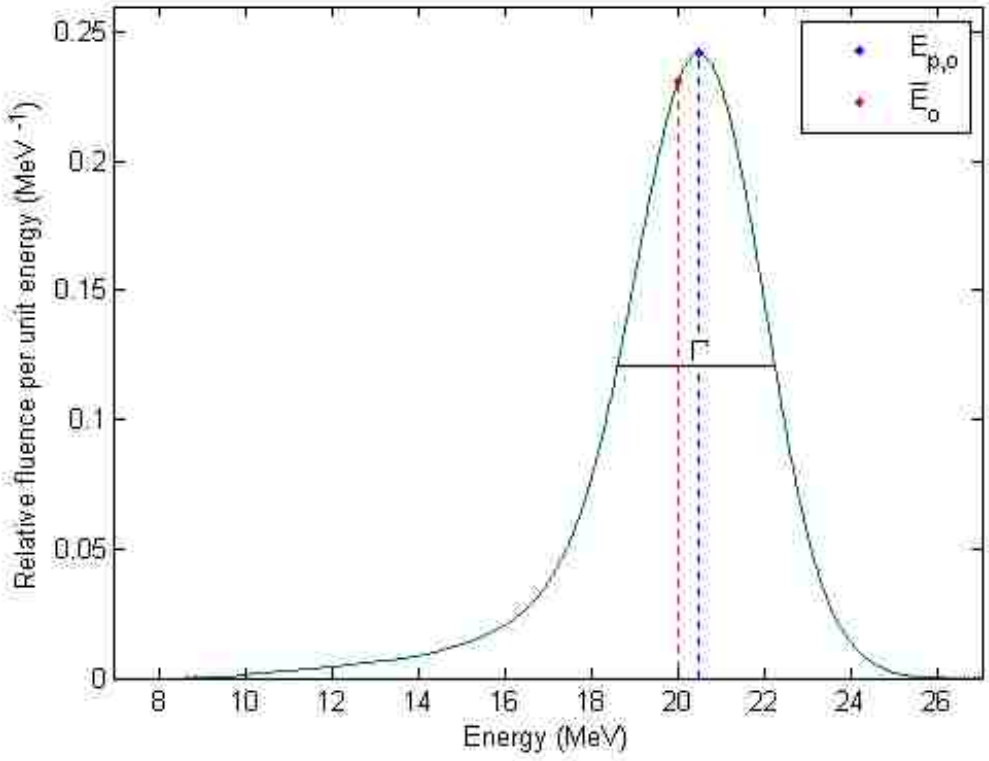

Figure 1.3. Example 20 MeV electron beam energy spectrum. Illustrated are the peak energy ($E_{p,o}$), mean energy ($\bar{E}_o$), and full width at half the maximum (Γ) of the energy spectrum at isocenter.

Besides the most probable energy of the incident spectrum, $E_{p,o}$, the mean energy, $\bar{E}_o$, and full width at half the maximum (FWHM), Γ, are displayed. In Figure 1.3, $E_{p,o}$ equals 20.5 MeV, $\bar{E}_o$ equals 20.0 MeV, and Γ equals 3.6 MeV. Sometimes Γ is specified as a percentage of $E_{p,o}$, i.e. 17.7% in Figure 1.3.

It is worth noting that a clinical electron beam energy spectrum contains two major components, a peak region and a low-energy tail. In Figure 1.3, the peak region is the portion of the

energy spectrum greater than about 17 MeV, and the low-energy tail is the portion of the energy spectrum less than about 16 MeV. The peak region, which is approximately Gaussian in shape, is where the majority of the area under the spectrum is found. In Figure 1.3, the peak region consists of a single peak (approximately Gaussian), but this may not always be the case. In Figure 1.15 in section 1.1.5, it is clear that the peak region could consist of the sum of three or more Gaussians. The reasons for this will be explained in section 1.1.5. The low-energy tail takes up a much smaller portion of the area under the energy spectrum. It is connected to the side of the peak region and declines down to zero as you move to lower energies. The low-energy tail is due to energy-straggling, which is the non-uniform loss of large amounts of energy through delta-ray and bremsstrahlung production as the electron beam passes through a material (ICRU 35 1984). Energy straggling also broadens the peak region of the energy spectrum. Most of the energy straggling happens in the primary scattering foil.

1.1.4. Effect of energy spectra on electron beam %DD curves

Different energy spectra at the surface of a phantom will produce different %DD curves. Energy spectra that are composed of higher energy electrons will penetrate further, resulting in deeper penetration. This is apparent from the two traditional equations relating range parameters in water to energy parameters of the energy spectrum at the water's surface. The most probable incident energy ($E_{p,o}$) and the mean incident energy ($\bar{E}_o$) of a broad parallel electron beam at the surface of a water phantom are related to the practical range (R_p) and the depth of the 50% dose point (R_{50}), respectively by

$$E_{p,o}(MeV) = 0.22MeV + 1.98\frac{MeV}{cm} * R_p + 0.0025\frac{MeV}{cm^2} * (R_p)^2 \qquad 1.1$$

and

$$\bar{E}_0(MeV) = 2.4\frac{MeV}{cm} * R_{50}\,, \qquad 1.2$$

where all range parameters are in centimeters (ICRU 35 1984, Khan *et al* 1990). To use these equations with R_p and R_{50} values taken from measured %DD curves produced by the divergent beams found in a clinical setting, all data points of the %DD curves must be corrected using the inverse of the spherical-divergence correction, though this correction was ignored throughout this study as it has a negligible effect below 20 MeV (Khan *et al* 1990).

Additionally, it is thought that increases in FWHM values of the energy spectrum correspond to increases in the length of the dose falloff region of the %DD curve. This length is sometimes specified using the difference between R_{10} and R_{90}, i.e. R_{90-10}, where R_{10} and R_{90} are the depth of the 10% and 90% dose points of the %DD curves, respectively. However, the literature reveals that the shapes and FWHMs of the incident energy spectra have a small effect on the %DD curves as long as the energy spectra are not too wide, as is the case for most therapeutic electron beams.

Kainz *et al* (2004) determined the R_{90-10} values for electron beam %DD curves generated using Monte Carlo (MC) techniques. They simulated point, monodirectional electron beams with mean energies of 9, 12, 15, 18, and 21 MeV through a scattering foil system and water phantom. A unique scattering foil system was designed for each energy. The energy spectra of the electron beams prior to interacting with the scattering foils, i.e. the initial spectra, were modeled as rectangle functions with widths, i.e. ΔE, of 0.5, 2.5, 4.5, and 6.5 MeV centered on the mean energies. The resulting %DD curves for these four rectangle function widths are plotted in Figure 1.4 for the 9 and 15 MeV beams.

The R_{90-10} values are plotted versus the R_{90} values for all mean energies and all rectangular function widths in Figure 1.5. The five R_{90} points of increasing depth correspond to the five electron beams of increasing mean energy. Note that the rectangular spectra with ΔE of 4.5 and 6.5 MeV have significantly larger R_{90-10} values as compared to the rectangular spectra with ΔE values of 0.5 and 2.5 MeV. This is also apparent in Figure 1.4. As these results show, noticeable increases in R_{90-10} values beyond those corresponding to the rectangular spectra with ΔE of 0.5 MeV only result for fairly

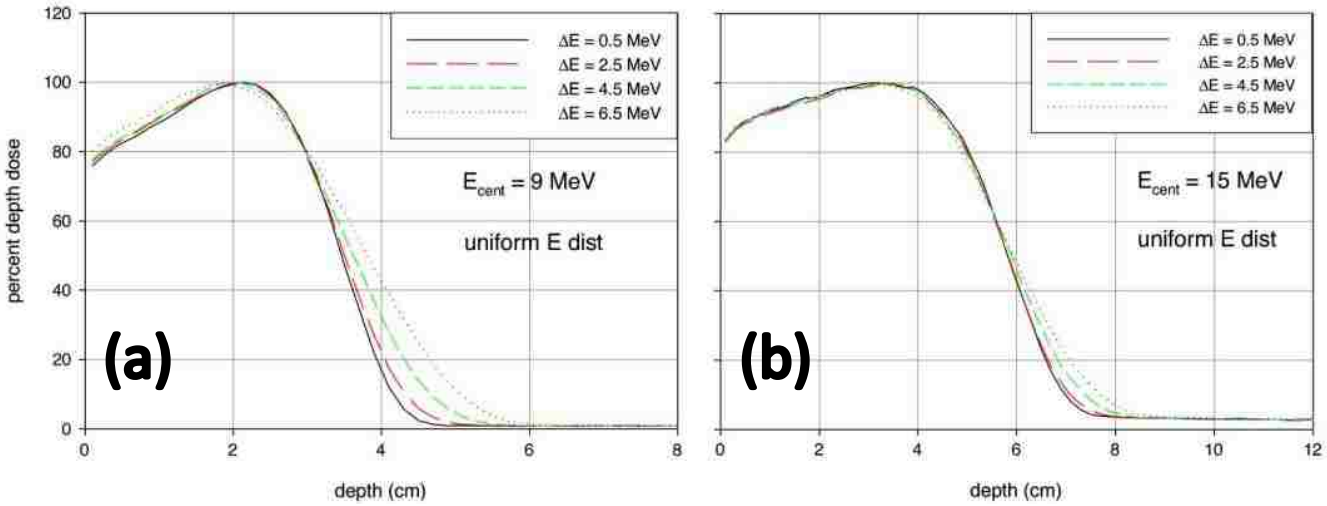

Figure 1.4. MC simulated %DD curves for rectangular initial energy spectra of various ΔE. These rectangle functions were centered on (a) 9 MeV and (b) 15 MeV and had widths of 0.5, 2.5, 4.5, and 6.5 MeV (modified from Kainz et al 2004).

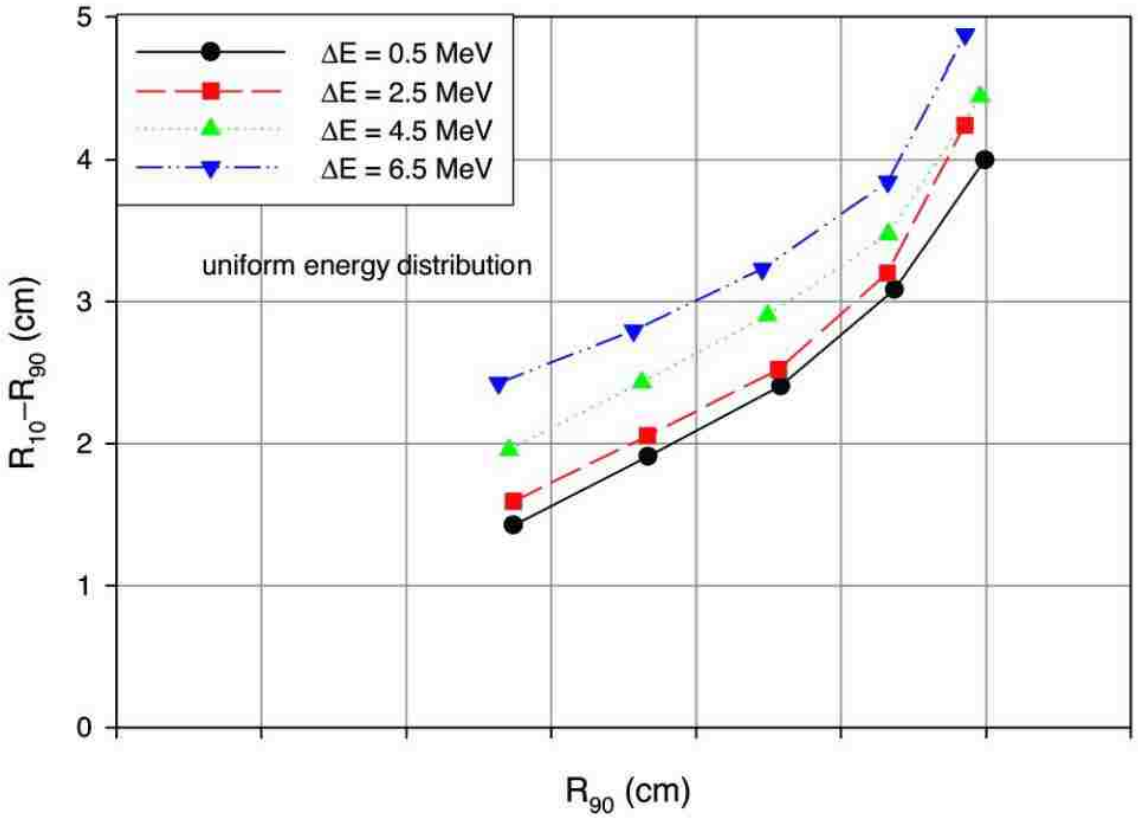

Figure 1.5. Penumbral widths versus R90 for various ΔE. Plotted are penumbral widths, R_{90-10} (labeled R_{10-90} by Kainz), versus R_{90} for the five mean energies and four rectangular function widths assumed for the initial energy spectra (modified from Kainz *et al* 2004).

significant increases in ΔE. This is because by the time the electrons reach R_{90}, they have experienced significant energy-straggling. Therefore, unless the spectral width prior to the dual scattering foil is relatively large, the spectral broadening due to energy-straggling in the scattering foils and first couple centimeters of water will dominate, masking the effect of any initial energy width.

Johnsen *et al* (1983) took electron %DD curves and energy spectra measurements at 6 MeV and 12 MeV using a single linear accelerator and irradiation geometry. Thin foils and lead bricks were used to simulate scattering foils and clinical collimation systems, respectively. They varied the shapes of the energy spectra while keeping the $E_{p,o}$ values of the spectra the same. They found only small differences in the dose falloff region and range parameters due to changes in the FWHMs, yet noticeable shifts in the practical range with the mean energy of the spectral peak structure. This is apparent in Figure 1.6, where both the narrow and broad 6 MeV electron beams had a $\bar{E}_o$ of 5.8 $\pm$ 0.2 MeV and a $E_{p,o}$ of 6.1 $\pm$ 0.2 MeV. The narrow and broad 6 MeV spectra had FWHMs of 0.1 and 0.8 MeV, respectively. The %DD curves for these beams in Figure 1.6 demonstrate that the practical ranges are almost identical. This is not the case with the broad and narrow 12 MeV electron beams, even though they both had peak energies of 12.2 $\pm$ 0.3 MeV. This is because the mean energies of the 12 MeV beams differed noticeably, being 11.8 $\pm$ 0.3 MeV for the narrow spectrum and 11.4 $\pm$ 0.3 MeV for the broad spectrum. The narrow and broad 12 MeV spectra had FWHMs of 0.2 MeV and 1.2 MeV, respectively. Note that in Figure 1.6 the R_{50} values for the broad-spectrum and narrow-spectrum 12 MeV beams differ by about 0.4 cm, yet the $\bar{E}_o$ values only vary by 0.4 MeV, which is inconsistent with equation 1.2.

This work indicates that the practical range is more closely related to the mean energy of the energy spectrum's peak structure than $E_{p,o}$. This is in contradiction to convention, which relates the practical range to the $E_{p,o}$ of the energy spectrum. Johnsen *et al*'s work also indicates that below a certain threshold, the FWHM of the spectra has little to no effect on any part of %DD curve except the build-up region.

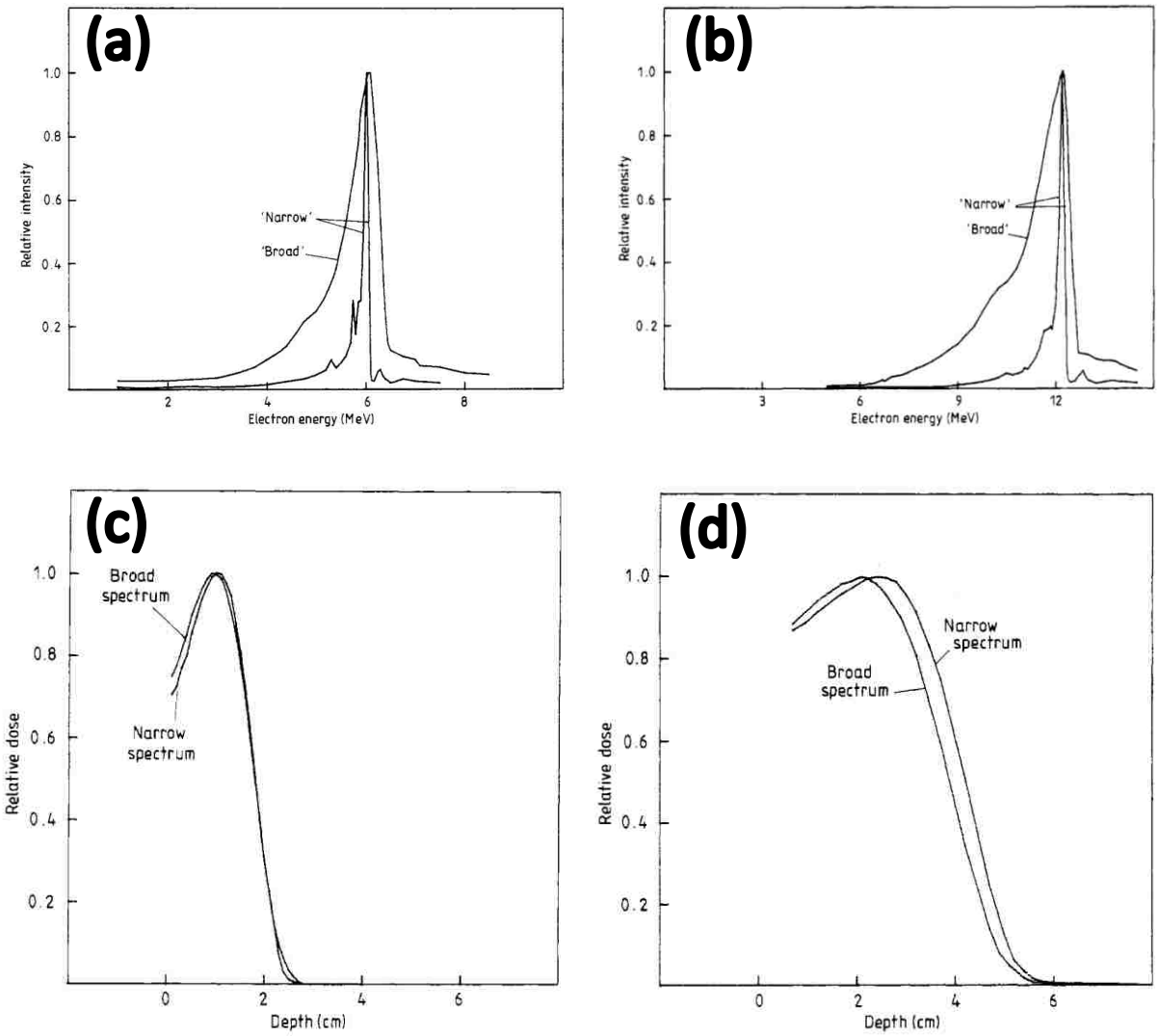

Figure 1.6. Narrow and broad energy spectra and their %DD curves. Plotted are (a) measured narrow and broad energy spectra and (c) corresponding %DD curves for a 6 MeV beam as well as (b) narrow and broad energy spectra and (d) corresponding %DD curves for a 12 MeV beam (from Johnsen et al 1983).

Other MC simulations performed by Andreo *et al* (1989) also studied the effect of different energy distributions on the %DD curves. Like Kainz *et al*, they simulated monoenergetic, monodirectional point beams through a scattering foil system. Then, they scored the energy spectra of electron beams within a 10-cm diameter circle on the surface of water phantom after they had been transported through a lead foil of varying thicknesses followed by one meter of air. Initial monoenergetic energies of 11.5, 10.49, and 10.25 MeV were used in combination with 1.0, 0.3, and 0.1

mm of lead, respectively. These three lead thickness and initial energy combinations were selected because they all produced $E_{p,o}$ values of 10 MeV (± 0.02 MeV) at the surface of the water phantom yet had different spectral distributions and mean energies of the peak structure. These energy spectral distributions are illustrated in Figure 1.7. The narrowest distribution corresponds to the 0.1 mm foil, and the broadest distribution corresponds to the 1.0 mm foil, with the 0.3 mm foil falling in-between. At the surface, electron beams with 1.0, 0.3, and 0.1 mm of lead had mean energies of 8.56, 9.48, and 9.73 MeV, respectively, and FWHMs of 0.57, 0.13, and 0.04 MeV, respectively.

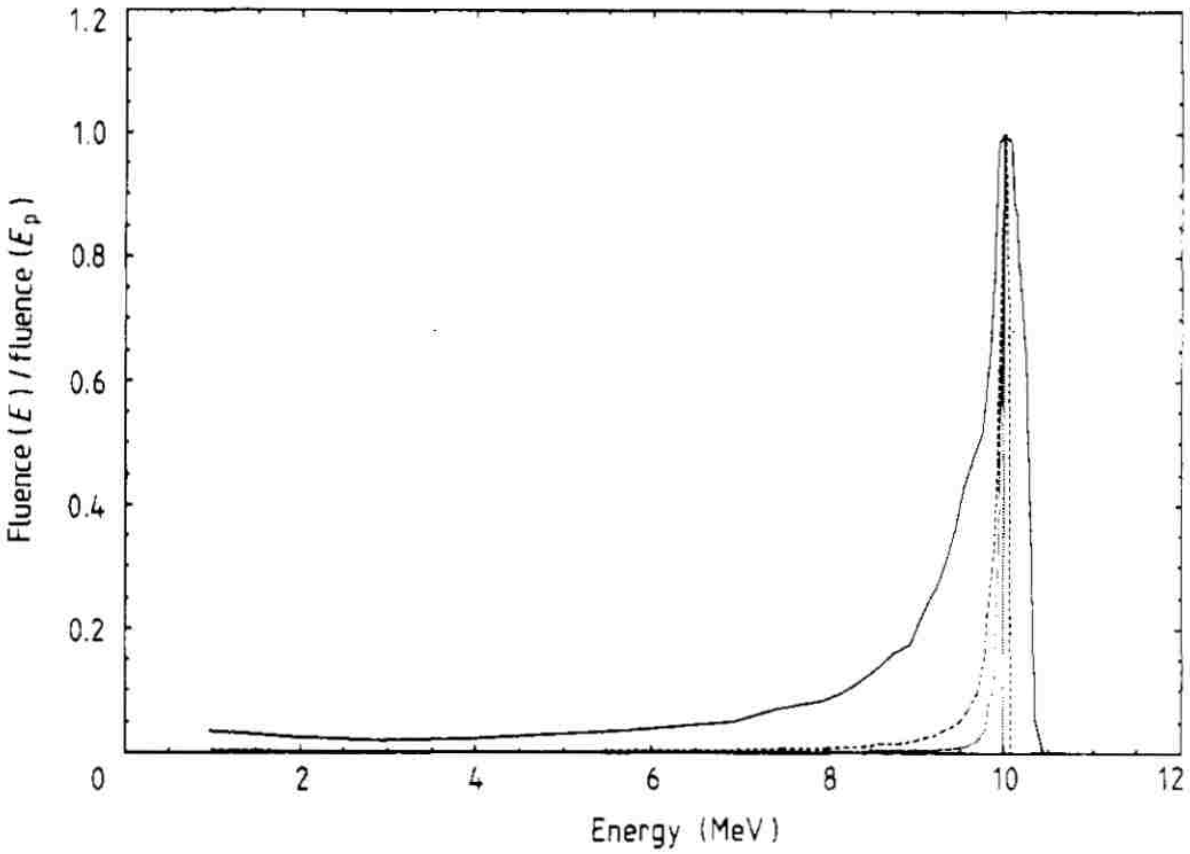

Figure 1.7. Variable width MC simulated energy spectra. Plotted are the energy spectra for three MC simulated electron beams transported through varying thickness of lead foils to the surface of a water phantom. The electron beams had energy spectra with FWHMs of 0.57, 0.13, and 0.04 MeV and $\bar{E}_o$ of 8.56, 9.48, and 9.73 MeV corresponding to lead foil thicknesses of 1.0, 0.3, and 0.1 mm, respectively. All the electron beams had $E_{p,o}$ values of 10 MeV (from Andreo *et al* 1989).

Andreo *et al* then simulated %DD curves using single point, monodirectional electron beams normally incident upon a water phantom that had the energy spectra shown in Figure 1.7. The reciprocity theorem was applied to the resulting dose distributions to calculate %DD curves of a broad plane-parallel electron beam (ICRU-35, 1984). Four %DD curves were calculated in this way, three with the three energy distributions illustrated in Figure 1.7, and a fourth with a 10 MeV monoenergetic energy distribution. The resulting %DD curves are plotted in Figure 1.8. The most penetrating %DD curves are, in order of increasing R_{50}, 1.0mm lead, 0.3mm lead, 0.1mm lead, and the monoenergetic beam.

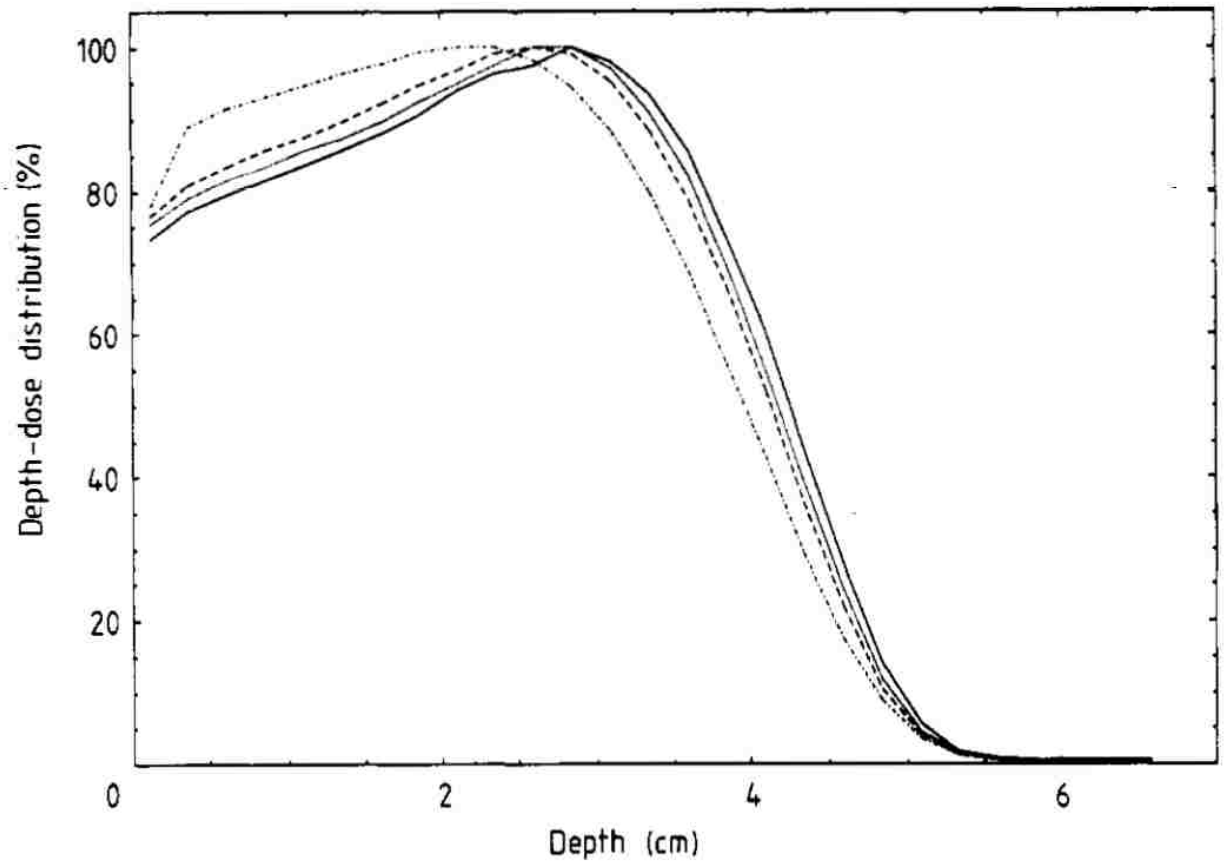

Figure 1.8. MC simulated %DD curves generated from the energy spectra plotted in Figure 1.7. The most penetrating %DD curves are, in order of increasing R_{50}, 1.0mm lead, 0.3mm lead, 0.1mm lead, and the 10 MeV monoenergetic beam (from Andreo *et al* 1989).

From Figure 1.8, it is apparent that the practical ranges of the electron beams vary noticeably even when the peak energies are almost identical. Clearly, the variations in R_p values are not attributable to the $E_{p,o}$ values. Interpreted through Johnsen *et al*'s work, this is probably because the mean energies in the electron beams' peak spectral structure are significantly different. Additionally, the R_{90-10} values increase significantly with the thickness of the lead foil. This is due to a significant increase in low-energy electrons created via energy-straggling. This increase in low-energy electrons also reduces the depth of R_{100} values and increases the surface dose and dose in the build- up region.

The above studies motivated the analytical methods employed by Deasy *et al* (1992 and 1994). Deasy modified equation 1.1, arguing that the left side of the equation should be the mean of the peak structure of the incident energy spectra, i.e.$\langle E \rangle_o^*$, rather than the $E_{p,o}$. The star in $\langle E \rangle_o^*$ denotes that the mean is taken only over the peak region. A more exact definition of $\langle E \rangle_o^*$ is given in section 3.1.4.2.1. Additionally, he relates the R_{50} and slope of the dose falloff region to $\langle E \rangle_o^*$, arguing that those %DD curve parameters are more strongly correlated with $\langle E \rangle_o^*$ than they are with $\bar{E}_o$ and FWHM, respectively.

Secondary electrons scattered from the beam collimation are another component of the energy spectrum that affect the %DD curves. Udale-Smith (1988) showed that secondary electrons deposit most of their energy at the surface of a water phantom and then fall off exponentially, as shown in Figure 1.9, becoming totally negligible at a depth of about 2.0 cm. Her study was performed with the 10 MeV beam on the SL75-20 accelerator, which used solid-walled applicators that produce more secondary electrons than current trimmer bar applicators. The total dose from the secondary electrons at the surface using this accelerator was about 5%. The secondary electrons rarely make much if any contribution to the portion of the %DD curve outside of the surface dose and buildup region, unlike the straggled electrons, which can affect practically all regions of the %DD curve excluding the most distal portions.

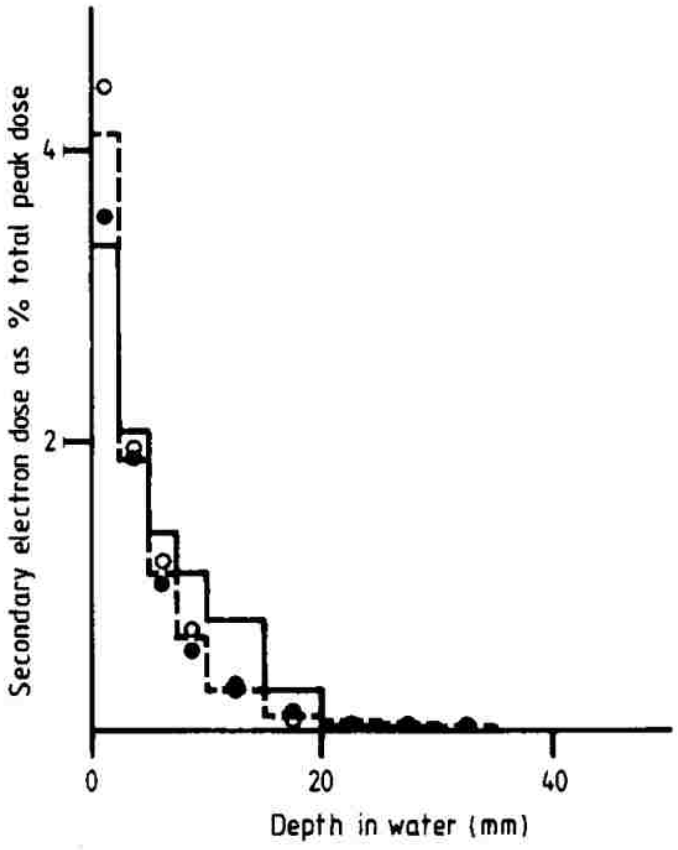

Figure 1.9. Secondary electron dose contribution versus depth. Plotted are deposited doses due to secondary electrons scattered from collimation versus depth in a water phantom for MC simulated 10 MeV electron beams. The different symbols correspond to different field sizes of solid-walled electron applicators use in the simulations (from Udale-Smith 1988).

1.1.5. Elements that affect Elekta Infinity accelerator energy spectra

In the Elekta Infinity linear accelerator, there are several major components that affect the energy spectra at isocenter. Some of these components are part of the treatment head, such as scattering foils and collimation, while others have to do with how the accelerating RF power is generated and transported to the traveling waveguide. The latter can be modified in service mode by "tuning" the energy spectra of the electron beams. Tuning is usually performed during accelerator installation or when the electron beam's range parameters have moved out of tolerance. Several of these components are presented below in the order in which they affect the electron beam.

The most essential accelerator setting related to the electron beam energy spectrum is the charge rate setting, titled “Chargerate” in Elekta’s service mode. Changing this parameter changes the kinetic energy of the electrons at the exit of the traveling waveguide. This parameter is always changed in tandem with the magnetron magnet current, titled “M.Mag ctrl” in service mode. The “Chargerate” setting modifies the magnitude of the DC voltage pulse applied to the magnetron. The greater the magnitude of this pulse, the higher the amplitude of the RF power sent from the magnetron to the injection point of the traveling waveguide. At the injection point, the electron bunches are formed and synchronized so that they enter the traveling waveguide at the peak strength of the RF power’s electric field, as electron bunches ride the crest of a single wave of the RF power’s electric field down the traveling waveguide. The greater the amplitude of the RF power, the greater the acceleration of the electron bunches. Because the electrons very quickly approach the speed of light, the magnitude of the RF power has a significant effect on the kinetic energy, but little effect on the speed. This is why one traveling waveguide, which can only be operated at one frequency, works for all electron beam energies. Thus, changing the magnitude of the DC voltage pulse changes the kinetic energy of the electrons exiting the traveling waveguide. The traveling waveguide was designed for RF power of a frequency around 3.0 GHz (private communications, McCann, Elekta engineer), meaning electron bunches enter the traveling waveguide about every 0.33 nanoseconds throughout the duration of the DC voltage pulse.

The DC voltage pulse is created when the pulse forming network (PFN), modeled as a series of capacitors and inductors in the top right portion of Figure 1.10, is discharged. This type of circuit releases the stored energy from the capacitors sequentially instead of simultaneously, allowing the release time to be extended to several microseconds (Karzmark *et al* 1992). The PFN is charged by the high voltage power supply illustrated in the top left portion of Figure 1.10 and discharged to the magnetron at regular intervals by a thyratron, which is a type of switch used in high-power RF circuits.

By increasing the charge rate to the PFN with the HT control system illustrated in the bottom left portion of Figure 1.10, the resulting DC voltage pulse applied across the magnetron is increased in magnitude. In this way, the charge rate setting increases the kinetic energy of electrons exiting the traveling waveguide. This setting is modified in tandem with the magnetron the "M.Mag ctrl" setting to maintain proper operation.

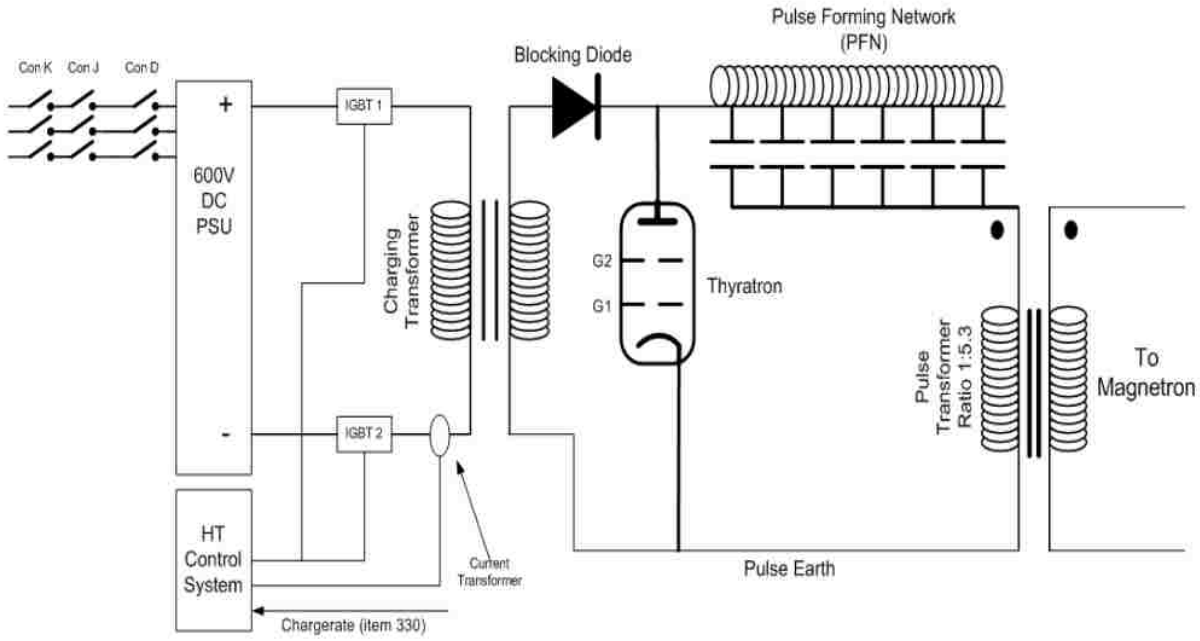

Figure 1.10. Elekta Infinity accelerator pulse forming network. Illustrated is a circuit diagram of Elekta's PFN related components. The HT control system generates a pulse in the PFN that is fed to the magnetron where it generates RF power (from Elekta Limited 2007).

Another important setting for the Elekta Infinity accelerator is the High Power PHase shifter (HPPH), which is a part of the recycling waveguide system. The recycling waveguide system is needed because magnetrons cannot produce RF power with a large enough amplitude to accelerate electrons to energies above 15 MeV. To compensate for this, some of the RF power is recycled throughout the duration of the DC voltage pulse, while the rest is dissipated in the RF load. This is done using the recycling waveguide system illustrated schematically in Figure 1.11 and pictorially in Figure 1.12.

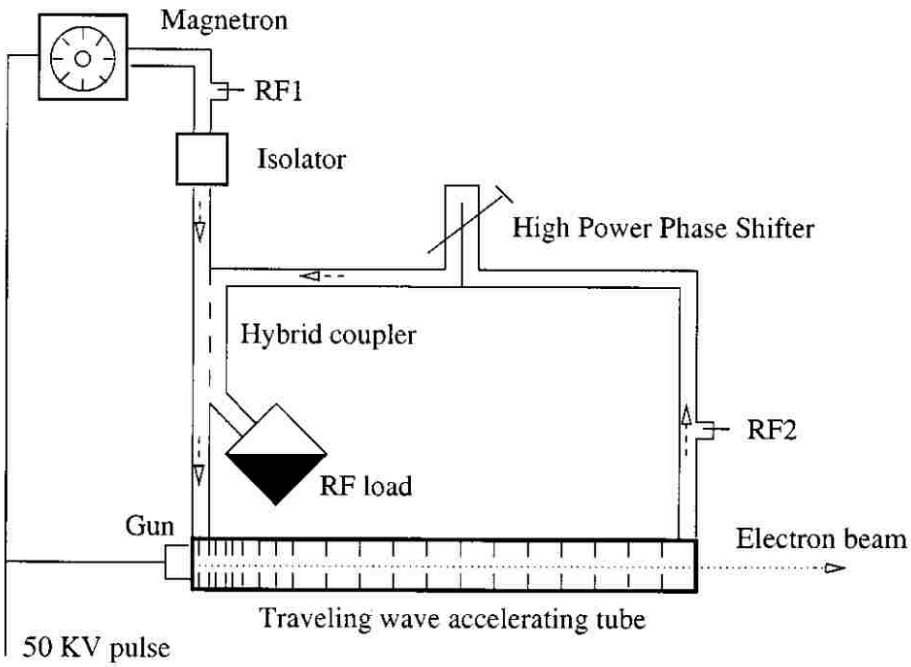

Figure 1.11. Traveling and recycling waveguide schematic. Illustrated is the traveling and recycling waveguide system for the Elekta, previously Phillips, SL25 accelerator. The HPPH is illustrated in a section of the recycling waveguide's length, as is the RF load where excess RF power is dissipated. Kok and Welleweerd sampled the RF power at the point labeled RF2 (Kok and Welleweerd 1999).

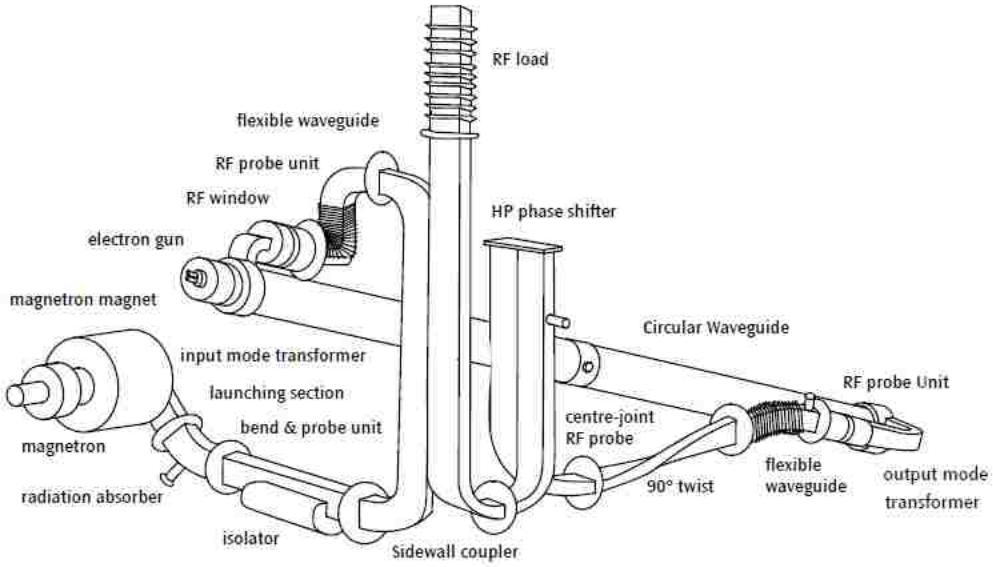

Figure 1.12. Traveling and recycling waveguide physical layout. Illustrated is the physical layout of the traveling and recycling waveguide shown schematically in Figure 1.11. The HPPH and RF load are visible in the illustration, as are the RF probe points Kok and Welleweerd used to sample the RF wave (from private communications, McCann, Elekta engineer).

After the RF power reaches the end of the traveling waveguide, the electron bunches are sent to the bending magnets, and the remaining RF power is circulated back to the injection point of the traveling waveguide. In doing so, the recycled RF power passes through the HPPH show in Figure 1.11 and Figure 1.12. The HPPH is a section of the recycling waveguide with variable RF path length. The RF path length can be modified by the operator in service mode. Ideally, the path length of the HPPH is set so that the recycled RF wave adds to the RF wave at the injection point at the correct phase. If the phase is incorrect, then the recycled RF wave will add to the RF wave coming from the magnetron in a way that is either too constructive or too destructive.

The effects of suboptimal HPPH settings on SL25 spectra were studied by Kok and Welleweerd (1999). Illustrated in Figure 1.13 are measurements of the accelerating RF wave's amplitude at the RF2 measurement point shown in Figure 1.11. Different HPPH settings change the way the RF wave amplitude changes with time. The duration of the RF pulse shown in Figure 1.13 is about 3.0 μs, as the DC voltage pulse that produced it lasted about 3.0 μs. The RF power amplitude seems to change in 1.0 μs steps, which is due to the fact that it takes about 1.0 μs for the RF power to cycle from the injection point through the traveling and recycling waveguide system and back to the same point. Most of this delay is due to the 0.86 μs filling time of the traveling waveguide (Kok and Welleweerd 1999). Thus, after the first microsecond, the RF amplitude increases in each of the proceeding 1.0 μs steps due to recycled RF being added to the RF injected from the magnetron. Changing the HPPH setting changes the phase at which this recycled RF is added back into the traveling waveguide, modifying the magnitude of the increase in RF amplitude during the second and third 1.0 μs steps.

The energy spectra that result from the HPPH settings in Figure 1.13 are plotted in the left column of Figure 1.14. The best way to understand the relationship between the RF amplitude plot in Figure 1.13 and the energy spectra measured at isocenter is to approximate the three 1.0 μs segments of the pulse in Figure 1.13 with rectangle functions that produce their own Gaussian energy spectra.

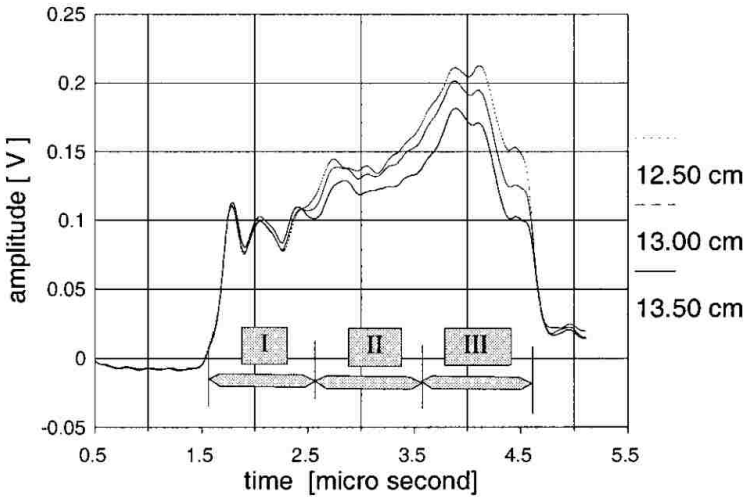

Figure 1.13. RF amplitude measured at RF2 point shown in Figure 1.11. Region 1, 2, and 3 correspond to the original RF power, addition of the first recycled power, and addition of the second recycled power, respectively. The shape of this curve varies with the phase of the recycled power, which is a function of the HPPH setting shown on the right (Kok and Welleweerd 1999).

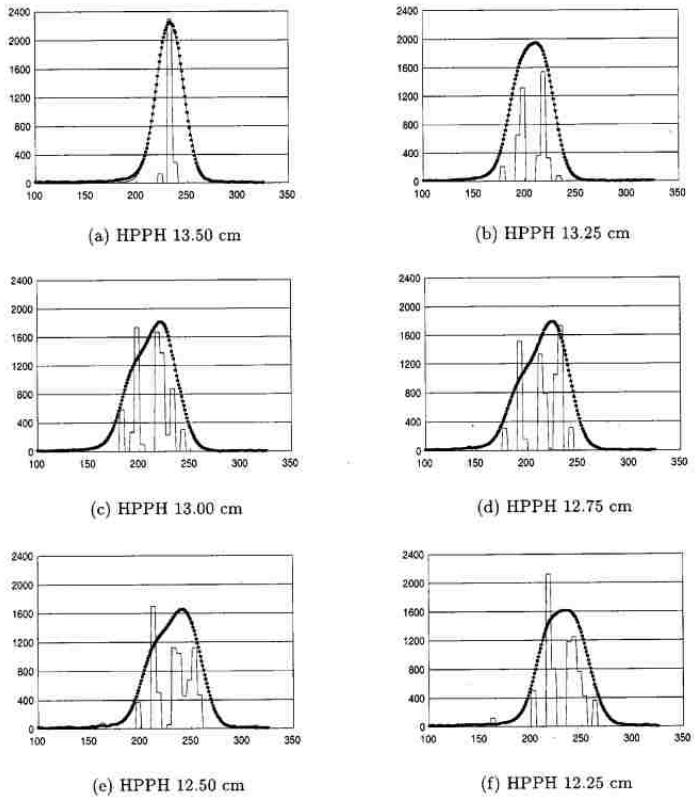

Figure 1.14. Elekta SL25 energy spectra with varied High Power Phase shifter settings. The x-axes are pixel numbers (distance) produced by the film scanner, which are roughly proportional to energy. The y-axes are relative fluence per unit distance. The three energy spectra on the left correspond to the three RF amplitude versus time plots shown in Figure 1.13 (Kok and Welleweerd 1999).

Each rectangle function will produce a single Gaussian energy spectrum, with the total energy spectrum being the compilation of three the Gaussian distributions. If the three sections of the RF pulse all have similar amplitudes, then the three Gaussian energy spectra that are summed up will have their peaks centered on the same energy. Thus, the total energy spectrum will approximate a single Gaussian, which is ideal. If the three sections of the RF pulse all have very dissimilar amplitudes, the total spectrum will look more like three single Gaussians that were shifted left and right relative to one another before being added together. This explains why the HPPH settings in Figure 1.13 that produce more level RF amplitudes across the duration of the RF pulse produce narrower spectra in Figure 1.14. In reality, the energy spectra at the end of the traveling waveguide is a product of the fine structure of the RF amplitude plot in Figure 1.13 and components beyond the traveling waveguide that modify the spectra.

Kok *et al*'s study of the HPPH's effect on the energy spectra was in part motivated by another study performed by Deasy *et al* (1996). Deasy *et al* measured energy spectra of the Phillips SL25 prior to its acquisition by Elekta, measuring the energy spectra plotted in Figure 1.15. It seems likely that suboptimal HPPH settings caused the multiple peaks observed in the spectra Deasy measured, though it is unclear why these spectra deviate so much further from the ideal single, narrow Gaussian than anything Kok *et al* were able to produce. It is possible that improvements were made to the SL25 after acquisition by Elekta.

The SL25 used for Kok *et al*'s measurements contained momentum slits in the slalom bending magnet that limited the energy spectra to $\pm$9% of the nominal energy (Kok and Welleweerd 1999). These slits, labeled "S" in Figure 1.16, when used in combination with the fine and coarse bending magnet currents of the slalom magnet, act as a variable band pass filter for the energy spectra exiting the traveling waveguide. The achromatic slalom magnet was designed to bend and focus electrons of various energies to a single focal point and direction at the exit window. The course bending magnet

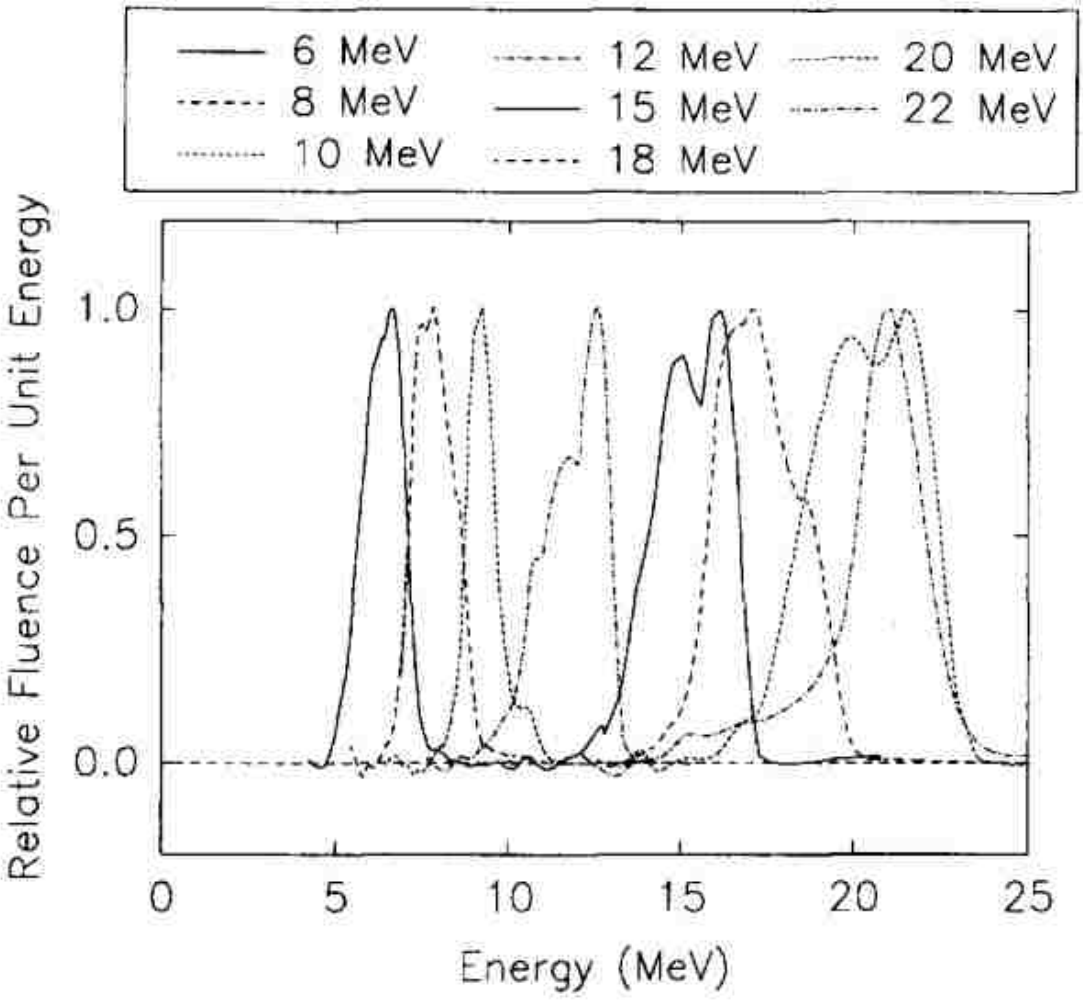

Figure 1.15. Measured electron energy spectra for 6-22 MeV beams from a Phillips SL25 accelerator. Many of the plotted energy spectra have two or more distinction peaks and aberrant shapes (Deasy *et al* 1996).

current, titled "Bending C." in Elekta's service mode, is a single current that is driven through three electromagnet pairs that make up the slalom magnet shown in Figure 1.16. In order to achieve proper bending, the portion of the slalom magnet that bends electrons 112.5° has an additional, separate electromagnet called the fine bending magnet which has its own current setting, titled "Bending F." in service mode. The fine and coarse bending magnet currents cannot vary independently, but must maintain a ratio of currents. By varying these currents in tandem, focusing can be maintained while

selecting different portions of the energy spectrum exiting the traveling waveguide for passage through the energy slits. An example of energy slit selection is shown in Figure 1.17.

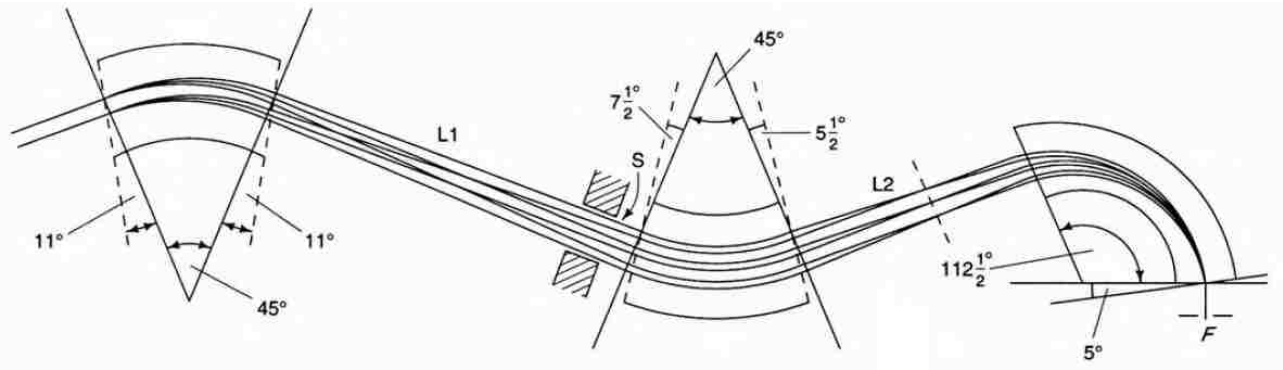

Figure 1.16. Slalom bending magnet for a Phillips SL25. The slits, labeled S, limit the spectrum of electron momentums that can pass through the slalom bending magnet, acting as a bandpass filter for the energy spectrum that exists prior to the bending magnet (Karmark *et al* 1992).

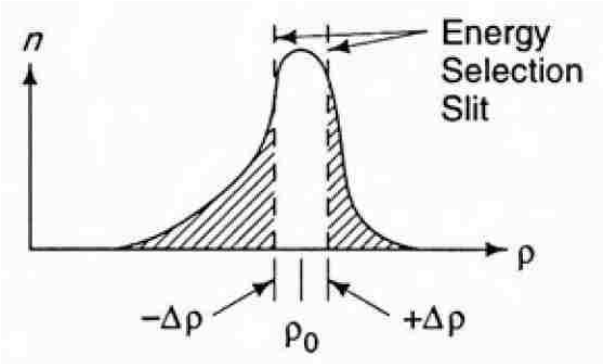

Figure 1.17. Energy selection using slits in the bending magnet. Illustrated is the portion of the electron fluence prior to the bending magnet allowed to pass through the slits shown in Figure 1.16 in terms of the electron fluence's momentum spectrum. The shaded portion of the spectrum is removed by the slits (modified from Karmark *et al* 1992).

After being transported through the slalom bending magnet, the energy spectra are modified by Elekta's dual scattering foil system illustrated in Figure 1.18. This system is composed of a primary foil, which spatially broadens the beam, and a secondary foil, which spatially flattens the beam. In the Elekta Infinity, as with all clinical accelerators, the primary scattering foil is made of a high Z material while the secondary foil is made of aluminum, a relatively low Z material.

In the process of shaping the beam, the scattering foils also reduce and broaden the energy spectrum and add a low-energy tail. This is illustrated in Figure 1.19, where a modeled energy spectrum

for the 11 MeV beam on the Elekta Infinity at MBPCC is Monte Carlo simulated from the (blue) exit window to the (green) collimator plane at 95-cm source to collimator distance (SCD) (Harris, 2012). Harris's simulation included a detailed physical model of the entire treatment head configured for electron therapy. The spectrum at 95-cm SCD, which is essentially at the patient, gained a low-energy tail due to more intense energy-straggling of some of the electrons. The shifting and broadening of the spectrum, including addition of the low-energy tail, is primarily due to the primary scattering foil. The energy spectra prior to the scattering foil system are obviously not perfect Gaussian spectra, as modeled by Harris, but rather products of the fine structure of the RF amplitude plotted versus time in Figure 1.13 and the energy-defining slits. The scattering foil system should smooth any fine structure as it reduces and broadens the energy spectra.

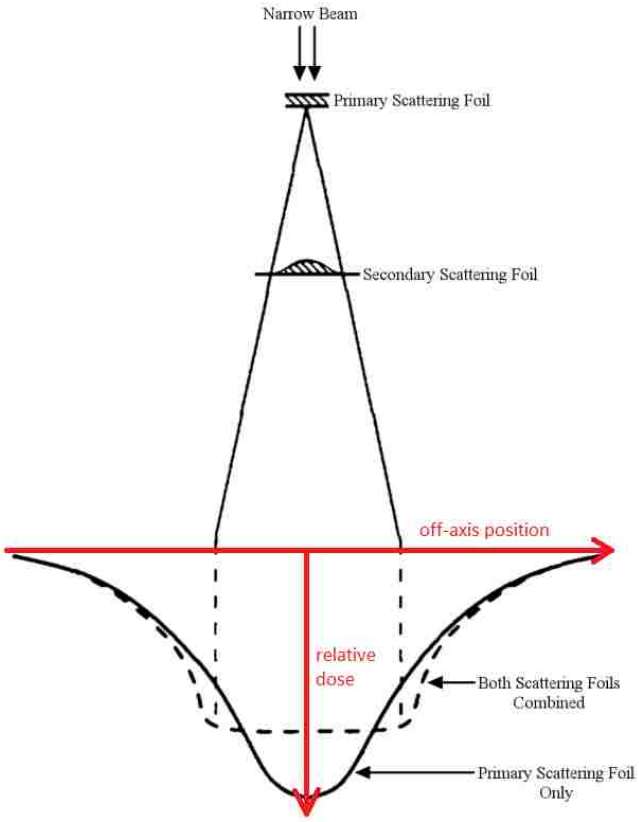

Figure 1.18. Dual-scattering foil system. Illustrated is the dual-scattering foil system used to create broad, flat electron beams at the patient. Dose distributions in a water phantom created both with and without the secondary scattering foil are illustrated, with the positive magnitude inverted for illustrative purposes (modified from Karzmark *et al* 1992).

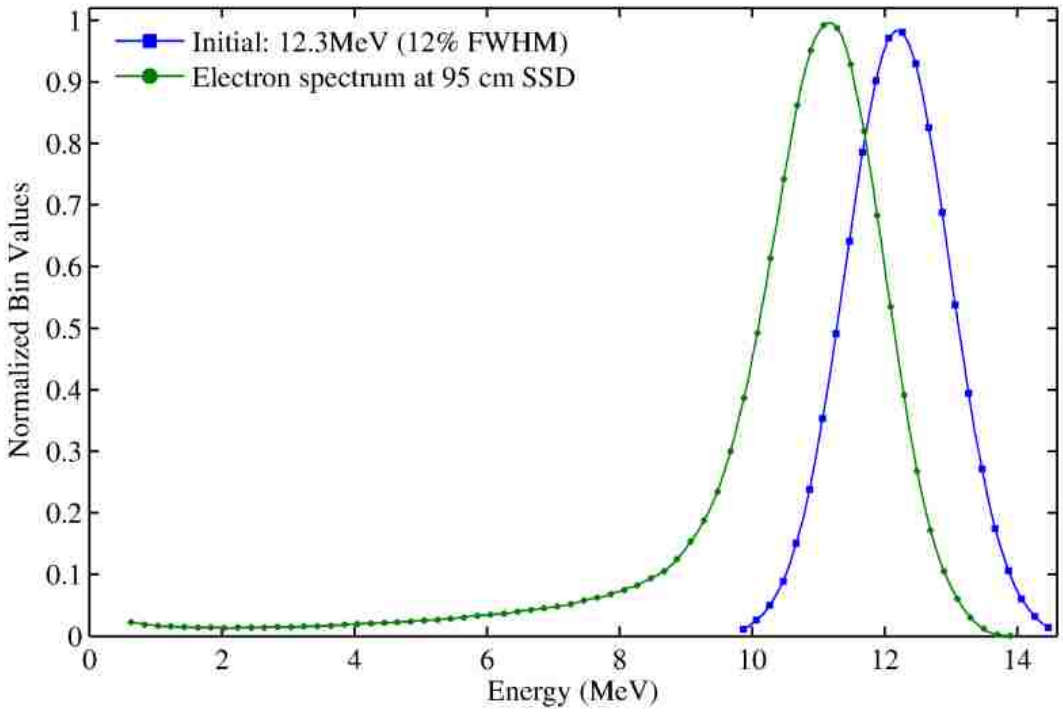

Figure 1.19. Energy spectra of electron beam simulated from source to 95-cm SCD. Illustrated are the energy spectra of the 11 MeV electron beam with an assumed Gaussian energy spectrum at the (blue) exit window MC simulated to (green) 95-cm SCD. The simulation included a detailed model of the accelerator treatment head and 14 x 14 cm^2 applicator of an Elekta Infinity accelerator (from Harris 2012).

1.1.6. Electron beam matching at MBPCC

Currently MBPCC has six Elekta Infinity accelerators that are commissioned for clinical use. These accelerators are located in Baton Rouge (BR), Gonzales (Gonz), Hammond (Ham), Houma, and Covington (CV1 and CV2), Louisiana, with plans to commission additional Elekta accelerators in the coming years. These accelerators were configured to deliver electron beams with nominal energies of 7, 9, 10, 11, 13, 16, and 20 MeV in order to achieve R_{90} values of 2.0, 2.5, 3.0, 3.5, 4, 5.0, and 6.0 centimeters, respectively, for the 14 x 14 cm^2 applicator. By matching the electron beams of the different accelerators to one reference, MBPCC can greatly reduce the commissioning time and effort, as only one set of beam data from one accelerator needs to be measured and processed for use in MU calculation software, treatment planning systems, and QA procedures. Without beam-matching, this data would need to be measured and processed for each accelerator, a process which would require

approximately two man months per accelerator. Additionally, beam matching allows patients to be moved between accelerators without replanning to accommodate accelerator outages or patient scheduling issues.

At MBPCC, a single Elekta accelerator was chosen as the reference for beam matching. All other accelerators were matched, within defined specifications, to this reference. Initially, the Elekta Infinity accelerator at the Gonzales satellite was the reference, as this was MBPCC's first Elekta accelerator. Subsequently, beam matching requires that (1) central axis %DD curves for the 14 x 14 cm^2 open applicator, (2) off-axis ratios (OARs) for the 25 x 25 cm^2 open applicator, and (3) dose output for the 14 x 14 cm^2 open applicator are matched. This is achieved by (1) tuning the energy spectra (i.e. beam tuning), (2) ensuring identical X-ray jaw settings exist for the same energy-applicator combination, and (3) possibly making minor modifications to the scattering foil systems, which is by far the least desirable solution. Criteria for agreement are (1) $\pm$2% or $\pm$0.05 cm distance to agreement (DTA) for all data points of the central-axis %DD curves, (2) $\pm$1% for OARs along diagonal and major axes with the 25 x 25 cm^2 open applicator attached at depths of 1.0 cm for $E_{p,o}$ values of 9 MeV and below and 2.0 cm for $E_{p,o}$ values above 9 MeV, and (3) $\pm$1% for dose output. MBPCC's matching criteria are the objective but in practice have not always been achieved. Therefore, the medical physicist may match the R_{90} through R_{20} points in the dose falloff region but fail to match R_{10} to within 0.05 cm. Also, the medical physicist may accept a $\pm$1.5% agreement in OAR for a large field far off axis. Matched electron beams for two different accelerators which fail the central axis %DD criteria are plotted in Figure 1.20.

To achieve these matching criteria, the Elekta engineer will tune each electron beam by modifying the accelerator settings mentioned in section 1.1.5 until the %DD curves match those of the reference accelerator at commissioning. This requires an iterative process of modifying accelerator parameters, taking %DD curve measurements, and then checking the %DD curves versus those of the reference accelerator's %DD curves.

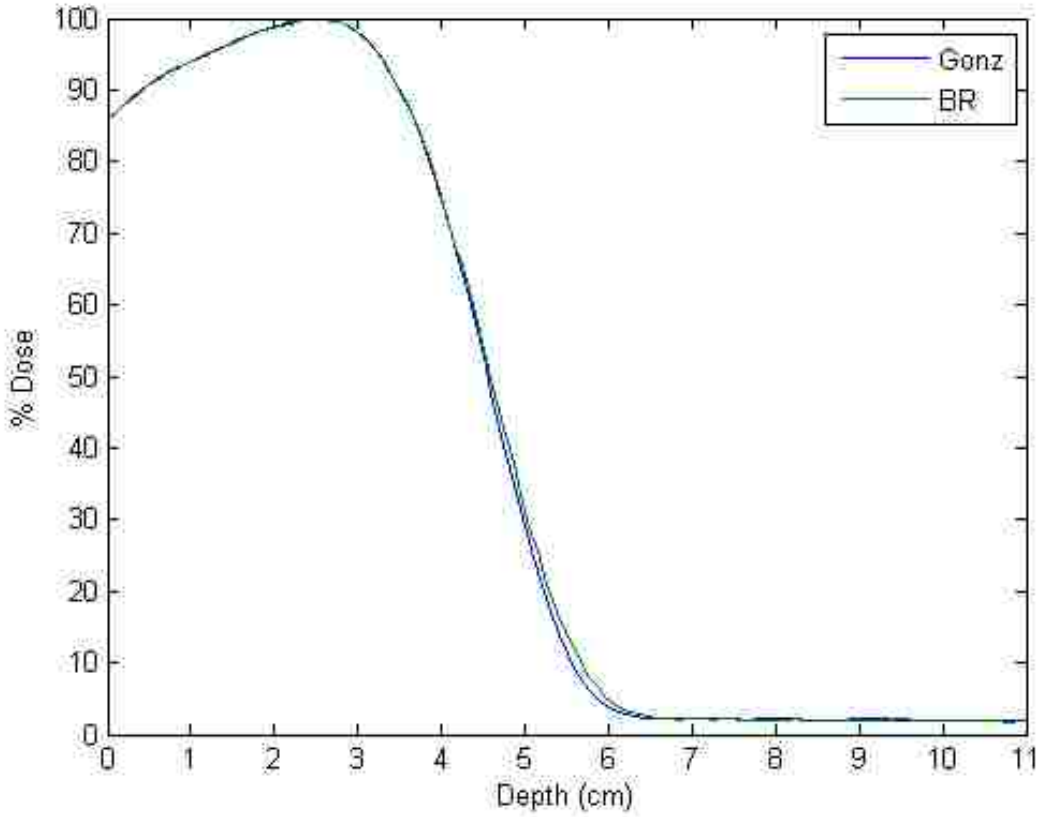

Figure 1.20. Matched 11 MeV Elekta Infinity accelerator electron beams. The plotted %DD curves were measured by MBPCC's clinical staff during commissioning at their (blue) Baton Rouge facility and (green) Gonzales satellite facility. The Baton Rouge %DD curve fails to meet MBPCC's 0.05 cm matching criteria with the Gonzales %DD curve around R_{10}.

1.2. Permanent magnet electron energy spectrometer

There are several different methods available for measuring the energy spectra of electron beams, most of them having serious drawbacks. Total absorption scintillators or semi-conductor detectors, i.e. counting detectors, can determine the kinetic energy of incoming electrons but are impractical because the high fluence rate of the therapeutic electron beams causes pulse pile-ups. Gas Cherenkov detectors measuring light intensity versus gas pressure can measure energy spectra, but have severe experimental conditions, such as requiring high gas pressures and very low noise, as the derived energy spectra are proportional to the second derivative of the light-intensity vs. pressure curves (ICRU 35 1984). To date, the most practical method for measuring electron beam energy spectra is magnetic spectroscopy. A limitation to magnetic spectroscopy is that the required collimation only

allows nearly completely forwarded directed electrons through to the detecting medium. This disallows secondary and highly straggled electrons from contributing to the measured energy spectrum, as their angles are rarely forward directed. However, information about such electrons can be gained using MC simulations.

Deasy *et al* (1994) constructed a magnetic spectrometer by using an electromagnet to sweep a collimated electron beam across a slit placed in front of an electron-counting scintillating detector and correlating the electromagnet current to the energy of the electrons that would be allowed to interact with the detector, thus determining the relative fluence within an energy bin. The collimation also reduced the electron fluence to a level that would not cause significant pulse pile-up in the scintillator. Additional shielding was added to guard the scintillator against bremsstrahlung X-rays. A helium-filled chamber was used to reduce the electron scatter inside the bending magnet cavity. Though described by Deasy *et al* (1994) as small and lightweight, the dimensions and mass of its most essential and massive component, the powered electromagnet, were 31 x 17 x 28 cm^3 (H x L x W) and 50kg (110lb), respectively. Transporting such a system would be cumbersome, reducing clinical applicability. Furthermore, the power supply needed for the electromagnet and the helium-filled chamber are added experimental constraints that further reduce clinical applicability.

The magnetic spectrometer used for this study is significantly smaller that Deasy's. Its most essential component is the permanent magnet block, pictured in Figure 1.21, which has a volume of 6.4 x 16.5 x 7.7 cm^3 (W x L x H) and mass of approximately 4kg (9lb). The magnet block (provided to LSU by Professor Edison Liang's research group in the Dept. of Physics and Astronomy at Rice University in Houston, TX) consisted of two permanent neodymium magnets separated by two iron end pieces. This assembly was then encased in aluminum plates. The magnets bend the trajectories of electrons that enter the front aperture of the magnet block. The bending takes place in the gap between the permanent magnets that is at equilibrium with the ambient air, meaning no power supply or helium-

filled/vacuum chamber is necessary. The lack of a helium-filled/vacuum chamber is acceptable, as the distance traveled by the electrons in the air gap between the permanent magnets is less than the distance traveled by electrons in Deasy's helium cavity. A beam defining aperture consisting of a hole drilled in a copper block, i.e. the spectrometer aperture, abutted to the front of the magnet block is required for the magnet block to serve as a spectrometer.

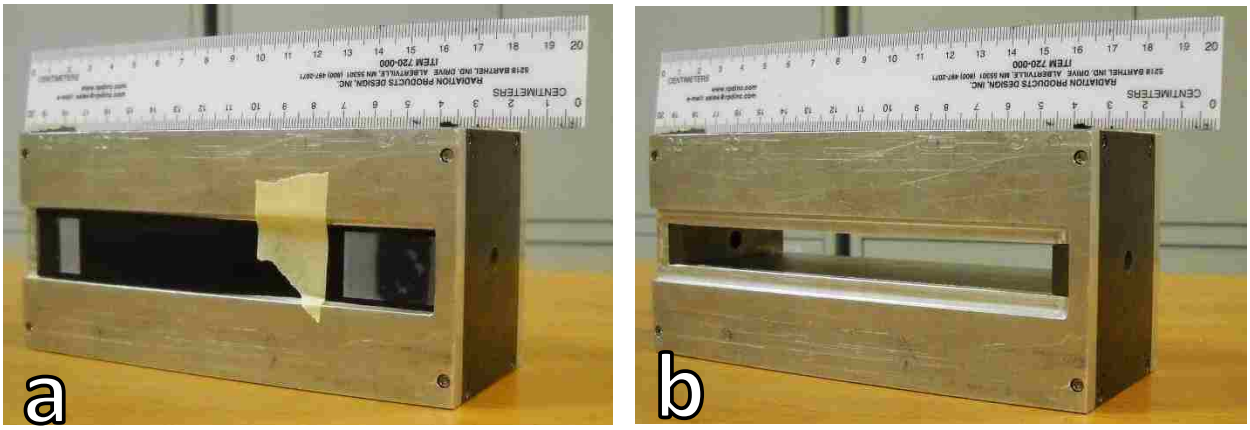

Figure 1.21. Permanent magnet block used for electron beam energy spectroscopy. The pictured magnet block is shown both (a) with and (b) without the CR strip inserted in its slot. The visible circular aperture is an entry point where the electrons enter the magnet block, and the visible slot is where the electrons exit the magnet block's air gap and intercept the CR strip.

Additional bremsstrahlung collimation was included in the magnetic spectrometer. This collimation, along with the copper spectrometer block, had a mass of about 17.7kg (39.0lb), bringing the mass of the entire device to 21.7kg (48lb). While still heavy, this compact device is easily transportable in pieces by a single user. Whereas Deasy *et al* (1994) used an electron-counting scintillator detector or radiographic film, this study's magnetic spectrometer used Computed Radiography (CR) plates cut into 6" X 1" strips for the detection medium. These strips were taped into a slot in the side of the magnet block at a reproducible position where they would intercept defelcted electrons. The electrons deposit energy into the photostimulable layer of the CR strips at positions that varied with the kinetic energy of the electrons. A laser scanner then triggered photostimulated luminescence and recorded the intensity of the luminescence as a function of strip position, forming CR strip images where the signal intensity of

the pixels were proportional to the deposited energy. These CR strip images were analyzed to determine the energy spectra at 95-cm SCD. Details of spectrometer design, data acquisition, and data analysis are explained in subsequent chapters of this thesis.

1.3. Motivation for study

Though the current method for tuning the electron beam energies to achieve matched beams produces satisfactory dosimetric results, the process is tedious, time-consuming, and suboptimal. It requires the user to measure a %DD curve every time adjustments are made to accelerator parameters that change the energy spectra. This requires the operator to setup a scanning water tank, and also requires the clinical medical physicist to infer aspects of the energy spectra from the %DD curves. By measuring the energy spectra directly, the scanning water tank used to measure %DD curves could possibly be eliminated from the beam tuning process, being used only for final verification. This should quicken the beam tuning process, and probably improve matching quality as %DD curves only indicate aspects of the energy spectra rather than the entire energy spectra. Regular measurements of the energy spectra could possibly replace current quality assurance (QA) checks of the energy that use Plastic Water® phantom slabs and a Farmer chamber.

1.4. Hypothesis

The purpose of this work was to use a permanent magnet electron beam energy spectrometer to measure and compare electron beam energy spectra on matched electron beams at MBPCC. Specifically, this work tested the following hypothesis:

Matched electron beams on MBPCC's six Elekta Infinity linear accelerators will have energy spectra that are sufficiently matched. Two spectra will be considered sufficiently matched if their incident modified peak mean energies, $\langle E \rangle^{*}_{m,o}$ (defined in section 3.1.4.2.1), and FWHM agree to within 0.12 MeV and 2.0 MeV, respectively, which corresponds to 0.05 cm and 0.1 cm agreement in the R_{50} and R_{80-20} values of the %DD curves, respectively.

1.5. Specific aims

The Hypothesis will be determined using the following four aims:

Aim 1 – Develop methods for measuring suitable CR strip images and intensity profiles

Determine the accelerator geometry, the geometry of additional electron beam collimation, the geometry of additional X-ray shielding, and the level of exposure to the CR strips that is required to obtain a suitable CR strip image and corresponding intensity profile (defined in section 2.1.7) for each of the seven electron beam energies using the permanent magnet spectrometer. Suitable implies the image was created with (1) an electron beam exposure that delivers, but does not exceed, 1.0 cGy peak dose to the CR strip, i.e. an exposure limitation inherent to the CR strip readout device used in this study (2) an irradiation time sufficiently long to minimize the variation in the beam phase space inherent to the first few milliseconds of irradiation, i.e. > 5sec, but short enough to be convenient, i.e. < 60sec, (3) a sufficiently parallel electron beam so that divergence does not need to be included in the electron beam model used for data analysis, (4) a diameter small enough to ignore electron beam spread outside the 1" width of the CR strip and provide good energy resolution in the corresponding intensity profile, and (5) a peak signal to X-ray background ratio of approximately 1.5:1 or better for the intensity profile.

Aim 2 – Develop methods for transforming measured intensity profiles into energy spectra at 95-cm SCD

Develop the methodology to transform a measured intensity profile into an energy spectrum on central axis at 95-cm SCD. This was done by (1) extracting and smoothing net dose profiles (defined in section 3.1.1) from the intensity profiles, (2) transforming the net dose profiles into energy spectra at the spectrometer aperture, and (3) transforming the energy spectra at the spectrometer aperture to those on central axis at 95-cm SCD. Because the above tasks used equation 2.7 (defined in section 2.1.2), a fit of equation 2.7 to clinically derived energy and position parameters was performed to obtain values for the parameters B_z and x_o used in equation 2.7. This analysis, performed using MATLAB

R2012a, was verified with a calculated net dose profile derived from an assumed energy spectrum at the spectrometer aperture in place of a measured net dose profile.

Aim 3 - Compare energy spectra of matched electron beams

Determine the energy spectra on central axis at 95-cm SCD for each of the seven electron beams on each of the six MBPCC Elekta Infinity accelerators by applying the analysis techniques of Aim 2 to intensity profiles measured in Aim 1. Compare all matched electron beam energy spectra.

Aim 4 - Correlate measured energy spectra metrics with %DD curve metrics

For every electron beam whose energy spectrum was measured, compare the $\langle E \rangle_{m,o}^{*}$ values and FWHM values of the energy spectra with the R_{50} and R_{80-20} values. Values for R_{50} and R_{80-20} were determined from relative ionization measurements in Plastic Water® phantom slabs taken in tandem with the energy spectra measurements.

Chapter 2 Aim 1 – Develop methods for measuring suitable CR strip images and intensity profiles

Aim 1: Determine the accelerator geometry, the geometry of additional electron beam collimation, the geometry of additional X-ray shielding, and the level of exposure to the CR strips that is required to obtain a suitable CR strip image and corresponding intensity profile (defined in section 2.1.7) for each of the seven electron beam energies using the permanent magnet spectrometer. Suitable implies the image was created with (1) an electron beam exposure that delivers, but does not exceed, 1.0 cGy peak dose to the CR strip, i.e. an exposure limitation inherent to the CR strip readout device used in this study (2) an irradiation time sufficiently long to minimize the variation in the beam phase space inherent to the first few milliseconds of irradiation, i.e. > 5sec, but short enough to be convenient, i.e. < 60sec, (3) a sufficiently parallel electron beam so that divergence does not need to be included in the electron beam model used for data analysis, (4) a diameter small enough to ignore electron beam spread outside the 1" width of the CR strip and provide good energy resolution in the corresponding intensity profile, and (5) a peak signal to X-ray background ratio of approximately 1.5:1 or better for the intensity profile.

2.1. Methods and materials

2.1.1. Overview of permanent magnet electron energy spectrometer

The basic irradiation geometry of the permanent magnet spectrometer used in this study is illustrated in Figure 2.1. A two-aperture design was used for the collimation of the electron beam, with the first aperture being a hole drilled in a Cerrobend® applicator insert positioned at 95-cm SCD and the second aperture, henceforth the spectrometer aperture, being a hole drilled in a copper block that abuts the magnet block. The two-aperture collimation design reduces the electron fluence rate at the CR strip, allowing suitability criteria (1) and (2) of Aim 1 to be achieved simultaneously. Second, it creates a highly parallel electron beam for passage into the magnet block and limits its diameter, achieving suitability criteria (3) and (4) of Aim 1, respectively. Using a parallel electron beam for this

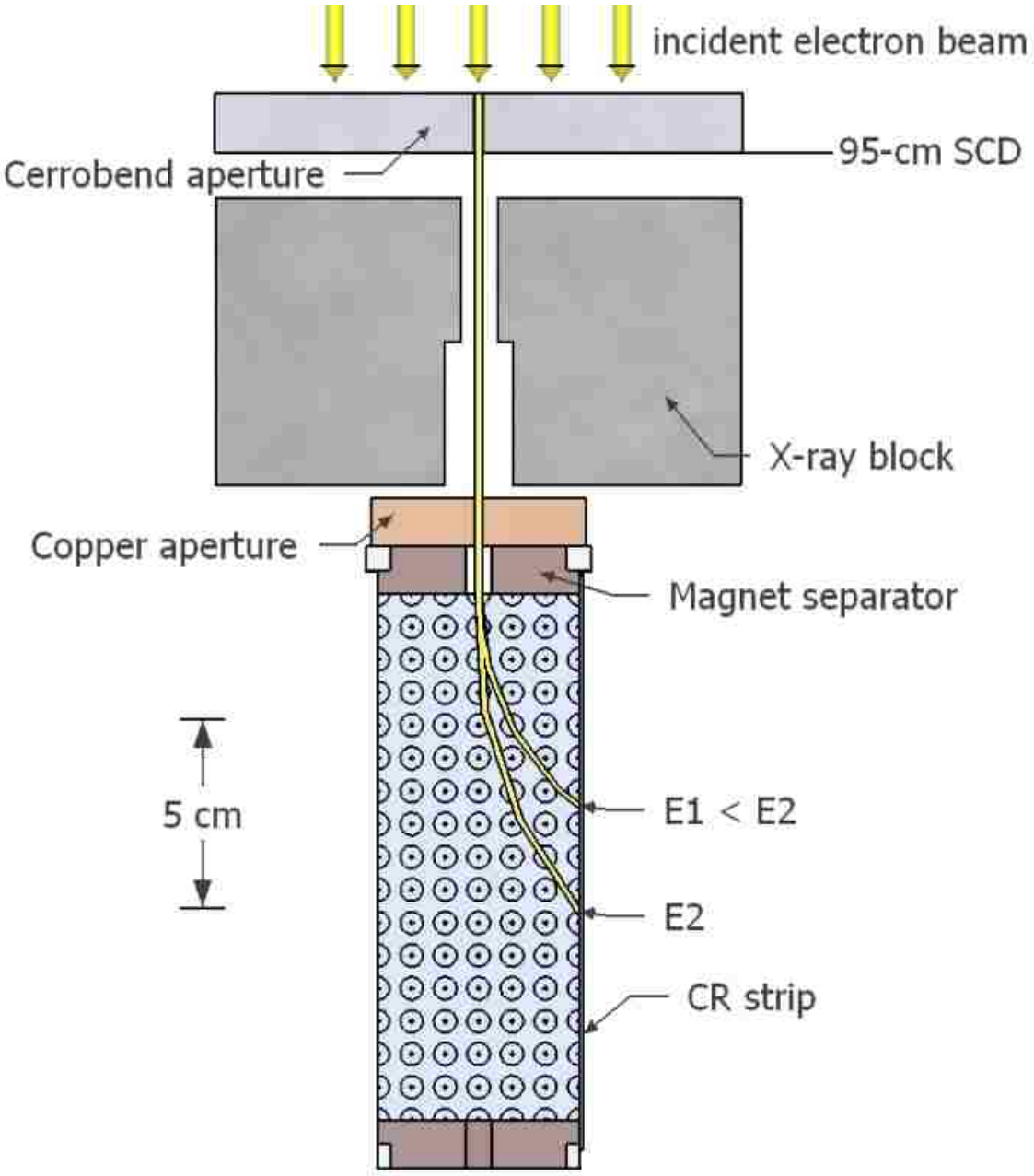

Figure 2.1. Cross-section of the magnetic spectrometer and beam collimation components. Illustrated is a top-down view of a cross-section of the magnet block, its idealized magnetic field model, and example electron paths. The magnetic field vectors that comprise the magnetic field point out of the page. The incident electron beam is collimated into a small circular beam by the first aperture made of Cerrobend®. The second aperture made of copper defines the beam's diameter before it enters the magnet block. The two together create a highly parallel beam and reduce the number of electrons entering the magnet block. The dipole magnetic field (blue area) bends electrons according to the Lorentz force law, dispersing different energies such that higher energy electrons (E2) travel further downstream than lower energy electrons (E1) prior to striking the CR strip. The lead X-ray block shields the CR strip from bremsstrahlung X-rays emitted by beamline components, primarily the primary scattering foil. All dimensions are to scale.

study greatly simplified the detector measurement theory for Aim 2 (Chapter 3). The lead block in Figure 2.1 limited the amount of bremsstrahlung X-rays reaching the spectrometer's CR strip, achieving suitability criterion (5) of Aim 1. More detailed schematics of the complete magnetic spectrometer and collimation apparatus are available in Appendix A.

The perpendicular magnetic field created by the permanent magnets in the magnet block is illustrated as the dotted-circle, blue region inside the magnet block in Figure 2.1. This magnetic field bends the electron trajectories to one side. The higher the kinetic energy of the electrons, the further downstream, i.e. away from the source, the electrons will travel in the air gap before colliding with the CR strip placed to the side. Thus, there is a relationship between where an electron deposits energy on the CR strip and the kinetic energy of the electron. Therefore, the spread in deposited energy that forms the latent image in the CR strip's sensitive layer contains information about the spectrum of the kinetic energies incident on the spectrometer aperture in front of the magnet block. This information was analyzed to determine the energy spectrum of the electron beam (Aim 2, Chapter 3).

Figure 2.2 illustrates the magnetic spectrometer and beam collimation of Figure 2.1 setup on MBPCC's Baton Rouge Elekta Infinity accelerator for energy spectra measurements. Additional details of the principal of operation, magnetic field, measurement geometry, exposure conditions, detection medium now follow.

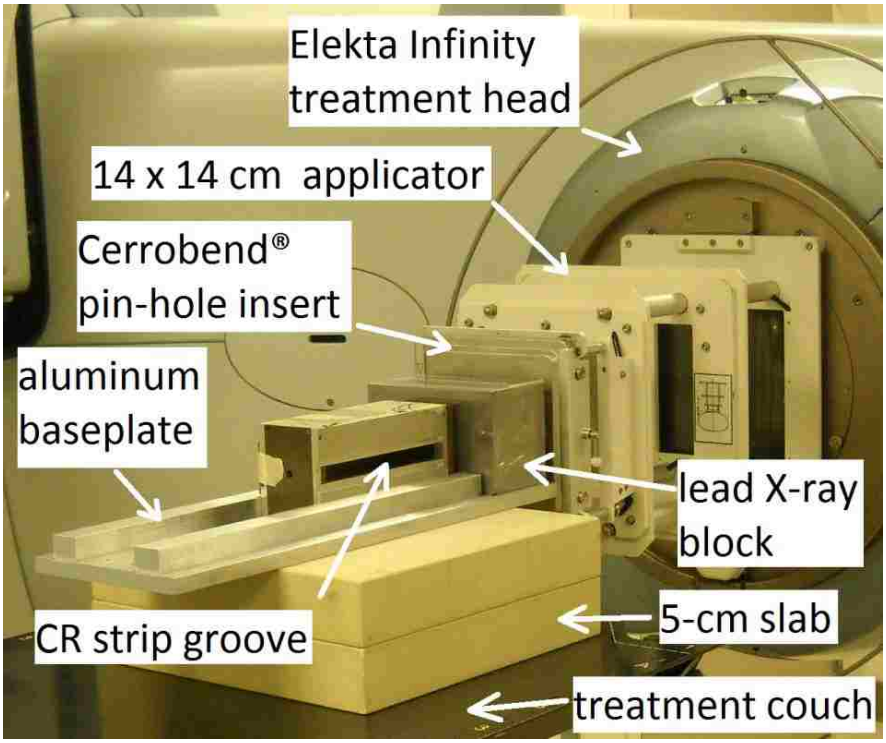

Figure 2.2. Complete irradiation geometry. The irradiation geometry in Figure 2.1 is pictured with respect to the Elekta Infinity accelerator rotated to 90°, producing a horizontal beam collimated by its 14 x 14 cm^2 applicator. The magnet and X-ray block were constrained by rails and screws, respectively, on an aluminum base plate added for alignment purposes. The baseplate was set on top of two 5-cm Plastic Water® blocks placed on the treatment table to make it easier for a user to look down the rails and align the apparatus so that apertures are concentric. After turning off the vault lights, cardboard was taped over the unoccupied magnet block slot opposite the slot occupied by the CR strip to shield the CR strip's sensitive layer from any left-over ambient light, as visible light erases CR strips.

2.1.2. Principle of spectrometer operation and Lorentz force law

The fundamental principal of operation behind this study's magnetic spectrometer is a one-to-one correlation between the kinetic energy of the electrons entering the magnet block and the position at which the electrons strike the CR strip. A single CR strip position is not correlated to a single kinetic energy of a monoenergetic electron beam because a single beam energy projects to a finite distribution at the CR strip, i.e. the detector response function. This distribution, modeled in section 3.1.2.1, is ignored here. The derivation of the relationship between electron energy and CR strip position, as well as other aspects of this study's analysis, require the definition of a cartesian coordinate system relative to the magnet block. Such a coordinate system is defined in Figure 2.3.

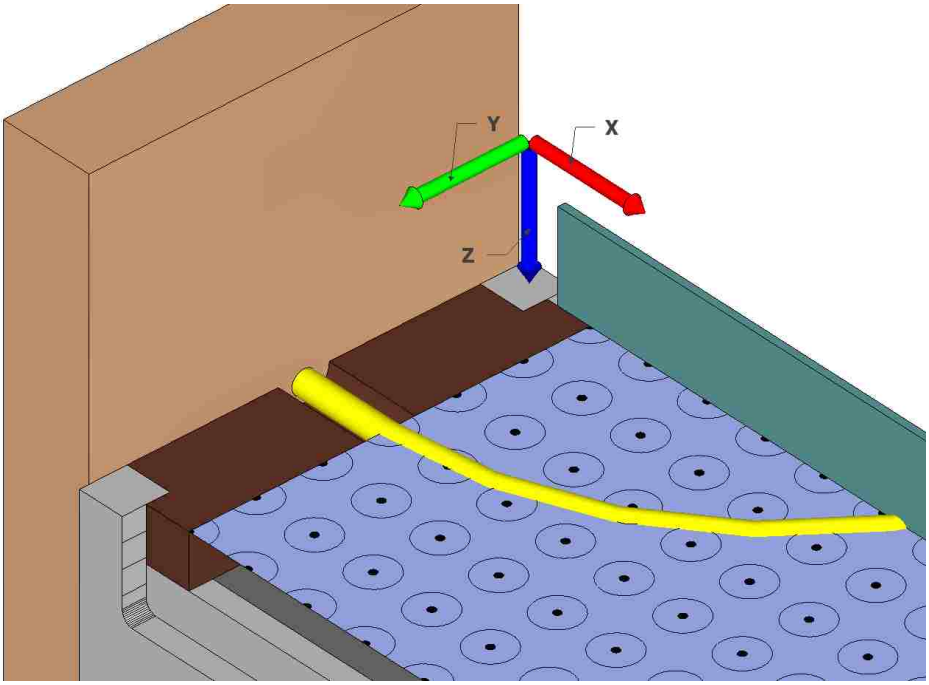

Figure 2.3. Spectrometer coordinate system. The Cartesian coordinate system is defined with respect to the enlarged view of the magnetic spectrometer of Figure 2.1. It shows the x direction in red, which is the aligned with the CR strip, the y direction in green, which is parallel to the front face of the magnet block, and the z direction in blue, which is parallel to the magnetic field vectors. An example collimated electron beam trajectory is illustrated in yellow. All dimensions are to scale.

The position to energy relationship is based on a simplified model of the electron beam and the magnetic field in the magnet block's air gap. The magnetic field is modeled as not having a vector component in any of the directions orthogonal to the z direction referenced in Figure 2.3, hence B_x = B_y = 0. The magnetic field strength in the z direction, B_z, is assumed to be perfectly uniform throughout the blue shaded region illustrated in Figure 2.1, Figure 2.3, and Figure 2.4, which represents the physical cross section of the magnets, and zero outside of it. The edges of this blue dotted region are defined by the CR strips, the back face of the air gap near the exit aperture, and the effective entrance edge that starts at distance x_o downstream of $x = 0$, the CR strip origin. In Figure 2.4, the origin is the edge of the CR strip in the x-direction nearest the magnet block's entrance aperture. This means that in the model, the incoming electron beam sees no fringe field. Additionally, the electron beam is modeled as forward-directed, infinitely narrow, and centered in the middle of the magnet block's entrance aperture.

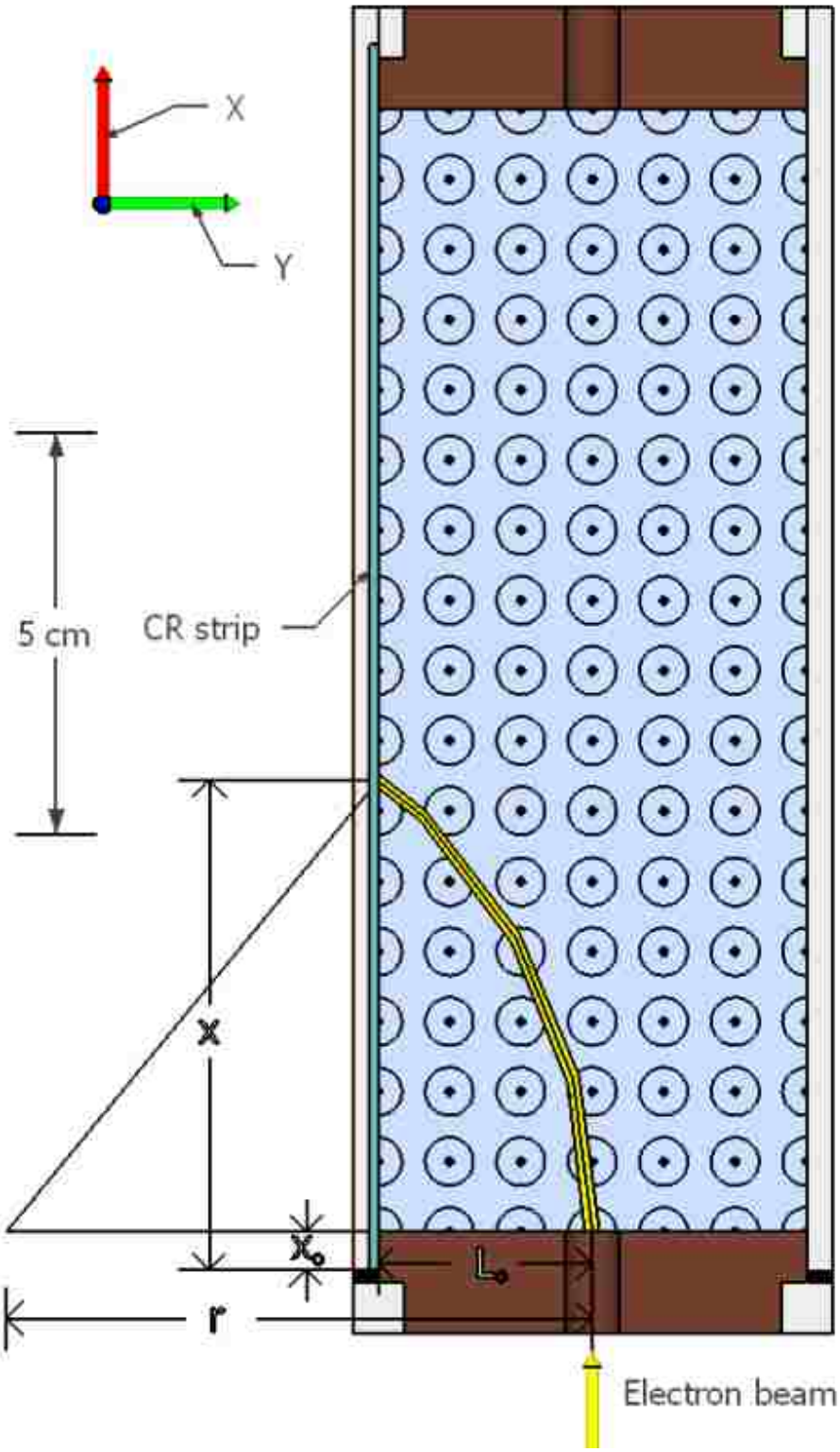

Figure 2.4. Electron trajectory variables for a point beam. An enlarged view of an example electron trajectory in Figure 2.1 shows the electron's radius of curvature, r, CR strip impact position, x, magnetic field offset relative to the edge of the CR strip nearest the source, x_o, and distance between CR strip and center of entrance aperture, L_o. All dimensions are to scale.

Equating the Lorentz force law to the centripetal force on an electron gives

$$F = \left|e\left(\vec{v} \times \vec{B}\right)\right| = \frac{mv^2}{r}, \tag{2.1}$$

where e is the charge of the electron, $\vec{v}$ is the velocity vector of the electron, $\vec{B}$ is the magentic field vector in the air gap, m is the mass of the electron, and r is the radius of curvature of the electron inside the magnetic field illustrated in Figure 2.4.

Solving for r yields,

$$r = \frac{p}{eB_z}, \tag{2.2}$$

where $p = mv$ is the momentum of the electron and B_z is the strength of the magnetic field in the negative z direction, i.e. the direction perpendicular to the plane of motion.

Geometrically,

$$r^2 = (r - L_o)^2 + (x - x_o)^2 , \tag{2.3}$$

where x is the position along the CR strip where the electrons deposit energy, x_o is the effective edge of the magnetic field with respect to the CR strip origin (i.e. $x = 0$) and L_o is the distance between the CR strip and the center of entrance aperture, all of which are illustrated in Figure 2.4.

Substituting equation 2.2 into equation 2.3 and solving for p results in,

$$p = \frac{eB_z}{2L_o}(x - x_o)^2 + \frac{eB_z L_o}{2}. \tag{2.4}$$

The momentum of an electron is related to its kinetic energy, E, and rest energy, E_o, by,

$$E = [p^2c^2 + {E_o}^2]^{\frac{1}{2}} - E_o , \tag{2.5}$$

where c is the speed of light. Substituting equation 2.4 into 2.5 gives

$$E = \left[\left\{\left(\frac{ec}{2L_o}(x - x_o)^2 + \frac{ecL_o}{2}\right)B_z\right\}^2 + {E_o}^2\right]^{\frac{1}{2}} - E_o . \tag{2.6}$$

Substituting actual values for the constants into equation 2.5 and converting the units results in,

$$E = \left[\left\{\left(0.517\frac{MeV}{cm^2 Tesla}(x - x_o)^2 + 4.35\frac{MeV}{Tesla}\right)B_z\right\}^2 + 0.261MeV^2\right]^{\frac{1}{2}} - 0.511MeV\,, \quad 2.7$$

where x and x_o are in centimeters and B_z is in Tesla. Note that x is the independent variable while x_o and B_z are parameters that were determined by fitting equation 2.7 to clinically-dervied energy and position parameters drawn from calibration measurements.

According to this model, when the radius, r, of an electron beam equals half of L_o, then it will complete a half circle and just barely impact the CR strip parallel to its face at CR strip position x_o. Electron beams with lower energies will miss the CR strip entirely. Hence, the lowest energy electron that can strike the CR strip, E_{cutoff}, is

$$E_{cutoff} = [\left(\frac{eB_z L_o}{2}\right)^2 c^2 + {E_o}^2]^{\frac{1}{2}} - E_o\,. \quad 2.8$$

2.1.3. Description of permanent dipole bending magnet block

The core of the permanent magnet spectrometer used throughout this study was the permanent dipole bending magnet block illustrated in Figure 2.5, henceforth called the magnet block. The magnetic field inside the magnet block was created by two rectangular 6" x 2" x 1" permanent N42 neodymium rare-earth magnets (Model NB085-5; Applied Magnets, Plano, TX) placed above and below the 9/16"-thick air opening. Collimated electron beams enter this air space after passing through the entrance aperture in the iron end piece labeled (1) in Figure 2.5. 9/16" of separation is created between these two magnets with internal lips formed by extruded portions of the two iron pieces placed at each end of the magnet block. These iron end pieces also help contain the magnetic field lines at the entrance and exit aperture ends of the magnet block, reducing the fringe fields there. The magnets and iron end pieces are surrounded by four aluminum plates whose dimensions are partially illustrated in Figure 2.5. Recessed areas cut in the two side aluminum plates, one of which is labeled (4) in Figure 2.5, accept CR plates cut into 1" x 6" strips for recording the spatial dispersion of electrons. These

permanent magnets, along with the iron and aluminum structure enclosing them, comprise the magnet block. This magnet block was loaned to LSU/MBPCC for this study by Professor Liang's research group in the Dept. of Physics and Astronomy at Rice University (Houston, TX).

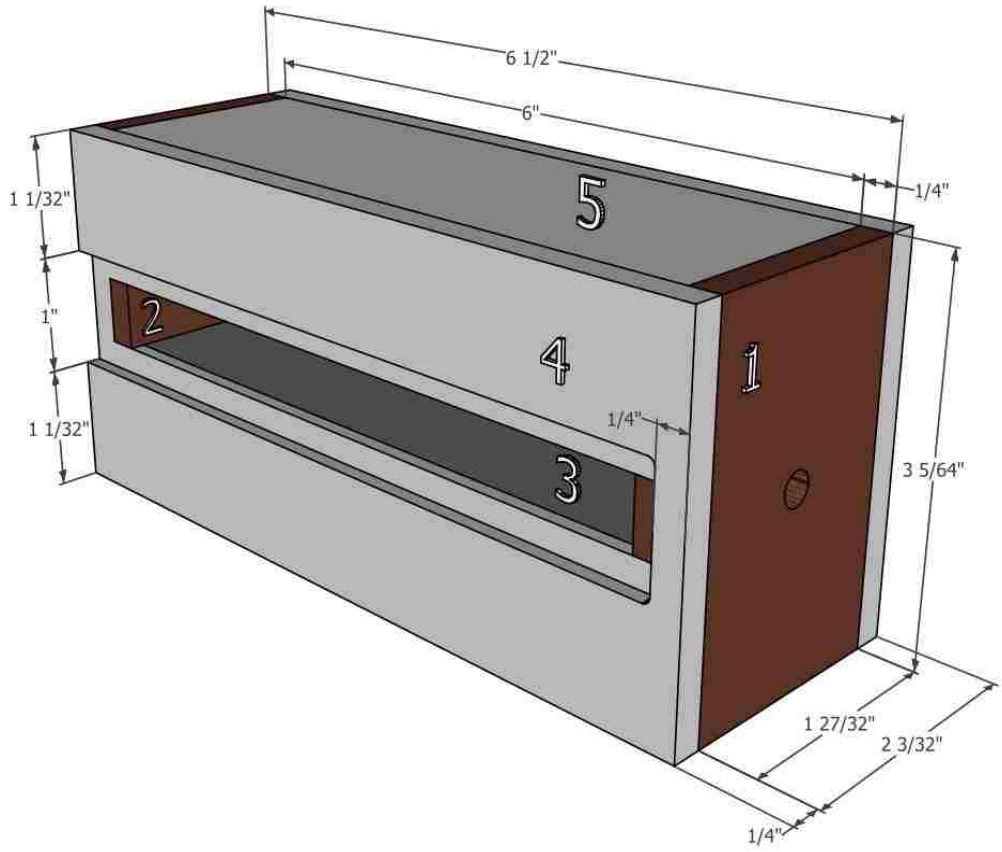

Figure 2.5. Magnet block dimensions. Labeled are (1) the face of iron magnet separator nearest the source and (2) furthest from the source, (3) the bottom of two the permanent neodymium magnets, (4) one of the two side aluminum plates with a slot cut into it, and (5) the top aluminum plate, with the bottom one being identical. The entrance aperture, which unlike the exit aperture is visible in this illustration, was drilled in the iron magnet separator nearest the source. Also, the CR strips were only placed in the visible slot as the opposite slot would only be useful for positron collection. All dimensions are to scale.

A map of B_z versus position for several xy planes, three of which are plotted in Figure 2.6, was provided by Liang *et al*. Measured B_z values vary from about 0.35 to 0.625 Tesla in the central portion of the air gap where the electrons travel, though for the vast majority of their trajectories electrons experience B_z values greater than 0.5 Tesla. Hence, B_z values were not spatially-uniform as assumed in the magnetic field model used in this study, though this discrepancy was ignored to simplify the analysis.

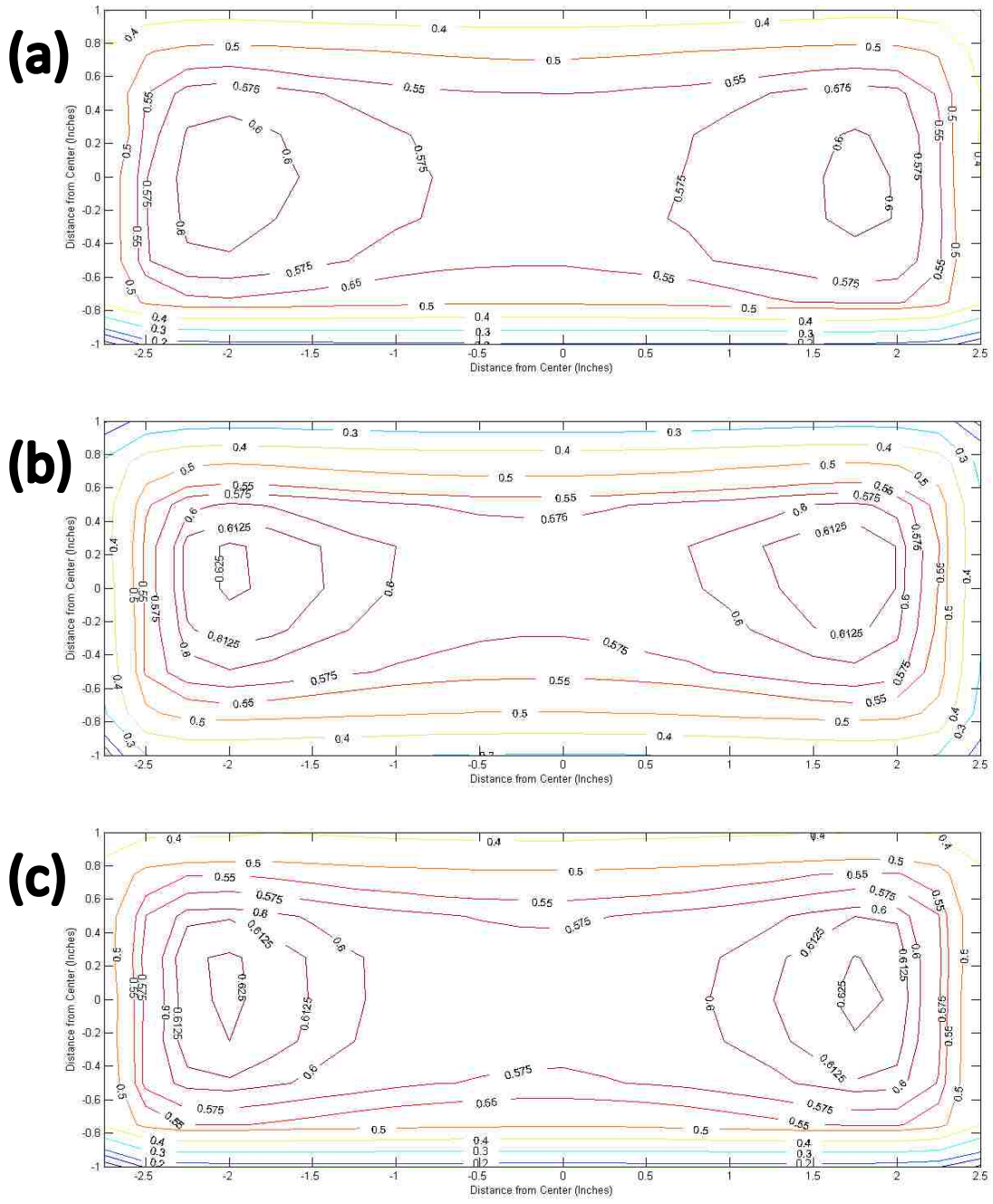

Figure 2.6. Map of Bz between inside the magnet block. Contours of B_z in Tesla for horizontal planes located (a) midway between the surface of the top magnet facing the air gap and midplane of the air gap, (b) at midplane of the air gap, and (c) midway between the the surface of the bottom magnet facing the air gap and midplane of the air gap.

2.1.4. Description of measurement geometry

2.1.4.1. Accelerator orientation

The magnetic spectrometer and its collimation was designed to lie flat on a horizontal surface and accept a horizontal beam. Hence, it was placed on the Elekta Infinity accelerator's treatment couch with the couch rotated to 270°, the gantry to 90°, and the collimator to 0° with the 14 x 14 cm^2 applicator attached, as shown in Figure 2.7. The magnetic spectrometer was oriented on the couch so that its central axis was collinear with the central axis of the electron beam during irradiation, as illustrated in Figure 2.1 and Figure 2.2.

Figure 2.7. Accelerator configuration during irradiation. The accelerator's gantry angle was set to 90°, collimator angle to 0°, and couch angle to 270° to deliver a horizontal beam to the magnetic spectrometer. During irradiation, the Cerrobend® aperture insert replaced the open-field applicator insert shown here.

2.1.4.2. Electron beam collimation

As stated earlier, a two-aperture design was used for the electron beam collimation. The two-aperture collimation design creates an approximately parallel electron beam with a limited diameter for passage into the magnet block and restricts the fluence striking the CR strip. These objectives were

achieved by adjusting the distance between the upstream Cerrobend® and downstream spectrometer apertures and their diameters.

Varying the diameter of the Cerrobend® aperture varies the number of electrons that are allowed to pass, meaning the Cerrobend® aperture diameter controls the electron fluence reaching the spectrometer aperture. Varying the distance between the two apertures also modifies the electron fluence reaching the downstream spectrometer aperture as the electron beam exiting the Cerrobend® aperture has an angular spread. Additionally, increasing the distance between the two apertures makes the beam entering the magnet block more parallel. Beyond 10.6 cm of separation the beam was considered parallel (divergence < 1.52°). Finally, increasing the diameter of the spectrometer aperture increases the diameter of the electron beam entering the magnet block.

Note that in selecting the diameter of the Cerrobend® aperture and the distance between the two apertures, there was an inherent tradeoff between meeting the Aim 1 objectives related to (2) irradiation time and (5) peak signal to X-ray background ratio. This trade-off exists because as the distances between the two apertures increases, the electron component of the signal decreases much more rapidly than the X-ray component, hence decreasing the signal to X-ray background ratio. Also, the irradiation time required to reach a maximum dose of 1.0 cGy to the CR strip increases because the electron fluence rate at the spectrometer aperture decreases. Similarly, reducing the size of the Cerrobend® aperture reduces the electron component of the signal but does not affect the X-ray background, hence reducing the signal to X-ray background. Also, reducing the fluence rate at the spectrometer aperture increases the irradiation time required to reach a max dose of 1.0 cGy to the CR strip.

The equations used to design the collimation geometry in this study, which were derived in section 2.1.5, were also used to calculate the appropriate number of MUs to deliver for each beam energy. These equations were used to determine the initial diameters of the apertures and the distance

between them. After determining a rough design with these equations, the design was fine-tuned with a series of test measurements to arrive at the design described below and illustrated in Figure 2.8.

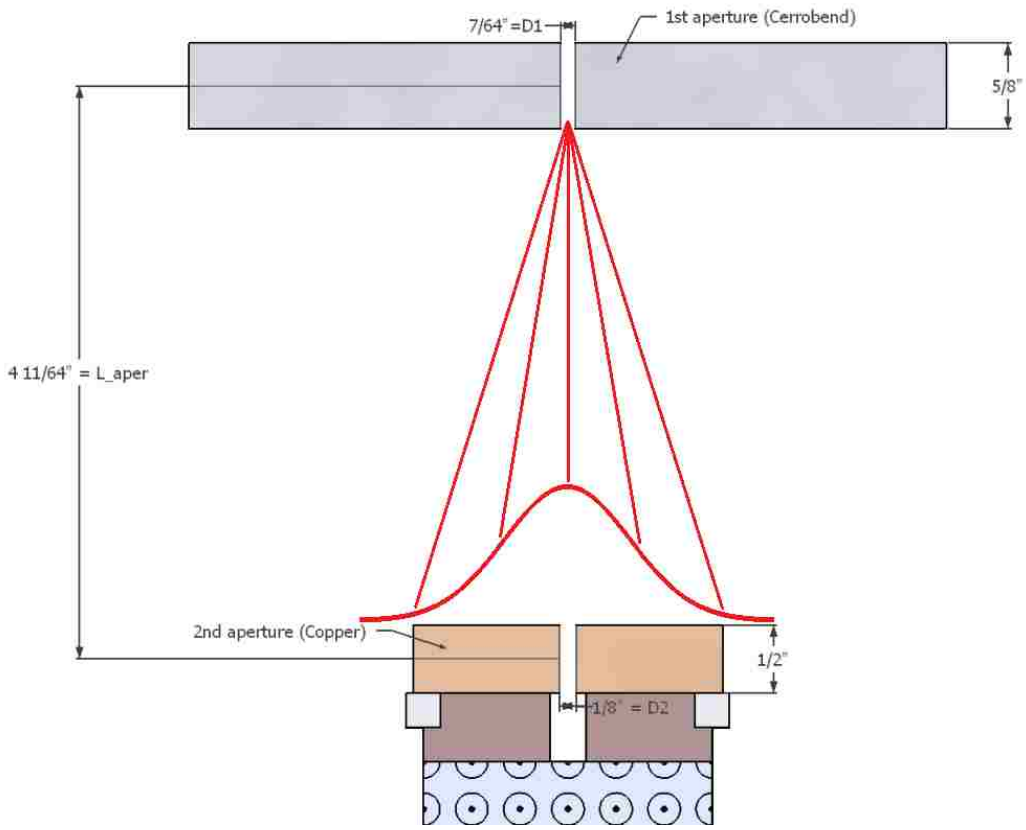

Figure 2.8. Electron beam collimation cross-section without the X-ray block. Schematic illustrates the thicknesses of the copper block and Cerrobend® insert, distance between the apertures, and diameter of the apertures with the X-ray block removed for illustrative purposes. The electron beam, illustrated in red, has an angular spread at the Cerrobend® aperture that spreads out to form a Gaussian spatial distribution at the spectrometer aperture. All dimensions are to scale except those of the Gaussian distribution, whose width was increased by about 50% beyond the width of a 7 MeV distribution.

As illustrated in Figure 2.8, the centers of the apertures were placed 4 11/64" (10.6 cm) apart. This separation was sufficient to ensure that the electron beam entering the magnet block can be approximated as parallel (divergence < 1.52°). The first aperture was a 7/64" hole drilled in the center of a Cerrobend® applicator insert. The Cerrobend® insert, shown in Figure 2.9 (a) and (b), as well as in Figure 2.8, was poured to 5/8" thickness using the 14 x 14 cm^2 Elekta applicator mold. The downstream spectrometer aperture, pictured in Figure 2.9 (c) and (d), as well as in Figure 2.8, consisted of a 1/8" hole drilled in a 1/2" thick copper block.

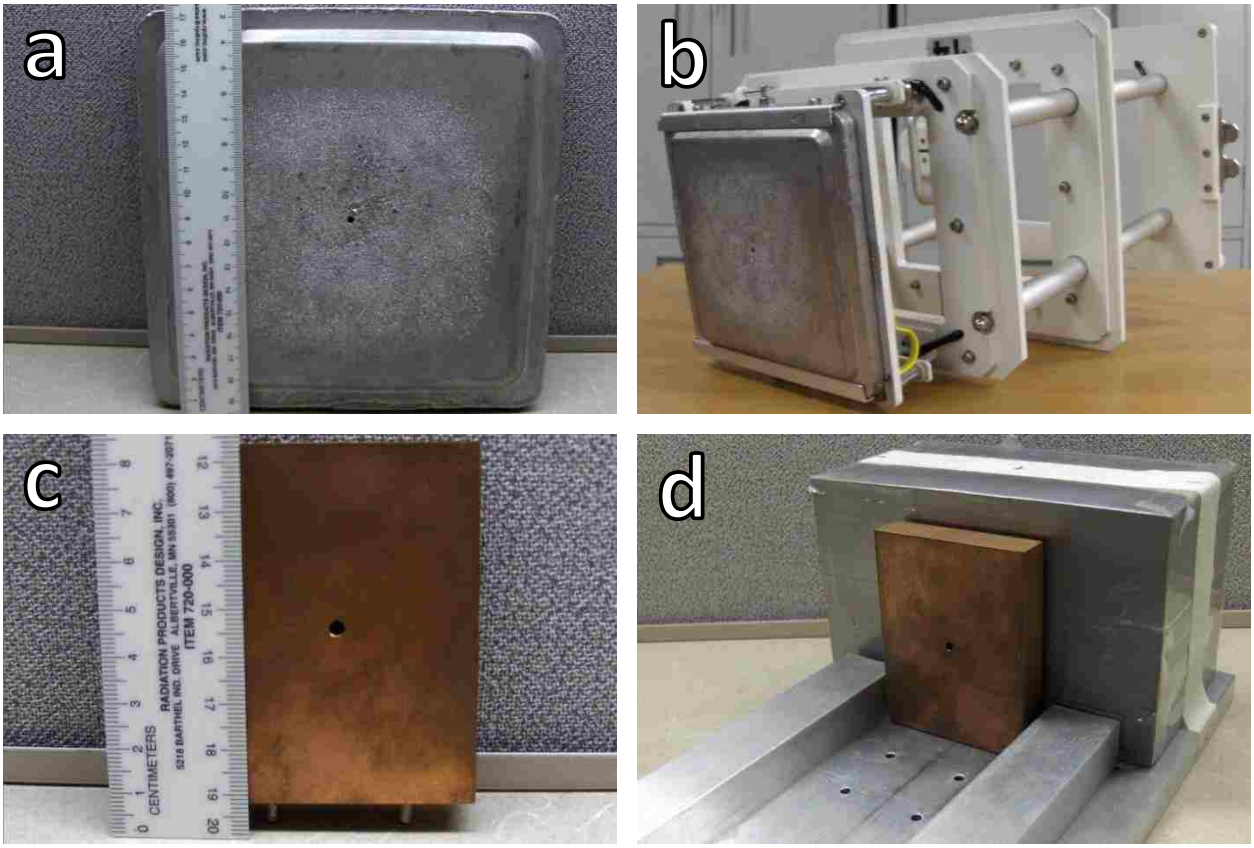

Figure 2.9. Electron beam collimating apertures. Pictured are the (a) Cerrobend® insert with 7/64" aperture, (b) Cerrobend® insert placed into the 14 x 14 cm^2 applicator, (c) copper block with 1/8" aperture and alignment pins on the bottom, (d) and copper block placed in the aluminum base plate downstream of X-ray block with the downstream magnet block removed for viewing purposes.

The spectrometer aperture and magnet block were held in place by the aluminum base plate pictured in Figure 2.9 (d). The copper spectrometer block was held rigid relative to the base plate by inserting the block's attached pins, visible in Figure 2.9 (c), into the one of the hole pairs drilled into the aluminum base plate. Two sets of such hole pairs are shown vacant in Figure 2.9 (d) with the third set occupied by the copper spectrometer block. The magnet block, constrained laterally by two aluminum rails attached to the base plate, was free to slide along the length of the base plate. For the purposes of this study, measurements were only taken with the front face of the magnet block pushed flush against the copper spectrometer block. The Cerrobend® aperture insert was held in place by the 14 x 14 cm^2 applicator, as shown in Figure 2.9 (b). Because the aluminum base plate and applicator are not attached

to one another, the position of the spectrometer aperture relative to the Cerrobend® aperture is adjustable.

To achieve the irradiation geometry shown in Figure 2.2 and Figure 2.8, the aluminum base plate was manually aligned using the positioning lasers and the concentricity between the Cerrobend® and spectrometer apertures. First, the front edge of the aluminum baseplate nearest the Cerrobend® insert was made co-linear with the overhead sagittal alignment laser and then moved towards the Cerrobend® insert using longitudinal couch shifts. Then, the concentricity of the spectrometer aperture relative to the Cerrobend® aperture was improved with vertical and lateral couch adjustments. The concentricity between the two apertures was judged by staring upstream through all four apertures (i.e. the exit and entrance apertures of the magnet block, the spectrometer aperture, and the Cerrobend® aperture) while standing downstream of the magnet block. An illustration of perfect concentricity between the spectrometer and Cerrobend® apertures from this view is illustrated in Figure 2.10.

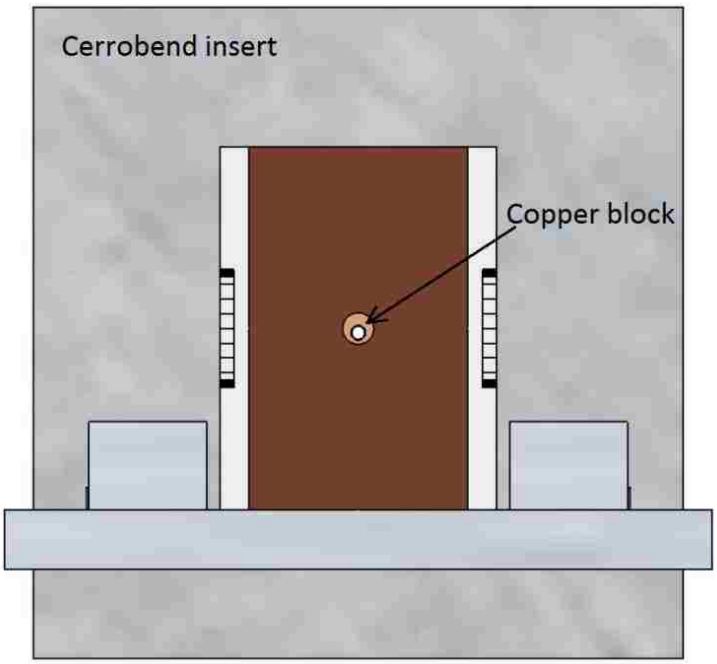

Figure 2.10. Illustration of aperture concentricity. White light is illustrated emanating through the concentric Cerrobend® and copper apertures. Concentricity cannot include the magnet block apertures because their centers were displaced vertically above the center of the copper aperture. The X-ray block was removed for illustrative purposes. All dimensions are to scale.

2.1.4.3. X-ray shield for CR strips

After the collimation in section 2.1.4.2 was designed, tests indicated that additional shielding was needed between the major sources of bremsstrahlung X-rays (primary scattering foil, secondary scattering foil, applicator trimmer bars, Cerrobend insert) and the magnet block to reduce the X-ray fluence reaching the CR strips and achieve goal (5) of Aim 1. These bremsstrahlung X-rays created the background portion of the CR strip image on top of which the electron beam portion sat. Reducing the background X-ray portion allowed the percentage of the CR strip image that is due to the electron beam to be maximized while not exceeding the 1.0 cGy max CR strip dose limit.

Lead was chosen for the X-ray block shielding material due to its high density (11.34 $g \cdot cm^{-3}$). It was screwed to the aluminum baseplate in the available space between the Cerrobend® insert and the spectrometer aperture. Based on preliminary measurements, a thickness of 3" was chosen for the lead shielding, which filled nearly all the space between the Cerrobend® insert and spectrometer aperture.

The X-ray block was designed to reduce the bremsstrahlung X-ray contribution to the CR strip image but have minimal effect on the transmitted electron beam. Hence, a 13/32" hole was drilled halfway through the lead block, and a 51/64" hole was drilled through the other half, creating a stepped aperture, illustrated in Figure 2.11, that did not interact with most electrons that passed through the Cerrobend® aperture. To demonstrate this, one only needs to prove that the X-ray block has minimal effect for the lowest energy electron beam on MBPCC's Elekta Infinity accelerators (7 MeV), as electron scattering power decreases as energy increases.

Electrons exiting the Cerrobend® aperture can be modeled as a divergent point source with a Gaussian angular distribution around central axis. From the point source at the exit of the Cerrobend® aperture, the angle between the central axis of the electron beam and the most limiting lip of the X-ray block is $\pm 5.89°$, or 11.78° from edge to opposite edge of the limiting lip, as illustrated in Figure 2.11. The standard deviation of the point source's Gaussian angular distribution in the xy plane, σ_{θ_y}, is 4.01°

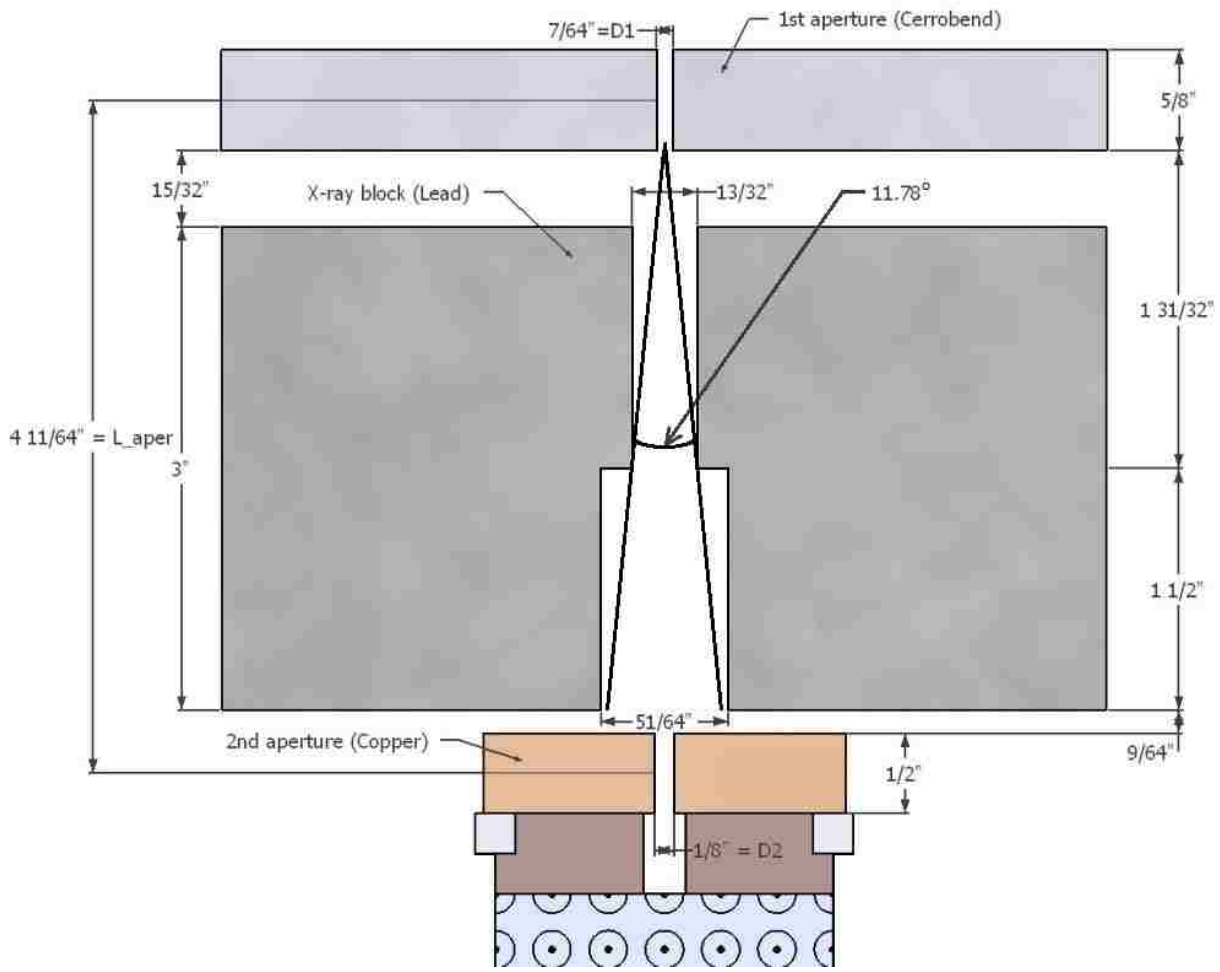

Figure 2.11. Electron beam collimation cross-section with the X-ray block. Schematic illustrates the thicknesses of the copper block, Cerrobend® insert, and X-ray block. Additionally, the diameters and lengths of the stepped X-ray block aperture are illustrated along with the X-ray block's acceptance angle for electrons diverging from at a point source placed in the middle of the exit of the Cerrobend® aperture. All dimensions are to scale.

for an $E_{p,o}$ of 7.14 MeV, i.e. the $E_{p,o}$ of the 7 MeV beam. In terms of a 2D Gaussian distribution in the xy plane, this means the X-ray block would allow electrons inside approximately $1.47\sigma_{\theta_y}$ to pass assuming Fermi-Egyes MCS. This means 85% of the electrons in the xy plane pass through the X-ray block. In terms of a 3D Gaussian distribution, the fraction electrons inside $1.47\sigma_{\theta_r}$, i.e. those passing through the X-ray block, equals 66%. Hence, the majority of the electrons passing through the Cerrobend® aperture also pass through the X-ray block, even for the lowest energy electron beams. Electrons that do not pass through the X-ray block were unlikely to have been scattered back into the spectrometer aperture

anyway. Therefore, it was assumed that the X-ray block had insignificant effect on the energy spectrum at the spectrometer aperture.

2.1.5. Determining monitor units for each beam energy

Once the irradiation geometry was established, exposure levels were determined for each of the seven electron beam energies. The number of MUs that could be delivered was constrained by the fact that the max dose limit for the CR strip readout device was approximately 1.0 cGy, beyond which the readout device saturates. The maximum deposited dose on the CR strip was within the electron spot. Therefore, for each energy the appropriate number of MUs to deliver was estimated by approximating dose within the electron spot.

This was done by determining the electron fluence per MU at the upstream Cerrobend® aperture at 95-cm SCD and then determining the ratio of fluence at the spectrometer aperture to fluence at the Cerrobend® aperture. Combining these relationships resulted in the electron fluence per MU at the spectrometer aperture. Next, the electron fluence per MU at the CR strip was assumed to be spread over an area larger than that of the spectrometer aperture. This, along with the 1.0 cGy max dose limit for the CR strips, allows one to calculate the proper amount of MUs to deliver for each of the seven electron beam energies. These calculations, which are described below, were used in tandem with multiple test irradiations to arrive at the final MUs shown in Table 2.1 below. Test irradiations were necessary primarily because the bremsstrahlung X-ray contribution to the CR strip image was not calculated.

Electron fluence within a water phantom is related to the dose by,

$$D = \phi \left(\frac{S}{\rho}\right)^{E}_{col,water}, \qquad 2.9$$

where ϕ is electron fluence, D is dose, and $\left(\frac{S}{\rho}\right)^{E}_{col,water}$ is the mass collisional stopping power in water for an electron of energy E. Solving for fluence and dividing both sides by the MUs delivered results in,

$$\frac{\phi}{MU} = \frac{D}{MU}\left[\left(\frac{S}{\rho}\right)^{E}_{col,water}\right]^{-1}. \qquad 2.10$$

Accelerators at MBPCC are calibrated to deliver 1.0 cGy/MU on central axis using the 14 x 14 cm^2 open applicator at depth of maximum dose in a water phantom whose surface is at 100-cm SSD. The dose per MU at the surface is obtained by multiplying the dose per MU at the calibration point, i.e. R_{100}, by the surface percent dose factor, i.e. $\%D(d=0,E)$, resulting in,

$$\left(\frac{\phi}{MU}\right)_{100-cm\ SSD} = \frac{1.0\ cGy}{MU}\left(\%D(d=0,E)\right)\left[\left(\frac{S}{\rho}\right)^{E}_{col,water}\right]^{-1}. \qquad 2.11$$

Including the inverse square correction to find fluence per MU at the applicator results in,

$$\left(\frac{\phi}{MU}\right)_{95-cm\ SCD} = \frac{1.0\ cGy}{MU}\left(\%D(d=0,E)\right)\left(\frac{100}{95}\right)^{2}\left[\left(\frac{S}{\rho}\right)^{E}_{col,water}\right]^{-1}. \qquad 2.12$$

Because $\left(\frac{S}{\rho}\right)^{E}_{col,water}$ varies little with E for therapeutic electron beams, a value of 1.968 $MeV * cm^2/g$ was assumed for all beams, resulting in,

$$\left(\frac{\phi}{MU}\right)_{95-cm\ SCD} = \frac{3.519 * 10^7\ electrons}{cm^2 * MU}\%D(d=0,E)\,. \qquad 2.13$$

Assuming the electron source could be treated as a point source inside the Cerrobend® aperture, the electron fluence in the spectrometer aperture is approximated by

$$\phi_{105.6-cm\ SSD} = \phi_{95-cm\ SCD}\frac{(R1)^2}{2(\sigma_{\theta_y})^2(L\_aper)^2}, \qquad 2.14$$

which is a result of Fermi-Eyges multiple Coulomb scattering (MCS) that holds when $R1 \ll L\_aper * \sigma_{\theta_y}$, where $R1$ is the radius of the Cerrobend® aperture (0.139 cm) and L_aper is the distance between the Cerrobend® and spectrometer apertures (10.6 cm). The values for all of these variables are shown in Figure 2.11. Note that $R1$ is half of $D1$, the diameter of the Cerrobend ® aperture.

Combining equations 2.13 and 2.14 and solving for $\phi_{105.6-cm\ SSD}$ results in,

$$\phi_{105.6-cm\ SSD} = \left[\frac{(R1)^2}{2(\sigma_{\theta_y})^2(L\_aper)^2}\right]\left[\frac{3.519 * 10^7\ electrons}{cm^2 * MU} * \%D(d=0,E)\ * MU\right]. \quad 2.15$$

To account for the spread of the electrons in the x direction (due to dispersion in the energy spectrum) and z direction (due to divergence in the xz plane) prior to reaching the CR strip, the electron fluence of the beam at the spectrometer aperture at 105.6-cm SSD from equation 2.15 was multiplied by 0.1, resulting in

$$\phi_{peak@strip} = 0.1\left[\frac{(R1)^2}{2(\sigma_{\theta_y})^2(L\_aper)^2}\right] * \left[\frac{3.519E^7\ electrons}{cm^2 * MU} * \%D(d=0,E)\ * MU\right]. \quad 2.16$$

where $\phi_{peak@strip}$ is the peak electron fluence at the CR strip. Assuming the sensitive layer of the CR strip is water equivalent,

$$D_{peak@strip} = \phi_{peak@strip}\left(\frac{S}{\rho}\right)^{E}_{col,water}, \quad 2.17$$

where $D_{peak@strip}$ is the peak dose at the CR strip. Using equations 2.16 and 2.17, the relationship between MU and $D_{peak@strip}$ was determined for each beam energy in Table 2.1.

Table 2.1. Relationship between MU and peak dose at the CR strip for each beam energy. Listed are the σ_{θ_y} and $\%D(d=0,E)$ values used in equation 2.16 as well as the delivered MUs and resulting $D_{peak@strip}$. The σ_{θ_y} and $\%D(d=0,E)$ values were derived from MBPCC clinical data for each of the nominal beam energies, E_{nom}. In these calculations $R1$ = 1.39 mm and L_aper = 10.6 cm.

E_{nom} (MeV)	σ_{θ_y} (rads)	$\%D(d=0,E)$	MU	$D_{peak@strip}$ (cGy)
7	0.070	0.80	300	0.47
9	0.058	0.83	200	0.47
10	0.050	0.83	120	0.38
11	0.044	0.85	90	0.38
13	0.038	0.88	75	0.43
16	0.031	0.92	65	0.59
20	0.024	0.93	55	0.85

2.1.6. Overview of CR strips and CR strip readout device

To measure the CR strip images from which the energy spectra were extracted, CR plates cut into 1" wide by 6" long strips were taped into the slot on the side of the magnet block, as shown in Figure 1.21. When irradiated, the electron beam entering the magnet block was deflected towards the CR strip by the permanent magnets and interacted with the CR strip. The electrons deposited energy in the sensitive photostimulable phosphor layer of the strip, forming the latent image that was later readout by a laser scanning system. The principle of operation of the CR strips and readout device are detailed in Appendix B.

In this study, CR strips were irradiated with clinical electron beams and then transported in light-tight envelopes to LSU where they were readout by Dr. Polad Shikhaliev using his model C431200 Cyclone Plus Storage Phosphor System (PerkinElmer, Waltham, MA) laser scanner pictured in Figure 2.12 (a). As visible light erases CR strips, all room lights in the vault were turned off during irradiation and cardboard was placed over the CR strip slot opposite the CR strip slot that was occupied by a strip to reduce the ambient light exposure to the strip. CR strip measurements were taken this way for all seven beam energies of a single Elekta Infinity accelerator. For the purposes of this study, the time between measurements and readouts, which varied between two to five days, was not long enough to appreciably degrade the resulting CR strip images.

The CR plates used were Agfa MD-10 storage phosphor plates (Agfa-Gevaert N.V., Belguim), pictured in Figure 2.12 (b). Though the manufacturer did not specify, the grains used in the CR strips' sensitive layer were assumed to be BaFBr crystals doped with Eu^{+2} activators, also written BaFBr:Eu^{+2}. The crystal lattice contained Ba:F:Br in a 1:1:1 proportion. The CR strips were 0.46 mm thick, 0.26 mm of which was the sensitive layer and 0.2 mm of which was the flexible backing.

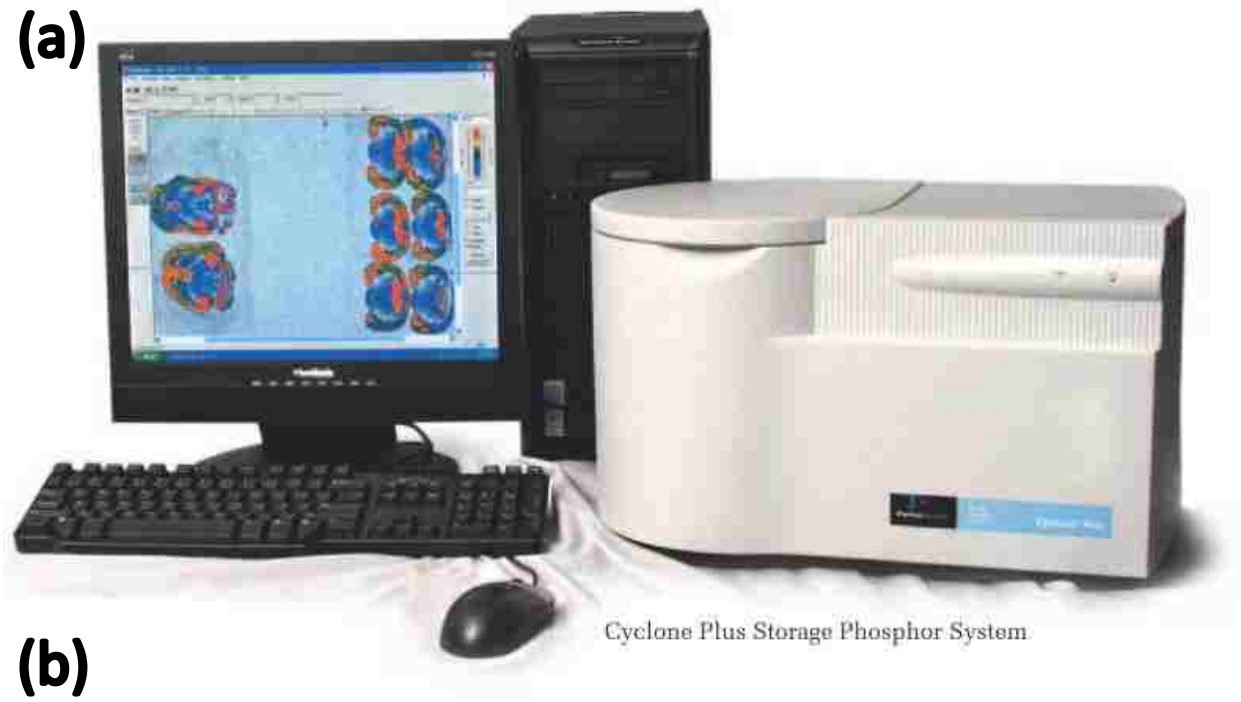

Figure 2.12. CR strip readout device and CR strips. Pictured is the (a) (right) Model C431200 Cyclone Plus Storage Phosphor System and its (left) monitor display as well as the (b) (top) active layer and (bottom) flexible plastic backing layer of example 1" x 6" Agfa MD-10 CR strips used in this study (top picture from PerkinElmer Inc.)

The CR strips were readout using the phosphor readout device in Figure 2.12 (a). The strips were taped horizontally onto the readout device's carousel. The medium format carousel was used for the Cyclone Plus Storage Phosphor System. The lowest resolution setting, i.e. 150 dots per inch (DPI), was used during readout as it produced the fastest scan times. The result of a single readout was a .tiff

image file that contained a 2D array of pixel values, each value being the square root of the signal intensity for that pixel. The square root of the signal intensities for each pixel was produced rather than the unmodified signal intensities due to hardware limitations of the readout device. Hence, to obtain the correct signal intensities all pixel values were converted from 16-bit to 32-bit values and then squared using ImageJ software (National Institutes of Health, Bethesda, MD). The result was an image file with signal intensities for each pixel that were approximately proportional to deposited dose, as is apparent in the signal intensity to dose calibration curve plotted in Figure 3.2 in section 3.1.1.1. Four example CR strip images in a single .tiff image file from a single readout are pictured in Figure 2.13. Notice that the signal due to the electron beam appears as a white electron spot in each CR strip image. After the CR strips were readout, they were erased using the integrated CR plate eraser found in the Kodak ACR-2000i CR plate reader (Eastman Kodak, Rochester, NY) and reused.

For the energy spectra generated in this study, it was assumed that the dose deposited per unit of incident fluence did not vary with position along CR strip. As the photons produced due to the mass radiative stopping power of electrons are unlikely to be reabsorbed in the CR strip's sensitive layer, the energy deposited in the strip due to the mass collisional stopping power dominates. As is illustrated in Figure 2.14, the mass collisional stopping power of the sensitive layer of the CR strip varies little with energy, and hence position of the incident electron beams. The low-energy cutoff to the permanent magnet spectrometer is about 2.0 MeV and practically no electrons above 25 MeV are generated. Additionally, the electrons for a single beam will span an energy range of about 15 MeV at maximum, with the majority of the area under the spectrum falling within a 8 MeV range for the broadest spectra. Also, deposited dose in the sensitive layer due to backscatter from the CR strip backing is around 3% and does not vary much with electron energy, hence was ignored. Therefore, the assumption of uniform response with electron energy is reasonable (i.e. 8 MeV range corresponds to a maximum deviation of $\pm$3% from uniform response).

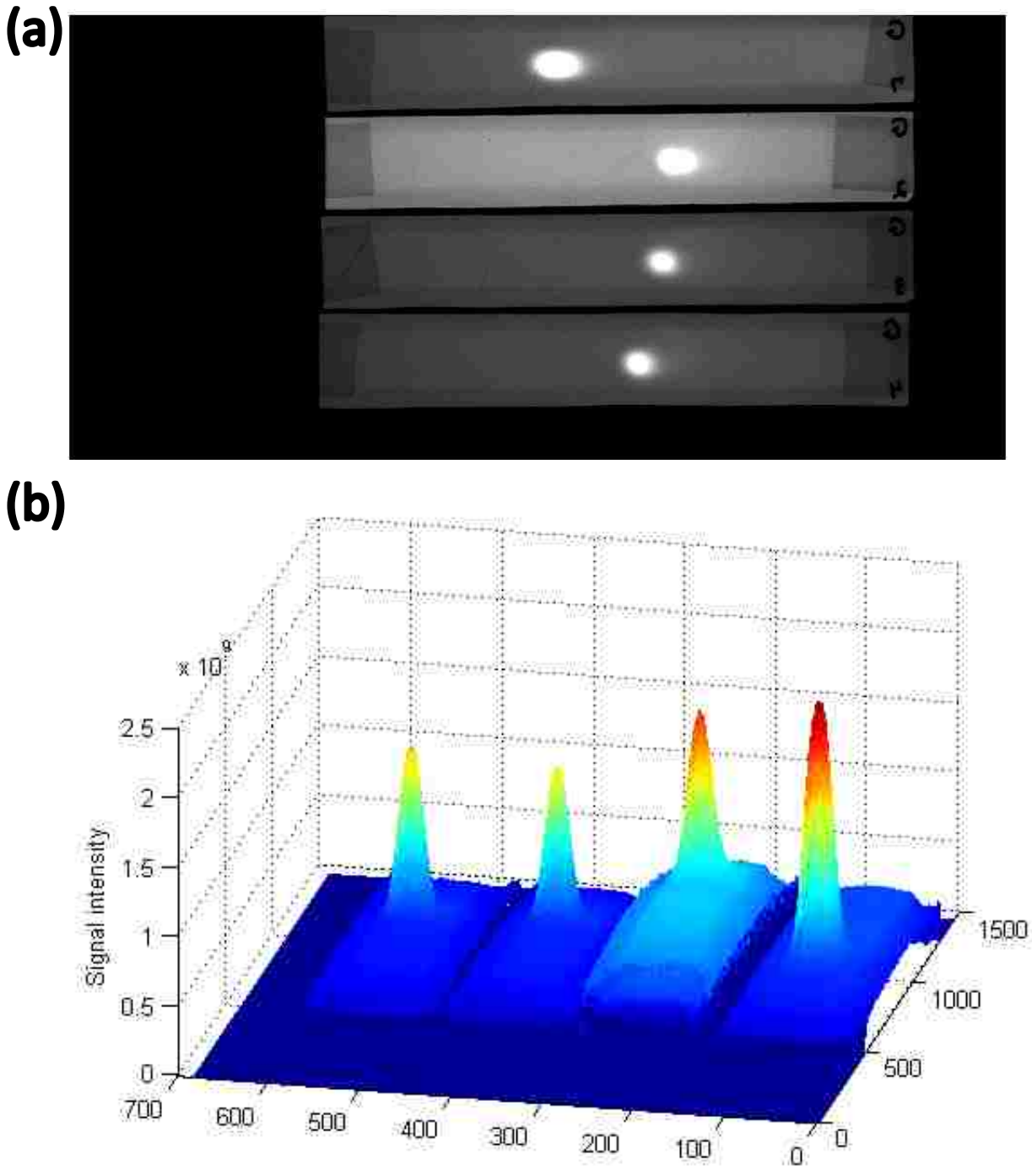

Figure 2.13. .tiff image of a CR strip readout. A .tiff image file resulting from a single readout illustrated as (a) a 2D grayscale image and (b) a colorized 3D image. This .tiff image file had all its pixel values converted to 32-bit and squared, making the signal intensities approximately proportional to deposited dose. Four CR strip images are contained within this .tiff image file, as four CR strips were taped to the readout device's carousel.

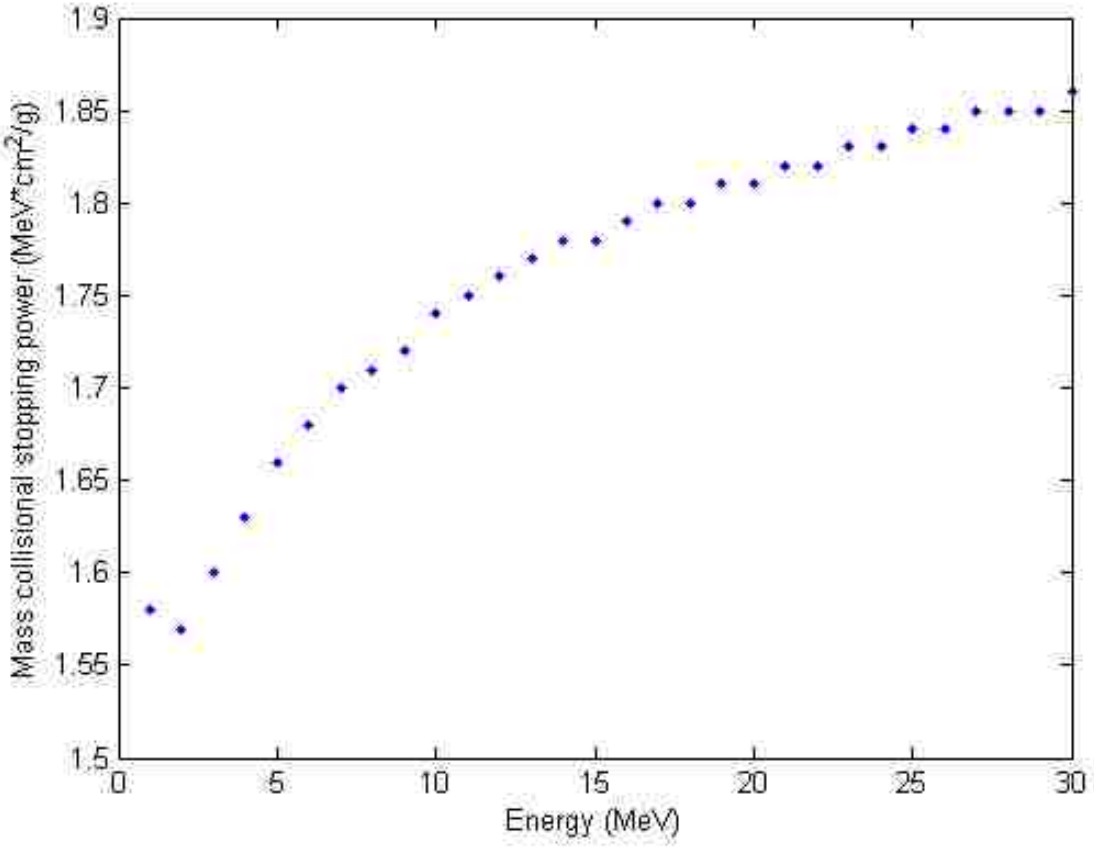

Figure 2.14. Mass collisional stopping power of the CR strip's sensitive layer for electron energies between 1 and 30 MeV. Assuming the sensitive layer of the CR strip was 45% BaFBr crystal (assumed density of 5.1 g/cm^3) and 55% polyethylene (assumed density of 0.93 g/cm^3) (Rowlands 2002), a unique material composed of 26.2% Ba, 3.6% F, 15.2% Br, 7.9% H, and 47.1% C by mass, with a density of 1.48 g/cm^3, was inserted in the NIST data base to gather the plotted mass collisional stopping powers.

In addition to minimal variation in signal intensity with electron energy, it was essential that the CR strip response did not vary much with position. This was demonstrated with irradiations of the 1" x 6" face of the CR strips with broad, uniform, normally incidience electron beams. These irradiations are described in greater detail in section 3.1.1.1. The CR strip images that resulted from these irradiations were summed in the z direction along their 1" widths to produce the average signal intensity per column versus CR strip position plots in Figure 2.15. These plots were sufficiently flat to be considered spatially uniform for this study, especially since the electron peak structure of the CR strip image occupied only a small segment of the total 6" length.

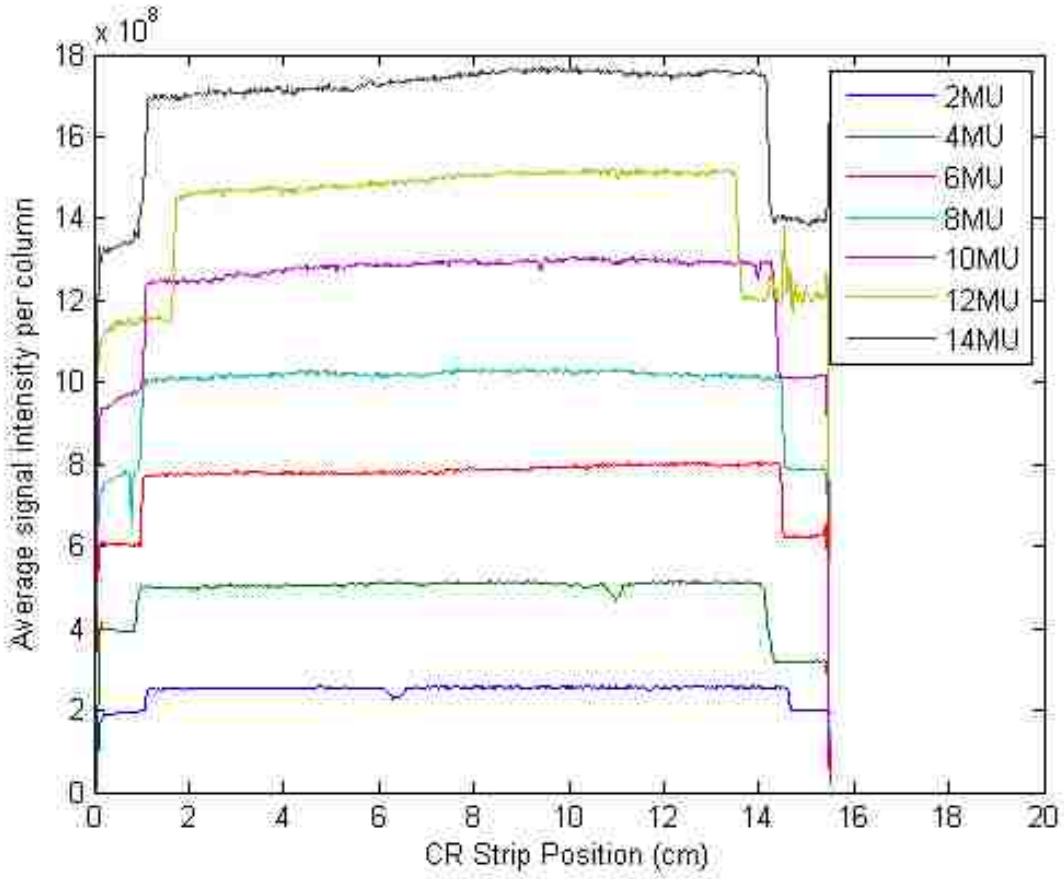

Figure 2.15. Spatial uniformity of CR strip response. Plotted are signal intensities of uniformly irradiated CR strips averaged along the 1" strip width versus the 6" strip length, i.e. x direction, for various levels of exposure. The measurements used to generate these plots are described in section 3.1.1.1.

2.1.7. Generating intensity profiles

To determine the usability of the CR strip images, the average signal intensity per column versus CR strip position was calculated. This was done by averaging the signal intensity per pixel along a column of pixels oriented in the z direction, i.e. the 1" width direction, of the CR strip image, for all such columns along the x direction, i.e. the 6" length direction, of the CR strip image. Four such measured CR strip images from a single readout are illustrated in Figure 2.16, with the horizontal direction and vertical directions of the .tiff image aligning with the x and z axes, respectively. The plot of average signal intensity per column versus CR strip position, x, will henceforth be referred to as the intensity profile. During the analysis in Aim 2, energy spectra were extracted from these intensity profiles.

The heights of the columns used for averaging did not extend across the entire 1" width of the CR strip image, as the electron spot only fell within the central portion of the CR strip image's 1" width. Hence, there was an insignificant contribution of signal from the electron beam outside the central portion of the strip to the edges of the CR strip image. Also, a significant portion of the CR strip image comes from bremsstrahlung X-rays depositing energy in the strip's sensitive layer. Though these X-rays contribute to the signal throughout the entire CR strip image, their contribution varies with the level of attenuation experienced by the X-rays. Notably, the lip of the slot cut into the side aluminum plate of the magnet block creates additional attenuation for X-rays reaching the edges of the CR strip, creating the lip attenuation shadows illustrated in Figure 2.16. These lip attenuation artifacts are also visible in

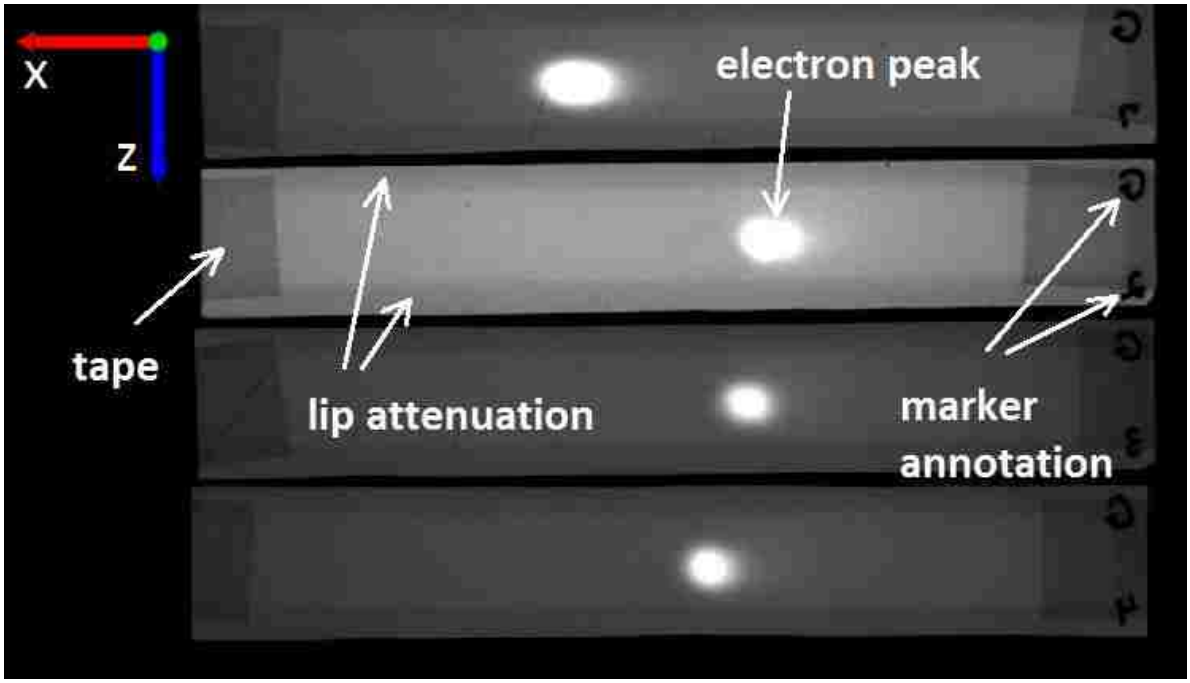

Figure 2.16. Measured gray scale CR strip images from a single readout. The coordinate system of the spectrometer is illustrated in the top left of the this .tiff image file. From top to bottom, the CR strip images come from the 20 MeV, 9 MeV, 10 MeV, and 11 MeV beam of MBPCC's Baton Rouge Elekta Infinity accelerator. The right edge of each strip's image defines x=0 for that strip (marker annotations correspond to the edges of the CR strips nearest the entrance aperture of the magnet block). The bright spots contain the electron energy spectra information. The artifacts from the marker annotations and scotch tape used to attach strips to the carousel obscured stimulating laser light and resulting photostimulated luminescence (PSL) photons that were too far from the electron peak to be of concern. On the other hand, the lip attenuation artifacts, which were positioned near the electron peaks, had to be avoided during column integration as illustrated in Figure 2.17.

the 3D image in Figure 2.13 (b). These lip artifacts should be excluded from the columns used for averaging as they have abnormally low signal intensities compared to the rest of the CR strip's width. Therefore, a limited portion of the CR strip image called the averaging window was used for averaging. For each CR strip image, the top and bottom edges (z direction) and left and right edges (x direction) of its averaging window defined the top and bottom pixels of the vertical averaging range for averaging columns and the left and right pixels of the horizontal range over which the columns were averaged, respectively.

The windows were selected to include as much of the electron beam spot as possible while excluding the lip attenuation artifacts and the regions just above and below the edges of the electron beam spot in the z direction. Throughout this study, the width of the averaging window in the z direction was 63 pixels from edge to edge, including the edge pixels, which corresponds to a distance of 1.06 cm. The decision to use 63 pixels was somewhat subjective, but slight variations in this width (1-10 pixels) had no significant effect on the results. The central pixel of the averaging window's 63 pixel width was drawn from a fit of a 2D 5^{th} order polynomial over the electron peak portion of the CR strip image, i.e. the portion of the image that had signal intensities greater that 50% of the max signal intensity for the .tiff image. Taking the pixel with the maximum signal intensity from the fit rather than from the raw CR strip image mitigates the effect of noise in the electron peak structure. To find the length of the averaging window, a program was written to move horizontally outward from the electron peak structure to the left and right edges, i.e. x direction edges, of the CR strip image. Along the way, the program determined whether or not the signal intensities of pixels were below a threshold that was set above the background signal intensity yet below the lowest CR strip image signal intensity and ceased operation if they were. When this happened, the program recorded the coordinates, producing the left and right edge pixels of the CR strip image. Hence, the 63 pixel width and this length defined the dimensions of the averaging window.

An example averaging window generated in this way is illustrated in Figure 2.17, along with the resulting intensity profile. The peak signal to X-ray background ratio for intensity profiles was defined as the peak (maximum) average signal intensity per column divided by the average signal intensity per column of the X-ray background at the CR strip position of the peak. The method for determining the X-ray background is described in section 3.1.1.2, though all the average signal intensities per column were converted to dose first. This conversion if nearly linear though, so the peak signal to X-ray background ratios change insignificantly.

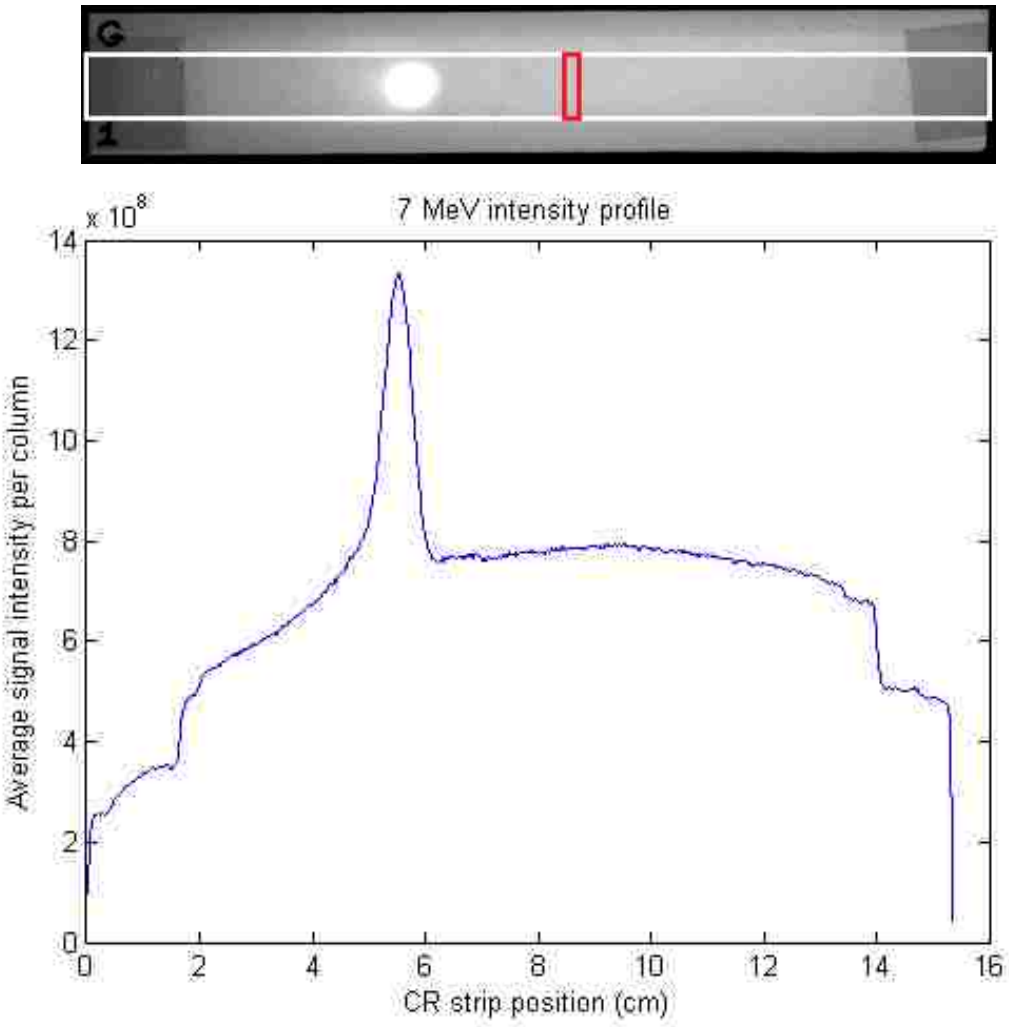

Figure 2.17. Example averaging window and resulting intensity profile. Illustrated on top of a CR strip image is an example averaging window in white and one of the resulting columns used for averaging in red. The window contains averaging columns that are 63 pixels tall. Below the CR strip image is the intensity profile that resulted from the averaging window shown.

2.2. Results and discussion

2.2.1. CR strip images and intensity profiles

Illustrated in Figure 2.18 are the CR strips images for the 7, 9, 10, 11, 13, 16, and 20 MeV beams, along with their corresponding intensity profiles, measured on the Baton Rouge Elekta Infinity accelerator on Jan/14/2013. The CR strip images and intensity profiles measured on MBPCC's other Elekta Infinity accelerators are of similar quality to those shown here.

Of note, the horizontal orientation of the CR strips on the laser scanner readout carousel was neither perfect nor completely uniform. For example, the CR strip shown in Figure 2.18 (a) is more horizontal than the CR strip shown in Figure 2.18 (b). The effect this had on the resulting energy spectra was small and hence ignored in this study. Also, the tape artifacts visible in the CR strip images also show up in the resulting intensity profiles, visible as sharp reductions in average signal intensity per column at the edges. It is also worth noting that even for the lowest energy electron beam, where the area of the electron peak structure as a percent of the total area under the intensity profile was the smallest, the electron peak structure was still prominent. Additionally, there was a clear increase in the distance between the origin of the CR strip, i.e. x=0, and the position of the electron peak with increasing energy, as was expected.

During the analysis described in section 3.1.1.1, average signal intensities per column were converted to doses with the signal intensity to dose calibration curve plotted in Figure 3.2. Using this calibration curve, the max signal intensity per CR strip image was converted to dose for all seven beam energies on each of MBPCC's six Elekta Infinity accelerators. These max doses are listed in Table 2.2 below. Note that the max dose to the CR strip exceeded 1.0 cGy by a small margin in only a few cases where the energy spectra were narrower than normal. Hence, the CR strip images that resulted from the irradiation geometry and exposure levels described in this aim were close enough to meeting objective (1) to be used in further analysis.

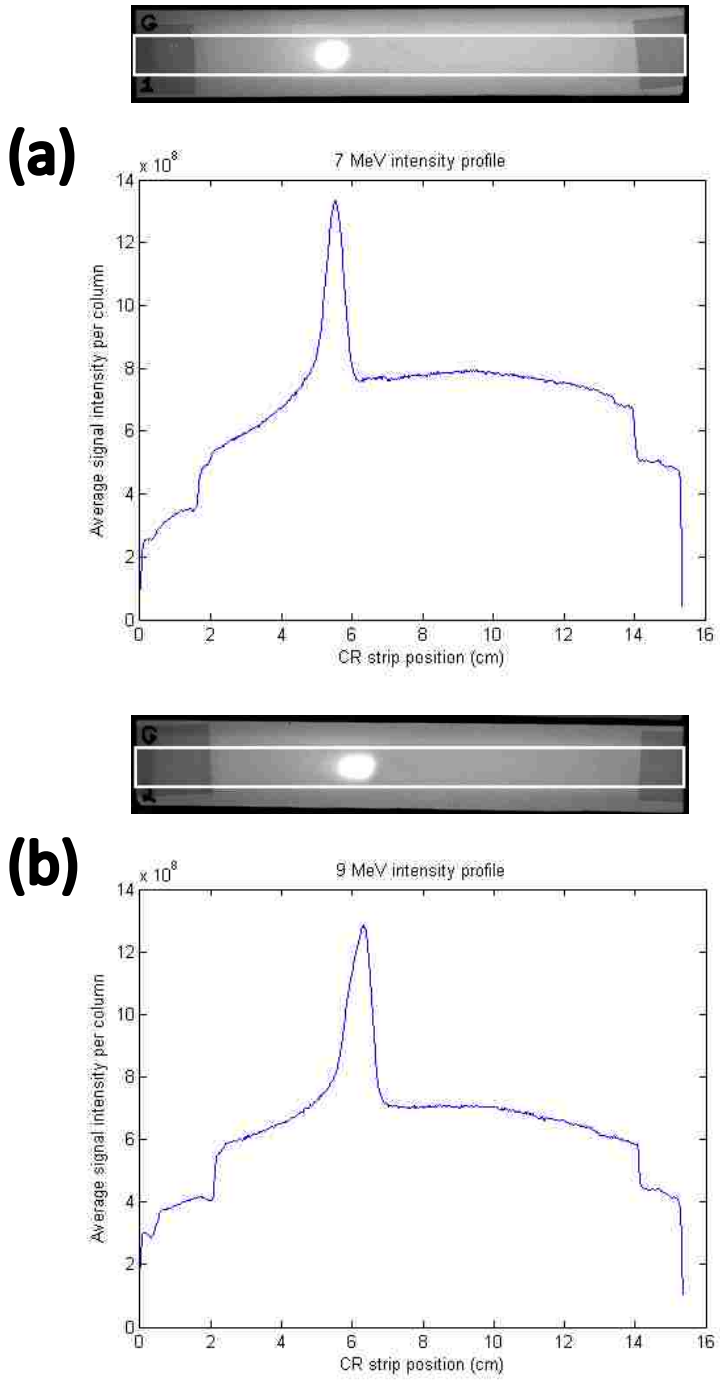

Figure 2.18. Plots of average signal intensity per column versus CR strip position. These plots show the average signal intensity per column versus CR strip position extracted from the CR strip image above the plot for Baton Rouge Elekta electron beams at: (a) 7 MeV, (b) 9 MeV, (c) 10 MeV, (d) 11 MeV, (e) 13 MeV, (f) 16 MeV, and (g) 20 MeV. x = 0 corresponds to the upstream edge of the strip, and the falloff at approximately 15.2cm (6") indicates the downstream edge of the strip. The energy spectra information is contained in the peak regions superimposed on the background curve created by bremsstrahlung X-rays.

(Figure 2.18 continued)

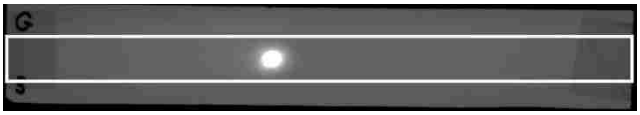

(c)

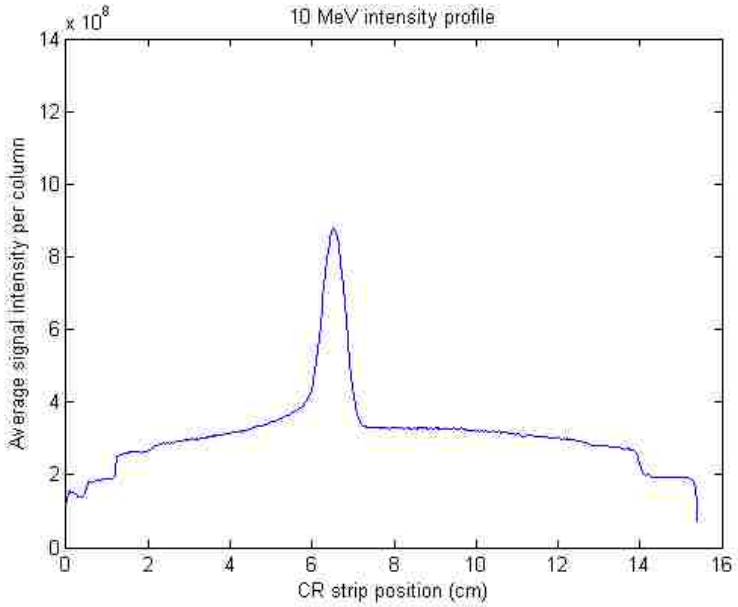

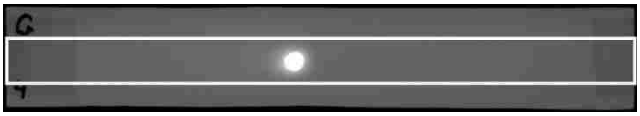

(d)

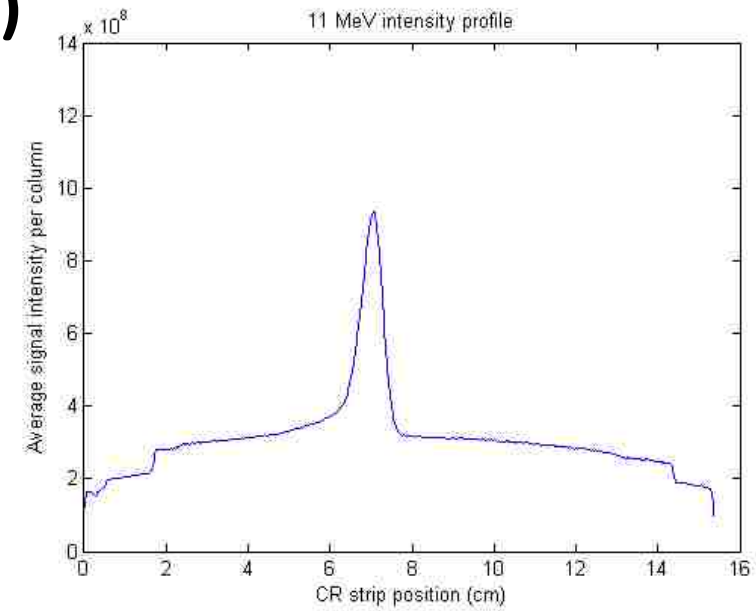

(Figure 2.18 continued)

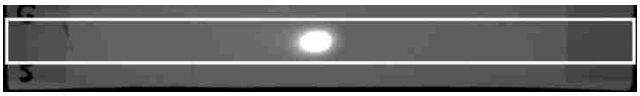

(e)

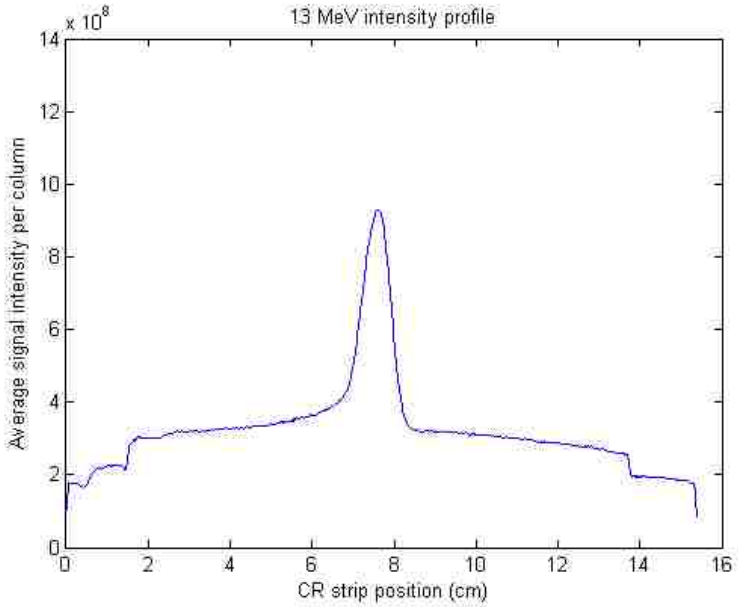

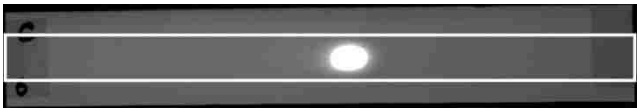

(f)

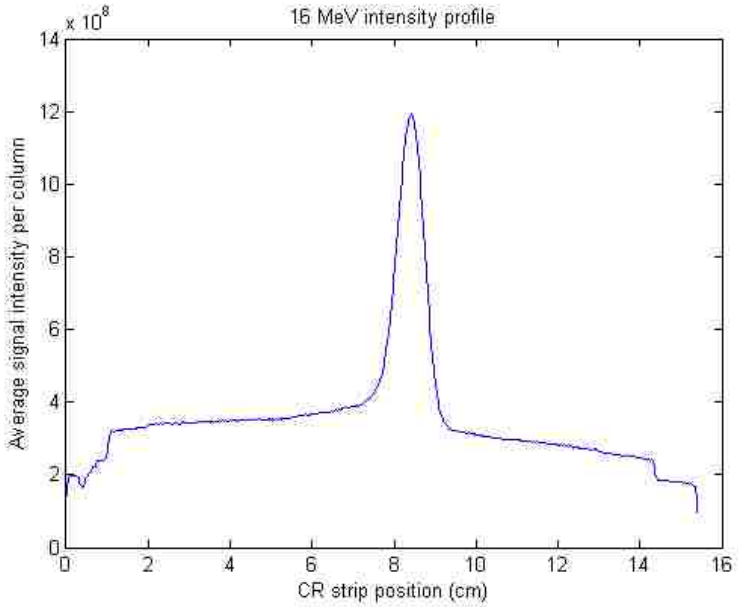

(Figure 2.18 continued)

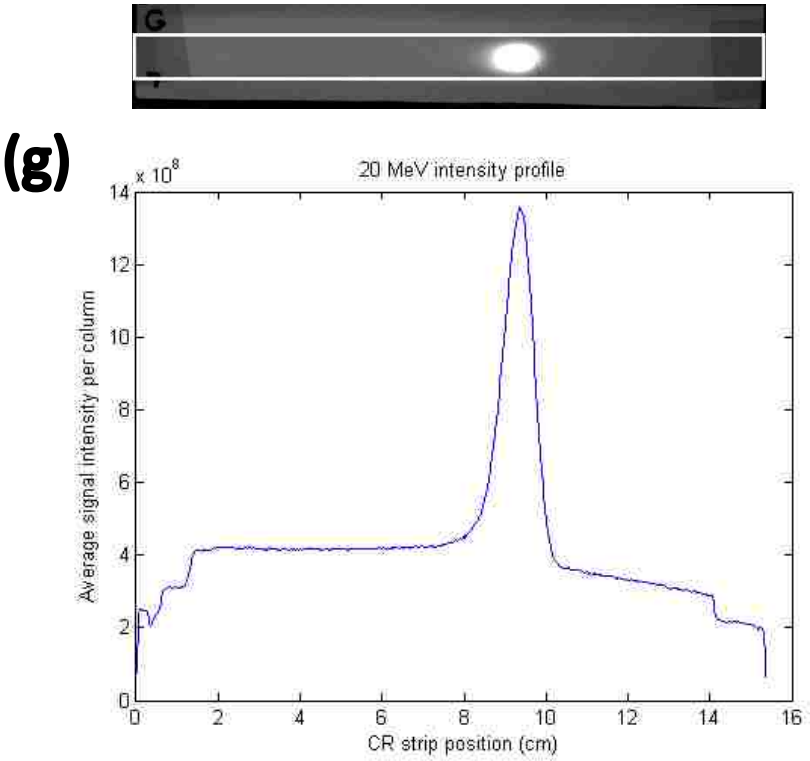

Table 2.2. Maximum doses per CR strip. Tabulated are the maximum doses in cGy per CR strip for the intensity profile measurements performed for each beam energy of each accelerator at MBPCC. The maximum doses that exceeded 1.0 cGy are highlighted in grey.

Max dose	Gonz	BR	CV1	CV2	Houma	Ham
7 MeV (cGy)	0.893	0.962	0.757	1.092	0.718	0.852
9 MeV (cGy)	0.819	0.909	0.803	1.093	0.763	0.777
10 MeV (cGy)	0.546	0.678	0.531	0.702	0.631	0.562
11 MeV (cGy)	0.647	0.741	0.574	0.704	0.620	0.530
13 MeV (cGy)	0.674	0.725	0.485	0.739	0.608	0.545
16 MeV (cGy)	0.796	0.976	0.691	1.029	0.724	0.705
20 MeV (cGy)	0.867	1.075	0.760	1.221	0.898	0.951

As the Elekta Infinity accelerators at MBPCC delivered radiation at rate of about 400 MU/min, the irradiation times resulting from the exposure levels in Table 2.1 consistently fell between 5 seconds and 50 seconds , hence meeting objective (2) of Aim 1. The electron beam that passed into the spectrometer aperture had a divergence of less than 1.52°, which was deemed small enough to ignore. Hence, objective (3) of Aim 1 was achieved, allowing the beam to be modeled as parallel in further

analysis. Additionally, as is visible in Figure 2.18, the diameter of the spectrometer aperture produced electron spots that fell inside the 1" width and lip attenuation artifacts and provided sufficient energy resolution for further analysis. This trend was true for all other accelerators, meaning objective (4) of Aim 1 was met.

Finally, the peak signal to X-ray background ratios, were 1.87, 1.89, 2.69, 2.95, 2.86, 3.71, and 3.64 for the intensity profiles of the 7, 9, 10, 11, 13, 16, and 20 MeV beams plotted in Figure 2.18, respectively. As was expected, there was a general increase in signal to background ratios with beam energy due to the increasing percentage of electrons reaching the CR strip. These peak signal to X-ray background ratios are similar to those calculated for all other MBPCC Elekta Infinity accelerators, meaning objective (5) of Aim 1 was met.

Chapter 3 Aim 2 – Develop methods for transforming measured intensity profiles into energy spectra at 95-cm SCD

Aim 2: Develop the methodology to transform a measured intensity profile into an energy spectrum on central axis at 95-cm SCD. This was done by (1) extracting and smoothing net dose profiles (defined in section 3.1.1) from the intensity profiles, (2) transforming the net dose profiles into energy spectra at the spectrometer aperture, and (3) transforming the energy spectra at the spectrometer aperture to those on central axis at 95-cm SCD. Because the above tasks used equation 2.7 (defined in section 2.1.2), a fit of equation 2.7 to clinically derived energy and position parameters was performed to obtain values for the parameters B_z and x_o used in equation 2.7. This analysis, performed using MATLAB R2012a, was verified with a calculated net dose profile derived from an assumed energy spectrum at the spectrometer aperture in place of a measured net dose profile.

3.1. Methods and materials

3.1.1. Extracting net dose profiles from intensity profiles and smoothing

Three steps were required to obtain smoothed net dose profiles: (1) transform intensity profiles into gross dose profiles, (2) subtract the X-ray background portions from the gross dose profiles to obtain net dose profiles, and (3) smooth the resulting net dose profiles.

3.1.1.1. Transforming intensity profiles into gross dose profiles

To simplify later calculations of energy spectra, the average signal intensities per column of the intensity profiles were converted to doses. This conversion from average signal intensity per column to dose was marginally necessary, as results showed the average signal intensity per column scaled almost linearly with dose.

To obtain the signal intensity to dose calibration curve, CR strips were irradiated with the 6 MeV electron beam on MBPCC's Varian Clinac 21EX S/N 1412 (Varian Medical Systems, Palo Alto, CA) using the 25 x 25 cm^2 open applicator. The gantry was rotated to 270° so that the electron beam traveled horizontally. A 5-cm thick Plastic Water® (CIRS Inc., Norfolk, VA) slab was placed at 300-cm SSD on its

side so that the electron beam struck at normal incidence to the slab's square surface, as pictured in Figure 3.1. The same 1" wide x 6" long CR strips used in the measurements described in Aim 1 were placed in modified radiographic film packets to shield them from ambient light and then oriented horizontally and taped to the center of the slab's surface such that the middle of the strips were on central axis, as pictured in Figure 3.1. After placement, the strips were irradiated individually with 0, 2, 4, 6, 8, 10, 12, and 14 MUs. These strips were then readout using the laser scanning readout device described in section 2.1.6, producing CR strip images. Because the 75-cm field width at 300-cm SSD was so much greater than the 6" strip length, the electron fluence was assumed uniform across the CR strip.

The MUs delivered were converted to dose at the CR strip in two steps. First, the delivered MUs were converted to dose at 100-cm SSD using MU calculations. Then, this dose was converted to dose at the CR strip, i.e. at 300-cm SSD, using relative ionization measurements. The dose output at 100-cm SSD was calculated using,

$$\dot{D}(d = 0, SSD = 100cm, FS = 25x25cm^2) = \dot{D}_{cal} * S_e * \%D(0)\,, \qquad 3.1$$

where $\dot{D}_{cal}$ equals the calibration dose output on central axis at R_{100} in water at 100-cm SSD when using the 10 x 10 cm^2 open applicator (1.0 cGy/MU), S_e equals the output factor for the 25 x 25 cm^2 open applicator (1.008), and $\%D(0)$ equals the percent dose at the surface of a water phantom at 100-cm SSD when using the 25 x 25 cm^2 open applicator (69%). Inserting the values for these factors into equation 3.1 results in,

$$\dot{D}(d = 0, SSD = 100cm, FS = 25x25cm^2) = \frac{0.6955\ cGy}{MU}\ . \qquad 3.2$$

This dose output was converted to the dose output at the surface of a water phantom at 300-cm SSD with the relative ionization measurements. The ionization output in nC/MU was measured for the 6 MeV beam with the 25 x 25 cm^2 open applicator. The measurement took place at the surface of a Plastic Water® phantom placed at 100-cm SSD using a model TN34001 parallel plate chamber (CNMC

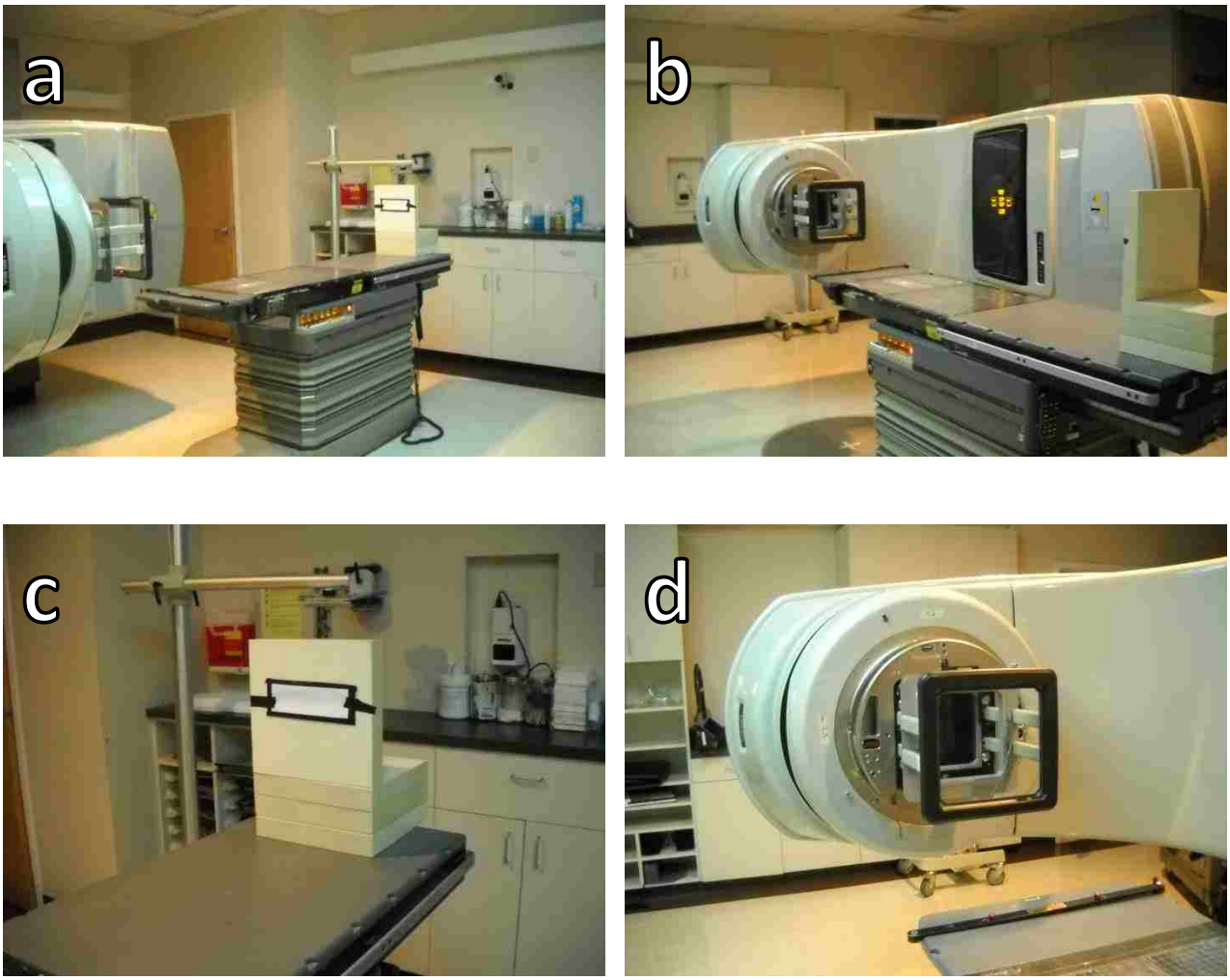

Figure 3.1. Irradiation geometry for the average signal intensity to dose calibration. Pictured is (a) (b) the Varian Clinac 21EX rotated to 270° to deliver a broad 6 MeV beam at normal incidence to CR strips. The CR strips were (c) placed in modified radiographic film packets and taped to the surface of 5-cm of Plastic Water® slab material. Irradiations were performed using the (d) 25 x 25 cm^2 open applicator.

Company Inc., Nashville, TN). This measurement was repeated, except with the phantom placed at 300-cm SSD. As 300-cm SSD was achieved by placing the Plastic Water® slab on its side and orienting the gantry horizontally, a thin piece of masking tape was used to ensure the parallel plate chamber did not fall out of the Plastic Water® chamber slab. Since the placement of the tape was constant for both the 100-cm SSD and 300-cm SSD measurements, it had no effect on the relative ionization outputs between the two setups. No build-up material was placed between the ionization chamber and the source, but 5-cm of Plastic Water® slab material was placed immediately downstream of the chamber flush to the chamber slab to generate full backscatter. The ratio of the ionization output at 300-cm SSD to the

output at 100-cm SSD was 0.0846. This ratio was assumed equal to the ratio of the dose output at 300-cm SSD to the dose output at 100-cm SSD and hence multiplied by the dose output at 100-cm SSD, i.e. 0.6955 cGy/MU, to obtain the dose output at 300-cm SSD where the CR strips were placed, i.e. 0.0588 cGy/MU.

Then, for each of the resulting CR strip images, the average signal intensity from a central 1.6 cm high x 2.5 cm long, rectangular portion of the CR strip image was calculated using ImageJ. Care was taken to avoid any dark streaks in the CR strip image that existed due to scratches in the sensitive phosphor layer of the CR strip. The resulting average signal intensities and corresponding doses were fit to a second order polynomial, i.e.

$$D = a_1(\bar{I})^2 + a_2(\bar{I}) + a_3\,, \qquad 3.3$$

where D was dose and a_1, a_2, and a_3 were constants determined by the fit. From the fit, $a_1 = 3.357E^{-19}$, $a_2 = 7.392E^{-9}$, and $a_3 = 0.04385$.

As we can see from the plot of this fit on top of the data points in Figure 3.2, the relationship between dose and average signal intensity is almost linear, i.e. a_2 is much larger than a_1. Therefore, assuming a linear conversion from signal intensity to dose would have produced results within $\pm$2% of the correct values.

Using this conversion, intensity profiles, like those plotted in Figure 2.18, were converted to gross dose versus CR strip position plots, i.e. gross dose profiles[1]. An example gross dose profile is plotted in Figure 3.3 (b). Next, the dose due only to electrons, i.e. the net dose, was determined by subtracting the dose due to the bremsstrahlung X-ray contribution, i.e. the background dose.

[1] Ideally, the conversion to dose should be applied to the signal intensity of each pixel of a CR strip image rather than to the average signal intensities per column of the intensity profiles. However, in the present study it was applied after the column averaging performed in section 2.1.7. Because of the higher degree of linearity, the present method should have an error of less than 1%.

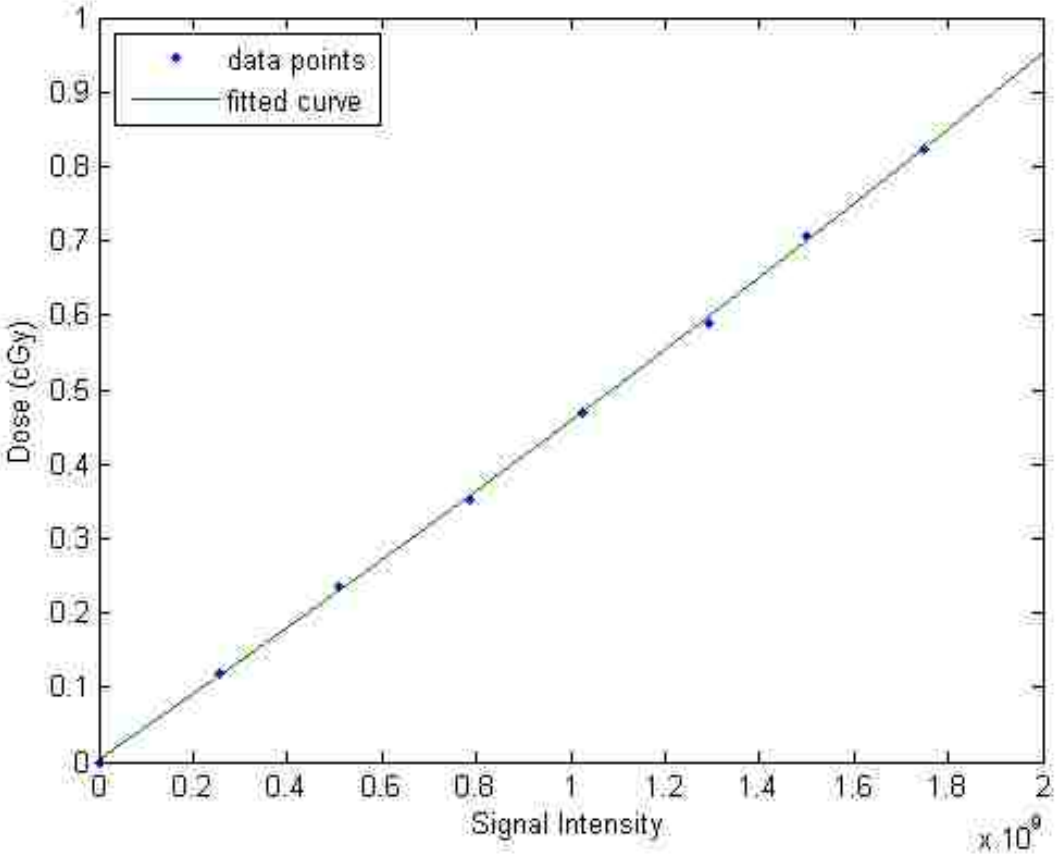

Figure 3.2. Signal intensity to dose calibration curve. Plotted are (blue dots) doses delivered to each CR strip in cGy and the average signal intensity that resulted from averaging the signal intensities within rectangular portions of the middle of the CR strips. Also plotted is (green) the result of fitting equation 3.3 to these data points.

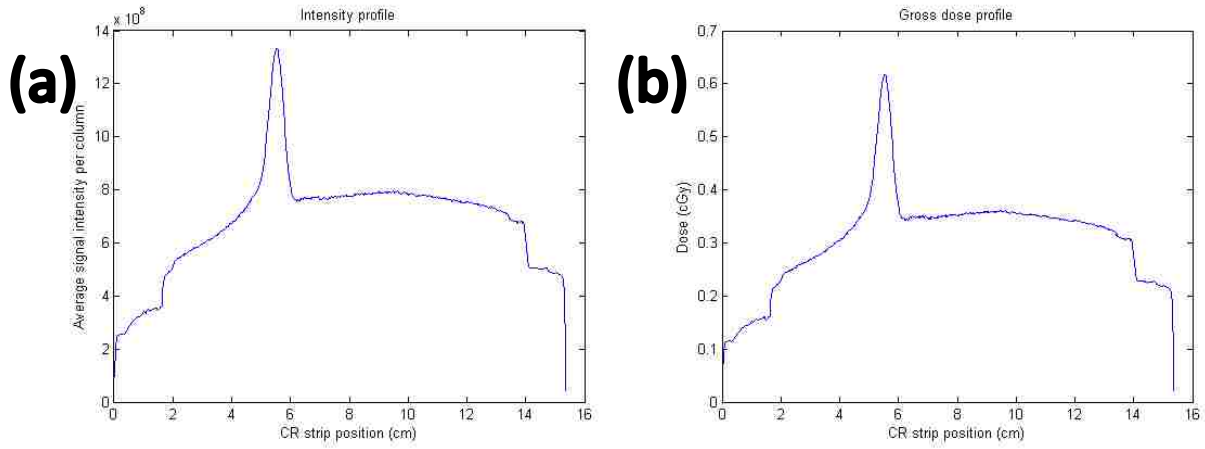

Figure 3.3. Intensity profile to gross dose profile conversion. Plotted is the (a) measured intensity profile from the 7 MeV beam on MBPCC's Baton Rouge Elekta Infinity accelerator and (b) its resulting gross dose profile. The steps at each end of each profile are due to tape artifacts.

3.1.1.2. Subtracting X-ray background from gross dose profiles

After obtaining the gross dose profile, the bremsstrahlung X-ray background was subtracted to obtain the net dose profile. In Figure 3.3, this background structure is the gradually sloping, hill-like shape upon which the electron peak structure lies. This structure also contains the tape artifacts that resulted from affixing the CR strips to the carousel with scotch tape.

To remove the background structure from the plot, a 3rd or 4th degree polynomial was fit to the portions of this background structure that fell inside the tape artifacts at the edges yet outside of the

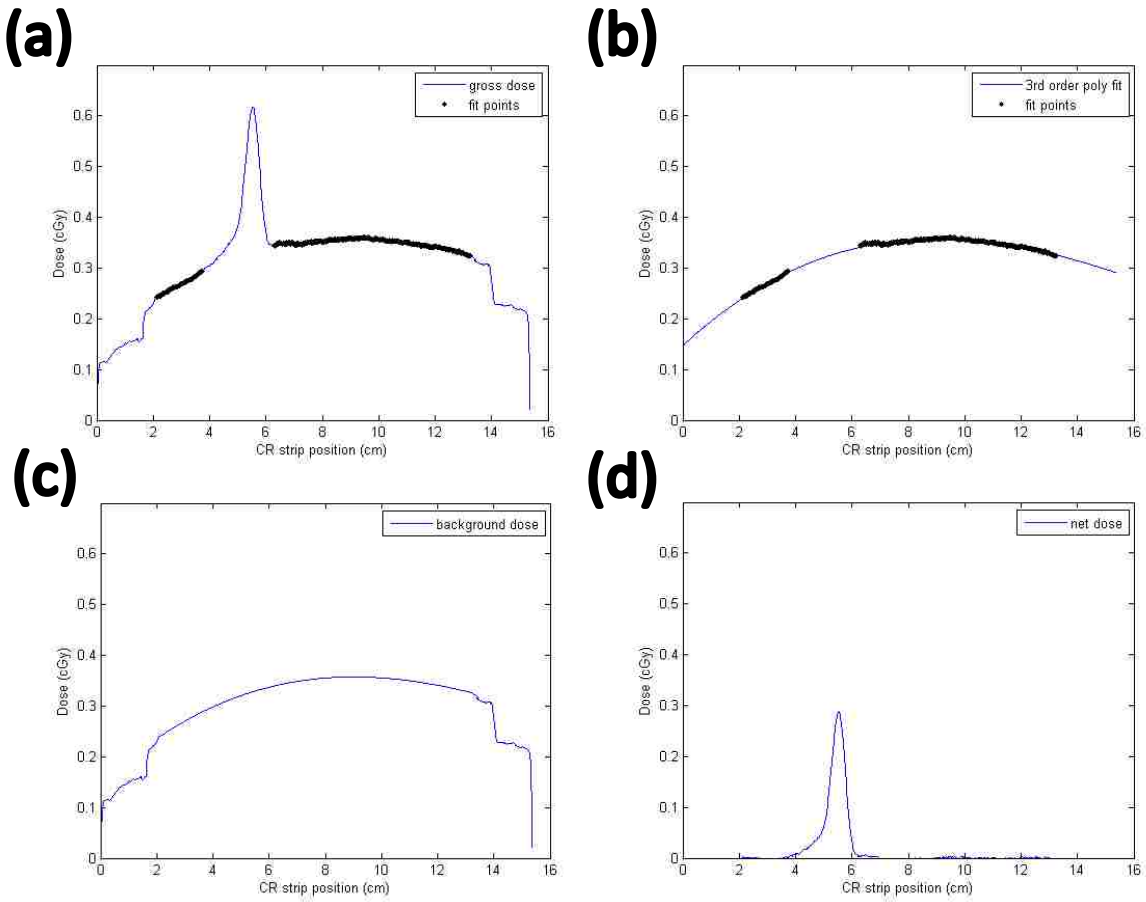

Figure 3.4. Background subtraction process. Plotted are (a) (blue) the gross dose profile and (black) the two regions of the gross dose profile to which the background polynomial was fit, (b) (blue) the result of this fit, (c) the background dose profile resulting from replacing the two portions of the gross dose profile corresponding to the fit regions and data points between the two with the result of the fit, and (d) the net dose profile resulting from the subtraction of the background dose profile from the gross dose profile.

electron peak structure. These portions were selected manually after MATLAB prompted for the boundaries of these two regions. Sample fit regions are shown in black in Figure 3.4 (a) and (b). There must always be two regions included in the fit, one on each side of the electron beam peak structure. 4^{th} order polynomials were only used for some 7 MeV and 9 MeV beams whose background structures had too many kinks for a 3^{rd} order polynomial to fit properly.

The portion of the gross dose profile corresponding to the data points of the fit regions and the data points between the fit regions were then replaced with values from the resulting polynomial fit. The result of this replacement was the background dose profile, an example of which is plotted in Figure 3.4 (c). The background dose profile was subtracted from the gross dose profile, an example of which is plotted in Figure 3.4 (a), resulting in the net dose profile, an example of which is plotted in Figure 3.4 (d).

3.1.1.3. Smoothing net dose profiles

A smoothing function was created to smooth the net dose profiles, as the transformation described in section 3.1.3 amplified noise in the low-energy portions of the energy spectra. This smoothing function allowed the user to manually smooth the net dose profiles using three smoothing subfunctions: a zeroing smoothing subfunction, a moving average smoothing subfunction, and a polynomial fit smoothing subfunction.

The first smoothing subfunction, the zeroing subfunction, replaced values within specified ranges with zeros. This is commonly used to flatten portions of the position spectra that fall well outside of the electron peak structure.

The second subfunction was the polynomial fit smoothing subfunction, which laid several polynomial curves on top of a net dose profile and used their central values to replace the original points. Each of these curves was the result of fitting a polynomial of user-specified order to a user-specified range of data points centered on the data point that was being replaced. This resulted in each data point being replaced, with the fit value for the fit centered on that point. If used properly, this

smoothing function further reduced the spatial noise while maintaining the general shape of the curve. The use of this subfunction was restricted to the peak structure.

For the third subfunction, the moving average smoothing subfunction, MATLAB's built-in function *smooth()*, was used. When using *smooth()*, the range over which *smooth()* would operate and the span of the averaging kernel were specified manually. For each element in the range over which *smooth()* operated, the element was replaced with the average of the elements within an averaging kernel centered on that element. The number of adjacent points used, plus the central point of the kernel, was the span. Since the span expanded evenly around the central element that was being replaced, the specified span required an odd number of data points. Further details about how *smooth()* works, including how it handles elements at the edges of the range of operation, is found within MATLAB help documentation. The moving average subfunction was used to smooth the transition between the zeroed regions and the peak region smoothed with the polynomial fit smoothing subfunction.

Using a combination of the subfunctions found in this smoothing function, the net dose profiles were smoothed to reduce noise. An example unsmoothed renormalized net dose profile, and the smoothed version of it resulting from the use of the smoothing function, are plotted in Figure 3.5 (a) and (b), respectively. Though artificially manipulating data in this way is not ideal, further analysis produced more well-behaved results if smoothing was performed. Most importantly, without at least zeroing the low-energy region to the left of the peak, the transformation described in section 3.1.3 would magnify noise in that region to heights greater than that of the electron peak. The energy metrics drawn from the resulting energy spectra, i.e. $\langle E \rangle^{*}_{m,o}$ (described section 3.1.4.2.1) and FWHM, are not appreciably affected by such smoothing, so the resulting error was ignored in this study.

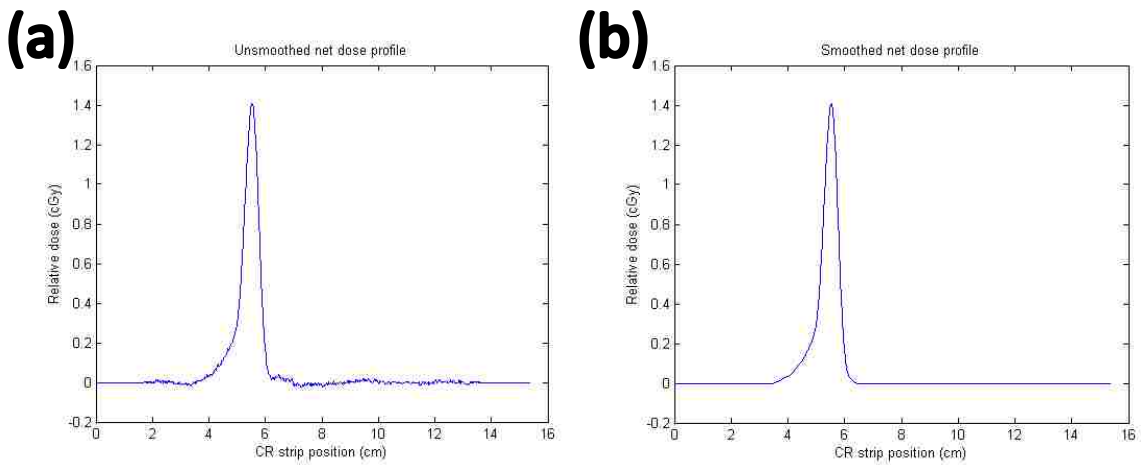

Figure 3.5. Net dose profile smoothing. Plotted is (a) an unsmoothed net dose profile renormalized to have an area of unity and (b) the smoothed version of it created with the smoothing function. The unsmoothed net dose profile was generated from the measured intensity profile of the 7 MeV beam on the Baton Rouge Elekta Infinity accelerator.

3.1.2. Transforming net dose profiles into energy spectra at spectrometer aperture

The next step of the analysis was the conversion of the net dose profiles into energy spectra at the spectrometer aperture. This conversion required (1) deriving the theory behind calculating net dose profiles at the CR strip given known energy spectra at spectrometer and (2) using this theory to create an inversion algorithm for determining the energy spectra at the spectrometer given the measured net dose profiles.

3.1.2.1. Theory of operation: transforming energy spectra at spectrometer aperture into net dose profiles

In this section, the relationship between the energy spectrum of an electron beam at the spectrometer aperture and the net dose profile it creates at the CR strip is derived. This relationship was first derived for monoenergetic electron beams and then generalized to polyenergetic beams. The magnetic field model described in section 2.1.2 was used here. The electron beam, while still modeled as perpendicular to the yz-plane hence parallel to the central axis, was not assumed to be a point beam as it was in section 2.1.2. Rather, the electron beam was assumed circular with radius equal to that of

the spectrometer aperture, b, illustrated in Figure 3.6 (a). The electron fluence inside the spectrometer aperture pictured in Figure 3.6 (a) was assumed spatially uniform.

The deposited dose in the CR strip is related to electron fluence by

$$D(x,z) = \phi_{CR}(x,z)\left(\frac{S}{\rho}\right)_{CR}^{E}, \tag{3.4}$$

where $D(x,z)$ is the net dose deposited in the CR strip's sensitive layer, $\phi_{CR}(x,z)$ is electron fluence at point (x,z) on the CR strip, and $\left(\frac{S}{\rho}\right)_{CR}^{E}$ is the electron mass stopping power for the CR strip for kinetic energy E. The CR strip was assumed sufficiently thin that the net dose and electron fluence did not vary with depth of penetration, y, into the strip's sensitive layer, hence y does not appear in equation 3.4.

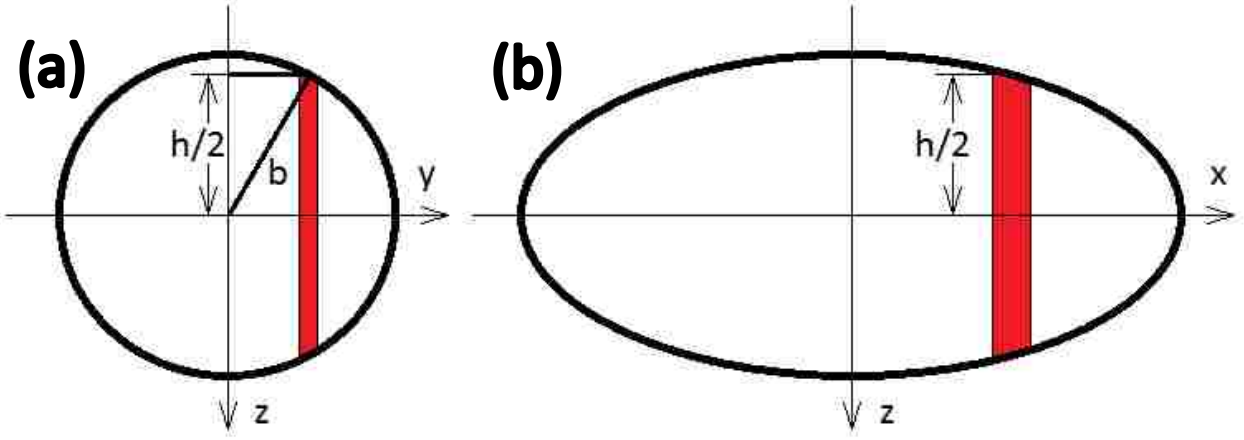

Figure 3.6. Mapping of electron fluence from the spectrometer aperture to the CR strip. The total number of electrons inside the red differential area is conserved as the electrons move from the (a) spectrometer aperture to the (b) CR strip. The labels $h/2$ and b are half the height of the aperture at the center of the red area and the radius of the aperture, respectively. Note that the heights of the apertures at the centers of the red areas in (a) and (b) are equal. Though the ellipse at the CR strip is illustrated as a larger in area than the spectrometer aperture, it is possible for electrons in the spectrometer aperture to map to smaller area at the CR strip.

To create a net dose profile, $\overline{D}(x)$, the dose must be averaged for each column, resulting in,

$$\overline{D}(x) = \frac{1}{2\Delta z}\int_{-\Delta z}^{\Delta z}\left(\frac{S}{\rho}\right)_{CR}^{E}\phi_{CR}(x,z)\,dz\,, \tag{3.5}$$

where Δz is large enough to capture all electron fluence even if there is spreading in the z direction. Assuming no electron spreading and a monoenergetic beam, the limits change such that

$$\bar{D}(x) = \frac{1}{2\Delta z} \int_{-h(y)/2}^{+h(y)/2} \left(\frac{S}{\rho}\right)_{CR}^{E} \phi_{CR}(x,z)dz\,, \tag{3.6}$$

where $\Delta z = h(y)$, illustrated in Figure 3.6 (a), is the height of the spectrometer aperture seen by electrons at a particular position y. Geometrically,

$$h(y) = 2(b^2 - y^2)^{1/2} \quad \text{for} \quad |y| \leq b\,, \tag{3.7}$$

where b is the radius of the spectrometer aperture.

Because the fluence is constant in the z direction over the limits of integration,

$$\bar{D}(x) = \frac{1}{2\Delta z}\left(\frac{S}{\rho}\right)_{CR}^{E} \phi_{CR}(x,0) \int_{-h(y)/2}^{+h(y)/2} dz\,. \tag{3.8}$$

Evaluating the integral gives

$$\bar{D}(x) = \frac{1}{2\Delta z}\left(\frac{S}{\rho}\right)_{CR}^{E} \phi_{CR}(x,0)h(y)\,. \tag{3.9}$$

The electrons entering through a differential width $y + \Delta y$ of the spectrometer aperture, shown in red in Figure 3.6 (a), are conserved and spread over an area bound by $x + \Delta x$ on the CR strip, shown in red in Figure 3.6 (b), meaning

$$\phi_{spect}^{P}(y,0)h(y)\Delta y = \phi_{CR}^{P}(x,0)h(y)\Delta x\,, \tag{3.10}$$

where ϕ_{spect}^{P} is the planar fluence at the spectrometer aperture and ϕ_{CR}^{P} is the planar fluence at the CR strip. At the spectrometer aperture, the electron fluence is equal to the electron planar fluence, as the beam is parallel and perpendicular to the yz plane. Additionally, the electron planar fluence is spatially uniform inside the spectrometer aperture, meaning

$$\phi_{spect}^{P}\Delta y = \phi_{CR}^{P}(x,0)\Delta x\,. \tag{3.11}$$

Note that there is no longer any indication of spatial dependence in ϕ_{spect}^{P}.

At the CR strip, the electron fluence, $\phi_{CR}(x,0)$, is given by

$$\phi_{CR}(x,0) = \frac{\phi_{CR}^{P}(x,0)}{\cos\big(\theta(x,y)\big)}\,, \tag{3.12}$$

where θ is the angle of incidence of electrons on the CR strip relative to normal incidence. Increasing the obliquity with which electrons impact the CR strip increases the deposited dose as the electrons will have longer track lengths through the sensitive layer of the CR strip. Since a specific CR strip position x will be struck by electrons from various spectrometer aperture positions, θ is a function of both x and y. Geometrically, using Figures 2.4 and 3.6,

$$\frac{1}{\cos\big(\theta(x,y)\big)} = \left[1 + \frac{(r-L)^2}{(x-x_o)^2}\right]^{1/2}, \tag{3.13}$$

for $L = L_o + y$ and $r = \frac{p}{eB_z}$ (eqn. 2.2), which gives

$$\frac{1}{\cos\big(\theta(x,y)\big)} = \left[\frac{r^2}{2rL - L^2}\right]^{1/2}. \tag{3.14}$$

Combining equations 3.11, 3.12, and 3.14 reduces to

$$\phi_{CR}(x,0) = \phi_{spect}^{P}\left[\frac{r^2}{2rL - L^2}\right]^{1/2}\left|\frac{\Delta y}{\Delta x}\right|, \tag{3.15}$$

and substituting equation 3.15 into equation 3.9 results in

$$\overline{D}(x) = \frac{1}{2\Delta z}\left(\frac{S}{\rho}\right)_{CR}^{E}\phi_{spect}^{P}\left[\frac{r^2}{2rL - L^2}\right]^{1/2}\left|\frac{dy}{dx}\right| h(y)\,. \tag{3.16}$$

Based on the geometry in Figures 2.4 and 3.6

$$y = r - L_o - [r^2 - (x - x_o)^2]^{1/2}\,, \tag{3.17}$$

and taking the derivative of y with respect to x gives

$$\left|\frac{dy}{dx}\right| = \left[\left(\frac{r}{x - x_o}\right)^2 - 1\right]^{-1/2}. \tag{3.18}$$

Substituting equation 3.7, 3.17, and 3.18 into equation 3.16 and simplifying results in the net dose profile for a monoenergetic electron beam being

$$\bar{D}(x) = K\phi_{spect}^{P}\left[\left(\frac{r^2}{r^2-(x-x_o)^2}\right)\left(b^2-\left\{r-L_o-[r^2-(x-x_o)^2]^{1/2}\right\}^2\right)\right]^{1/2}, \qquad 3.19$$

where

$$K = \frac{1}{\Delta z}\left(\frac{S}{\rho}\right)_{CR}^{E}. \qquad 3.20$$

Note that equation 3.19 is only valid as long as $|y| \leq b$. Integrating equation 3.19 across an electron's beam entire momentum spectrum and assuming $\left(\frac{S}{\rho}\right)_{CR}^{E}$, and thus K, is constant throughout the therapeutic electron beam energy range (3-20 MeV) gives,

$$\bar{D}(x) = K\int_{p_{min}(x)}^{p_{max}(x)}\phi_{spect}^{P}(p)\left[\left(\frac{r^2}{r^2-(x-x_o)^2}\right)\left(b^2-\left\{r-L_o-[r^2-(x-x_o)^2]^{1/2}\right\}^2\right)\right]^{1/2}dp\,, \qquad 3.21$$

where $\phi_{spect}^{P}(E)$ is the momentum spectrum at the spectrometer aperture and $p_{max}(x)$ and $p_{min}(x)$ are the maximum and minimum momentums of electrons that the spectrometer aperture allows to reach a certain position x on the CR strip, respectively, where

$$p_{max}(x) = \frac{eB}{2}\left[\frac{(x-x_o)^2}{(L_o-b)}+(L_o-b)\right], \qquad 3.22a$$

and

$$p_{min}(x) = \frac{eB}{2}\left[\frac{(x-x_o)^2}{(L_o+b)}+(L_o+b)\right]. \qquad 3.23a$$

In the energy domain, eq. 3.21 becomes

$$\overline{D}(x) = K \int_{E_{min}(x)}^{E_{max}(x)} \phi_{spect}^{P}(E) \left[\left(\frac{r^2}{r^2 - (x - x_o)^2} \right) \left(b^2 - \left\{ r - L_o - [r^2 - (x - x_o)^2]^{1/2} \right\}^2 \right) \right]^{1/2} dE, \quad 3.24$$

where:

$$E_{max}(x) = \left[(p_{max}(x) * c)^2 - {E_o}^2 \right]^{1/2} - E_o \, , \quad 3.22b$$

and

$$E_{min}(x) = \left[(p_{min}(x) * c)^2 - {E_o}^2 \right]^{1/2} - E_o \, . \quad 3.23b$$

Alternatively, equation 3.24 can be written as

$$\overline{D}(x) = K \int_{E_{cutoff}}^{+\infty} \phi_{spect}^{P}(E) DRF(E, x) dE \, , \quad 3.25$$

where E_{cutoff} comes from equation 2.8 except L_o was replaced by $L_o + b$, and $DRF(E, x)$ is the detector response function, i.e. CR strip dose per electron incident on the spectrometer aperture, i.e.

$$DRF(E, x) = \left[\left(\frac{r^2}{r^2 - (x - x_o)^2} \right) \left(b^2 - \left\{ r - L_o - [r^2 - (x - x_o)^2]^{1/2} \right\}^2 \right) \right]^{1/2}, \quad 3.26a$$

when $E_{min}(x) \leq E \leq E_{max}(x)$, and elsewhere (i.e. $E \leq E_{min}(x)$ or $E \geq E_{max}(x)$)

$$DRF(E, x) = 0 \, , \quad 3.26b$$

$$r = \frac{[E^2 + 2 * E * E_o]^{1/2}}{ecB_z} \, . \quad 3.27$$

3.1.2.2. Properties of detector response function

The detector response function, $DRF(E,x)$, given in equations 3.26a & b includes the effects of the (1) finite size of the aperture, (2) non-normal incidence of the electrons on the CR strip, and (3) the Jacobian of the transformation from the energy domain to the spatial domain. Example monoenergetic $DRF(E,x)$ plotted in red in Figure 3.7 (a) were created using the 1.59-mm radius of the spectrometer aperture for b in equation 3.26a. The widths of monoenergetic $DRF(E,x)$ vary with b, approaching zero as b approaches zero. The area under $DRF(E,x)$*$\cos\big(\theta(E,x)\big)$, examples of which are plotted in blue in Figure 3.7 (a), remains constant with E though the heights and widths of $DRF(E,x)$*$\cos\big(\theta(E,x)\big)$ decrease and increase, respectively, as E increases beyond about 5.5 MeV. This is indicative of the fact that the planar fluence was conserved between the spectrometer aperture and the CR strip while the cross-sectional area between the beam and the CR strip increased with E. Note $\cos\big(\theta(x,y)\big)$ in eqn. 3.14 was rewritten to $\cos\big(\theta(E,x)\big)$ to emphasize energy dependence. The widths of monoenergetic $DRF(E,x)$ also widen with E, though the decrease in heights is retarded by the fact that $DRF(E,x)$ is proportional to fluence, not planar fluence, meaning total area under $DRF(E,x)$ increases with E due to an increase in obliquity of incidence angle.

As the E of the $DRF(E,x)$ is lowered, $DRF(E,x)$ will encompass a $x-x_o$ value that equals r, meaning the $\left(\frac{r^2}{r^2-(x-x_o)^2}\right)$ term in equation 3.26a equals infinity. Physically, this can be understood as a convergence of monoenergetic electrons upon a single CR strip position, as is illustrated in Figure 3.8 (b). This creates a vertical asymptote inside $DRF(E,x)$ as long as the E of the $DRF(E,x)$ falls within this convergence range (≈4.0-4.6 MeV). The forming of this vertical asymptote is illustrated in Figure 3.9 (b). This asymptote is problematic, as equation 3.25 was executed via discrete integration with monoenergetic $DRF(E,x)$ sampled at CR strip positions, i.e. x values, corresponding to a constant 0.01 MeV sampling interval in the energy domain. Variations in the distance between the vertical asymptote and nearest x value of the sampling grid as E varied within the convergence range caused large

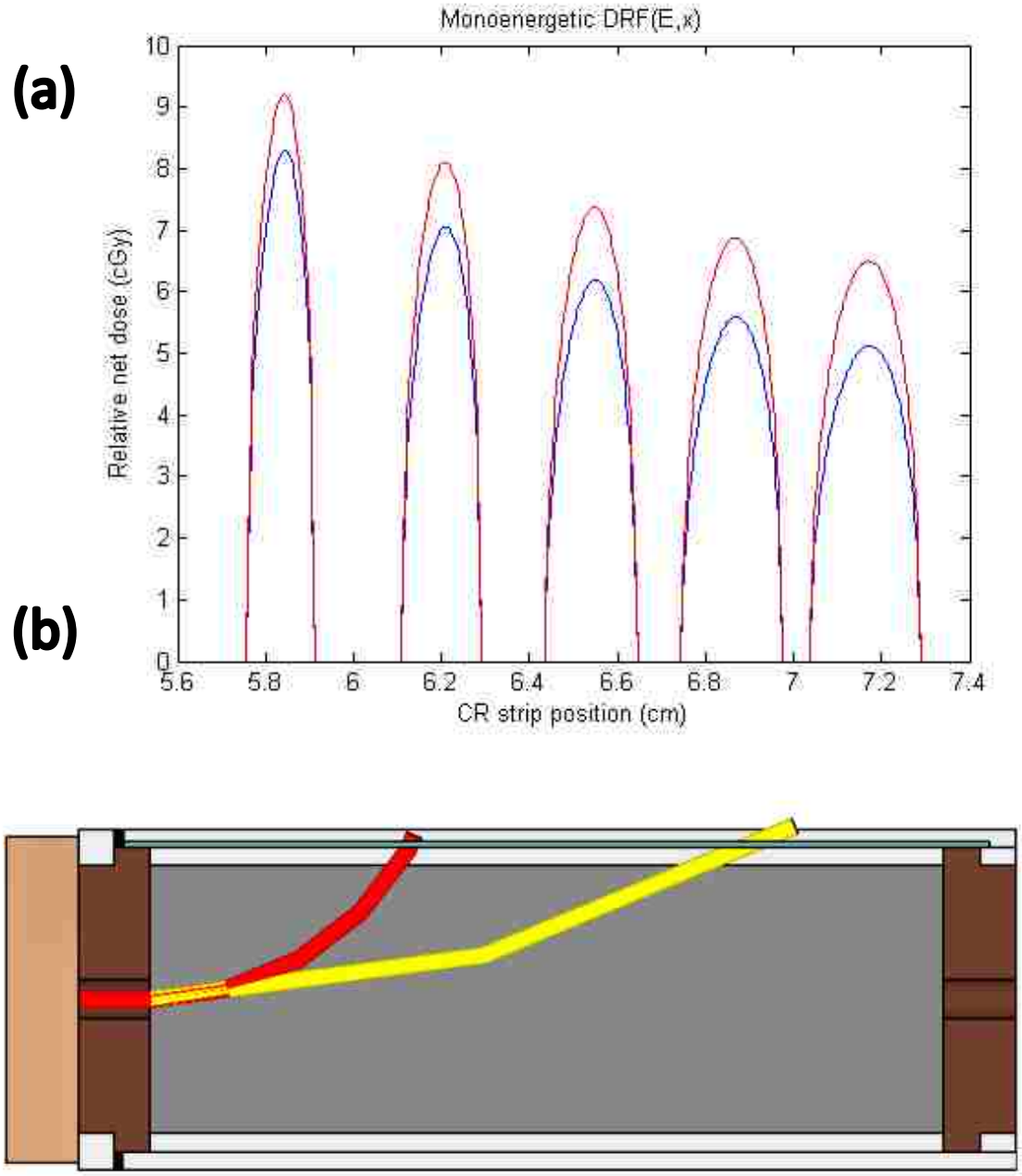

Figure 3.7. Illustration of DRF(E,x) characteristics. Plotted (a) are example (red) $DRF(E,x)$ and (blue) $DRF(E,x)$*$\cos(\theta(E,x))$ for equal-fluence, monoenergetic electron beams of energies of 8, 9, 10, 11, and 12 MeV assuming a 1.59-mm spectrometer aperture. Multiplying $DRF(E,x)$ by $\cos(\theta(E,x))$ removes the effect of non-normal electron incidence. The areas under the blue plots are unity, while the areas under the red plots are 1.11, 1.15, 1.19, 1.23, and 1.27 for the 8, 9, 10, 11, and 12 MeV beams, respectively. Also illustrated are (b) example monoenergetic electron beams with (red) low and (yellow) high beam energies demonstrating an increase in beam-CR strip cross-sectional area with beam energy. All dimensions are to scale.

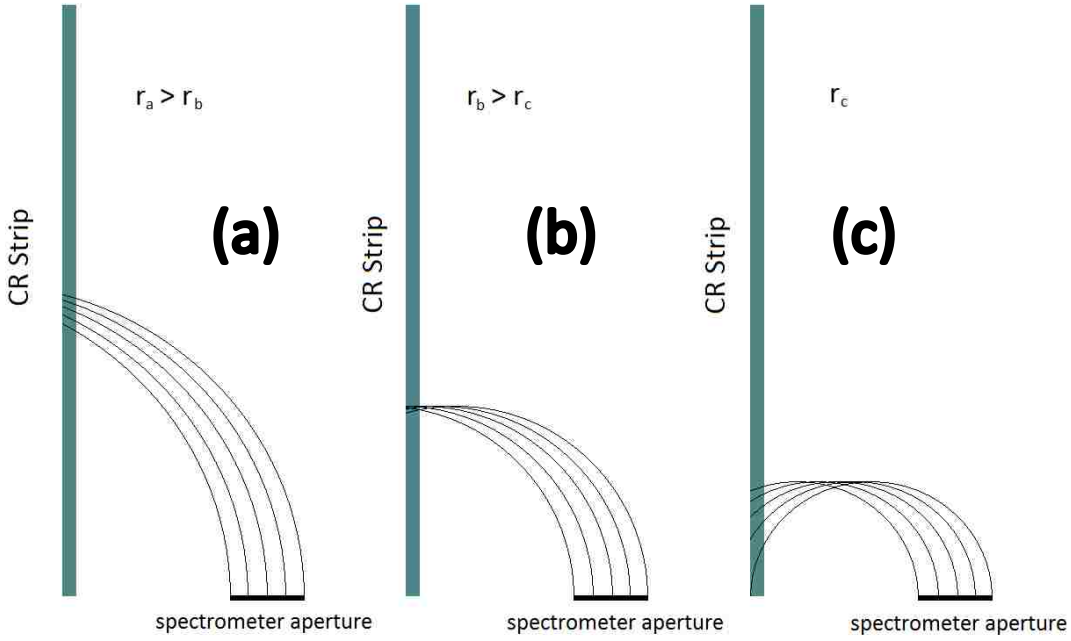

Figure 3.8. Electron beamlet convergence. Illustrated are electron beamlet trajectories for monoenergetic electron beams when the electrons are all (a) downstream-directed, (c) upstream-directed, and (b) both upstream and downstream-directed, as well as neither (i.e. striking at normal incidence) when they strike the CR strip. The direction of the electrons upon impact changes as the energy, E, hence radius of curvature, r, of the beam decreases. Notice that as the impact direction of the beamlets transitions from downstream to upstream, the impact positions on the CR strip trace over one another, creating spots of concentrated dose.

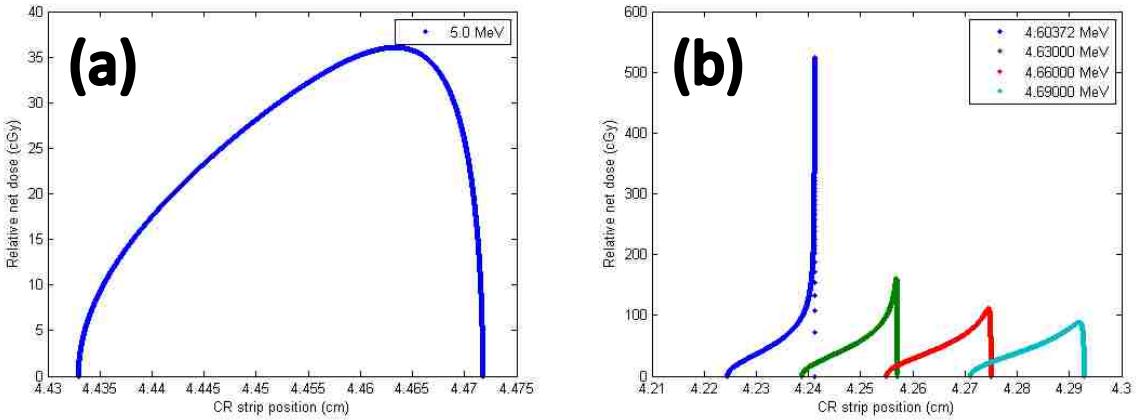

Figure 3.9. Formation of vertical asymptote in DRF. Plotted is (a) 5 MeV monoenergetic $DRF(E, x)$ demonstrating the bunching up of electrons in the most downstream portion of the CR strip prior to the formation of a vertical asymptote. The formation of the vertical asymptote becomes more apparent as (b) the energy of the $DRF(E, x)$ is lowered further and approaches the convergence region. The plotted $DRF(E, x)$ were sampled with a resolution of 10^{-8} MeV in the energy domain for illustrative purposes. In practice, a resolution of 0.01 MeV was used as increasing the resolution to 0.001 MeV or finer created prohibitively long run times. The 0.01 MeV sampling grid is fairly course in this region, as less than eight data points were sampled per $DRF(E, x)$ plotted in (b).

fluctuations in the maximum magnitude sampled per monoenergetic $DRF(E,x)$. As discrete integration in this study was performed by approximating the area per data point by multiplying the magnitude sampled by the width of the spatial bin, these fluctuations in maximum magnitude sampled per monoenergetic $DRF(E,x)$ caused the distribution of area within the approximated $DRF(E,x)$ to vary erratically with E. This is especially true since the sampling grid is very course relative to the widths of $DRF(E,x)$ in the convergence range. This causes significant errors in output of equation 3.25 when operating in the convergence range. More importantly, the sampled magnitudes were sometimes so large that their values could not be assigned to double-precision variables (i.e. 64 bits). In these cases, MATLAB assigns a value of infinity (Inf) to the magnitude, rendering further calculations impossible.

To deal with this problem, the calculated net dose, $\overline{D}_{calc}(x)$, was determined for the portion above and below 5.5 MeV separately. Then, these portions were added together, i.e.

$$\overline{D}_{calc}(x) = \overline{D}_{calc,lower}(x) + \overline{D}_{calc,upper}(x)\,, \tag{3.28}$$

where $\overline{D}_{calc,upper}(x)$ was obtained by changing the low-energy limit of equation 3.25 from E_{cutoff} to 5.5 MeV, which was a low-energy limit large enough to ensure no $DRF(E,x)$ were generated that were too narrow relative to the sampling grid or contained vertical asymptotes. The result was

$$\overline{D}_{calc,upper}(x) = a_1 \int_{5.5\ MeV}^{\infty} \phi_{spect}^{P}(E) DRF(E,x) dE\,. \tag{3.29}$$

where a_1 was a constant chosen such that for any energy greater than 5.5 MeV, if $DRF(E,x)$ did not include the effect of the variation in angle of incidence from the normal, then equation 3.29 would be an area conserving operation, i.e.

$$1 = a_1 \int_{-\infty}^{+\infty} DRF(E,x)\cos\big(\theta(E,x)\big)\,dx \quad \text{for } 5.5 \text{ MeV} < E\,. \tag{3.30}$$

$\overline{D}_{calc,lower}(x)$ was the portion of $\phi^{P}_{spect}(E)$ between E_{cutoff} and 5.5 MeV converted to the spatial domain, i.e.

$$\overline{D}_{calc,lower}\big(x(E)\big) = \frac{1.0\ cGy}{1/_{cm^2}}\phi^{P}_{spect}(E)\left|\frac{dE}{dx}\right| \quad \text{for } E_{cutoff} < E < 5.5 \text{ MeV}. \qquad 3.31$$

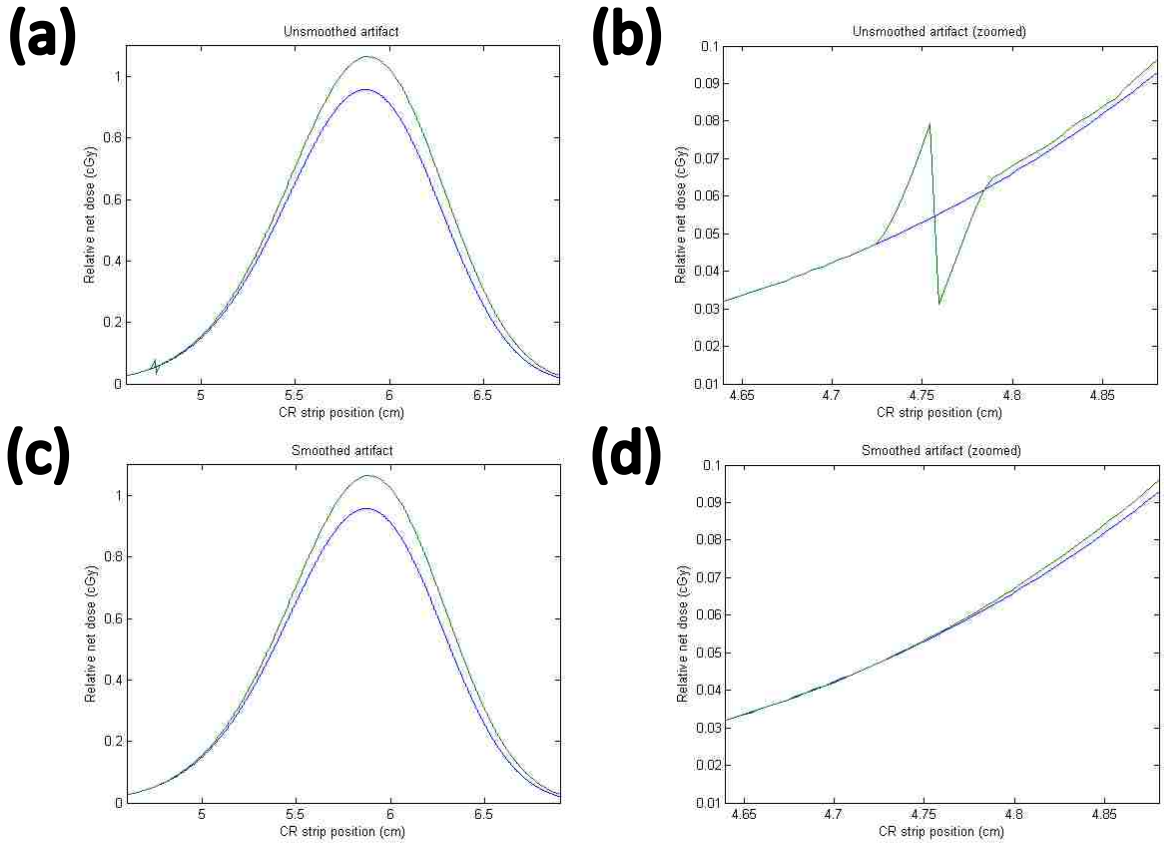

Figure 3.10. Smoothing of the low-energy cutoff artifact. Plotted above is the input (blue) to and output (green) from the inversion algorithm both without (a) (b) smoothing of the low-energy cutoff artifact and with (c) (d) smoothing of the low-energy cutoff artifact. Plots on the right (b) (d) are zoomed in versions of plots on the left (a) (c).

This work-around creates the "hill and valley" low-energy cutoff artifact seen in Figure 3.10 (a) and (b). This artifact was eliminated by fitting a 4th order polynomial to the regions to the immediate left and right of the artifact. The result of the fit was used to replace data points in the artifact region, resulting in smoothed artifact regions like the one pictured in Figure 3.10 (c) and (d). The result is a $\overline{D}_{calc}(x)$ that does not include the effects of the finite size of the aperture or the variation in the angle of incidence

from normal for CR strip positions corresponding to energies below 5.5 MeV. This discrepancy was ignored as it was small and existed only in the portion of $\phi^P_{spect}(E)$ that lies below 5.5 MeV, which is a minor fraction of the entire area under $\phi^P_{spect}(E)$ even for the lowest energy beams.

3.1.2.3. Solving for energy spectra at the spectrometer aperture

For a given measured net dose profile at the CR strip, $\overline{D}_{meas}(x)$, the energy spectrum at the spectrometer aperture, $\phi^P_{spect}(E)$, was determined by solving equation 3.28. The equation was solved using the following numerical process:

Step 1: The initial estimate of the energy spectrum at the spectrometer aperture, $\phi^P_{spect,est,1}(E)$, was determined by transforming $\overline{D}_{meas}(x)$ normalized to an area of unity, i.e. $\overline{D}_{meas,N}(x)$, into the energy domain, i.e.

$$\phi^P_{spect,est,1}\big(E(x)\big) = \frac{1/cm^2}{1.0\ cGy}\,\overline{D}_{meas,N}(x)\left|\frac{dE}{dx}\right|^{-1}. \qquad 3.32$$

This estimate of the energy spectrum ignores the effect of finite aperture size and variation in angle of incidence from the normal, $\theta(E,x)$.

Step 2: Next, the first estimate of the net dose profile calculated using equation 3.28, i.e. $\overline{D}_{calc,1}(x)$, was generated with $\phi^P_{spect,est,1}(E)$.

Step 3: Next, the difference between $\overline{D}_{calc,1}(x)$ and $\overline{D}_{meas,N}(x)$, $\Delta\overline{D}_1(x)$, was calculated, i.e.

$$\Delta\overline{D}_1(x) = \overline{D}_{meas,N}(x) - \overline{D}_{calc,1}(x)\,. \qquad 3.33$$

$\Delta\overline{D}_1(x)$ was transformed into the energy-domain, i.e.

$$\Delta\phi_1\big(E(x)\big) = \frac{1/cm^2}{1.0\ cGy}\Delta\overline{D}_1(x)\left|\frac{dE}{dx}\right|^{-1}. \quad 3.34$$

$\Delta\phi_1(E)$ indicates how $\phi^P_{spect,est,1}(E)$ needs to change to produce a calculated net dose profile that better matches $\overline{D}_{meas,N}(x)$.

Step 4: Prior to being added to $\phi^P_{spect,est,1}(E)$ to generate the next estimate of the energy spectrum at the spectrometer aperture, $\Delta\phi_1(E)$ was smoothed via an eight-Gaussian fit, i.e.

$$\Delta\phi_{Gauss,1}(E) = \sum_{k=1}^{N=8} a_{1,k}\, e^{\frac{-\left(E-a_{2,k}\right)^2}{a_{3,k}}}, \quad 3.35$$

where $a_{1,k}$, $a_{2,k}$, and $a_{3,k}$ were determined by fitting eight Gaussians distributions to $\Delta\phi_1(E)$. More details about the fit are available in section 3.1.2.4.

Step 5: An iterative process, i.e. $i = i + 1$, continued whereby

$$\phi^P_{spect,est,i}(E) = \phi^P_{spect,est,i-1}(E) + \Delta\phi_{Gauss,i-1}(E)\,. \quad 3.36$$

then steps (2-4) were repeated, i.e. the ith estimate of the net dose profile, $\overline{D}_{calc,i}(x)$, was calculated using equation 3.28 and $\phi^P_{spect,est,i}(E)$,

then,

$$\Delta\phi_i\big(E(x)\big) = \frac{1/cm^2}{1.0\ cGy}\Delta\overline{D}_i(x)\left|\frac{dE}{dx}\right|^{-1}, \quad 3.37$$

then

$$\Delta\phi_{Gauss,i}(E) = \sum_{k=1}^{N=8} a_{1,k}\, e^{\frac{-\left(E-a_{2,k}\right)^2}{a_{3,k}}}. \qquad 3.38$$

where $a_{1,k}$, $a_{2,k}$, and $a_{3,k}$ were determined by fitting eight Gaussians distributions to $\Delta\phi_i(E)$.

This process, henceforth the inversion algorithm, was executed from i=2 until i=N, where N was the number of iterations such that the total area under $\left|\Delta\phi_{Gauss,i}(E)\right|$ was less than 0.0001 for five consecutive iterations (i =N-4 through i =N). After N iterations, $\phi^P_{spect,est,i}(E)$ was assumed equal to $\phi^P_{spect}(E)$. In practice, N = 15 for most beams energies. Note that for iteration $i = 1$, $\phi^P_{spect,est,i}(E)$ will have an area of exactly one. For all other iterations $i > 1$, $\phi^P_{spect,est,i}(E)$ will not have an area of unity, though it will approach unity as i increases.

3.1.2.4. Details of Gaussian smoothing

In preliminary versions of the inversion algorithm described in section 3.1.2.3, $\Delta\phi_{i-1}(E)$ was not smoothed with the 8-Gaussian fit, i.e. $\Delta\phi_{Gauss,i}(E)$, prior to being added to $\phi^P_{spect,est,i-1}(E)$ to obtain $\phi^P_{spect,est,i}(E)$. Executing the inversion algorithm without modifying $\Delta\phi_{i-1}(E)$ produced erractic, unrealistic results. After several iterations, the inversion algorithm began to add narrow pieces of area back into $\phi^P_{spect,est,i}(E)$ at inappropriate energies, creating poorly behaved energy spectra like the green one plotted in Figure 3.11. Smoothing $\Delta\phi_{i-1}(E)$ with Gaussians first meant the inversion algorithm could only add or subtract area to or from $\phi^P_{spect,est,i-1}(E)$ in smooth, gradual portions and would do so mostly inside the bounds of the original estimate, $\phi^P_{spect,est,1}(E)$. To ensure the fitting algorithm called by the inversion algorithm did not get stuck continually trying to fit Gaussian distributions to just one portion of $\Delta\phi_{i-1}(E)$, the initial estimates of the centers of the eight Gaussian distributions used by the fitting algorithm, $a_{2,1}$, $a_{2,2}$, $a_{2,3}$, $a_{2,4}$, $a_{2,5}$, $a_{2,6}$, $a_{2,7}$, and $a_{2,8}$, were randomly selected from inside the 4-7, 7-10, 10-13, 13-16, 16-19, 19-22, 22-26, and 26-30 MeV ranges of $\Delta\phi_{i-1}(E)$, respectively, for each iteration.

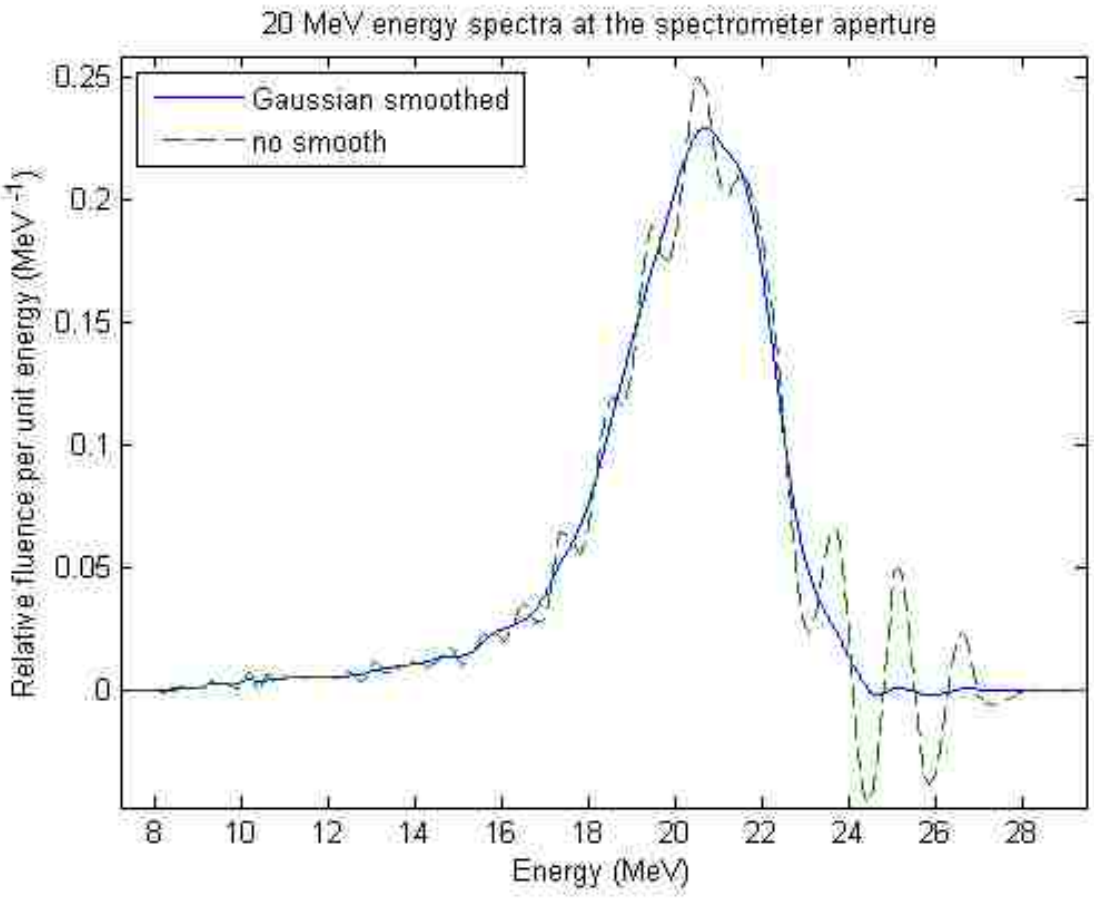

Figure 3.11. Inversion algorithm with and without Gaussian smoothing. Plotted are the results of the inversion algorithm described in section 3.1.2.3 after 15 iterations both (blue) with and (green) without Gaussian smoothing of $\Delta\phi_{i-1}(E)$. Note Gaussian smoothing results in more well-behaved and less noisy energy spectra at the spectrometer aperture.

3.1.3. Transforming energy spectra at spectrometer aperture into energy spectra at 95-cm SCD

The dual aperture, collimation design preferentially selects forward-directed, higher-energy electrons for passage into the magnetic spectrometer, meaning that for any single electron beam the energy spectrum at 95-cm source to collimator distance (SCD), $\phi^P_{95-cm\,SCD}(E)$, differs from $\phi^P_{spect}(E)$. Using Fermi-Eyges MCS theory, $\phi^P_{spect}(E)$ was determined given a known $\phi^P_{95-cm\,SCD}(E)$. Then, the process was inverted to determine $\phi^P_{95-cm\,SCD}(E)$ given a known $\phi^P_{spect}(E)$.

To determine the $\phi^P_{spect}(E)$ for a known $\phi^P_{95-cm\,SCD}(E)$, it was necessary to model the transport of the electron beam from the Cerrobend® aperture at 95-cm SCD to the spectrometer

aperture. Due to the small diameter of the Cerrobend® aperture relative to the distance between the two apertures, the electron beam was approximated as a point source centered in the middle of the Cerrobend® aperture. Then, the radial spread of the electrons away from the central axis as the beam travels from the point source to the spectrometer was modeled assuming a Gaussian angular distribution in the xy-plane and xz-plane at the point source.

Under these assumptions, the electron fluence at the face of the copper block was a Gaussian spatial distribution centered in the middle of the spectrometer aperture where the standard deviation of the spatial distribution in the xy-plane was much greater than the diameter of the spectrometer aperture. The magnitude of the electron fluence on central axis at the face of the copper block per incident electron at the Cerrobend ® aperture, ϕ_a , is given by

$$\phi_a \approx \frac{1}{2\pi\left(L_{surf}\right)^2(\sigma_{\theta_y})^2} \ , \tag{3.39}$$

where L_{surf} equals the distance between the upstream surfaces of the apertures and σ_{θ_y} is the standard deviation of the projected angular distribution in the xy-plane.

Because the diameter of the spectrometer aperture was small compared to the spread of the Gaussian spatial distribution at the upstream face of the copper spectrometer block, the entire area inside the spectrometer aperture was assumed to have an electron fluence per electron incident upon the Cerrobend® insert of ϕ_a. Because L_{surf} is constant, variations in ϕ_a are due solely to changes in σ_{θ_y}, which is related to electron energy by the approximation

$$\left(\sigma_{\theta_y}\right)^2 = a_1 * E^{-1.78} \ , \tag{3.40}$$

where a_1 is a constant of proportionality (Werner *et al* 1982). Data based on the work of Harris (2012) plotted in Figure 3.12 from MC simulations performed at MBPCC (courtesy of Dr. Robert Carver) demonstrated that this relationship is valid for electron beam energies above 3.25 MeV.

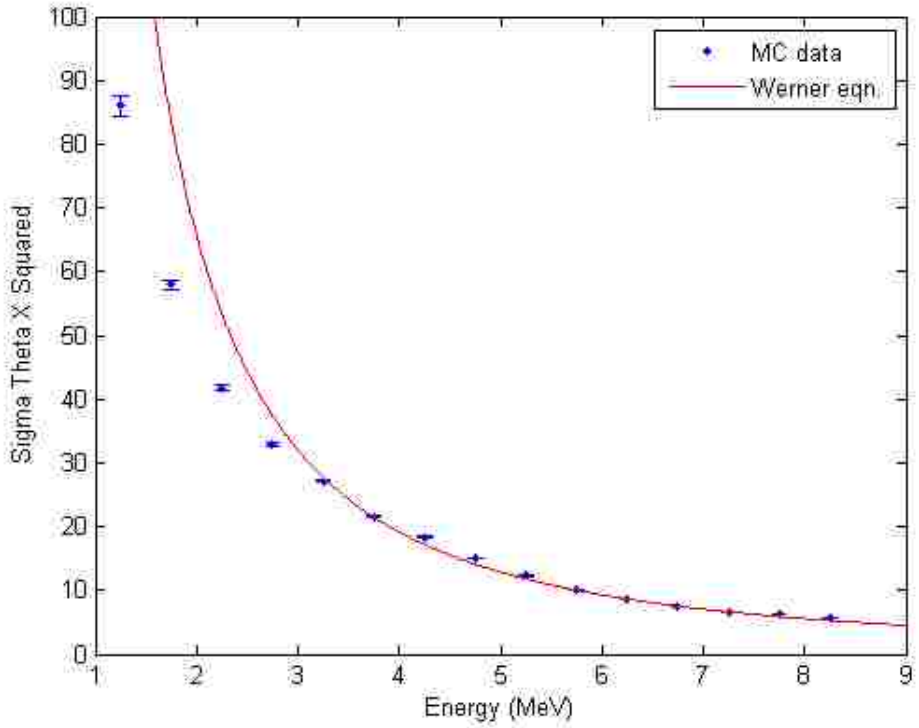

Figure 3.12. Validation of Werner's relationship. Plotted is (red) σ_{θ_y} versus E for scattering powers of air from Werner's relationship (equation 3.40) on top of (blue) results of MC simulated electron beam data. Simulations were performed at MBPCC by Dr. Robert Carver using a detailed physical model of the treatment head and applicator geometry (Harris 2012). Equation 3.40 with a_1=226.3 provided the best fit to the MC data points for E > 3.25 MeV.

Substituting equation 3.40 into equation 3.39 leads to,

$$\phi_a = b_1 * E^{1.78}\,, \tag{3.41}$$

where b_1 is a constant of proportionality. Hence,

$$\phi^P_{spect}(E) = c_1 * E^{1.78} * \phi^P_{95-cm\,SCD}(E)\,, \tag{3.42}$$

where c_1 was a constant whose value was chosen such that the area under $\phi^P_{spect}(E)$ was unity. Hence, the electron beams loses more low than high energy electrons in passing through the two-aperture collimation system, meaning the energy spectrum contains a disproportionally high percentage of higher energy electrons. Inversely,

$$\phi^P_{95-cm\ SCD}(E) = d_1 * E^{-1.78} * \phi^P_{spect}(E)\,, \qquad 3.43$$

where d_1 is a constant such that the area under $\phi^P_{95-cm\ SCD}(E)$ is unity.

3.1.4. CR strip position to electron energy calibration

The methods of section 3.1.2 use equation 2.7. The values for the parameters x_o and B_z in equation 2.7 were determined by a fit of the equation 2.7 to clinically derived energy and position parameters. These parameters were drawn from the calibration data, i.e. (1) the seven %DD curves in water and (2) the seven CR strip net dose profiles measured on Jan/14/2013 on the Baton Rouge Elekta Infinity accelerator. After the initial fit of equation 2.7 to determine the values for x_o and B_z, the energy spectra at 95-cm SCD were calculated using the methods described in sections 3.1.2 and 3.1.3. Then, the change in the energy spectra created by the passage of the electron beam through the two-aperture collimation system was used to adjust the energy parameters used in the fit, generating a second more accurate estimate of the values for x_o and B_z.

3.1.4.1. Calibration %DD curves and net dose profiles

Calibration data consisted of %DD curves in water and CR strip net dose profiles measured for all seven electron beams on MBPCC's Baton Rouge Elekta Infinity accelerator on Jan/14/2013. All calibration data were gathered on a single day to minimize the chance for energy spectra to drift between measurements. Hence, it was assumed that the measured %DD curves and net dose profiles for each nominal beam energy were produced by electron beams with the same energy spectra. To obtain measured %DD curves, percent depth ionization (%DI) curves were measured with the 14 x 14

cm^2 open applicator using a scanning water tank with a 0.13 cm^3 CC13 air ionization chamber (IBA, Louvain-la-Neuve, Belgium). These %DI curves, which were plots of percent ionization versus effective depth (physical depth minus $0.5r_{cav}$), were converted into the %DD curves used for calibrating the magnetic spectrometer. Percent ionization was converted to percent dose using the AAPM TG-70 protocol (Gerbi *et al* 2009) and TG-25 protocol (Khan *et al* 1990) with TG-51 values for relative stopping powers (Almond *et al* 1999), as implemented in the IBA data acquisition system (IBA, Louvain-la-Neuve, Belgium). Prior to being converted to %DD curves, the %DI curves were shifted deeper by 0.063 cm to align with same-day %DI measurements taken in Plastic Water® phantom slabs. These phantom slab measurements are explained in Aim 4.

3.1.4.2. Calibration energy and position parameters

The energy and position parameters used for the fit were the modified peak mean energy of an electron beam incident on the surface of a water phantom placed near isocenter, $\langle E \rangle_{m,o}^{*}$, and the modified peak mean position, $\langle x \rangle_{m}^{*}$, respectively. $\langle E \rangle_{m,o}^{*}$, the average energy of the peak region of the energy spectrum, was obtained from measured %DD curve R_p values and equation 3.45. $\langle x \rangle_{m}^{*}$ is an analogous parameter defined relative to $\langle E \rangle_{m,o}^{*}$ and drawn from measured CR strip net dose profiles.

3.1.4.2.1. Definition of modified peak mean energy

$\langle E \rangle_{m,o}^{*}$ is a modified version of the incident peak mean energy, $\langle E \rangle_{o}^{*}$, defined by Deasy (private communications 2012). $\langle E \rangle_{o}^{*}$ is the average energy within a limited range of the energy spectrum called the energy averaging range. The energy averaging range used to find $\langle E \rangle_{o}^{*}$ incorporates most of the electron peak structure of the energy spectrum. The lower energy limit of the energy averaging range, as defined by Deasy (2012) was $0.85E_{p,o}$, and the upper energy limit of the energy averaging range was $1.15E_{p,o}$, where $E_{p,o}$ was the drawn from measured energy spectra. A sample $\pm$15% energy averaging range is illustrated in Figure 3.13.

Deasy used $\langle E \rangle_o^*$ as a substitute for $E_{p,o}$ in equation 1.1, resulting in,

$$\langle E \rangle_o^*(MeV) = 0.22MeV + 1.98\frac{MeV}{cm} * R_p + 0.0025\frac{MeV}{cm^2} * (R_p)^2 \,, \qquad 3.44$$

where R_p is derived from measured electron beam %DD curves.

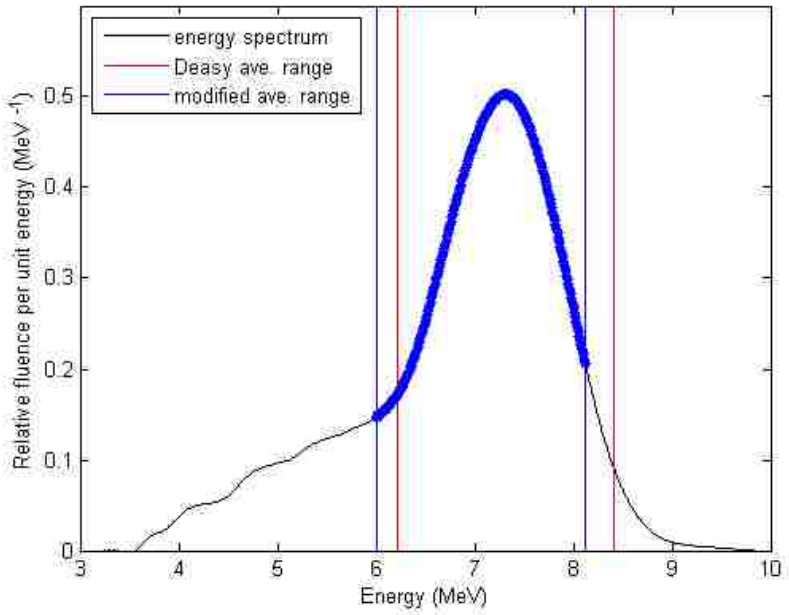

Figure 3.13. Energy averaging ranges used to calculate peak mean energy. Plotted is an (black) example 7 MeV energy spectrum from MBPCC's Baton Rouge Elekta Infinity accelerator and (red vertical lines) the edges of its energy averaging range calculated using Deasy's method (i.e. low-energy edge of range = $0.85E_{p,o}$ and high-energy edge of range = $1.15E_{p,o}$). Also plotted is the energy spectrum's (blue overlay and vertical lines) energy averaging range calculated using the modified Deasy method.

To understand Deasy's reasoning behind this substitution, it is necessary to understand that equation 1.1 was derived by simulating monoenergetic, monodirectional electron point beams normally incident upon the surface of a water phantom with MC techniques (ICRU 35, 1984). Then, the reciprocity theorem (ICRU 35, 1984) was used to calculate the %DD curve for a broad parallel electron beam of the same monoenergetic energy, E_{mono}. To compare these %DD curves to clinically measured %DD curves produced by the diverging beams of clinical linear accelerators, the inverse of the spherical-divergence correction should be applied to all data points of the measured %DD curves, though Deasy sometimes ignored this correction because its effect on R_p was negligible below 20 MeV. Because

electron beams used in the clinic are not monoenergetic, energy parameters drawn from measured energy spectra must be substituted for the E_{mono} values energy spectra used in the MC simulations. ICRU 35 (1984) recommends $E_{p,o}$, resulting in equation 1.1, while Deasy used $\langle E \rangle_o^*$, resulting in equation 3.44.

Deasy (1992) concluded that $\langle E \rangle_o^*$ was a better substitution for E_{mono} than $E_{p,o}$ by obtaining R_p values with the same methods used to derive equation 1.1, except with measured energy spectra from a Phillips SL25, now the Elekta Infinity, instead of with E_{mono}. As can be seen from Figure 3.14, the plot of R_p versus $\langle E \rangle_o^*$ overlaps the plot of the inverse of equation 1.1 better than the plot of R_p versus $E_{p,o}$, which led Deasy to the conclusion that equation 3.44 should be used in lieu of equation 1.1.

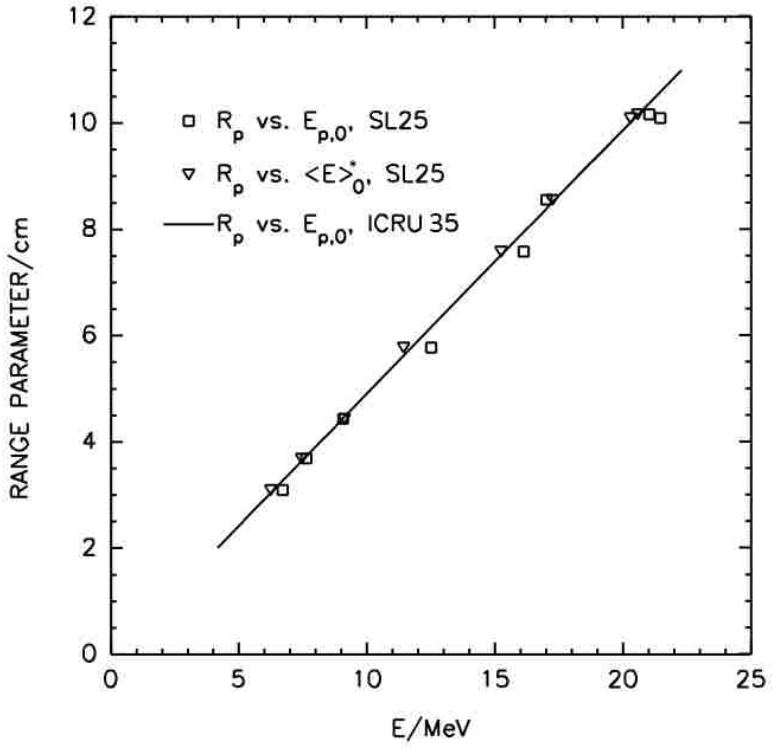

Figure 3.14. Comparison of simulated Rp plotted versus measured incident peak mean energy and incident peak energy. The $\langle E \rangle_o^*$ and $E_{p,o}$ values were drawn directly from the measured energy spectra, while the R_p values were drawn from MC simulated %DD curves generated using that same measured energy spectra. As is visible, plots of R_p versus $\langle E \rangle_o^*$ tend to overlap the plot of ICRU 35 equation 1.1 better than plots of R_p versus $E_{p,o}$, suggesting Deasy's energy parameter, $\langle E \rangle_o^*$, is a better substitution for E_{mono} in equation 1.1 than $E_{p,o}$ (modified from Deasy 1992).

Besides producing better agreement with the inverse of equation 1.1, $\langle E\rangle_o^*$ is also better at minimizing the effects of strangely-shaped spectra on the resulting R_p values. Consider the hypothetical situation where an energy spectrum has two noticeable peaks, like those in Figure 1.15, but with one peak only slightly taller than the other peak. The peak energy would lie underneath the tallest of the two peaks. If the second highest peak rises slightly, then it may become the highest peak, and the peak energy would shift such that it was underneath that peak. Depending on how far displaced the peaks are from one another, this very slight change in the energy spectrum could result in a relatively large shift in the peak energy, hence R_p value assuming equation 1.1 is correct. This is problematic, as the R_p values of energy spectra that are only slightly different should be practically the same. Additionally, even if there is only one noticeable peak in an energy spectrum, the shape of the spectrum can vary greatly, as shown in Figure 1.14 and Figure 1.15. There is no reason to assume that the exact placement of the highest point of the peak structure relative to the bulk of the peak structure is as important as the general distribution of relative fluence within the peak structure. Thus, Deasy's energy parameter, $\langle E\rangle_o^*$, is a more stable parameter than $E_{p,o}$.

Though Deasy's energy parameter was an improvement, the $\pm$15% energy averaging range used to calculate $\langle E\rangle_o^*$ is prone to the same problems as $E_{p,o}$ because it is uses $E_{p,o}$ as the central energy of the range. Therefore, slight modifications to the shape of the energy spectra may result in more significant changes in the placement of the energy averaging range used for calculating $\langle E\rangle_o^*$. To mitigate this problem, a "modified Deasy method" for finding the energy averaging range was used, resulting in the incident modified peak mean energy, $\langle E\rangle_{m,o}^*$, which will be used throughout this study instead of $\langle E\rangle_o^*$. Henceforth, R_p will be related to $\langle E\rangle_{m,o}^*$ instead of $\langle E\rangle_o^*$ by,

$$\langle E\rangle_{m,o}^*(MeV) = 0.22MeV + 1.98\frac{MeV}{cm} * R_p + 0.0025\frac{MeV}{cm^2} * (R_p)^2 \,. \qquad 3.45$$

To find $\langle E\rangle^*_{m,o}$, an algorithm was created to search for the central energy, E_{cent}, of the Deasy $\pm$15% energy averaging range that maximized the area of the energy spectrum that fell within said energy averaging range. In most cases, values for $\langle E\rangle^*_{m,o}$ and $\langle E\rangle^*_o$ were very close.

3.1.4.2.2. Definition of modified peak mean position

The position parameter used for the fit of equation 2.7 was $\langle x\rangle^*_m$, an analog to $\langle E\rangle^*_{m,o}$. $\langle x\rangle^*_m$ exists in the spatial domain and came from a measured net dose profile, $\overline{D}_{meas}(x)$, instead of existing in the energy domain and coming from an energy spectrum. $\langle x\rangle^*_m$ is the average CR strip position within a region of $\overline{D}_{meas}(x)$ known as the position averaging range. Because $\overline{D}_{meas}(x)$ exists only in the context of this study, the position averaging range was defined relative the energy averaging range of $\overline{D}_{meas}(x)$ transformed to the energy domain, i.e. $\phi^P_{meas}(E)$, which is a close first estimate of $\phi^P_{spect}(E)$. This is problematic, as transformations to the energy domain require values for the coefficients B_z and x_o, which are themselves determined by the fit of equation 2.7 to seven $\langle x\rangle^*_m$ and $\langle E\rangle^*_{m,o}$ values drawn from the calibration data. Hence, $\langle x\rangle^*_m$ was solved for using the following numerical process:

Step 1: A first estimate of $\langle x\rangle^*_m$, i.e. $\langle x\rangle^*_{m,est,1}$, was calculated by

$$\langle x\rangle^*_{m,est,1} = \frac{\int_{x_{min,est,1}}^{x_{max,est,1}} x * \overline{D}_{meas}(x)\,dx}{\int_{x_{max,est,1}}^{x_{max,est,1}} \overline{D}_{meas}(x)\,dx}, \tag{3.46}$$

where

$$x_{min,est,1} = 0.9x_{cent,est,1}\,, \tag{3.47}$$

and

$$x_{max,est,1} = 1.1x_{cent,est,1}\ . \qquad 3.48$$

where $x_{cent,est,1}$ was the center of a $\pm$10% averaging range found using the modified Deasy method on $\overline{D}_{meas}(x)$. The only difference between using the modified Deasy method in the spatial domain versus using it in the energy domain is that the x-axis has different units. Trial runs demonstrated that $\pm$10% produced a more accurate first estimate of the position averaging range than $\pm$15%.

Step 2: First estimates of coefficients B_z and x_o, i.e. $B_{z,est,1}$ and $x_{o,est,1}$, were determined by fitting equation 2.7 to the seven $\langle x\rangle^*_{m,est,1}$ and $\langle E\rangle^*_{m,o}$ values, where $\langle E\rangle^*_{m,o}$ values were determined using equation 3.45 and the R_p values drawn from the measured calibration %DD curves.

Step 3: Using $B_{z,est,1}$ and $x_{o,est,1}$ in equation 2.7, $\overline{D}_{meas}(x)$ was transformed to the energy domain, i.e.

$$\phi^P_{meas,1}\big(E(x)\big) = \frac{1/_{cm^2}}{1.0\ cGy}\overline{D}_{meas}(x)\left|\frac{dE}{dx}\right|^{-1}\ . \qquad 3.49$$

Step 4: The upper and lower limits of the energy averaging range for $\phi^P_{meas,1}(E)$, i.e. $E_{max,est,1}$ and $E_{min,est,1}$ respectively, were determined, where

$$E_{max,est,1} = 1.15E_{cent,est,1}\ , \qquad 3.50$$

and

$$E_{min,est,1} = 0.85E_{cent,est,1}\ , \tag{3.51}$$

where $E_{cent,est,1}$ was the center energy of the standard $\pm$15% energy averaging range in the energy domain determined by applying the modified Deasy method to $\phi^{P}_{meas,1}(E)$. Though $\phi^{P}_{meas,1}(E)$ is not a proper energy spectrum as the finite size of the spectrometer aperture and the variation in the angle of incidence from normal incidence were not accounted for when determining it, it was close enough for calibration purposes.

Step 5: An iterative process, i.e. $i = i + 1$, continues whereby $x_{max,est,i}$ and $x_{min,est,i}$ are determined by converting $E_{max,est,i-1}$ and $E_{min,est,i-1}$ to the spatial domain using the inverse of equation 2.7 and $B_{z,est,i-1}$ and $x_{o,est,i-1}$, then

$$\langle x\rangle^{*}_{m,est,i} = \frac{\int_{x_{min,est,i}}^{x_{max,est,i}} x * \overline{D}_{meas}(x)\,dx}{\int_{x_{min,est,i}}^{x_{max,est,i}} \overline{D}_{meas}(x)\,dx}, \tag{3.52}$$

then steps (2-4) are repeated, i.e. a fit of equation 2.7 to the seven resulting $\langle x\rangle^{*}_{m,est,i}$ and $\langle E\rangle^{*}_{m,o}$ values determines $B_{z,est,i}$ and $x_{o,est,i}$. Next,

$$\phi^{P}_{meas,i}\big(E(x)\big) = \frac{1/_{cm^2}}{1.0\ cGy}\,\overline{D}_{meas}(x)\left|\frac{dE}{dx}\right|^{-1}, \tag{3.53}$$

then,

$$E_{max,est,i} = 1.15E_{cent,est,i}\ , \tag{3.54}$$

and

$$E_{min,est,i} = 0.85E_{cent,est,i}\,. \qquad 3.55$$

This process was executed from iteration i=2 until iteration i=N, where N was chosen such that $\left|\langle x\rangle^{*}_{m,est,i} - \langle x\rangle^{*}_{m,est,i-1}\right| < 0.01$ for iterations i =N-2 through i =N. This usually occurred at N=5, at which point all estimates were assumed equal to the true values for their respective parameters. An example $\overline{D}_{meas}(x)$ and the (a) first and (c) second estimate of its position averaging range, as well as the (b) first and (d) second estimate of $\phi^{P}_{meas}(E)$ and its energy averaging range, are illustrated in Figure 3.15.

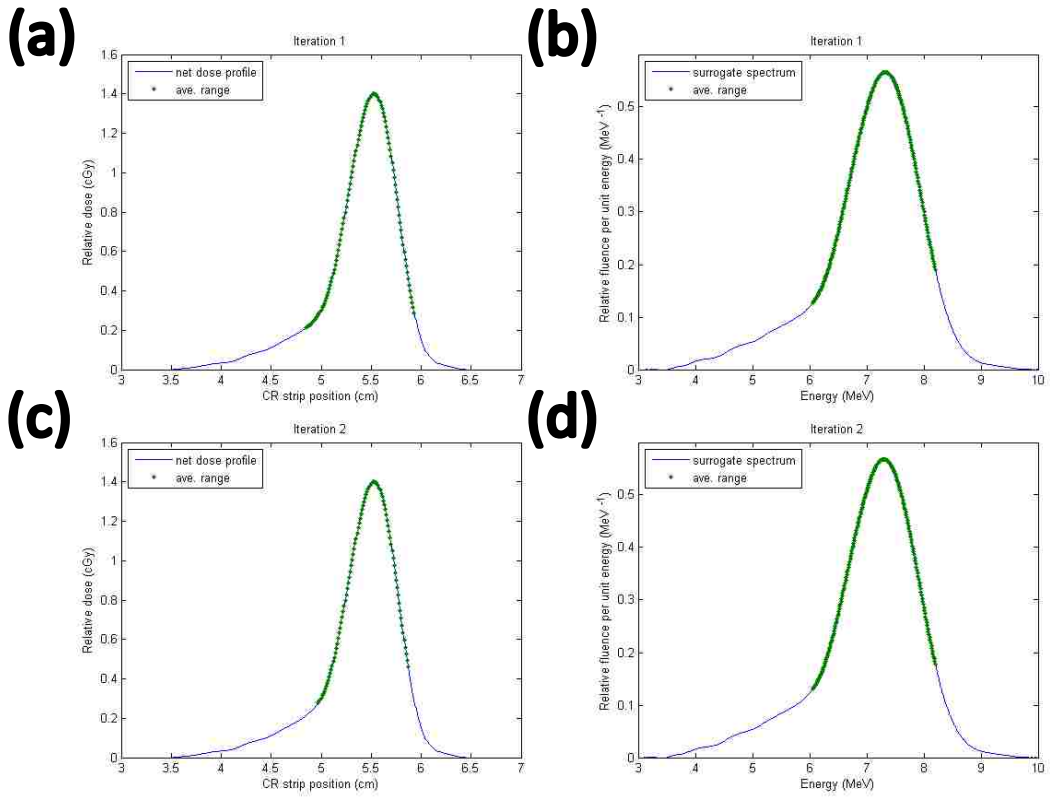

Figure 3.15. Position averaging range and energy averaging range estimates. Plotted are (a) an example $\overline{D}_{meas}(x)$ and the initial $\pm$10% estimate of its position averaging range, (b) $\phi^{P}_{meas,1}(E)$ and the first estimate of the energy averaging range, (c) $\overline{D}_{meas}(x)$ and the second estimate of its position averaging range, and (d) $\phi^{P}_{meas,1}(E)$ and the second estimate of the energy averaging range for the 7 MeV beam of MBPCC's Baton Rouge Elekta Infinity accelerator.

3.1.4.3. Recalibration

To determine B_z and x_o, equation 2.7 was fit to seven $\langle x\rangle_m^*$, $\langle E\rangle_{m,o}^*$ pairs measured on the Baton Rouge Elekta Infinity accelerator. The $\langle x\rangle_m^*$ values were obtained from measured CR strip net dose profiles, i.e. $\overline{D}_{meas}(x)$. The $\langle E\rangle_{m,o}^*$ values, henceforth $\langle E\rangle_{m,o}^{*,\%DD}$, were obtained by inserting R_p values drawn from measured %DD curves into equation 3.45. Implicit in this correlation is the assumption that for any one of the seven $\langle x\rangle_m^*$, $\langle E\rangle_{m,o}^{*,\%DD}$ pairs, the $\overline{D}_{meas}(x)$ and %DD curve from which these parameters were drawn were created by the same beam with the same energy spectrum. This assumption is incorrect, as the beam that created the %DD curve only passed through a 14 x 14 cm^2 open applicator, hence its energy spectrum was equivalent to $\phi_{95-cm\,SCD}^P(E)$, while the beam that created $\overline{D}_{meas}(x)$ passed through the two-aperture collimation system, hence its energy spectrum was equivalent to $\phi_{spect}^P(E)$. The transformation of $\phi_{spect}^P(E)$ into $\phi_{95-cm\,SCD}^P(E)$ in section 3.1.3, the results of which are plotted in Figure 3.21, creates a noticeable shift in the modified peak mean energies (≈0.13-0.28 MeV).

To account for these shifts, the seven $\phi_{spect}^P(E)$ and $\phi_{95-cm\,SCD}^P(E)$ distribution of the Baton Rouge Elekta Infinity accelerator were calculated using the initial B_z and x_o values that resulted from the initial fit of equation 2.7 to the seven $\langle x\rangle_m^*$, $\langle E\rangle_{m,o}^{*,\%DD}$ pairs, i.e. $x_{o,init}$ and $B_{z,init}$. The modified peak mean energies of $\phi_{spect}^P(E)$ and $\phi_{95-cm\,SCD}^P(E)$, i.e. $\langle E\rangle_{m,spect}^{*,mag}$ and $\langle E\rangle_{m,o}^{*,mag}$, were calculated using the modified Deasy method. The *mag* symbol in the superscripts of $\langle E\rangle_{m,spect}^{*,mag}$ and $\langle E\rangle_{m,o}^{*,mag}$ indicate that these parameters came from energy spectra measured with the magnetic spectrometer rather than from %DD curve measurements. The differences between $\langle E\rangle_{m,spect}^{*,mag}$ and $\langle E\rangle_{m,o}^{*,mag}$ were used to shift the $\langle E\rangle_{m,o}^{*,\%DD}$ values, resulting in

$$\langle E\rangle_{m,spect}^{*,\%DD} = \langle E\rangle_{m,o}^{*,\%DD} + \left[\langle E\rangle_{m,spect}^{*,mag} - \langle E\rangle_{m,o}^{*,mag}\right], \qquad 3.56$$

where $\langle E \rangle_{m,spect}^{*,\%DD}$ is the modified peak mean energy of the beam at the spectrometer aperture obtained from %DD curve measurements.

$\langle E \rangle_{m,spect}^{*,\%DD}$ was then used as the energy parameter in the second fit of equation 2.7, i.e. the recalibration, to determine the second set of x_o and B_z values, i.e. $x_{o,recal}$ and $B_{z,recal}$. Hence, it was assumed the differences between $\langle E \rangle_{m,spect}^{*,mag}$ and $\langle E \rangle_{m,o}^{*,mag}$ values calculated using $x_{o,init}$ and $B_{z,init}$ were equal to the differences between $\langle E \rangle_{m,spect}^{*,mag}$ and $\langle E \rangle_{m,o}^{*,mag}$ values calculated with $x_{o,recal}$ and $B_{z,recal}$. $x_{o,recal}$ and $B_{z,recal}$ were used throughout this study's analysis instead of $x_{o,init}$ and $B_{z,init}$. The energy spectra generated with $x_{o,recal}$ and $B_{z,recal}$ should be similar to the energy spectra generated with $x_{o,init}$ and $B_{z,init}$, except shifted to slightly higher energies.

3.2. Results and discussion

3.2.1. Subtracting X-ray background from gross dose profiles

Shown in Figure 3.16 are the gross, background, and net dose profiles measured on the Elekta Infinity at MBPCC's Baton Rouge facility. The gross dose profiles plotted in Figure 3.16 were obtained by transforming the intensity profiles in Figure 2.18 into gross dose profiles using the signal intensity to dose calibration curve plotted in Figure 3.2. These gross dose profiles are similar to those for all other MBPCC Elekta Infinity accelerators. Note that the size of the low-energy tail portion of the net dose profile relative to the rest of the net dose profile was somewhat dependent on how the fit regions were chosen and whether a 4th or 3rd degree polynomial was fit for background subtraction.

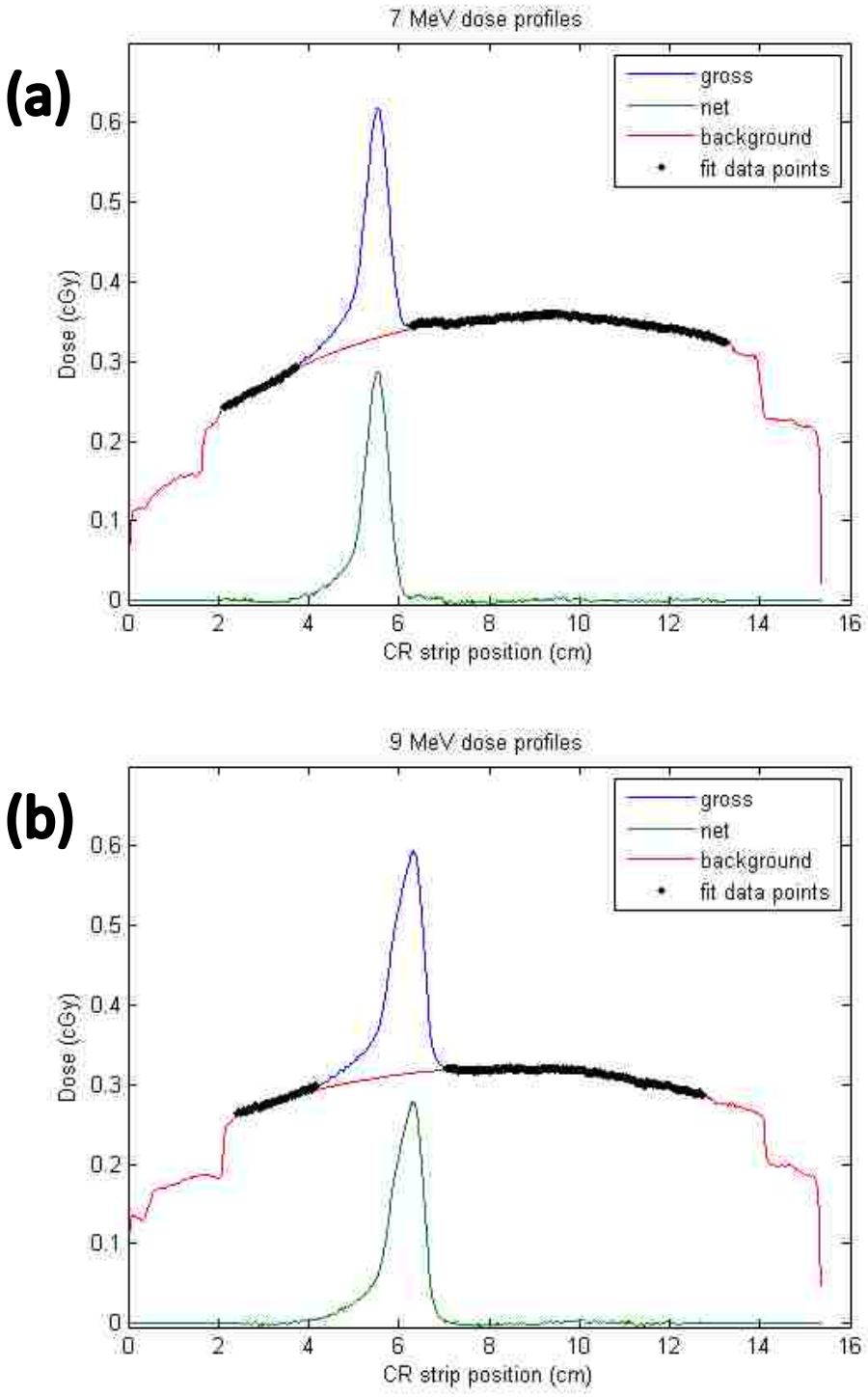

Figure 3.16. Background subtractions results for the Baton Rouge Elekta Infinity accelerator. Plotted are the (blue) gross dose profile (dose versus CR strip position), (red) background dose profile, and (green) net dose profile produced by subtracting the background dose profile from the gross dose profile measured for the (a) 7 MeV, (b) 9 MeV, (c) 10 MeV, (d) 11 MeV, (e) 13 MeV, (f) 16 MeV, and (g) 20 MeV beams on the Baton Rouge Elekta Infinity accelerator.

(Figure 3.16 continued)

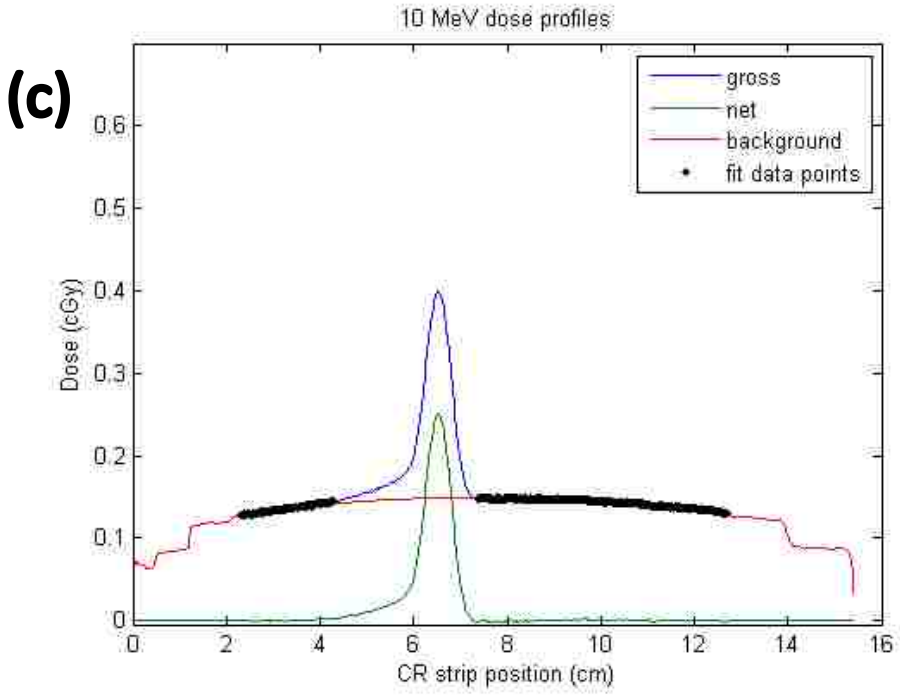

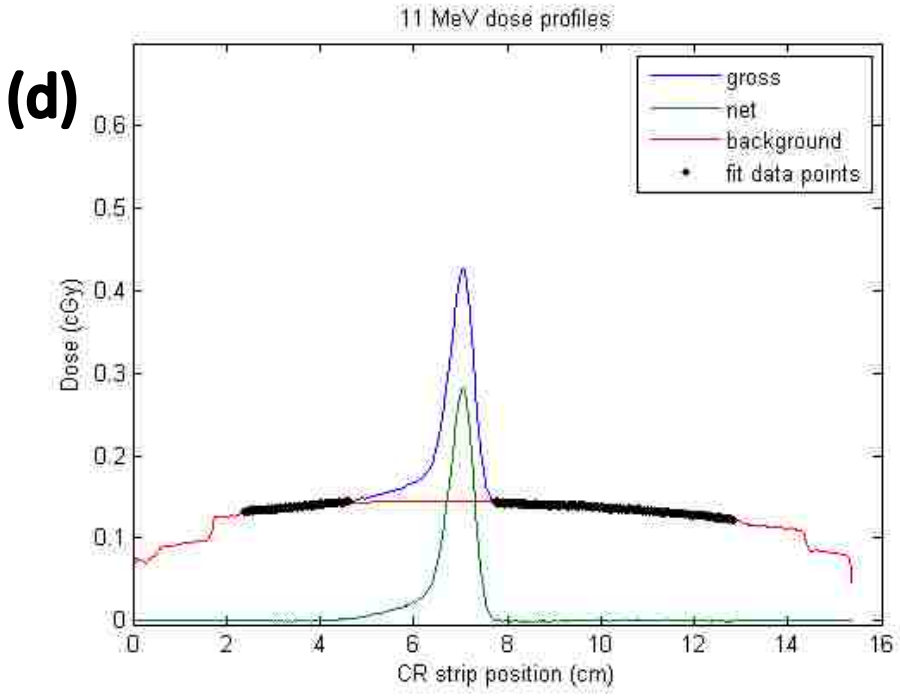

(Figure 3.16 continued)

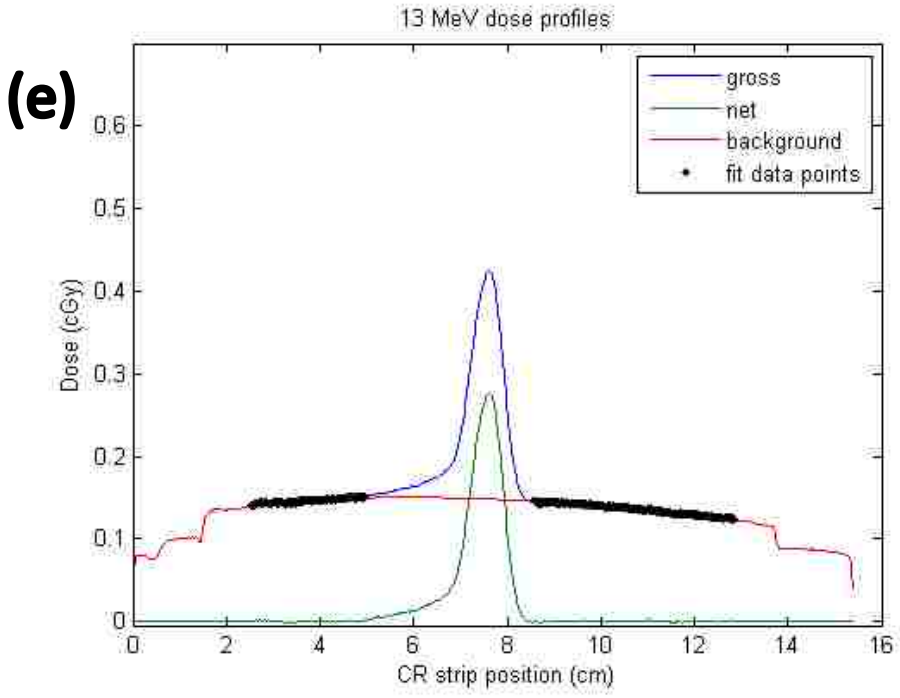

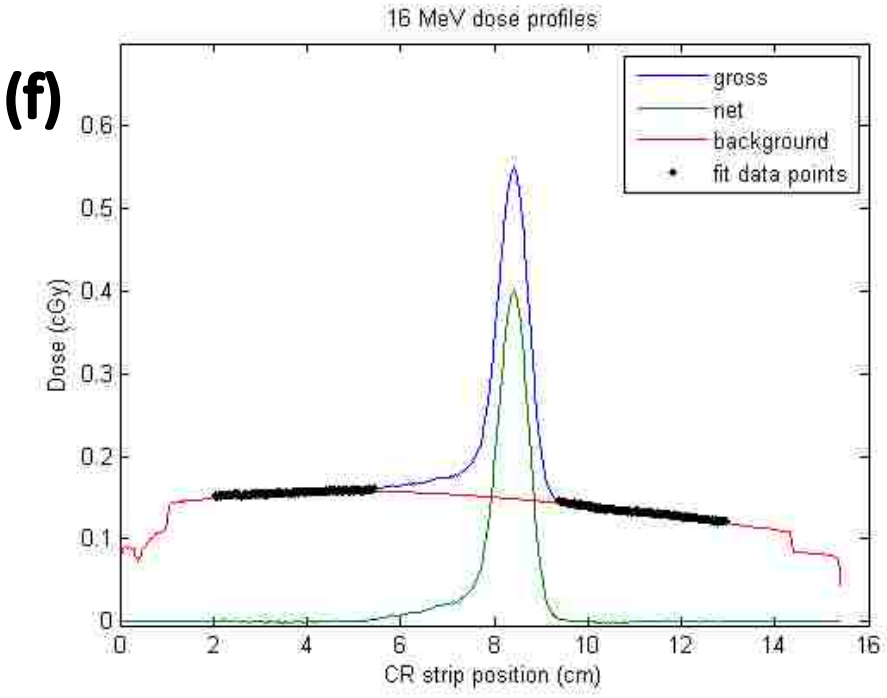

(Figure 3.16 continued)

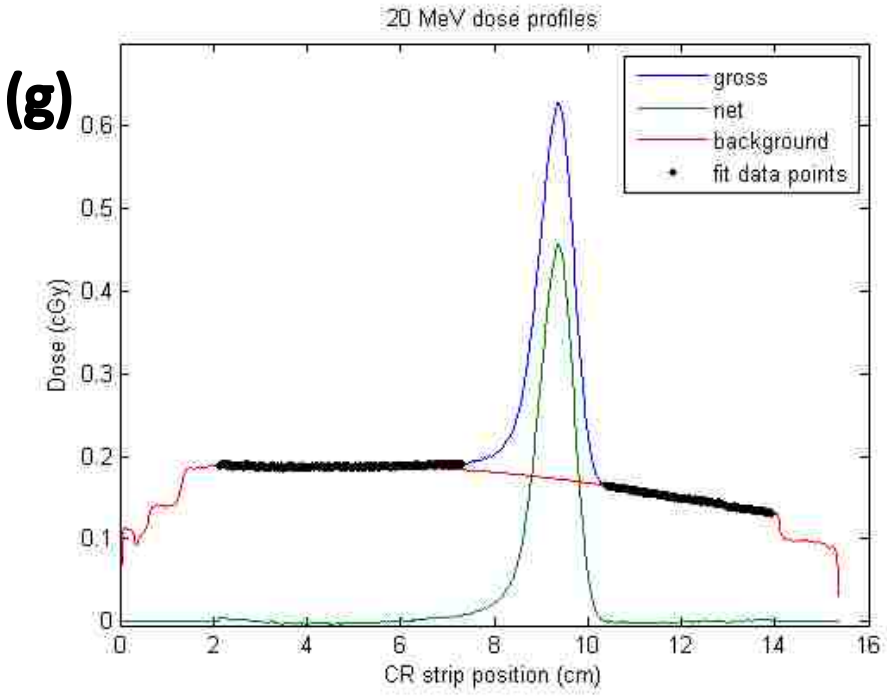

3.2.2. Smoothing net dose profiles

Plotted in Figure 3.17 are the unsmoothed and smoothed net dose profiles. Prior to smoothing, the unsmoothed net dose profiles were renormalized to have an area of unity, hence their y-axes have units of relative dose. Note the regions significantly to the left and right of the peak region are completely flat, as they were zeroed. These smoothed net dose profiles were considered acceptable for use in further analysis, hence objective (1) of Aim 2 was met.

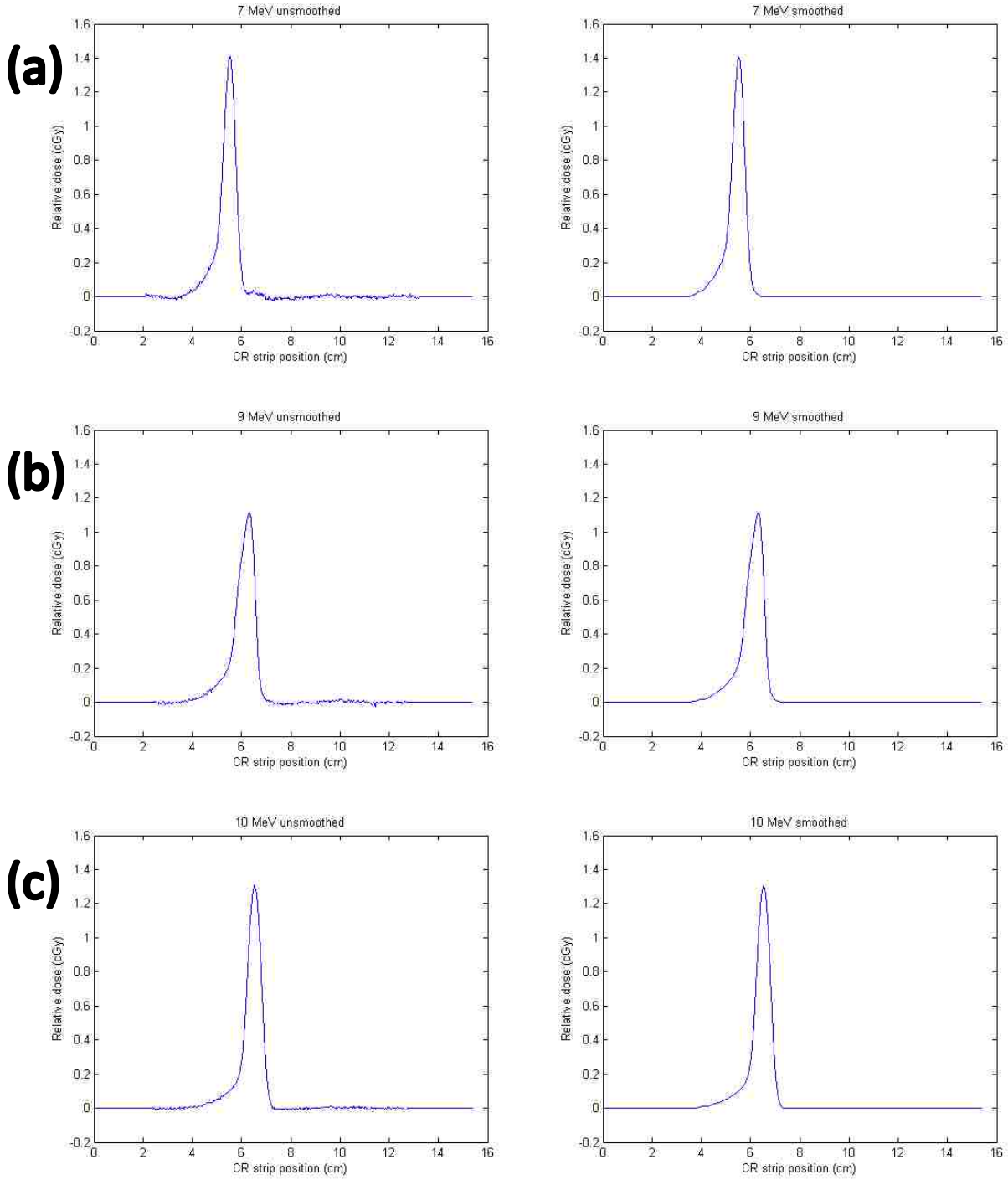

Figure 3.17. Unsmoothed and smoothed net dose profiles for the Baton Rouge Elekta Infinity accelerator. Plotted are the (left) unsmoothed and (right) smoothed net dose profiles (relative dose versus CR strip position) for the (a) 7 MeV, (b) 9 MeV, (c) 10 MeV, (d) 11 MeV, (e) 13 MeV, (f) 16 MeV, and (g) 20 MeV electron beams on MBPCC's Baton Rouge Elekta Infinity accelerator.

(Figure 3.17 continued)

(d)

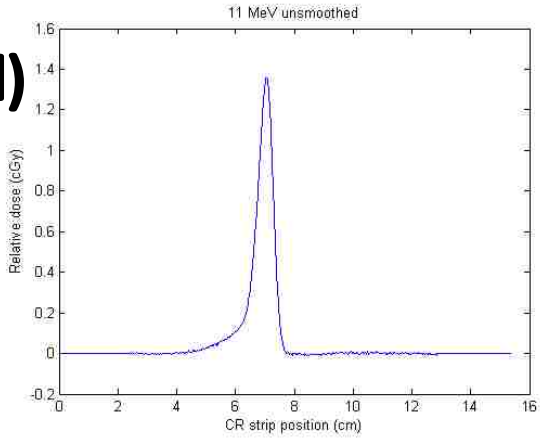

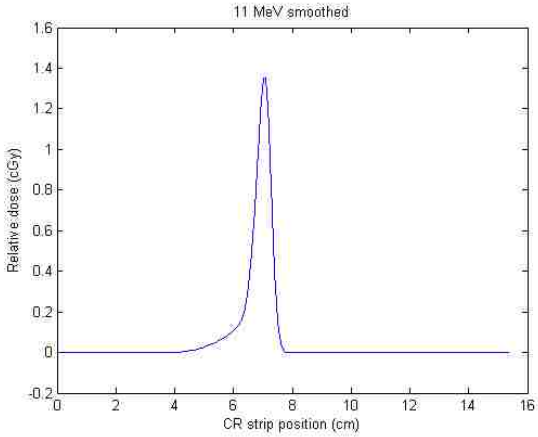

(e)

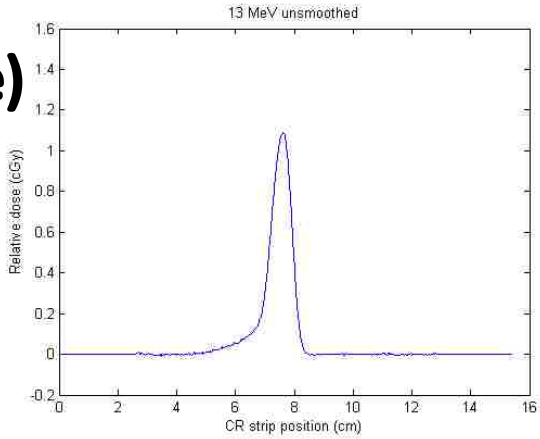

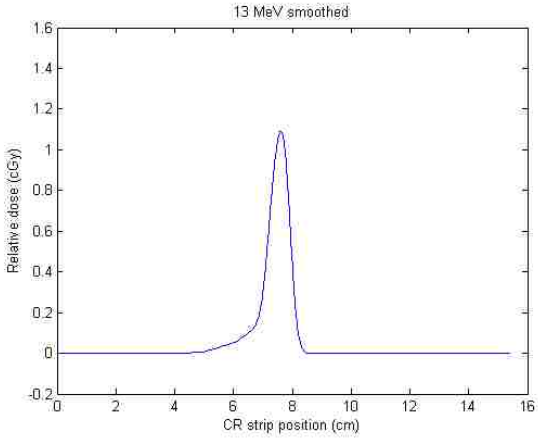

(f)

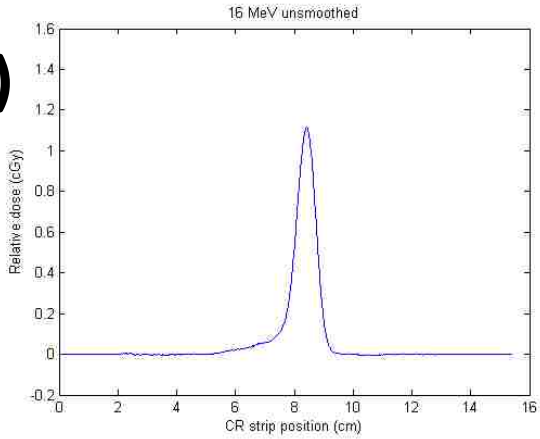

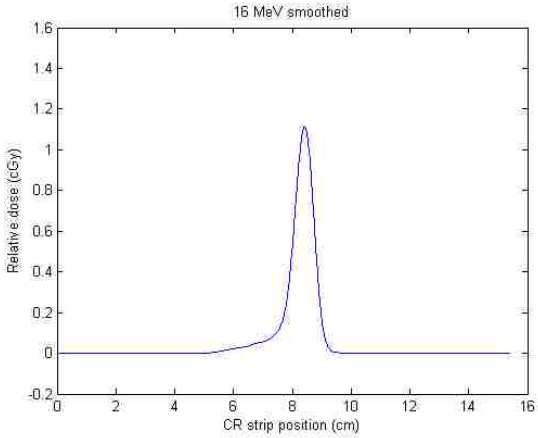

(Figure 3.17 continued)

(g)

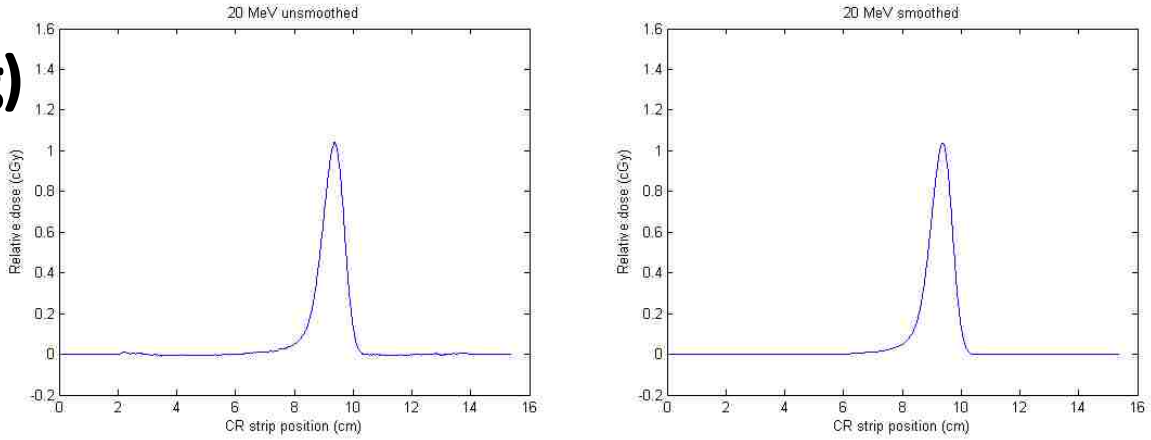

3.2.3. Transforming net dose profiles into energy spectra at spectrometer aperture

To validate the transformation of net dose profiles into energy spectra at the spectrometer aperture described in section 3.1.2, a Gaussian distribution centered on 15 MeV with a σ of 0.9 MeV and an area of unity was assumed for $\phi^{p}_{spect}(E)$. Using the theory described in section 3.1.2.1, a net dose profile at the CR strip was calculated with this energy spectrum. The energy spectrum and the resulting net dose profile are plotted in Figure 3.18 (a) and (b), respectively. Then, this calculated net dose profile was assumed the measured net dose profile, $\overline{D}_{meas}(x)$, for the purposes of calculating $\phi^{p}_{spect}(E)$ with the inversion algorithm described in section 3.1.2.3. Obtaining a $\phi^{p}_{spect}(E)$ from the output inversion algorithm that closely matched the original $\phi^{p}_{spect}(E)$ used to calculate the net dose profile in Figure 3.18 (b) would validate the inversion algorithm.

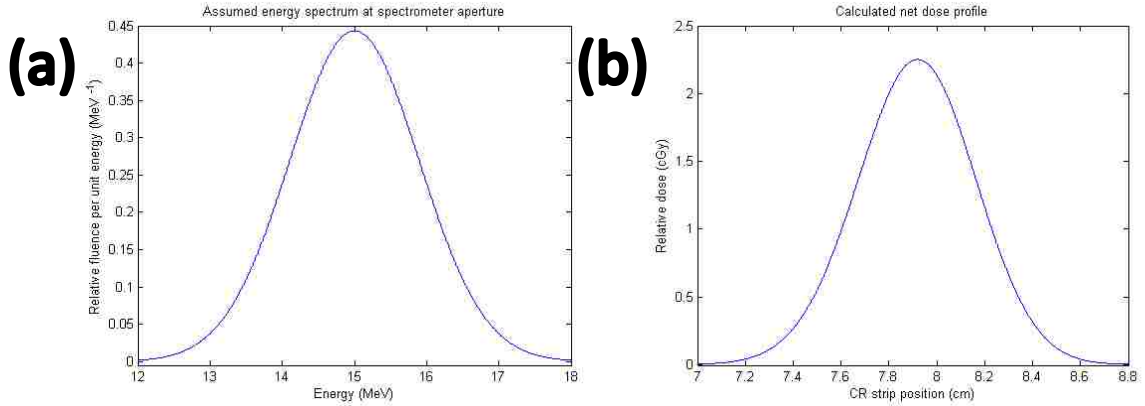

Figure 3.18. Assumed Gaussian energy spectrum and the resulting net dose profile. Plotted are (a) a Gaussian energy spectrum (relative fluence per unit energy versus energy) centered on 15 MeV with a σ of 0.9 MeV and (b) its resulting calculated net dose profile (relative dose versus CR strip position). Though the area under the energy spectrum is unity, the area under the net dose profile is greater than unity, as the replacement operation does not conserve area under the curve.

The first five estimates of $\phi^{p}_{spect}(E)$ from the inversion algorithm, along with the 15th and final estimate, are plotted in Figure 3.19. Additionally, the $\Delta\phi_{Gauss,i}(E)$ used in the first five iterations, along with the 15th iteration of $\Delta\phi_{Gauss,i}(E)$, are plotted in Figure 3.20 (a) and (b). The largest improvements happened in the first five estimates (iterations), after which improvement is marginal, as the 5th and 15th estimates are almost indistinguishable. This can also be observed from the reduction in the size of the $\Delta\phi_{Gauss,i}(E)$ plotted in Figure 3.20 (a), (b), and (c). Notice $\phi^{P}_{spect,est,i}(E)$ become narrower and taller as the iteration number, i, increased. This was expected, as including the physical effects of the finite aperture size in the determination of $\overline{D}_{calc,i}(x)$ broadens the results, hence the inversion algorithm must compensate by sharpening $\phi^{P}_{spect,est,i}(E)$. Though the match between the original and the higher iteration $\phi^{P}_{spect,est,i}(E)$ was not perfect, this error was deemed small enough to ignore in this study. Hence, the results of this algorithm were considered acceptable, meaning objective (2) of Aim 2 was met.

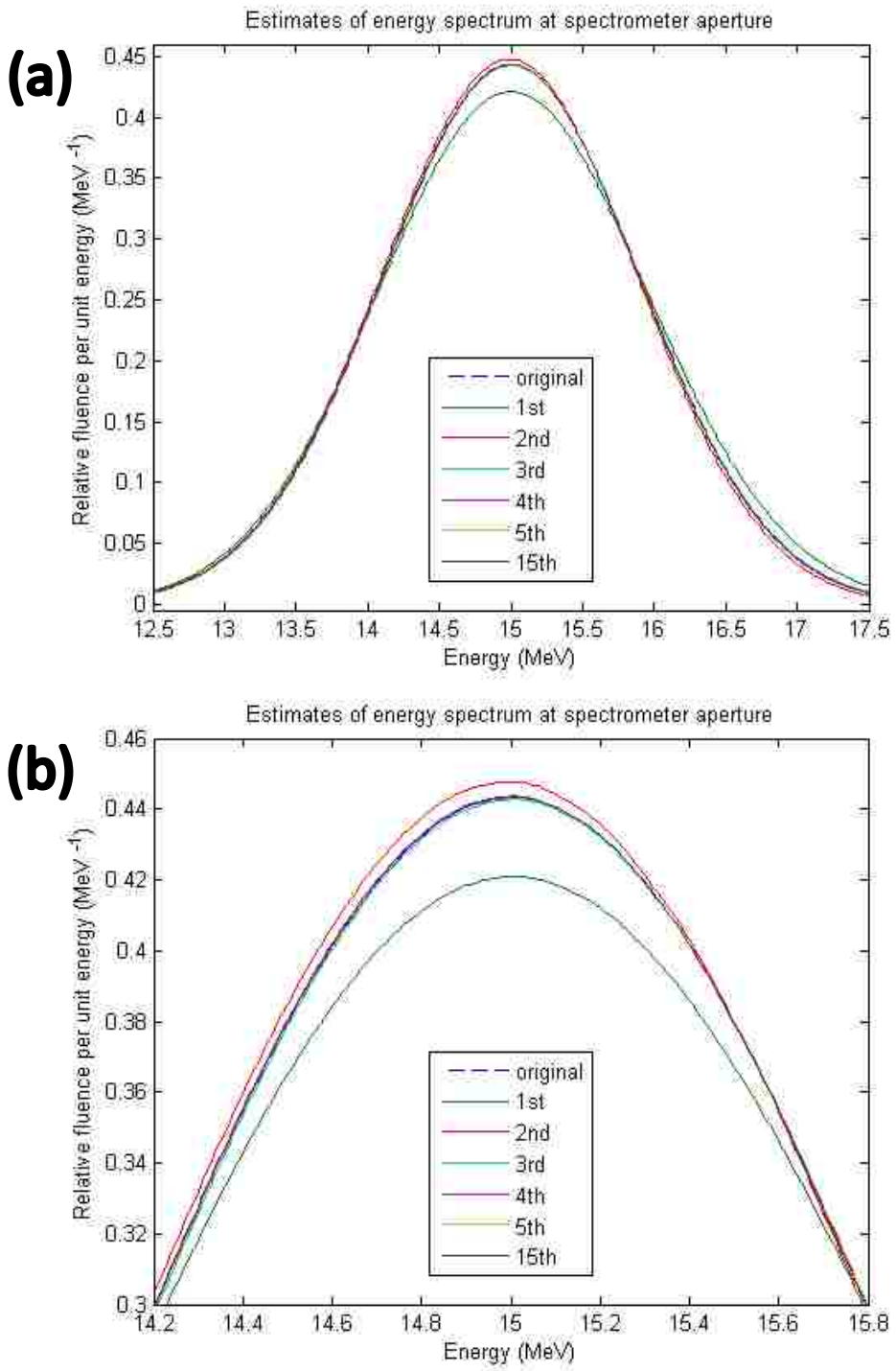

Figure 3.19. Estimates of the energy spectrum at the spectrometer aperture from the inversion algorithm. Plotted are (a) zoomed-out and (b) (c) zoomed-in views of the (green) 1st, (red) 2nd, (light blue) 3rd, (magenta) 4th, (yellow) 5th, and (black) 15th estimate of the energy spectrum at the spectrometer aperture, along with the (dashed blue) original energy spectrum used to calculate the net dose profile. All estimates of the energy spectra were normalized to have an area of unity prior to being plotted.

(Figure 3.19 continued)

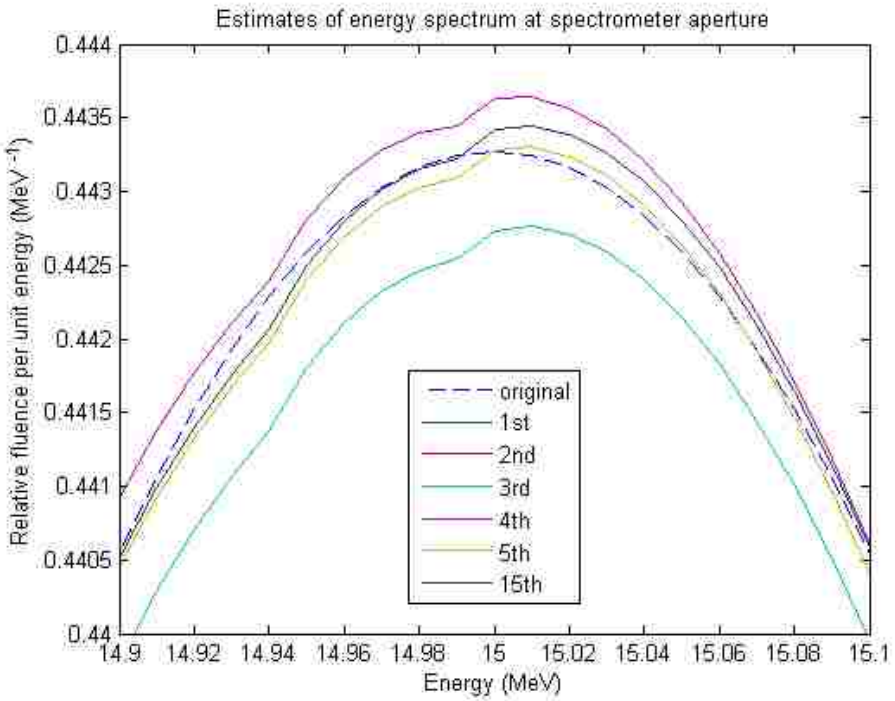

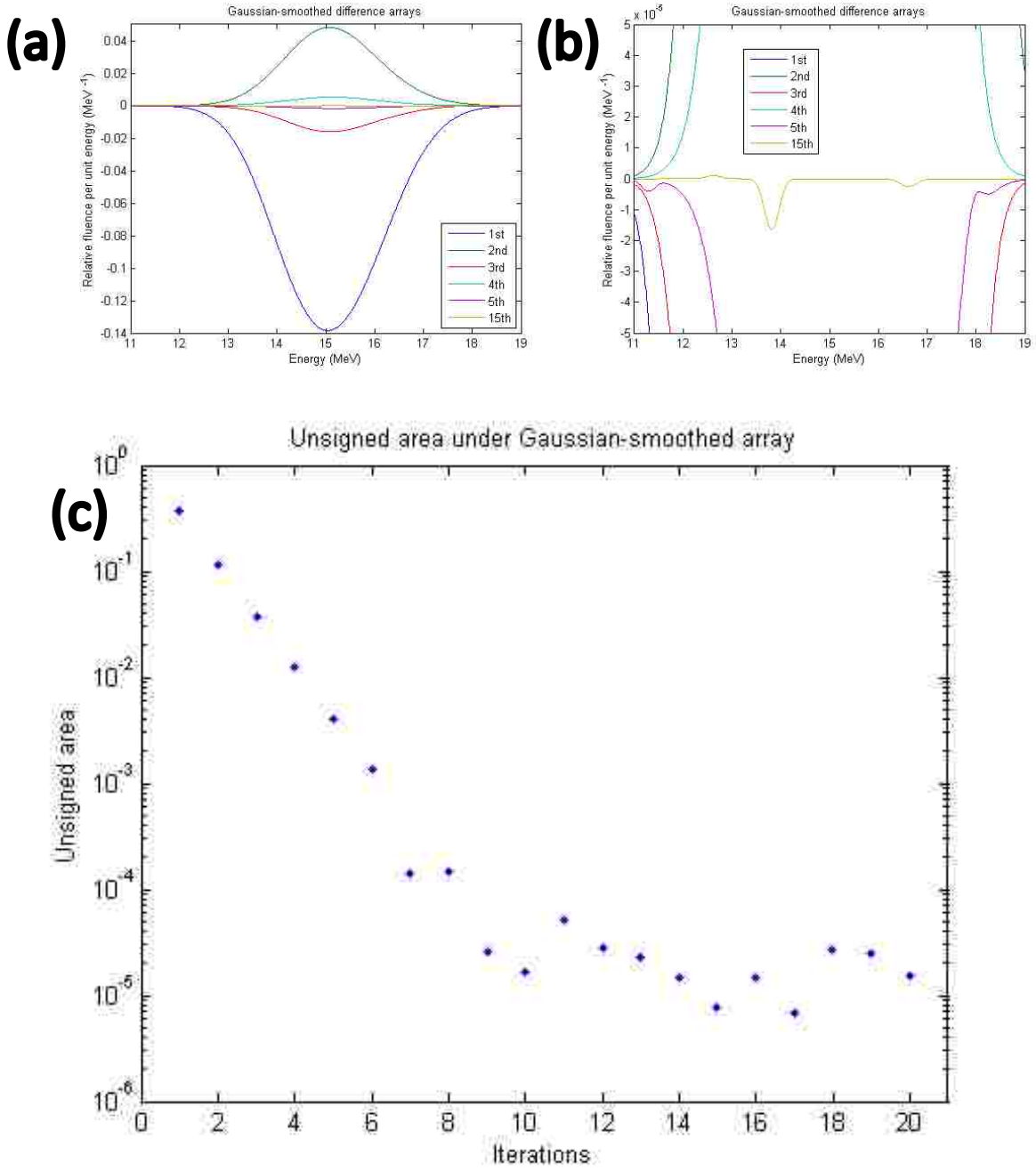

Figure 3.20. Decrease in modification array size during the progression of the inversion algorithm. Plotted are (a) zoomed-out and (b) zoomed-in views of the (blue) 1st, (green) 2nd, (red) 3rd, (light blue) 4th, (magenta) 5th, and (yellow) 15th iterations of $\Delta\phi_{Gauss,i}(E)$. Also plotted is (c) the area under $\Delta\phi_{Gauss,i}(E)$ after taking the absolute value of all of its magnitudes (unsigned area). The decrease in the unsigned area is marginal after about 15 iterations.

3.2.4. Transforming energy spectra at spectrometer aperture into energy spectra at 95-cm SCD

The energy spectra resulting from the inversion algorithm in section 3.1.2.3 were transformed from the spectrometer aperture to the Cerrobend® aperture, meeting objective (3) of Aim 2. The results of this transformation for selected beams are plotted in Figure 3.21. Notice how the transformation increases the magnitudes of the low-energy tail portions of the energy spectra at the expense of the magnitudes of the high-energy peak portions.

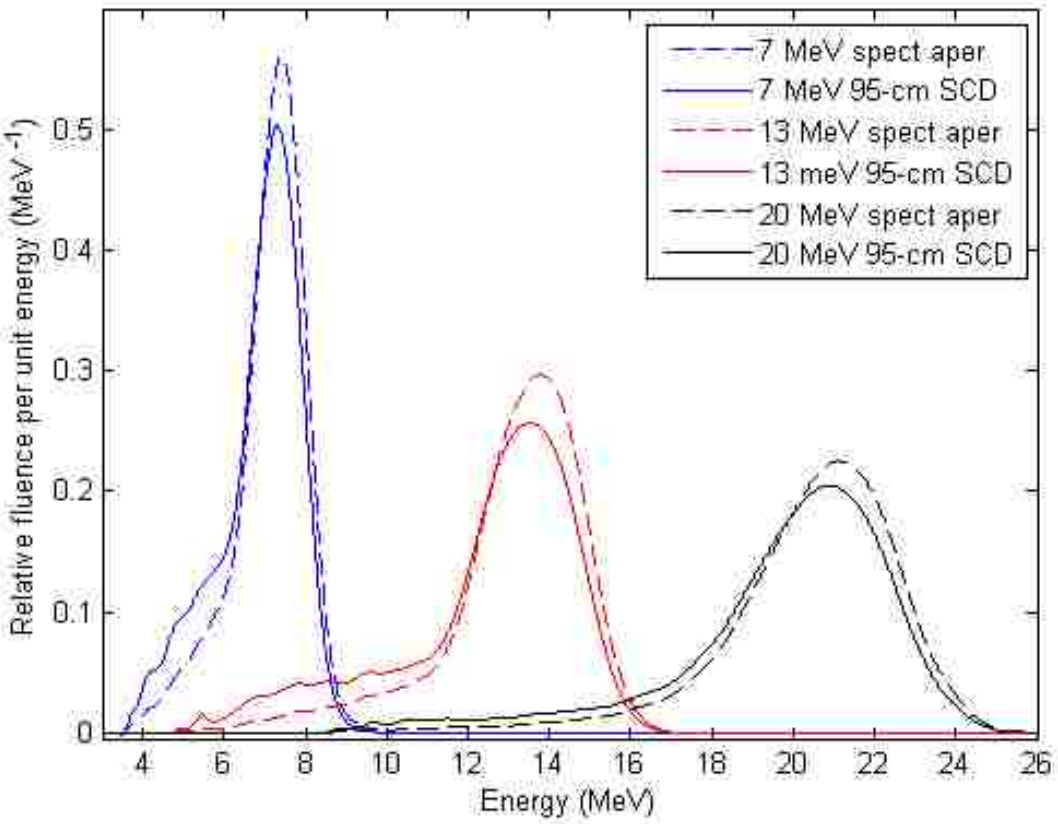

Figure 3.21. Transformation of energy spectra from the spectrometer aperture to 95-cm SCD. Plotted are the measured energy spectra at (solid line) the spectrometer aperture and (dashed line) 95-cm SCD (i.e. Cerrobend® aperture) for the (blue) 7 MeV, (red) 13 MeV, and (black) 20 MeV beams on MBPCC's Baton Rouge Elekta Infinity on Jan/14/2013.

3.2.5. CR position to electron energy calibration

Plotted in Figure 3.22 are the original and recalibrated CR strip position to energy calibration curves. These curves were determined by the fit of equation 2.7 to the calibration data measured for MBPCC's Baton Rouge Elekta Infinity accelerator on Jan/14/2013. Note that the recalibrated calibration curve transforms the same positions on the CR strip into greater energies when compared to the original calibration curve, as was expected. From the original calibration, (blue) $x_{o,init}$ equals 1.10 $\pm$ 0.18 ($\pm 1\sigma$) cm, and $B_{z,init}$ equals 0.540 $\pm$ 0.025 ($\pm 1\sigma$) Tesla. From the recalibration, (red) $x_{o,recal}$ equals 1.07 $\pm$ 0.20 ($\pm 1\sigma$) cm, and $B_{z,recal}$ equals 0.542 $\pm$ 0.027 ($\pm 1\sigma$). Using the recalibrated $x_{o,recal}$ and $B_{z,recal}$ values in equation 2.7 instead of the original values causes a slight shift (0.1 – 0.3 MeV) in the energy spectra to higher energies, as illustrated in Figure 3.23.

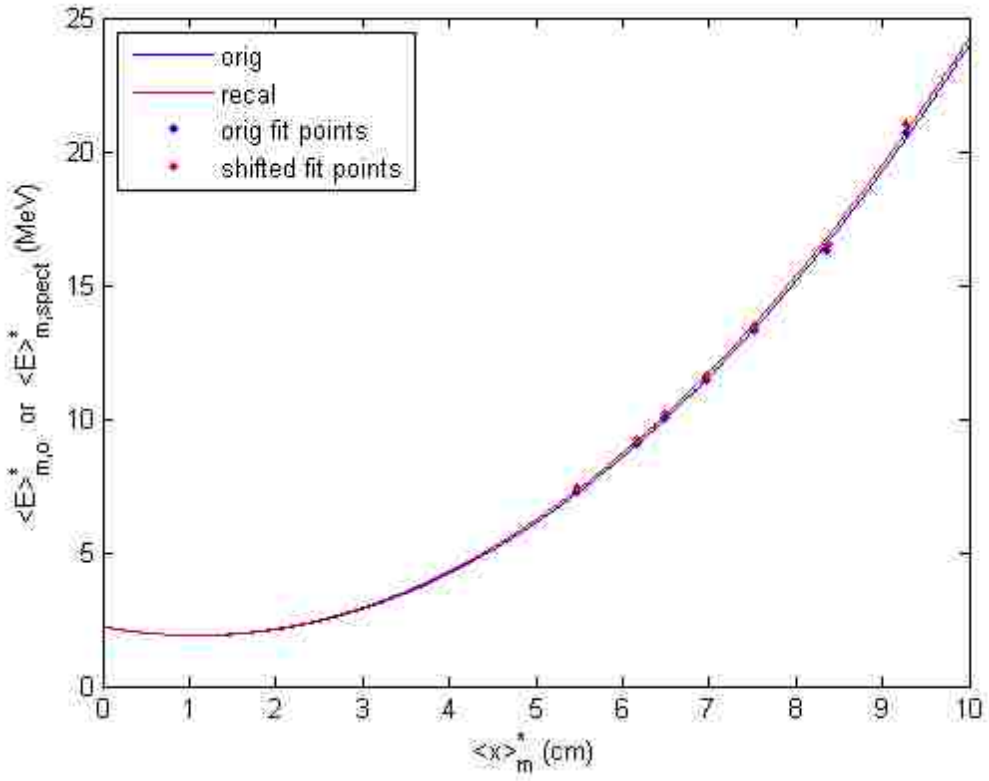

Figure 3.22. Original and recalibrated position to energy calibration curves. Plotted are the (blue) original calibration curve generated by fitting equation 2.7 to the (blue dots) original $\langle E \rangle^*_{m,o}$ versus $\langle x \rangle^*_m$ data points and the (red) recalibrated calibration curve generated by fitting equation 2.7 to the (red dots) $\langle E \rangle^*_{m,spect}$ versus $\langle x \rangle^*_m$ data points.

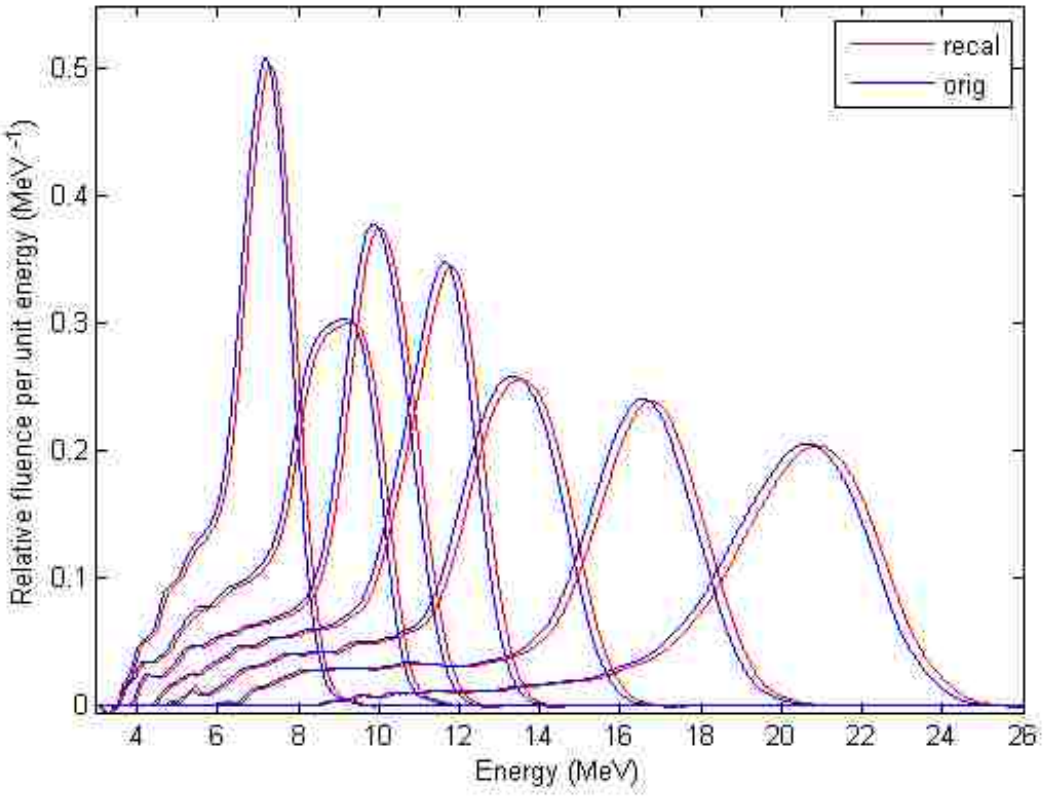

Figure 3.23. Shift in energy spectra due to recalibration. Plotted are the energy spectra (relative fluence per unit energy versus energy) for the (blue) original calibration and (red) final calibration from the Baton Rouge Elekta Infinity accelerator generated using the original and recalibrated x_o and B_z values, respectively.

3.2.6. Validation of use of modified peak mean energy

As explained in section 3.1.4.2.1, instead of using Deasy's $\langle E \rangle_o^*$ energy parameter, a modified energy parameter, $\langle E \rangle_{m,o}^*$, was used in this study. A plot of $\langle E \rangle_{m,o}^*$ values drawn from energy spectra measured on the MBPCC's Baton Rouge Elekta Infinity accelerator plotted versus the R_p values drawn from same-day measured %DD curves is pictured in Figure 3.24. As the plot of $\langle E \rangle_{m,o}^*$ versus R_p has a lower sum of squared residuals, i.e. 0.1431, compared to that of the plot of $E_{p,o}$ versus R_p, i.e. 0.4843, and the plot of $E_{p,o}$ versus R_p is noticeable more erratic, the use of $\langle E \rangle_{m,o}^*$ instead of $E_{p,o}$ in equation 1.1 was assumed more appropriate for this study.

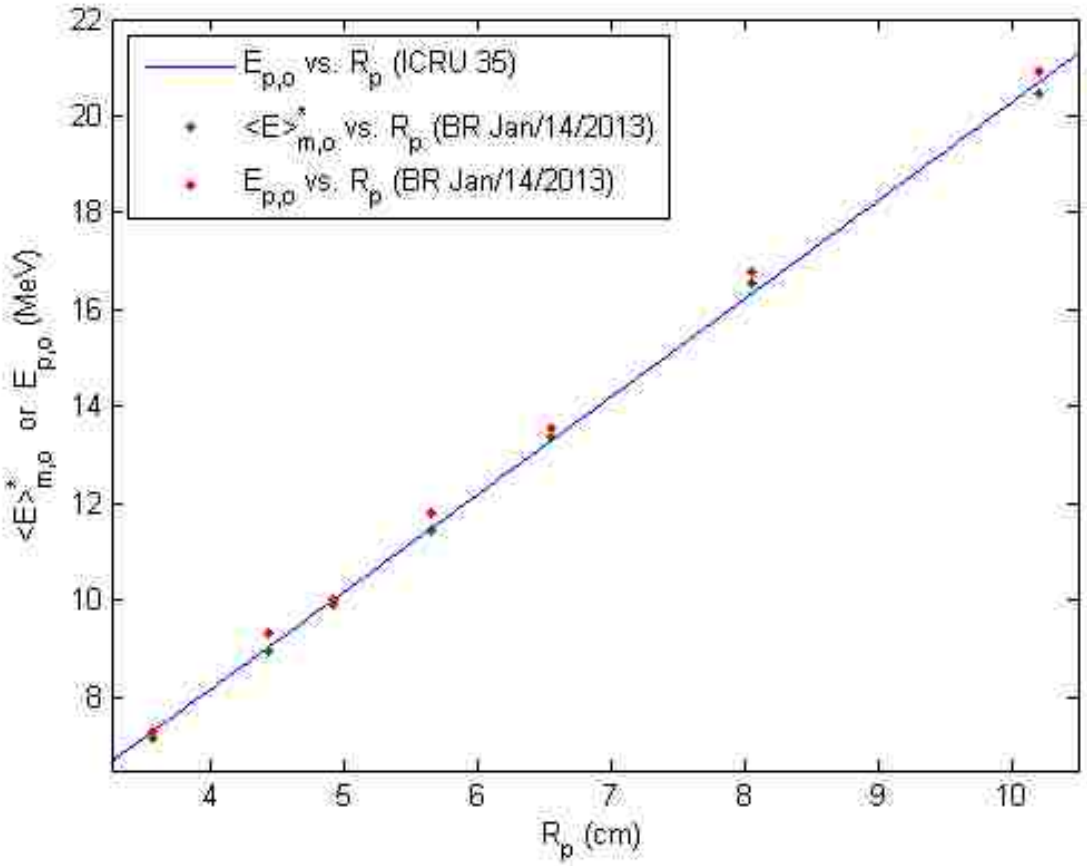

Figure 3.24. Validation of use of modified peak mean energy instead of peak energy. Plotted are the (solid line) $E_{p,o}$ versus R_p data points from ICRU 35 equation 1.1, (green dots) $\langle E \rangle^*_{m,o}$ versus R_p measured data points, and (red dots) $E_{p,o}$ versus R_p measured data points. The measured $\langle E \rangle^*_{m,o}$ and $E_{p,o}$ values were drawn from measured energy spectra and measured R_p values were drawn from same-day measured %DD curves on MBPCC's Baton Rouge Elekta Infinity accelerator.

Chapter 4 Aim 3 – Compare energy spectra of matched electron beams

Aim 3: Determine the energy spectra on central axis at 95-cm SCD for each of the seven electron beams on each of the six MBPCC Elekta Infinity accelerators by applying the analysis techniques of Aim 2 to intensity profiles measured in Aim 1. Compare all matched electron beam energy spectra.

4.1. Methods and materials

4.1.1. Reproducibility of measurement technique

The energy spectra of the 7 MeV, 11 MeV, and 16 MeV beams on the Baton Rouge Elekta Infinity were measured several consecutive times on the same day without disturbing the initial setup geometry. These spectra were measured using the methods described in Aims 1 and 2. Assuming the electron beam energy spectra were constant throughout the measurements, these measurements estimated the uncertainty of the measurement technique. It was believed that any variations in the energy spectra were due to mechanical errors in the placement of the CR strip in the slot, the placement of the CR strips on the carousel, variations in the dimensions of the CR strips, variations in the individual CR strip responses, and amplification of these effects by the data analysis methods.

4.1.2. Reproducibility of energy spectra

To assess accelerator stability (i.e. the reproducibility of energy spectra) over time, the same spectra were measured on a single accelerator on different days using the methods described in Aims 1 and 2. For the Baton Rouge Elekta Infinity accelerator, the energy spectra for the 7, 11, and 16 MeV beams were measured on Jan/14/2013 and May/3/2013. Additionally, for the Gonzales Elekta Infinity accelerator, the energy spectra for all seven beam energies were measured on Feb/14/2013 and April/11/2013.

4.1.3. Comparing energy spectra across multiple accelerators

The energy spectra were measured for each of the seven beam energies on each of the six MBPCC Elekta Infinity accelerators using the methods described in Aims 1 and 2. Then, the energy

spectra from the different Elekta Infinity accelerators were compared to the energy spectra of the accelerators to which they were matched, i.e. the reference accelerators, using the energy spectra matching criteria.

4.1.3.1. Metrics for comparing energy spectra

The metrics used for comparing the energy spectra were the incident modified peak mean energy, $\langle E \rangle_{m,o}^{*}$, and the full width at half maximum, FWHM. The definition of $\langle E \rangle_{m,o}^{*}$ is given in section 3.1.4.2.1. The FWHM were determined by fitting a Gaussian distribution to the portion of each energy spectrum that fell within its $\pm$15% energy averaging range. The standard deviations, σ, of the resulting Gaussian distributions were multiplied by 2.35 to obtain the FWHM values.

4.1.3.2. Matching criteria for energy spectra

For an electron beam's energy spectrum to be considered matched, its $\langle E \rangle_{m,o}^{*}$ must match the reference beam's $\langle E \rangle_{m,o}^{*}$ to within 0.12 MeV, which corresponds to a difference in R_{50} of approximately 0.05 cm. Additionally, its FWHM had to match the reference beam's FWHM to within 2.0 MeV, which corresponds to a difference in R_{80-20} of approximately 0.1 cm. Details of how the matching criteria were determined are available in Aim 4.

4.2. Results and discussion

4.2.1. Reproducibility of measurement technique

Plotted in Figure 4.1 are the consecutive, same-day energy spectra measurements of the 7, 11, and 16 MeV beams of the Baton Rouge Elekta Infinity accelerator. Notice that for these measurements, the portion of the area under an energy spectrum's tail versus its peak structure varies noticeably. This reduces the magnitudes of some spectra's peak regions relative to other spectra's peak regions, as all the spectra are normalized to have an area of unity. These variations are due to how the fit regions for the background subtraction were selected (section 3.1.1.2) and do not significantly affect the resulting $\langle E \rangle_{m,o}^{*}$ and FWHM values.

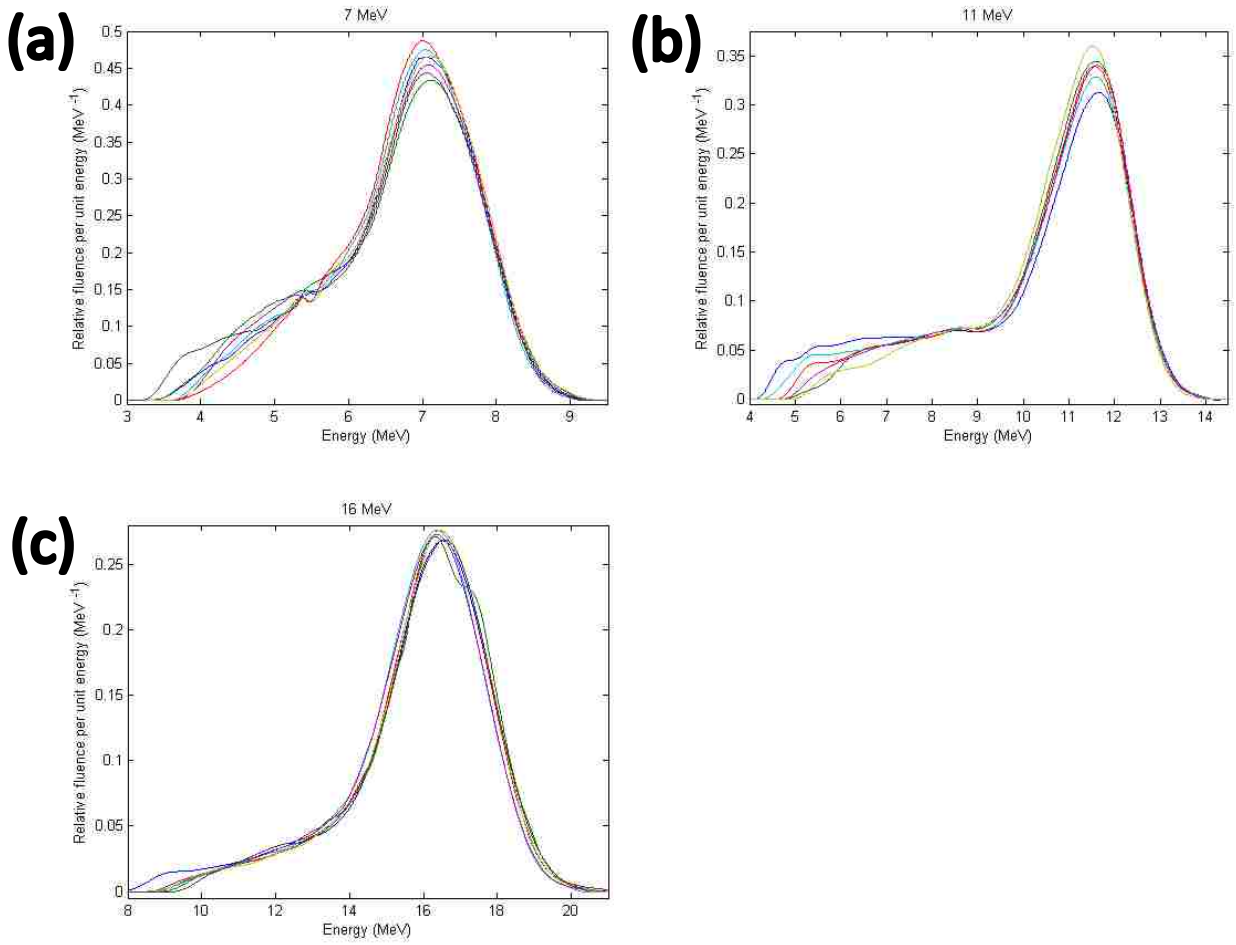

Figure 4.1. Consecutive, same-day spectral measurements. Seven consecutive same day measurements of the energy spectra of the (a) 7, (b) 11, and (c) 16 MeV beams on MBPCC's Baton Rouge Elekta Infinity accelerator. The seventh measurement of the energy spectra for 11 MeV beam was ruined during readout and hence is not displayed.

The $\langle E \rangle^*_{m,o}$, FWHM, and FWHM/$\langle E \rangle^*_{m,o}$ values of these energy spectra are listed in Table 4.1. The standard deviations of the $\langle E \rangle^*_{m,o}$ values were 0.030, 0.045, and 0.077 MeV at 7, 11, and 16 MeV, respectively. These values, although less than the 0.12 MeV matching criteria for $\langle E \rangle^*_{m,o}$, were significant particularly at the higher energies. Ideally, the uncertainty would be an order of magnitude less than the matching criteria, i.e. 0.012 MeV. Further investigation into the source of the uncertainty is warranted.

On the other hand, the standard deviations of the FWHM values were 0.031, 0.027, and 0.042 MeV at 7, 11, and 16 MeV, respectively, significantly smaller than the 2.0 MeV matching criteria. In other words, the standard deviations of the FWHM values were less susceptible to variations in the positioning of the CR strips than the standard deviations of the $\langle E \rangle_{m,o}^{*}$ values. The variations in the percent standard deviations of the $\langle E \rangle_{m,o}^{*}$ values across all three energies are fairly small.

Table 4.1. Energy metrics of consecutive, same-day measurements. The $\langle E \rangle_{m,o}^{*}$ (PME), FWHM, and FWHM/$\langle E \rangle_{m,o}^{*}$ (FWHM/PME) are listed for all seven measurements of the 7, 11, and 16 MeV beam, except for the 7th measurement of the 11 MeV beam which was ruined by a readout error. The mean (MEAN), standard deviation (STD DEV), and percent standard deviation (% STD DEV) of all the energy metrics are listed to the right.

		1	2	3	4	5	6	7	MEAN	STD DEV	%STD DEV
7MeV	**PME (MeV)**	7.00	7.01	6.94	6.94	7.00	7.00	7.00	6.99	*0.0300*	0.43
	FWHM (MeV)	1.78	1.87	1.83	1.79	1.81	1.83	1.80	1.82	*0.0308*	1.70
	FWHM/PME	0.254	0.267	0.264	0.258	0.259	0.262	0.257	0.26	*0.0044*	1.68
11MeV	**PME (MeV)**	11.29	11.23	11.27	11.23	11.27	11.17	N/A	11.24	*0.0450*	0.40
	FWHM (MeV)	2.39	2.40	2.33	2.41	2.39	2.38	N/A	2.38	*0.0271*	1.14
	FWHM/PME	0.212	0.213	0.207	0.214	0.212	0.213	N/A	0.21	*0.0026*	1.23
16MeV	**PME (MeV)**	16.32	16.33	16.27	16.14	16.17	16.28	16.32	16.26	*0.0768*	0.47
	FWHM (MeV)	3.19	3.32	3.21	3.21	3.22	3.22	3.25	3.23	*0.0422*	1.31
	FWHM/PME	0.196	0.203	0.197	0.199	0.199	0.198	0.199	0.20	*0.0024*	1.18

4.2.2. Reproducibility of energy spectra

The reproducibility of energy spectra on Elekta Infinity accelerators was determined by comparing energy spectra from the same accelerator measured on different days. For the Baton Rouge accelerator, the measurements described in section 4.1.1 and performed on May/3/2013 were compared against the 7, 11, and 16 MeV beams of the complete set of energy spectra measured on Jan/14/2013 and plotted in Figure 4.4 (b). This comparison is plotted in Figure 4.2. The values for the energy spectra metrics, $\langle E \rangle_{m,o}^{*}$, FWHM, and FWHM/$\langle E \rangle_{m,o}^{*}$ are listed in Table 4.2.

Additionally, energy spectra measurements were performed on the Gonzales accelerator on Feb/14/2013 and April/11/2013. The results are plotted in Figure 4.3. The values for $\langle E \rangle_{m,o}^{*}$, FWHM,

Table 4.2. Energy metrics from energy spectra measured on the Baton Rouge Elekta Infinity on separate days. The $\langle E \rangle^*_{m,o}$ (PME), FWHM, and FWHM/$\langle E \rangle^*_{m,o}$ (FWHM/PME) of the Baton Rouge energy spectra measured on separate days are listed along with the differences (DIF) between the metrics. The differences are the energy metrics from January subtracted from the energy metrics from May.

		Jan-14-2013	May-3-2013 (average)	DIF (May-Jan)
7 MeV	**PME (MeV)**	7.1687	6.9852	-0.1835
	FWHM (MeV)	1.6361	1.8178	+0.1817
	FWHM/PME	0.2282	0.2602	+0.0320
11 MeV	**PME (MeV)**	11.4461	11.2435	-0.2026
	FWHM (MeV)	2.4040	2.3830	-0.0210
	FWHM/PME	0.2100	0.2119	+0.0019
16 MeV	**PME (MeV)**	16.5441	16.2612	-0.2829
	FWHM (MeV)	3.2607	3.2293	-0.0314
	FWHM/PME	0.1971	0.1986	+0.0015

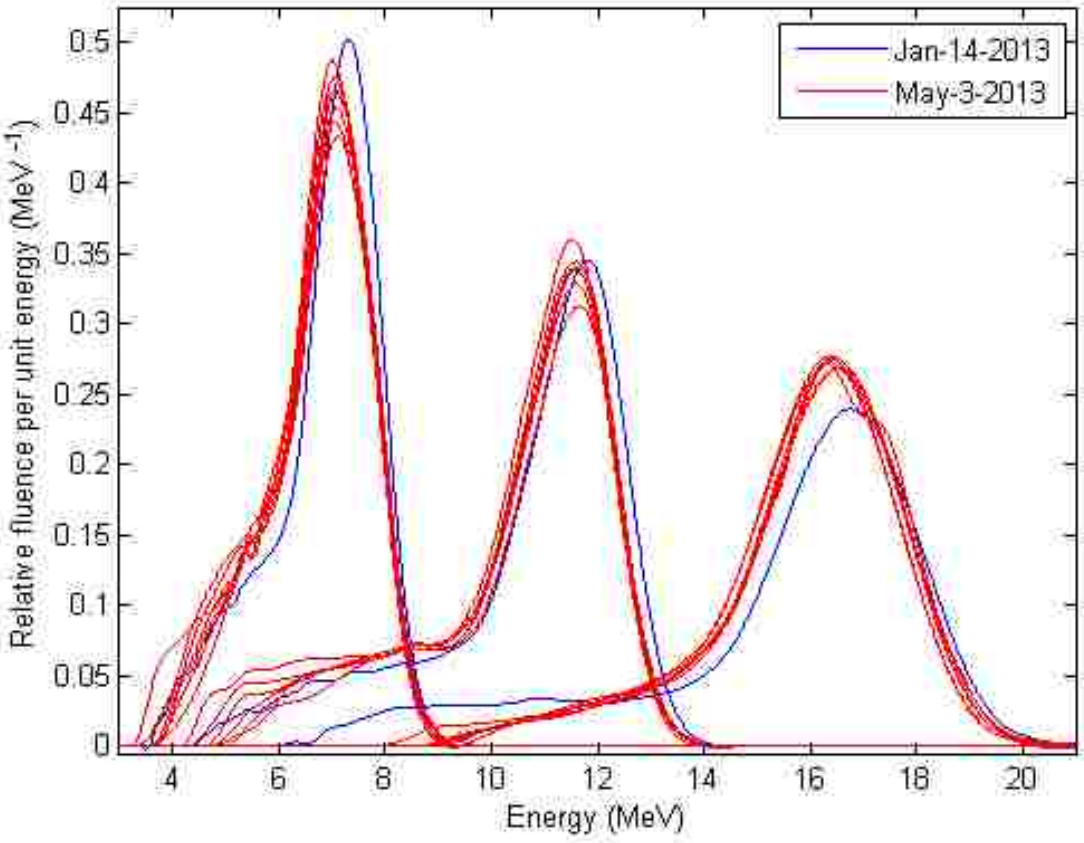

Figure 4.2. Energy spectra measured on the Baton Rouge Elekta Infinity on separate days. Plotted are the 7 MeV, 11 MeV, and 16 MeV beams measured on MBPCC's Baton Rouge Elekta Infinity accelerator on (red) May/3/2013 and (blue) Jan/14/2013.

and FWHM/$\langle E \rangle^*_{m,o}$ are listed in Table 4.3. Notice that the differences in the $\langle E \rangle^*_{m,o}$ values for different day energy spectra measurements are larger for the Gonzales accelerator than for Baton Rouge accelerator, yet for both accelerators the differences increase monotonically with energy.

For the Baton Rouge accelerator, shifts in $\langle E \rangle^*_{m,o}$ were -0.18, -0.20, and -0.28 MeV at 7, 11, and 16 MeV, respectively. For the Gonzales accelerator, shifts in $\langle E \rangle^*_{m,o}$ increased with energy, ranging from -0.29 to -0.69 MeV for the 7 to 20 MeV beams, respectively. The increasing shift with energy could be due to a systematic error in CR strip origin, as $\left|\frac{dE}{dx}\right|$ increases with energy (cf. Figure 3.22). The shifts in $\langle E \rangle^*_{m,o}$ in Table 4.3 all correspond to a shift of approximately 0.12 cm.

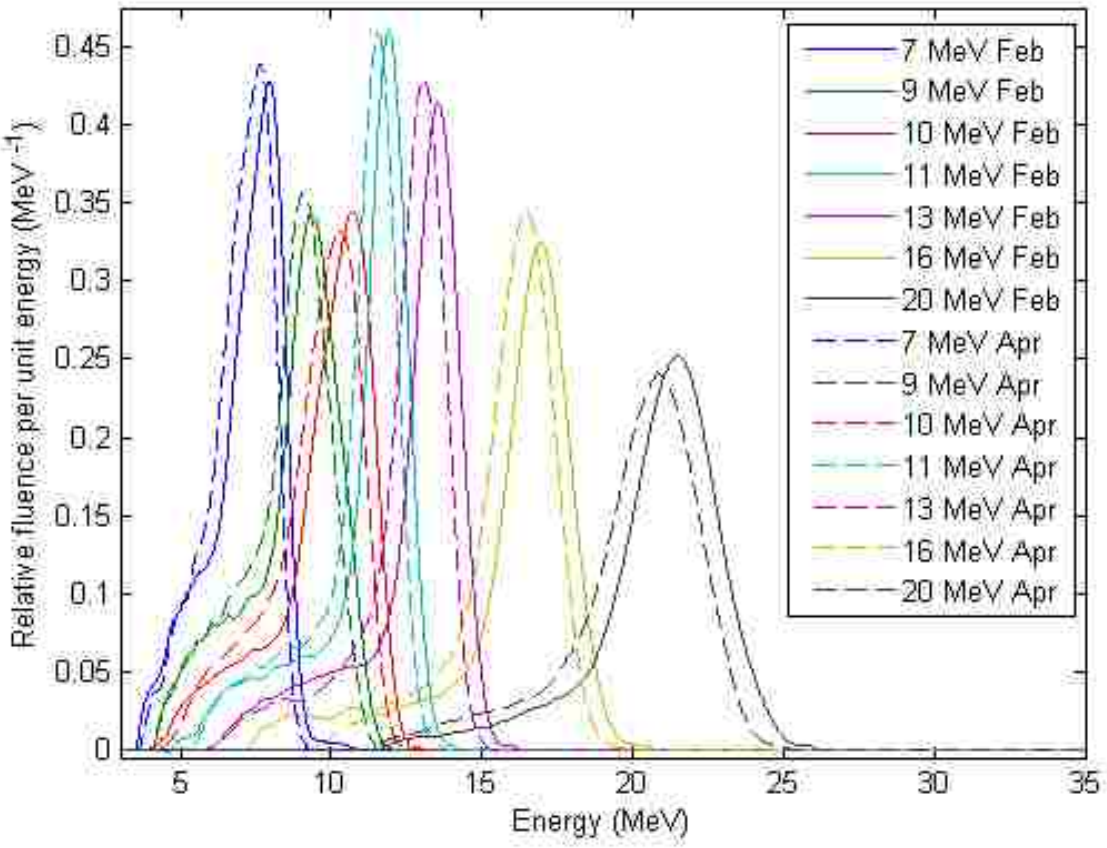

Figure 4.3. Energy spectra measured on the Gonzales Elekta Infinity on separate days. Plotted are the complete set of energy spectra measured on MBPCC's Gonzales Elekta Infinity accelerator on (solid) Feb/14/2013 and (dashed) Apr/11/2013.

When compared with the standard deviations of the $\langle E \rangle^*_{m,o}$ and FWHM values in Table 4.1, it is clear that the deviations of the energy metrics in Table 4.2 and Table 4.3 were due to drifting of the energy spectra with time rather than measurement error. The cause of these drifts is not clear, emphasizing the utility of a real-time version of this study's magnetic spectrometer developed for beam tuning and QA.

Table 4.3. Energy metrics from energy spectra measured on the Gonzales Elekta Infinity on separate days. The $\langle E \rangle^*_{m,o}$ (PME), FWHM, and FWHM/$\langle E \rangle^*_{m,o}$ (FWHM/PME) values of the Gonzales energy spectra measured on separate days are listed along with the differences (DIF) between the metrics. The differences are the energy metrics from February subtracted from the energy metrics from April.

		Feb/14/2013	Apr/11/2013	DIF (Apr-Feb)
7 MeV	**PME (MeV)**	7.5726	7.2814	-0.2912
	FWHM (MeV)	2.2136	2.2346	+0.0210
	FWHM/PME	0.2923	0.3069	+0.0146
9 MeV	**PME (MeV)**	9.3307	9.0101	-0.3207
	FWHM (MeV)	2.1993	2.1497	-0.0497
	FWHM/PME	0.2357	0.2386	+0.0029
10 MeV	**PME (MeV)**	10.3440	9.9349	-0.4091
	FWHM (MeV)	2.5241	2.6614	+0.1373
	FWHM/PME	0.2440	0.2679	+0.0239
11 MeV	**PME (MeV)**	11.6548	11.2805	-0.3743
	FWHM (MeV)	1.7067	1.7785	+0.0718
	FWHM/PME	0.1464	0.1577	+0.0112
13 MeV	**PME (MeV)**	13.2655	12.7945	-0.4709
	FWHM (MeV)	1.9374	1.9950	+0.0576
	FWHM/PME	0.1460	0.1559	+0.0099
16 MeV	**PME (MeV)**	16.6803	16.1329	-0.5474
	FWHM (MeV)	2.5092	2.6057	+0.0966
	FWHM/PME	0.1504	0.1615	+0.0111
20 MeV	**PME (MeV)**	21.1866	20.4952	-0.6914
	FWHM (MeV)	3.4881	3.7429	+0.2548
	FWHM/PME	0.1646	0.1826	+0.0180

4.2.3. Comparing energy spectra across multiple accelerators

The energy spectra for each Elekta Infinity accelerator at MBPCC are shown below in Figure 4.4. Though MBPCC had intended to match all accelerators to its original Elekta Infinity accelerator at Gonzales, attempts by local and factory Elekta engineers to do so on the Elekta Infinity accelerator installed at MBPCC's satellite in Houma were unsuccessful. Hence, separate commissioning data was taken for the Elekta accelerator at Houma, to which the subsequently installed Elekta accelerator at MBPCC's Hammond satellite was matched. Hence, there are two reference accelerators at MBPCC to which other accelerators were matched, the Elekta Infinity at its Gonzales satellite, which was the first Elekta accelerator installed at MBPCC, and the Elekta Infinity accelerator installed later at its Houma satellite. Both Elekta Infinity accelerators installed at MBPCC's Covington satellite, as well as the Elekta Infinity accelerator at MBPCC's main facility in Baton Rouge, were matched to the Gonzales reference accelerator. The Elekta Infinity accelerator at MBPCC's Hammond satellite facility was matched to the Elekta Infinity at MBPCC's Houma satellite. MBPCC intends to match all future Elekta Infinity accelerators to the reference accelerator at its Houma satellite.

All accelerators were tuned to give R_{90} values spaced every 0.5 cm (2.0, 2.5, 3.0, 3.5, and 4.0 cm) from 7 to 13 MeV and every 1.0 cm (4.0, 5.0, and 6.0) from 13 to 20 MeV. This results in evenly spaced energy spectra from 7 to 13 MeV and from 13 to 20 MeV. Visual exceptions to this are observed for the 9 MeV Covington 1, 10 MeV Covington 2, and 11 MeV Hammond beams.

As is visible in Figure 4.4, there is a general trend towards broader energy spectra as the energy of the electron beam increases, which is to be expected as higher energy electron beams require thicker scattering foils to broaden and flatten the beams, resulting in greater energy straggling. Interestingly, some accelerators have energy spectra that do not follow this trend monotonically. This indicates that electrons beams can have noticeably different spectral widths and yet have acceptably matching %DD

(a)

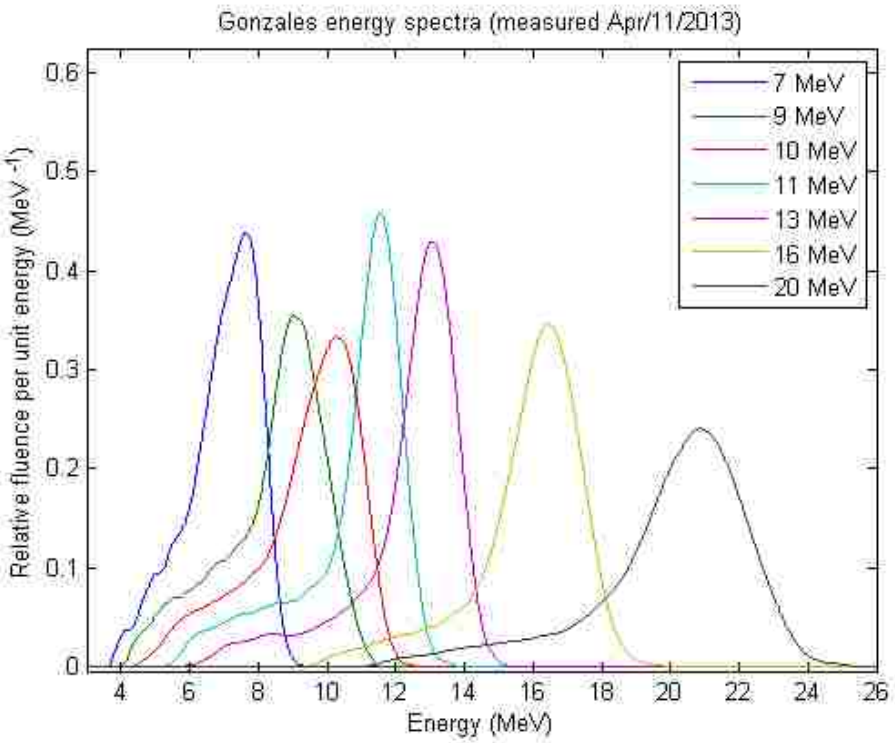

(b)

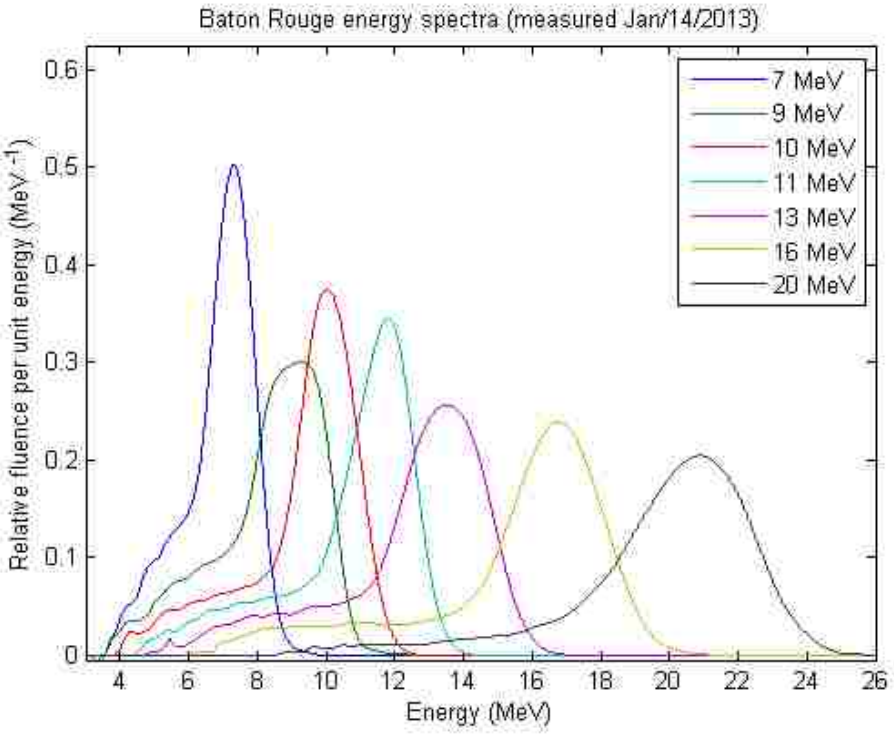

Figure 4.4. Measured energy spectra for each Elekta Infinity accelerator. Plotted are complete sets of energy spectra measured on the Elekta Infinity accelerators at (a) Gonzales, (b) Baton Rouge, (c) Covington 1, (d) Covington 2, (e) Houma, and (f) Hammond, listed in order of installation.

(Figure 4.4 continued)

(c)

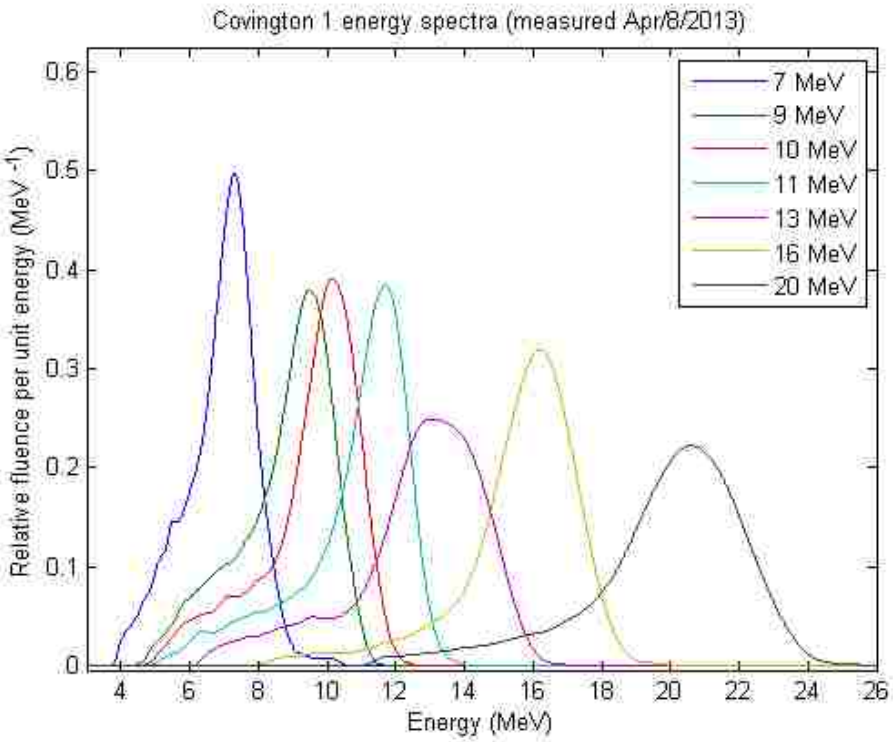

(d)

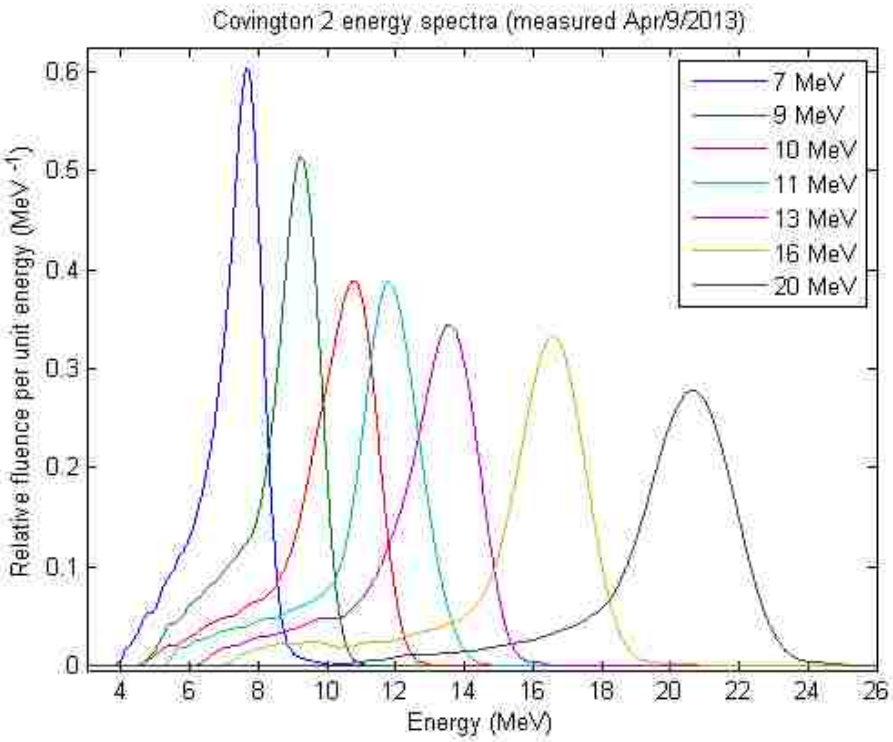

(Figure 4.4 continued)

(e)

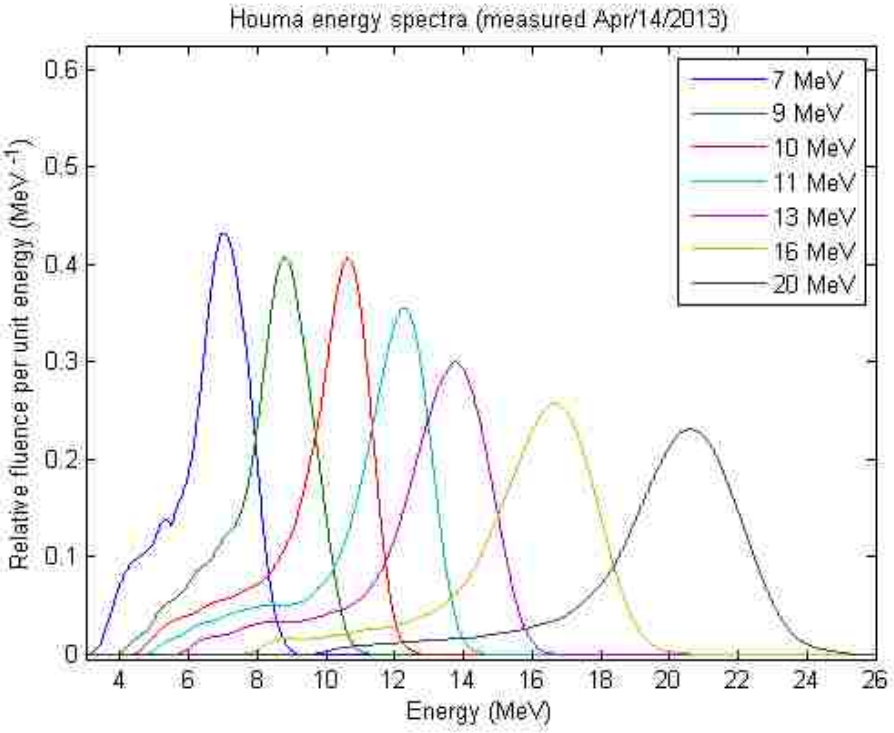

(f)

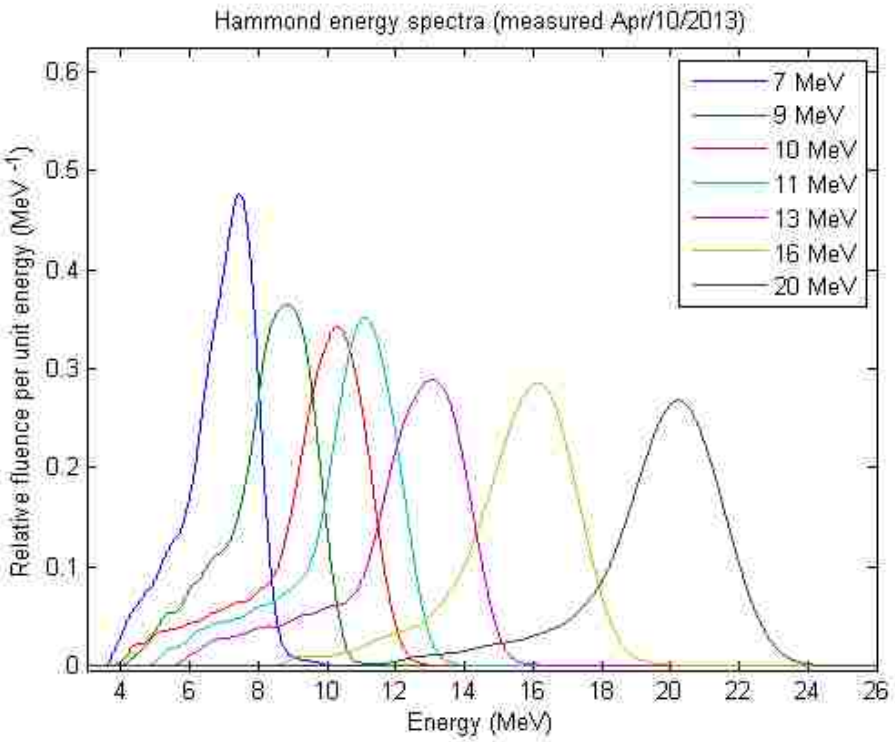

curves. It is worth noting that the variations in FWHM across the seven beam energies are comparable to the variations in spectral width of the rectangular spectra simulated by Kainz *et al* (2004).

While almost all energy spectra from this study have an electron peak structure that resembles a single Gaussian distribution, most energy spectra measured by Deasy in Figure 1.15 did not. In fact, most of the energy spectra in Figure 1.15 have two or more distinct peaks. The energy spectra measured in this study are likely more Gaussian due to improvements in the traveling waveguide design and/or tuning procedures since the time of Deasy *et al*'s SL25 Phillips measurements. Regardless, some multi-peaked energy spectra are still apparent, e.g. the 9 MeV Baton Rouge beam shown in Figure 4.4 (b) and the 13 MeV Covington 1 beam in Figure 4.4 (c). These multi-peaked energy spectra were likely due to suboptimal HPPH settings.

Though Deasy measured the energy spectra in Figure 1.15 using film and performed background subtraction on the film densitometry results in a fashion similar to the background subtraction described in section 3.1.1.2, the results have smaller low-energy straggling tails than the energy spectra measured in this study. Hence, Deasy either included a larger portion of the low-energy tails within his background fits, hence removing them, or the tails were never sufficiently visible. The prominence of the low-energy tails in this study's methods, in combination with the fact that the fit regions used for background subtraction were chosen manually, results in noticeable variations in the fraction of area of the energy spectra that fall under the low-energy tails versus the peak structures. These variations are most apparent in the energy spectra in Figure 4.1. In future work, it may be possible to mitigate these variations by further reducing the background contribution to the detection medium or subtracting the background with measured background subtraction.

The spectral tails in Deasy's study and in this study differ significantly from the MC simulated spectral tails of Harris's study, an example of which is illustrated in Figure 1.19. Further study of this discrepancy is only warranted if it remains after addressing the future work recommendations in the

above paragraph. However, the energy metrics used for comparison of energy spectra, $\langle E \rangle_{m,o}^{*}$ and FWHM, are not significantly affected by these variations in the low-energy tail.

Figure 4.5 below displays the same spectra shown in Figure 4.4, but on a per-energy as opposed to per-accelerator basis. Each plot was separated into the two matching groups used at MBPCC. The blue plots are the Gonzales reference accelerator and all the accelerators that were matched to it, and the red plots are the Houma reference accelerator and the Hammond accelerator that was matched to it. The energy spectra from the reference accelerators are displayed with solid lines. Also, the $\langle E \rangle_{m,o}^{*}$ (PME), FWHM, and FWHM/$\langle E \rangle_{m,o}^{*}$ (FWHM/PME) values for the energy spectra in Figure 4.5 are listed in Table 4.4.

At 7 MeV, the Houma reference spectrum has a lower $\langle E \rangle_{m,o}^{*}$ and lower FWHM (6.98 and 1.85 MeV) than the Gonzales reference spectrum (7.28 and 2.23 MeV). The reference Gonzales spectrum clearly contains at least two peaks. The Covington 2 spectrum is the narrowest (FWHM = 1.64 MeV). The Baton Rouge and Covington 1 spectra are the second narrowest and match almost exactly. The Hammond spectrum has a slightly greater $\langle E \rangle_{m,o}^{*}$ and FWHM (7.15 and 1.99 MeV) than its reference Houma spectrum (6.98 and 1.85 MeV).

At 9 MeV, the Houma reference spectrum was shifted to lower energies and had a slightly narrower width than the Gonzales reference spectrum (8.70 and 2.01 MeV versus 9.01 and 2.15 MeV for $\langle E \rangle_{m,o}^{*}$ and FWHM). The Covington 2 had the narrowest spectrum (FWHM = 1.75 MeV), as was the case at 7 MeV. The BR spectrum had the broadest spectrum (FWHM = 2.73 MeV), which is attributed to the multiple peaks (at least two). The Covington 1 spectrum clearly had a greater $\langle E \rangle_{m,o}^{*}$ than that of the reference Gonzales beam (9.22 versus 9.01 MeV). The Gonzales spectrum and all those matched to it have significantly different shapes and are clearly not matched. Contrastingly, the Hammond beam

(a)

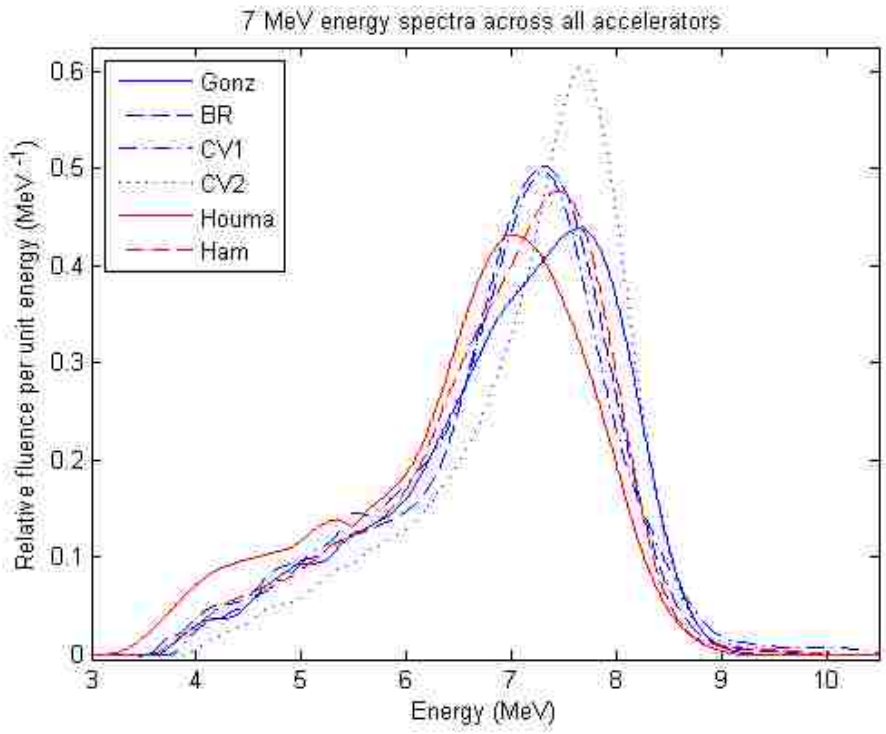

(b)

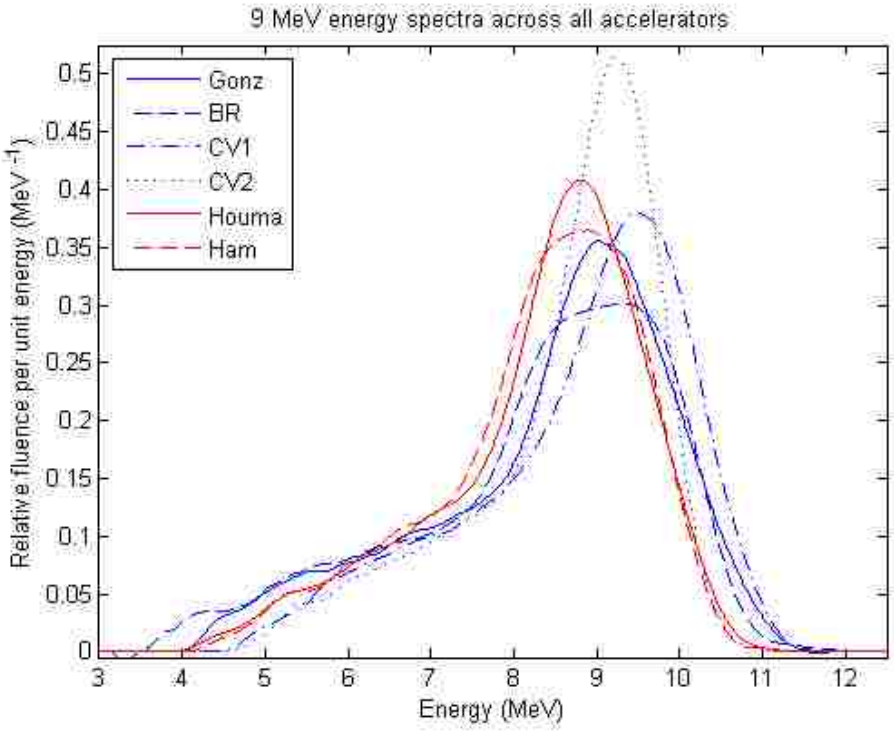

Figure 4.5. Measured energy spectra for each beam energy. Plotted are measured (a) 7, (b) 9, (c) 10, (d) 11, (e) 13, (f) 16, and (g) 20 MeV energy spectra for MBPCC's six Elekta Infinity accelerators. The energy spectra from the (solid line) reference accelerators are plotted, along with the rest of the energy spectra from the (blue) Gonzales matching group and the (red) Houma matching group.

(Figure 4.5 continued)

(c)

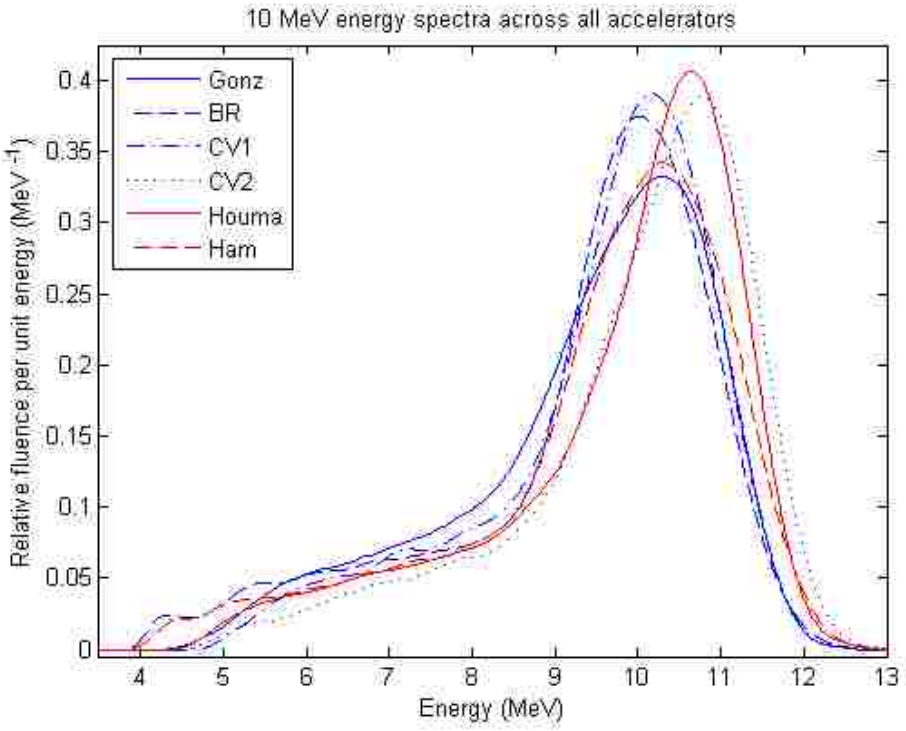

(d)

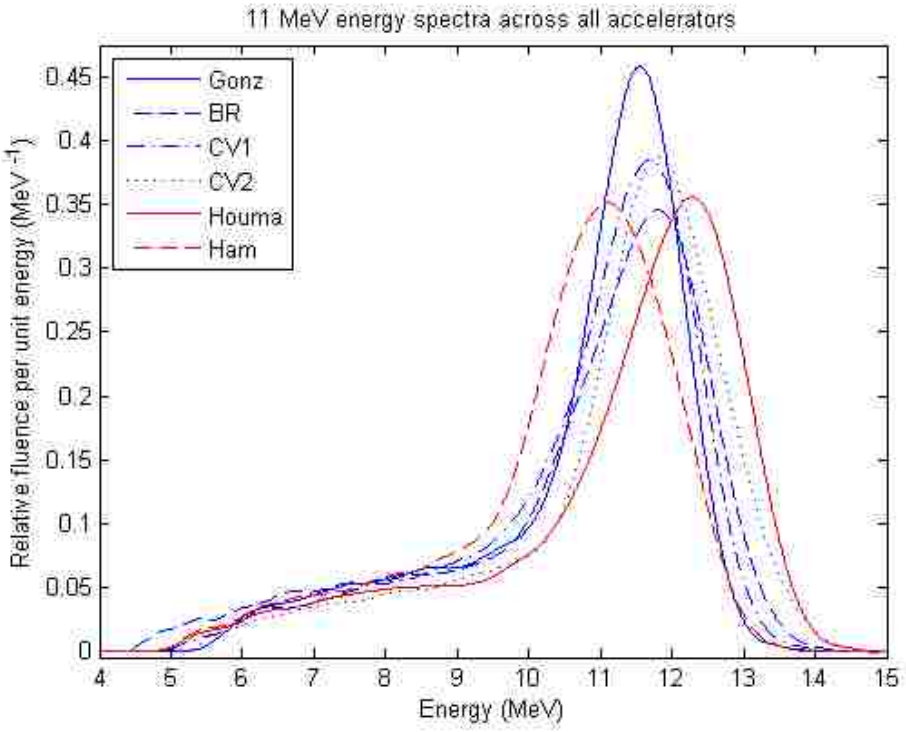

(Figure 4.5 continued)

(e)

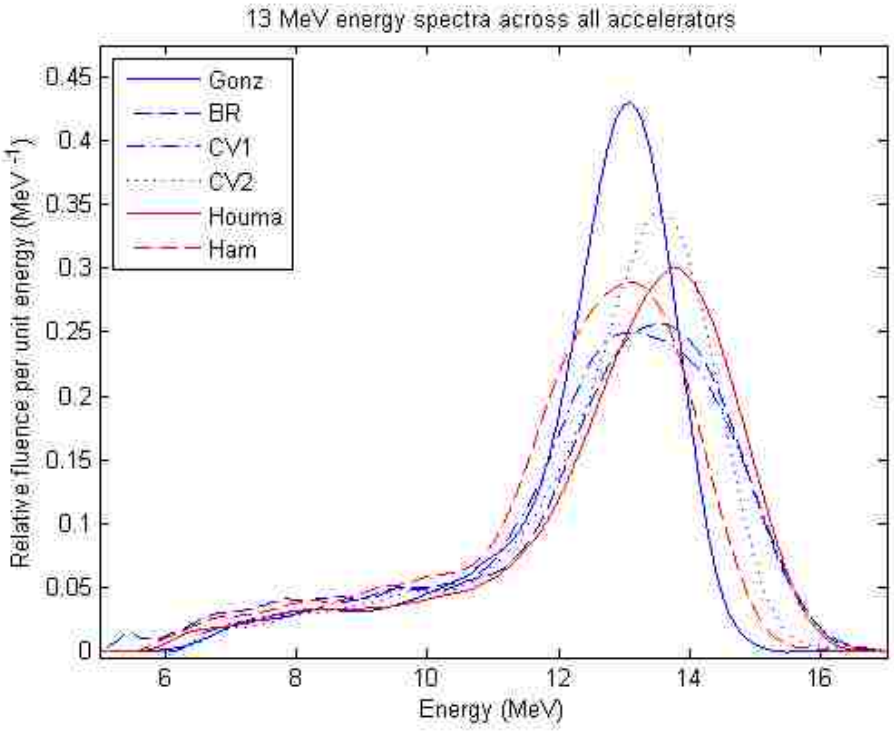

(f)

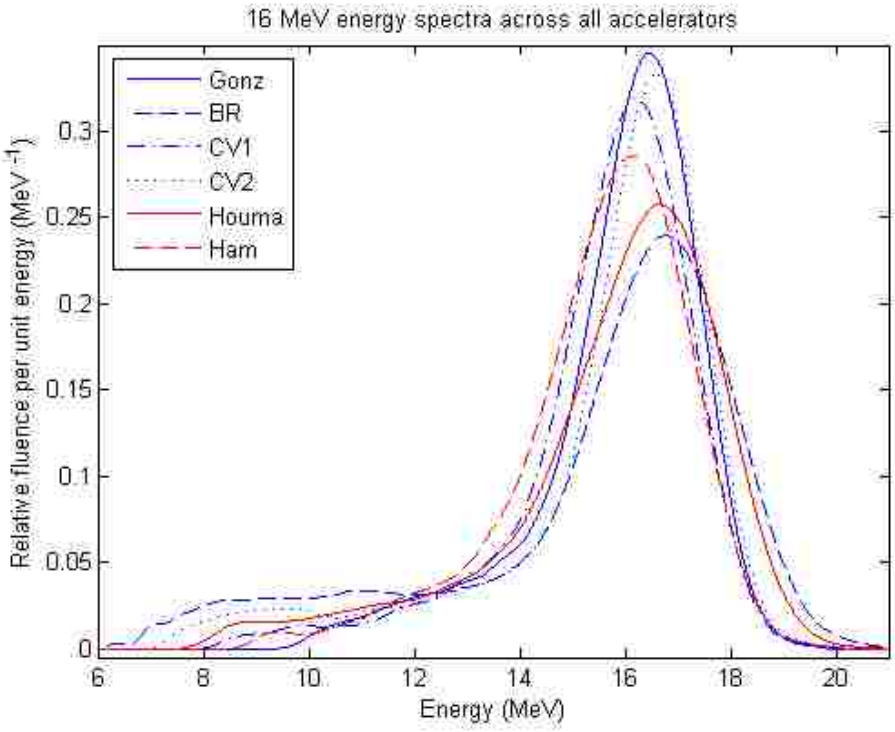

(Figure 4.5 continued)

(g)

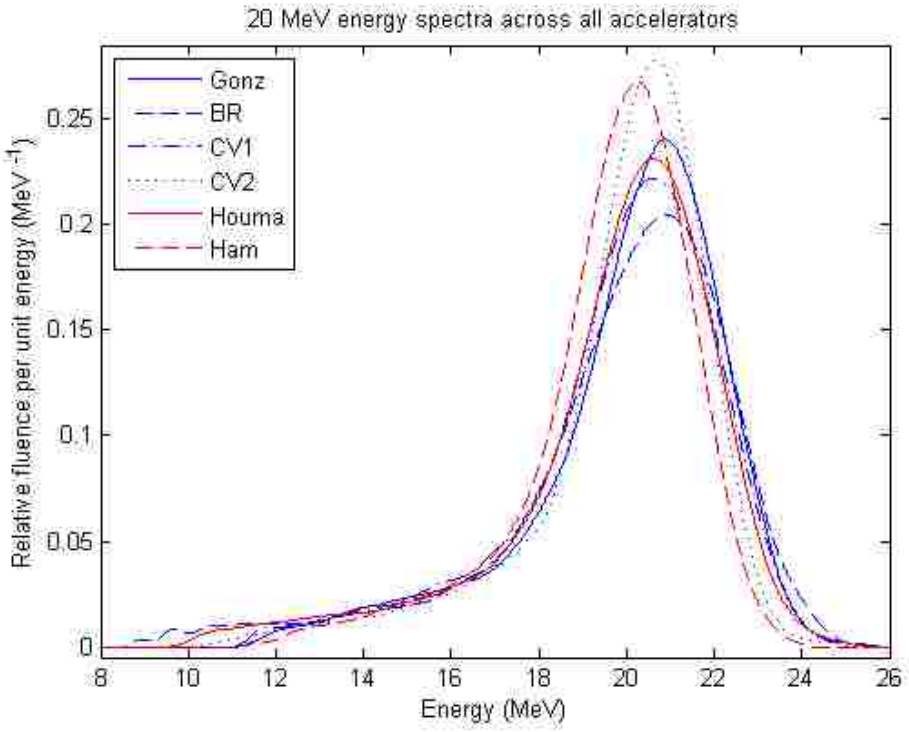

closely matches its reference spectrum, that of the Houma accelerator, being only slightly shifted to a lower energy and having only a slightly greater FWHM (8.68 and 2.32 MeV versus 8.70 and 2.01 MeV for $\langle E \rangle^*_{m,o}$ and FWHM).

At 10 MeV, the Houma reference spectrum is shifted to higher energies and has a slightly narrower width than the Gonzales reference spectrum. The BR and Covington 2 are similar to their reference spectra, the Gonzales spectrum, being only slightly narrower (2.05 and 2.35 MeV versus 2.66 MeV for FWHM). The Covington 2 spectrum shows the greatest difference from its reference spectrum, showing a significant shift to the higher energies (10.41 versus 9.93 MeV for $\langle E \rangle^*_{m,o}$), while the Covington 1 spectrum is only slightly more energetic (9.98 versus 9.93 for $\langle E \rangle^*_{m,o}$). Contrastingly, the Hammond spectrum, relative to its reference, shows a significant shift to a lower energies (10.12 versus 10.30 MeV for $\langle E \rangle^*_{m,o}$).

Table 4.4. Comparison of energy spectra metrics from MBPCC's six accelerators for all seven beam energies. Listed are the $\langle E \rangle_{m,o}^{*}$ (PME), FWHM, and the relative width values (FWHM/PME) for the seven beam energies on all six Elekta Infinity accelerators at MBPCC. The standard deviation (STD DEV) per beam energy for all three metrics are listed in the column to the right of the table. The $\langle E \rangle_{m,o}^{*}$ and FWHM of the reference accelerators are illustrated with light gray fill, with the energy metrics that do not match those of their reference accelerator being illustrated in dark gray fill for the (1) Gonzales matching group and the (2) Houma matching group. The matching criteria was 0.12 MeV for $\langle E \rangle_{m,o}^{*}$ and 2.0 MeV for FWHM.

				1			2	
		Gonz	BR	CV1	CV2	Houma	Ham	STD DEV
7 MeV	**PME (MeV)**	7.28	7.17	7.10	7.38	6.98	7.15	0.139
	FWHM (MeV)	2.23	1.64	1.71	1.64	1.85	1.99	0.234
	FWHM/PME	0.31	0.23	0.24	0.22	0.26	0.28	0.032
9 MeV	**PME (MeV)**	9.01	8.98	9.22	8.97	8.70	8.68	0.205
	FWHM (MeV)	2.15	2.73	2.34	1.75	2.01	2.32	0.336
	FWHM/PME	0.24	0.30	0.25	0.19	0.23	0.27	0.037
10 MeV	**PME (MeV)**	9.93	9.95	9.98	10.41	10.30	10.12	0.199
	FWHM (MeV)	2.66	2.05	2.15	2.35	2.21	2.39	0.216
	FWHM/PME	0.27	0.21	0.22	0.23	0.21	0.24	0.022
11 MeV	**PME (MeV)**	11.28	11.45	11.33	11.70	11.92	10.98	0.333
	FWHM (MeV)	1.78	2.40	2.29	2.07	2.40	2.33	0.246
	FWHM/PME	0.16	0.21	0.20	0.18	0.20	0.21	0.022
13 MeV	**PME (MeV)**	12.79	13.35	13.22	13.21	13.47	12.79	0.287
	FWHM (MeV)	2.00	3.04	3.38	2.59	2.85	2.86	0.467
	FWHM/PME	0.16	0.23	0.26	0.20	0.21	0.22	0.034
16 MeV	**PME (MeV)**	16.13	16.54	15.94	16.29	16.31	15.80	0.272
	FWHM (MeV)	2.61	3.26	2.80	2.49	3.42	3.20	0.385
	FWHM/PME	0.16	0.20	0.18	0.15	0.21	0.20	0.023
20 MeV	**PME (MeV)**	20.50	20.45	20.30	20.28	20.27	19.92	0.201
	FWHM (MeV)	3.74	4.34	4.01	3.17	3.80	3.37	0.421
	FWHM/PME	0.18	0.21	0.20	0.16	0.19	0.17	0.020

At 11 MeV, the Houma reference spectrum is shifted to higher energies than the Gonzales reference spectrum (11.92 versus 11.28 MeV for $\langle E \rangle_{m,o}^{*}$). BR, CV1, and CV2 are noticeably broader than their reference spectrum (2.40, 2.29, and 2.07 MeV versus 1.78 MeV for FWHM) and shifted to higher energies (11.45, 11.33, and 11.70 versus 11.28 MeV for $\langle E \rangle_{m,o}^{*}$). The Hammond spectrum is shifted to much lower energies than its Houma reference spectrum, though it has about the same width (10.98 and 2.23 MeV versus 11.92 and 2.40 MeV for $\langle E \rangle_{m,o}^{*}$ and FWHM).

At 13 MeV, the Houma reference spectrum is more energetic and significantly broader than the Gonzales reference spectrum (13.47 and 2.85 MeV versus 12.79 and 2.00 MeV). BR, CV1, and CV2 have higher energies and widths than their reference Gonzales spectrum (13.35 and 3.04, 13.22 and 3.38, 13.21 and 2.59 MeV versus 12.79 and 2.00 MeV for $\langle E \rangle^*_{m,o}$ and FWHM). Again, the BR, CV1, and CV2 spectrum all have fairly close $\langle E \rangle^*_{m,o}$ though their widths are not matched quite as well. Notably, CV1 and BR spectra are quite broad. The Hammond spectrum is shifted to much lower energies than the Houma spectrum though they have similar widths (12.79 and 2.86 MeV versus 13.47 are 2.85 MeV for $\langle E \rangle^*_{m,o}$ and FWHM).

At 16 MeV, the Houma reference spectrum is more energetic and broader than the Gonzales reference spectrum (16.31 and 3.42 MeV versus 16.13 and 2.61 MeV for $\langle E \rangle^*_{m,o}$ and FWHM). The spectra matched to the Gonzales reference spectrum are all shifted slightly from the $\langle E \rangle^*_{m,o}$ of Gonzales (15.94 to 16.54 MeV versus 16.13 MeV for $\langle E \rangle^*_{m,o}$), and the BR beam had a broader spectrum (3.26 versus 2.61 MeV for FWHM). The Hammond spectrum is both narrower and less energetic than its reference spectrum (15.80 and 3.20 MeV versus 16.31 and 3.42 MeV for $\langle E \rangle^*_{m,o}$ and FWHM).

At 20 MeV, the Houma reference spectrum is shifted to slightly lower energies than the Gonzales reference spectrum, but they have almost identical widths (20.27 and 3.80 MeV versus 20.50 and 3.74 MeV for $\langle E \rangle^*_{m,o}$ and FWHM). Most of the spectra matched to the Gonzales reference spectra are fairly close to the reference in $\langle E \rangle^*_{m,o}$ (20.28-20.45 versus 20.50 MeV for $\langle E \rangle^*_{m,o}$) with a slight spread in widths (3.17 – 4.34 MeV versus 3.74 MeV). The Hammond spectrum is narrower and less energetic than its reference spectrum (19.92 and 3.37 MeV versus 20.27 and 3.80 MeV for $\langle E \rangle^*_{m,o}$ and FWHM). Overall, the spectra at 16 and 20 MeV are slightly better matched in shape than the spectra at lower energies.

Table 4.4 cells are shaded dark grey to indicate which energy metrics did not match their reference accelerator energy metrics, which were shaded light grey. Interestingly, few of the energy

spectra matched exactly. A few are closely matched, yet some are significantly different. There could be several reasons that matched electron beams' energy spectra do not match, including errors in the original beam tuning, subsequent beam tuning, spectral drifting between tuning, error in the positioning of the CR strips, or a combination thereof.

Chapter 5 Aim 4 – Correlate measured energy spectra metrics with %DD curve metrics

Aim 4: For every electron beam whose energy spectrum was measured, compare the $\langle E \rangle_{m,o}^{*}$ values and FWHM values of the energy spectra with the R_{50} and R_{80-20} values. Values for R_{50} and R_{80-20} were determined from relative ionization measurements in Plastic Water® phantom slabs taken in tandem with the energy spectra measurements.

5.1. Methods and materials

5.1.1. Measuring R50 and R80-20

To study the correlation between the %DD curves of electron beams and their measured energy spectra, %DD curve metrics were drawn from same-day relative ionization measurements. Measuring energy spectra and %DD curve metrics on the same day minimized the potential for drifting of energy spectra in between the two types of measurements. Instead of using a beam scanner and a tank filled with water, relative ionization measurements were taken in Plastic Water® phantom slabs (CIRS Inc., Norfolk, VA), which eliminated the uncertainty in the depth that results from manually registering the position of the physical center of the scanning chamber at the water's surface prior to scanning. This error in the placement of the chamber would be systematic for a single tank setup, but random from setup to setup, meaning it would not affect intra-accelerator comparisons of %DD metrics, but would affect inter-accelerator comparisons. The importance of both types of comparisons motivated the use of the Plastic Water® phantom slabs over beam scanning in a water-filled tank. As MBPCC's 2% or 0.5 cm DTA matching criteria for electron beams was hardest to achieve in the dose falloff region of the %DD curves, Plastic Water® slab measurements were taken at depths such that R_{50} and R_{80-20} could be determined from the results. Ideally, if both R_{50} and R_{80-20} matched that of their reference accelerator, most if not all data points in the dose falloff region of the %DD curve should match.

Relative ionization measurements were taken with a 0.6 cm^3 Farmer chamber (TN 30013, PTW, Freiburg, Germany) with a cavity radius, r_{cav} ,of 0.3 cm. The Farmer chamber was placed in the Plastic

Water® slab designed to hold it, henceforth referred to as the chamber slab. Figure 5.1 shows the chamber slab (a) with and (b) without the Farmer chamber inserted into it. The chamber slab was 2.0 cm thick, with a 1-cm distance between the center of the chamber hole and the surface of either side of the slab. To increase the physical depth beyond 1.0 cm, additional Plastic Water® slabs were placed on top of the chamber slab between the chamber and the radiation source. Two 5-cm Plastic Water® slabs were placed below the chamber slab to provide sufficient backscatter. For all combinations of slab material used for the measurements, the surface of the phantom was placed at 100-cm SSD using the alignment lasers and irradiated with 100 MU using the 14 x 14 cm^2 open applicator.

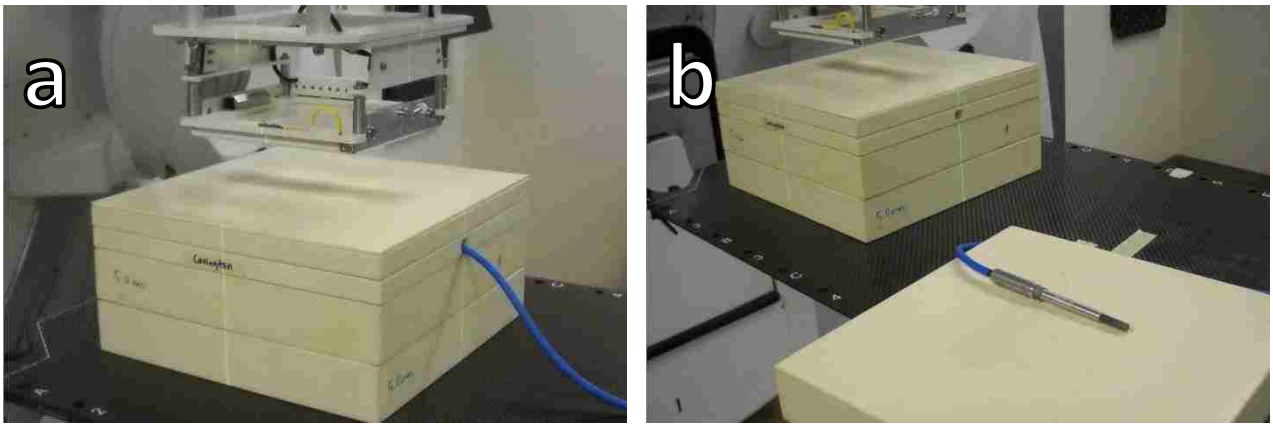

Figure 5.1. Setup for ionization measurement taken in Plastic Water®. Illustrated is the Plastic Water® phantom setup (a) with and (b) without the 0.6 cm^3 Farmer chamber inserted in the chamber slab. The chamber slab was placed on top of two 5-cm slabs to ensure sufficient backscatter was generated. Slab material was also placed above the chamber slab to increase the measurement depth. Visible above the slabs is the 14 x 14 cm^2 open applicator.

Since ionization can only be measured at one depth for a particular combination of Plastic Water® slabs, it is not feasible to take ionization measurements at the closely-spaced intervals possible for a single scan in a water-filled tank as the stepper motors of the beam scanner allow for depth measurements of a finer resolution than the thinnest, 1.0-mm Plastic Water® slab. Instead, ionization measurements were only taken at four depths, which were different for every beam energy. These depths, listed in Table 5.1, are the physical depths of the maximum ionization ($R_{100_{ion}}$), 80% ionization ($R_{80_{ion}}$), 50% ionization ($R_{50_{ion}}$), and 20% ionization ($R_{20_{ion}}$) of the percent ionization depth (%DI)

curves measured in water. However, the depths were rounded to the nearest millimeter so that they could be simulated with Plastic Water® slabs. %DI curves in water were measured for each beam energy of the Baton Rouge Elekta accelerator on Jan/14/2013 along with same-day %DI measurements in Plastic Water®. After measuring the ionization at the four specified physical depths for each beam energy, all four ionization values were divided by the max ionization value near depth $R_{100_{ion}}$ and multiplied by 100% to produce four percent ionization values. $R_{100_{ion}}$ was selected from the middle of the relatively flat maximum plateau region of the %DI curve measured in water to ensure spectral drift did not appreciably reduce the percent ionization measured from 100% when measuring ionization on other accelerators.

These %DI curves, which were plots of percent ionization versus effective depth (physical depth minus $0.5r_{cav}$), were converted into the %DD curves used for calibrating the magnetic spectrometer. Percent ionization was converted to percent dose using the AAPM TG-70 protocol (Gerbi *et al* 2009) and TG-25 protocol (Khan *et al* 1990) with TG-51 values for relative stopping powers (Almond *et al* 1999), as implemented in the IBA data acquisition system (IBA, Louvain-la-Neuve, Belgium). Prior to conversion, all effective depths of the %DI curves in water were increased by 0.063 cm to improve the match between the %DI curves in water and the four %DI data points in Plastic Water®, whose slab measurement depths were more reproducible. Like all other calibration data, these %DI curves were only measured for the Baton Rouge Elekta Infinity accelerator on Jan/14/2013.

Table 5.1. Physical depths of ionization measurements using Plastic Water® phantom slabs. Measurement depths are the physical depths of the $R_{100_{ion}}$, $R_{80_{ion}}$, $R_{50_{ion}}$, and $R_{20_{ion}}$ of the %DI curves measured in water on Jan/14/2013 on MBPCC's Baton Rouge Elekta Infinity accelerator.

	7MeV	9MeV	10MeV	11MeV	13MeV	16MeV	20MeV
$R_{100_{ion}}$ (cm)	1.6	2	2.2	2.5	2.4	2.6	1.7
$R_{80_{ion}}$ (cm)	2.4	3	3.5	4.0	4.6	5.7	6.8
$R_{50_{ion}}$ (cm)	2.8	3.5	4.0	4.6	5.3	6.6	8.2
$R_{20_{ion}}$ (cm)	3.3	4.2	4.6	5.3	6.2	7.6	9.6

To compare beams to one another, it was necessary to determine the depth of the 80%, 50%, and 20% dose values (e.g. R_{80}, R_{50}, and R_{20}) rather than the percent ionization values at the measured physical depths. First, the four percent ionization values measured for all seven beam energies on all six accelerators were converted to percent dose values by multiplying them by the ratio of percent dose to percent ionization at depth in water, where the %DD and %DI came from the beam scanning calibration data. Plotted in Figure 5.2 are example percent dose to percent ionization ratios versus depth for the 9 MeV beam, as well as the %DD and %DI curves used to get these ratios. Second, to determine R_{80}, R_{50}, and R_{20}, the four %DD data points were fit to an empirical function that closely models the %DD curve in the falloff region, i.e.

$$\%D(d) = (100\% - D_x)\frac{\mathrm{erfc}(a_1 d + a_2)}{2} + D_x\,, \qquad 5.1$$

where d is the effective measurement depth, D_x is the bremsstrahlung dose percent at R_p + 2.0 cm, erfc is the complimentary error function, and a_1 (slope of argument of erfc) and a_2 (offset of argument of erfc) are parameters determined by the fit. D_x which varies for each beam energy, was taken from clinical measurements. Example fits of equation 5.1 to the four %DD data points are plotted in Figure 5.3 for the 9 and 16 MeV beams of the Baton Rouge Elekta Infinity accelerator. For each beam, the R_{80}, R_{50}, and R_{20} values of the %DD curve were determined by the fit.

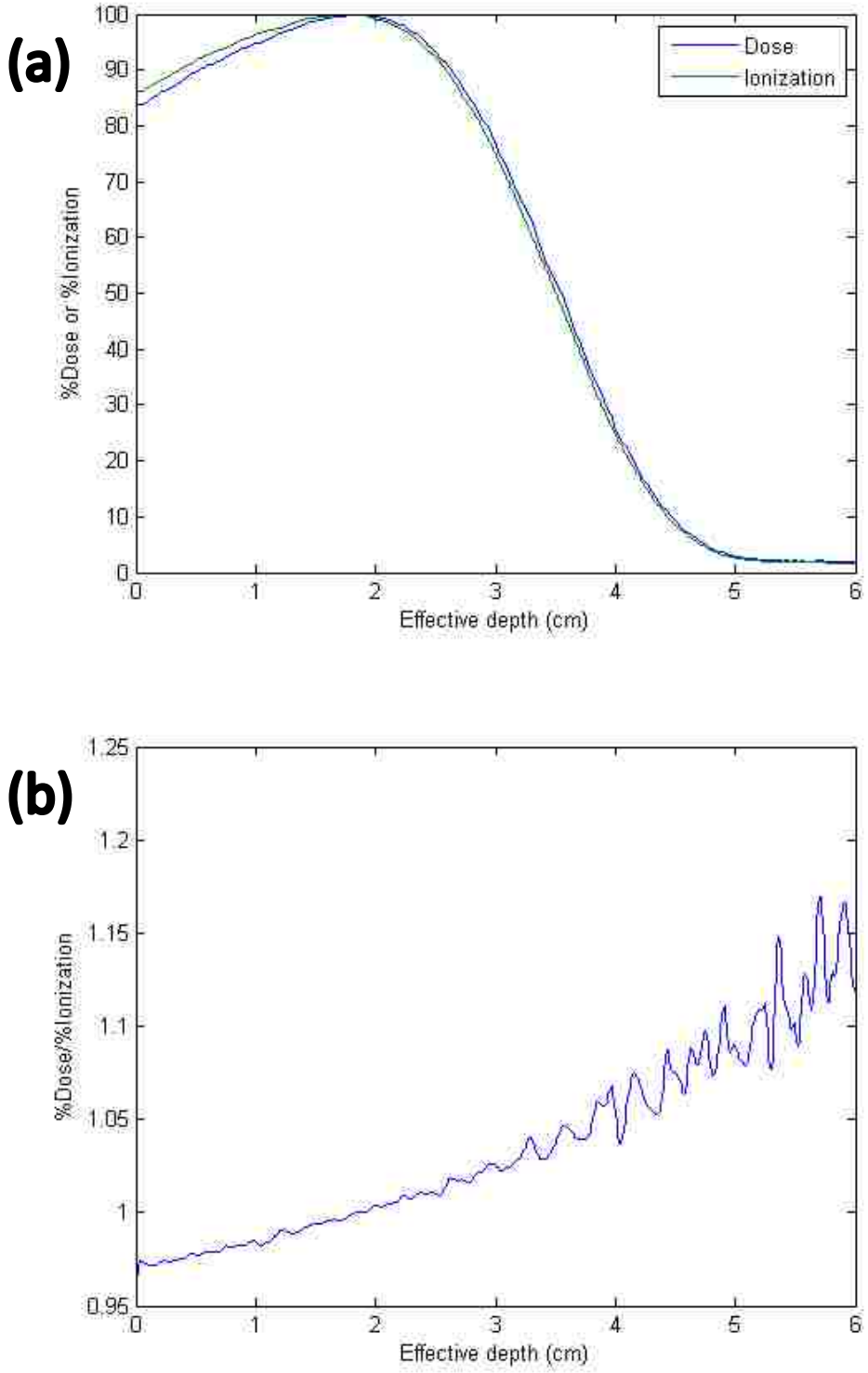

Figure 5.2. Ratios of percent dose to percent ionization. Plotted is a (a) comparison of %DD and %DI curves measured for the Baton Rouge Elekta Infinity 9 MeV beam with the 14 x 14 cm^2 open applicator and the (b) resulting ratios of percent dose to percent ionization versus effective depth. These measurements were part of the calibration measurements taken on Jan/14/2013.

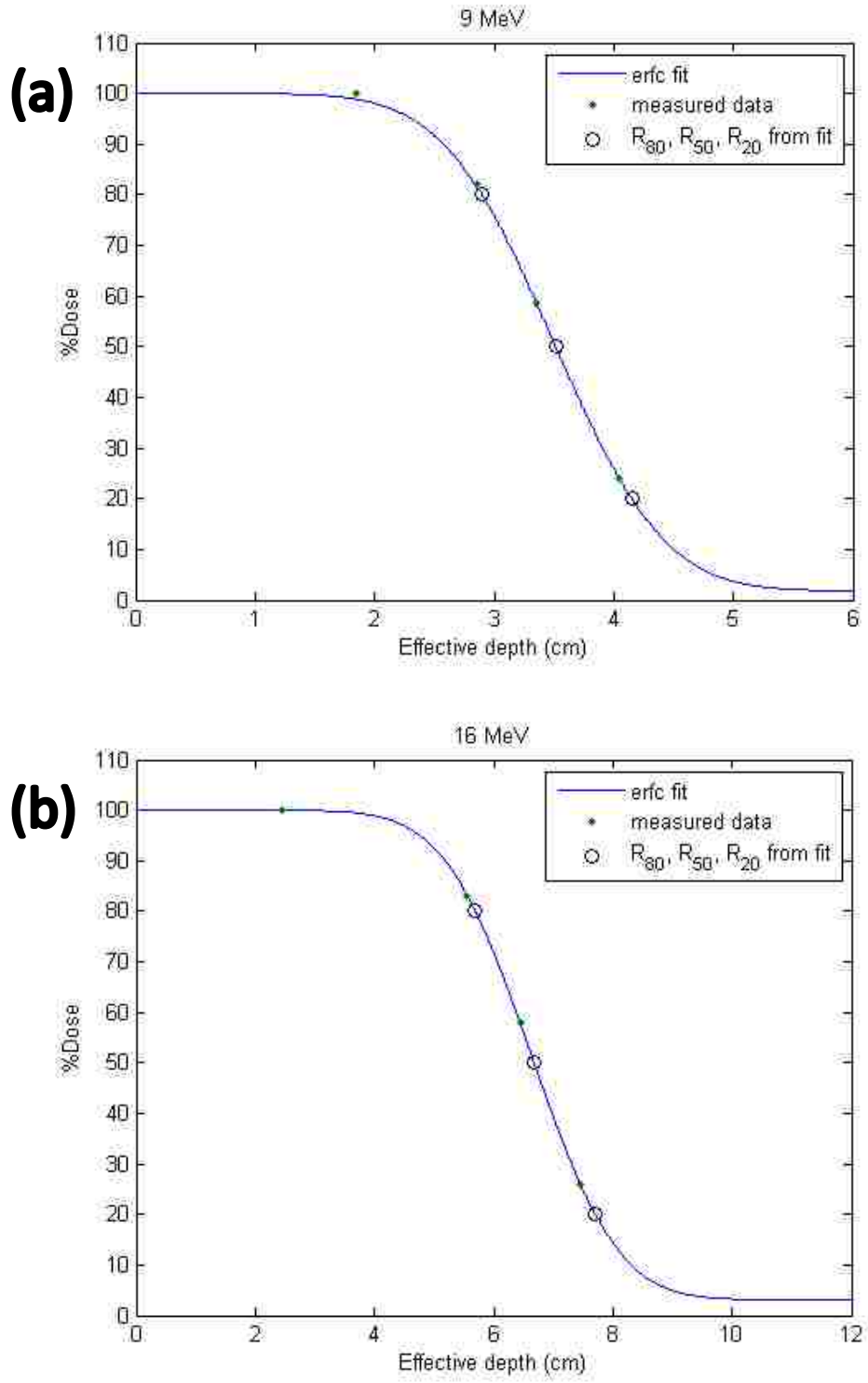

Figure 5.3. Fitting modified complementary error functions to the dose falloff region. Plotted are the (blue lines) results of fitting equation 5.1 to the (green dots) four measured %DD data points for the (a) 9 and (b) 16 MeV beams. Also plotted are the (black open circles) R_{80}, R_{50}, and R_{20} values drawn from these fits.

5.2. Results and discussion

5.2.1. R50 and R80-20 values

Using the methods described in section 5.1, the R_{50} and R_{80-20} values were determined for all seven electron beam energies on all six MBPCC Elekta Infinity accelerators. The results are listed in Table 5.2 below.

Table 5.2. R50 and R80-20 values. Displayed are the R_{50} and R_{80-20} values for all seven beam energies of all six Elekta Infinity accelerators at MBPCC. The matching groups are labeled 1 and 2. Within matching group 1, three accelerators were matched to (light grey fill) the Gonzales accelerator. Within matching group 2, one accelerator was matched to (light grey fill) the Houma accelerator. Also listed are the (Δ^{+}_{max}) maximum positive and (Δ^{-}_{max}) maximum negative deviations of accelerators' R_{50} and R_{80-20} values from their reference accelerators' R_{50} and R_{80-20} values for each beam energy.

		1				2			
		Gonz	**BR**	**CV1**	**CV2**	**Houma**	**Ham**	Δ^{-}_{max}	Δ^{+}_{max}
7 MeV	R_{50} **(cm)**	2.91	2.80	2.87	2.92	2.81	2.78	-0.105	0.013
	R_{80-20} **(cm)**	1.05	0.99	1.07	1.04	1.02	1.03	-0.059	0.020
9 MeV	R_{50} **(cm)**	3.59	3.52	3.72	3.57	3.47	3.39	-0.084	0.123
	R_{80-20} **(cm)**	1.27	1.25	1.29	1.21	1.20	1.19	-0.062	0.019
10 MeV	R_{50} **(cm)**	4.07	4.03	4.06	4.20	4.16	4.05	-0.109	0.128
	R_{80-20} **(cm)**	1.33	1.24	1.27	1.31	1.31	1.31	-0.084	0.006
11 MeV	R_{50} **(cm)**	4.64	4.61	4.68	4.78	4.85	4.48	-0.370	0.137
	R_{80-20} **(cm)**	1.45	1.46	1.50	1.53	1.52	1.43	-0.087	0.077
13 MeV	R_{50} **(cm)**	5.28	5.36	5.44	5.41	5.48	5.23	-0.250	0.163
	R_{80-20} **(cm)**	1.65	1.72	1.72	1.65	1.70	1.64	-0.061	0.067
16 MeV	R_{50} **(cm)**	6.67	6.68	6.68	6.72	6.65	6.54	-0.107	0.041
	R_{80-20} **(cm)**	2.06	2.01	2.00	1.97	2.08	2.04	-0.085	-0.035
20 MeV	R_{50} **(cm)**	8.29	8.28	8.33	8.22	8.25	8.12	-0.126	0.043
	R_{80-20} **(cm)**	2.76	2.80	2.83	2.70	2.78	2.69	-0.094	0.069

When matching electron beams at MBPCC, electron %DD curves' data points must match those of their reference accelerator's %DD curves to within 0.05 cm DTA or 2%. This matching criteria is applied to all %DD curve data points, not just the R_{50} values. Hence, to match electron beams it is important that the slope of the dose falloff region of the %DD curves match as well as the R_{50} values, otherwise data points near R_{90} and R_{10} will not match even if points near R_{50} do. For the purposes of this study, the slope metric of the %DD curve's dose falloff region was represented by its R_{80-20}. It was

assumed that if the R_{80-20} and R_{50} both match, all data points in the dose falloff region would match. Adding the individual 0.05 cm matching criteria for R_{80} and R_{20} together results in a maximum allowable difference of 0.1 cm in R_{80-20}.

In Table 5.2, the R_{50} values varied from their reference R_{50} values by as much as -0.37cm and +0.16cm. These variations are well outside the 0.05 cm matching criteria for R_{50}. Table 5.2 also shows that the R_{80-20} values can be as much as 0.08 cm greater or 0.09 cm less than the R_{80-20} values of their reference accelerators. These failures to meet MBPCC's matching criteria indicate that several beam energies were never sufficiently matched or that their energy spectra drifted due to changes in accelerator parameters.

5.2.2. Comparison of R50 and R80-20 values with energy spectra metrics

Traditionally, the mean energy of the energy spectra at the surface of a water phantom at 100-cm SSD, $\bar{E}_o$, is related to R_{50} by

$$\bar{E}_o = C_4(R_{50})\,, \tag{5.2}$$

where the recommended value for C_4 is 2.4 (TG-25 1990). Since $\bar{E}_o$ is similar to $\langle E\rangle^*_{m,o}$, all $\langle E\rangle^*_{m,o}$ were plotted versus R_{50} in Figure 5.4 to determine a correlation. Plotted on top of this data is

$$R_{50} = a_1\langle E\rangle^*_{m,o} + a_2\,, \tag{5.3}$$

where a_1 and a_2 were determined by a least square fit of equation 5.3 to all six accelerators' $\langle E\rangle^*_{m,o}$ and R_{50} values for seven beam energies. The value for a_1 was 0.4147 cm/MeV, hence ${a_1}^{-1}$ was equal to 2.411 MeV/cm, which agrees well with the recommended value of 2.4 MeV/cm for C_4. In combination with MBPCC's matching criteria of 0.05cm for R_{50}, 2.4 MeV/cm corresponds to a matching criteria of 0.12 MeV for $\langle E\rangle^*_{m,o}$, which was used throughout this study.

However, the 16 MeV beams have data points that vary from the fit by $\pm$0.3 MeV while agreeing to within 0.05 cm in terms of their R_{50} values. Hence, exceeding the 0.12 MeV match criterion for $\langle E\rangle^*_{m,o}$ values does not necessarily mean R_{50} values do not match. Such a dilemma suggests that

$\langle E \rangle^*_{m,o}$ alone is not a sufficient surrogate and that FWHM may also play a role. For example, the CV1 and BR accelerators have $\langle E \rangle^*_{m,o}$ values of 15.94 and 16.54 MeV, respectively, with identical R_{50} values of 6.68 cm. However, their FWHM values are 2.80 and 3.26 MeV, respectively.

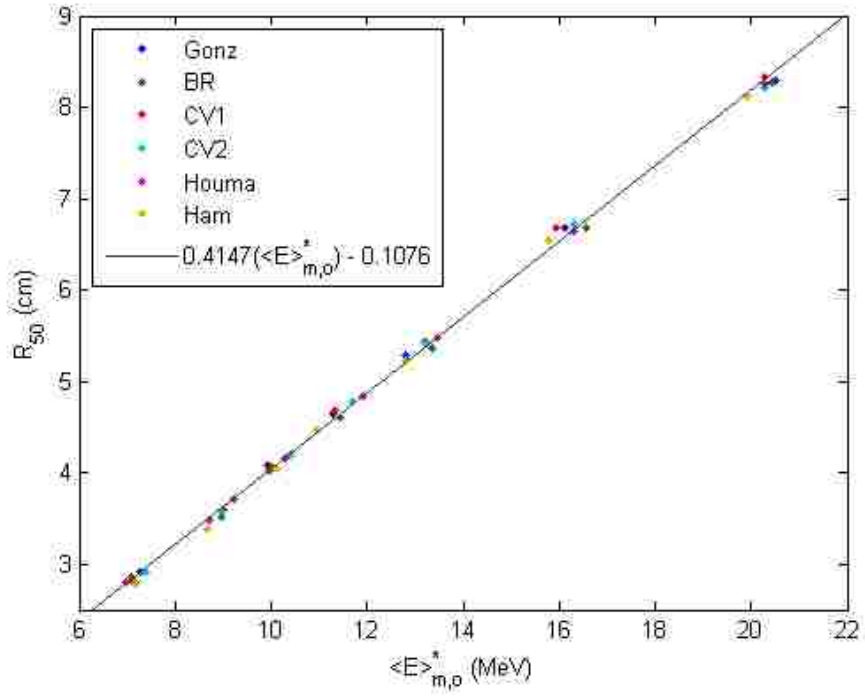

Figure 5.4. Correlation between R50 and incident modified peak mean energy. Plotted are the (colored dots) measured R_{50} values versus $\langle E \rangle^*_{m,o}$ values for all seven beam energies on all six Elekta Infinity accelerators at MBPCC and the result of the (solid line) fit of equation 5.3 to them.

R_{80-20} values for all seven beam energies on all six Elekta Infinity accelerators are plotted versus their respective $\langle E \rangle^*_{m,o}$ values in Figure 5.5. As the fit of a second order polynomial to this data demonstrates, R_{80-20} is primarily governed by the incident $\langle E \rangle^*_{m,o}$, increasing supralinearly with increasing $\langle E \rangle^*_{m,o}$ values. This can be attributed to an increase in range straggling with $\langle E \rangle^*_{m,o}$. However, variations amongst the six data points for each of the seven nominal energies indicate an additional, second order dependence on another factor, which is almost certainly the difference in the widths of the energy spectra. FWHM was selected as the spectral width metric, where

$$FWHM = 2.35\sigma\,, \tag{5.4}$$

where σ was the standard deviation of a Gaussian distribution fit to the portion of the energy spectra inside the energy averaging range used to calculated $\langle E \rangle^*_{m,o}$.

R_{80-20} values for all seven beam energies on all six Elekta Infinity accelerators are plotted versus FWHM in Figure 5.6. For each nominal energy, the R_{80-20} values had a second-order relationship with spectral width, increasing slightly with increases in FWHM. For example, for the 10 MeV beam there is a slope of about 0.05cm/MeV. Hence, this data confirms (1) that the FWHM of the energy spectra plays a minor, but important role, in beam matching and (2) that matching spectral widths would allow for finer beam matching and beam tuning than is possible with R_{80-20} or some other metric drawn from measured %DD curves. Variations from a straight line fit at each energy were due in part to variations in $\langle E \rangle^*_{m,o}$ values for all six accelerators at the same nominal energy. To better understand this data it was fit to a theory that relates the slope of the dose falloff region with $\langle E \rangle^*_{m,o}$ and FWHM.

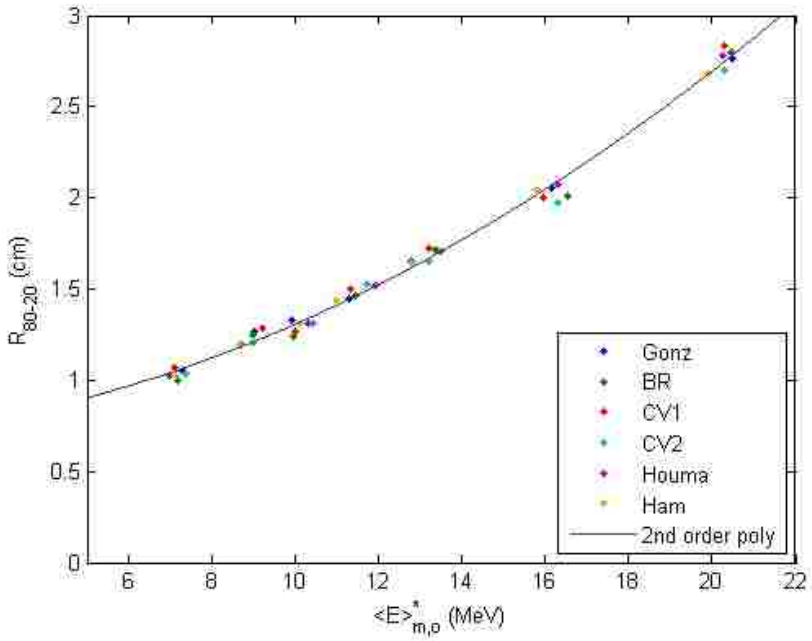

Figure 5.5. Plot of R80-20 versus incident modified peak mean energy. Plotted are the (colored dots) measured R_{80-20} values versus the $\langle E \rangle^*_{m,o}$ values for all seven beam energies on all six MBPCC Elekta Infinity accelerators. Also plotted is the (solid line) result of fitting an equation of the form $a_1 x^2 + a_2 x + a_3$ to the data, where a_1 equals 0.0038, a_2 equals 0.023, and a_3 equals 0.69 from the fit.

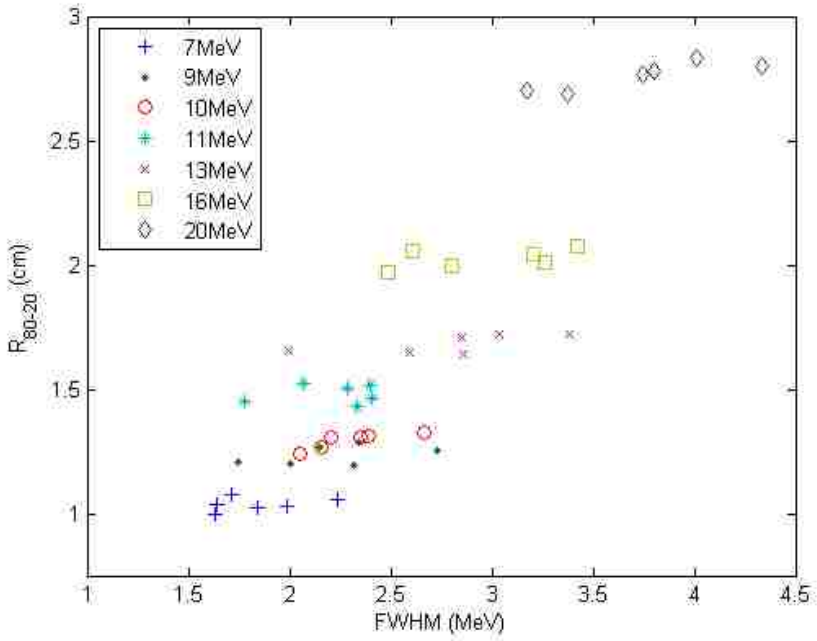

Figure 5.6. Plot of R80-20 versus FWHM. Plotted are the (colored dots) measured R_{80-20} values versus the FWHM values for all seven beam energies on all six MBPCC Elekta Infinity accelerators. The data for each beam energy illustrates a slight increase in R_{80-20} with FWHM.

The theory used to relate R_{80-20} to $\langle E\rangle^*_{m,o}$ and FWHM was a modified version of equation 6.35 in ICRU 35 (1984), i.e.

$$R_{80-20}\left(\langle E\rangle^*_{m,o}, FWHM\right) = R_{80-20}\left(\langle E\rangle^*_{m,o}, 0\right)\left[1 + a_1\left(\frac{FWHM}{\langle E\rangle^*_{m,o}}\right)\right], \qquad 5.5$$

where R_{80-20} at $\langle E\rangle^*_{m,o}$ for FWHM = 0 is modeled by

$$R_{80-20}\left(\langle E\rangle^*_{m,o}, 0\right) = a_2\left(\langle E\rangle^*_{m,o}\right)^2 + a_3\left(\langle E\rangle^*_{m,o}\right) + a_4\,. \qquad 5.6$$

The values for a_1, a_2, a_3, and a_4 were 0.394 $\pm$ 0.174, 0.003205 $\pm$ 0.000385, 0.03414 $\pm$ 0.0094, and 0.540 $\pm$ 0.071, respectively. These values were determined by fitting equation 5.5 to all the FWHM and $\langle E\rangle^*_{m,o}$ values in Table 4.4 and the corresponding R_{80-20} values in Table 5.2 using the non-linear, Marquardt algorithm option in the software package ProStat (Pearl River, NY). Plotted in Figure 5.7 are all the measured data as well as the calculated values from the fit of equation 5.5 to the data. Figure 5.7 shows excellent agreement (sum of least squares = 0.0389 cm^2) between the measurement data and

calculated points, which is consistent with a 0.03 cm uncertainty in the measured R_{80-20} data. Additionally, the plot of the calculated values for $R_{80-20}\left(\langle E\rangle^{*}_{m,o}, 0\right)$ versus the measured R_{80-20} values for the Therac 20 (Pfalzner and Clarke 1981) and Therac 25 (O'Brien *et al* 1985) accelerators in Figure 5.7 show reasonable agreement. The Therac 20 and Therac 25 are scanned beams, which having narrow energy spreads (Deasy *et al* 1996) are better for comparison to $R_{80-20}\left(\langle E\rangle^{*}_{m,o}, 0\right)$ than beams from other linear accelerators. Though these values are close, it is noteworthy that the measured R_{80-20} values are slightly less than the $R_{80-20}\left(\langle E\rangle^{*}_{m,o}, 0\right)$ values, which is the opposite of what one would expect.

Utilizing these results it is possible to correlate matching criteria comparing FWHM with the clinical value of 0.1 cm for R_{80-20}, i.e.

$$\Delta FWHM = \Delta R_{80-20}\left|\frac{dR_{80-20}\left(\langle E\rangle^{*}_{m,o}, FWHM\right)}{dFWHM}\right|^{-1}, \tag{5.7}$$

$$= \Delta R_{80-20}\left|\frac{R_{80-20}\left(\langle E\rangle^{*}_{m,o}, 0\right)}{\langle E\rangle^{*}_{m,o}} a_1\right|^{-1}, \tag{5.8}$$

where a_1 equals 0.394 $\pm$ 0.174. For $\langle E\rangle^{*}_{m,o}$ = 7, 13, and 20 MeV, $\Delta FWHM$ = 1.9, 2.16, and 2.03 MeV, respectively. Hence, an agreement of 0.1 cm in R_{80-20} corresponds to an agreement of approximately 2.0 MeV in FWHM.

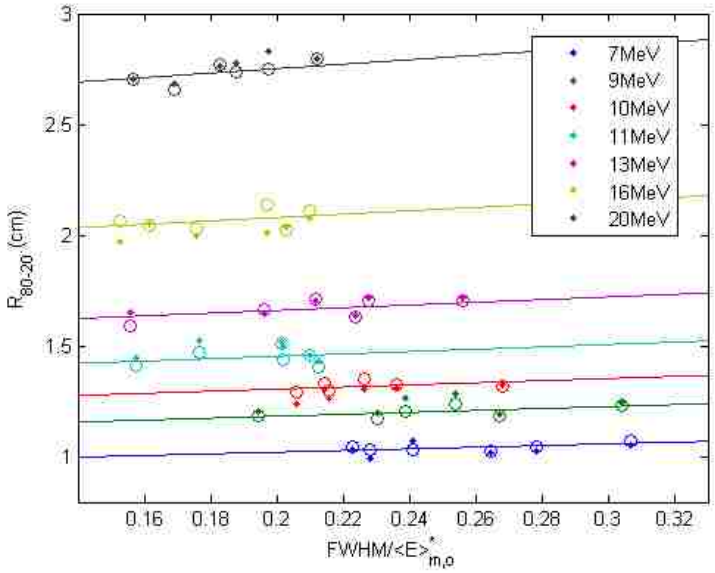

Figure 5.7. Plot of R80-20 versus the ratio of FWHM to incident modified peak mean energy. Plotted are (dots) measured R_{80-20} values versus FWHM/$\langle E\rangle^*_{m,o}$ values. Also plotted are the (open circles) results of the fit of equation 5.5 to the measured data at the same FWHM/$\langle E\rangle^*_{m,o}$ values. The solid lines result from the same fit with $\langle E\rangle^*_{m,o}$ being set equal to the average $\langle E\rangle^*_{m,o}$ for all six data points within a single nominal beam energy and the FWHM being allowed to vary, hence demonstrating the linear dependence of R_{80-20} on FWHM.

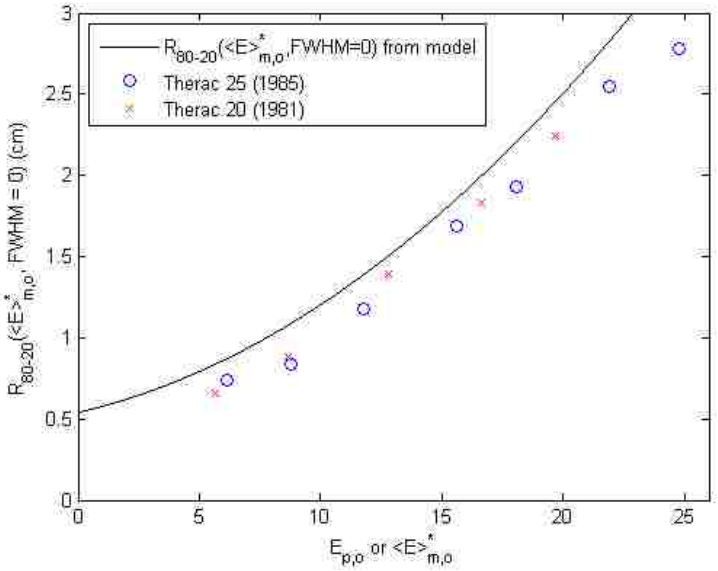

Figure 5.8. Comparison of R80-20(E,FWHM=0) from model to measured R80-20 measured for narrow energy spectra beams. Plotted are the (solid line) calculated values for $R_{80-20}(\langle E\rangle^*_{m,o}, FWHM = 0)$ versus $\langle E\rangle^*_{m,o}$ from the fit of equation 5.5 to the measured data and the measured R_{80-20} versus $E_{p,o}$ values for the (x points) Therac 20 (Pfalzner and Clarke 1981) and (open cirlces) Therac 25 (O'Brien *et al* 1985) accelerators, whose scanned beams have narrow energy spectra.

Chapter 6 - Conclusions and future work

6.1. Summary of results

- Development of magnetic spectrometer: A lightweight, permanent-magnet, electron energy spectrometer from Rice University was modified and configured to record maps of signal intensity from CR strip readouts. The signal was created by dose deposited in the CR strip's sensitive phosphor layer from electrons transported from the spectrometer aperture. These maps of signal intensity were transformed into intensity profiles, from which the energy spectra of electron beams at 95-cm SCD were extracted. Dual pin-hole collimators provided a parallel beam to the spectrometer and reduced the dose rate at the CR strip to appropriate levels, i.e. levels that created irradiation times between 5 and 50 seconds. Also, a 7.68-cm thick lead block lowered bremsstrahlung X-ray background to provide a peak signal to X-ray background ratio of 1.8:1 or greater.
- Transformation of intensity profiles into energy spectra: A method for extracting net dose profiles from the intensity profiles was developed. It was based on an analytical equation that related the net dose profiles at the CR strips to the incident electron beam energy spectra at the spectrometer aperture. An algorithm that solved the equation was developed, allowing the energy spectra at the spectrometer aperture to be determined from the measured net dose profiles. As these methods were analytical as opposed to statistical, they could be used in potential real-time versions of this study's magnetic spectrometer.
- Measurement of energy spectra for seven beam energies on six matched Elekta Infinity accelerators: The energy spectra for the seven beam energies on MBPCC's six Elekta Infinity accelerators were measured and compared. These electron beams had been previously tuned by Elekta service engineers to have matched %DD curves (match criteria was $\pm$0.05 cm for R_{50} and $\pm$0.10 cm for R_{80-20}). Results showed:

- For the three Elekta Infinity accelerators matched to the Gonzales accelerator, (1) the $\langle E \rangle^*_{m,o}$ varied from the reference $\langle E \rangle^*_{m,o}$ by as much as 0.18, 0.21, 0.47, 0.42, 0.56, 0.41, and 0.22 MeV for the 7, 9, 10, 11, 13, 16, and 20 MeV beams, respectively, and (2) the FWHM varied from the reference FWHM by as much as 0.6, 0.58, 0.61, 0.63, 1.39, 0.65, and 0.59 MeV for the 7, 9, 10, 11, 13, 16, and 20 MeV beams, respectively.
- For the one Elekta Infinity accelerator matched to the Houma accelerator, (1) the $\langle E \rangle^*_{m,o}$ varied from the reference $\langle E \rangle^*_{m,o}$ by 0.17, 0.02, 0.18, 0.95, 0.69, 0.51, and 0.35 MeV for the 7, 9, 10, 11, 13, 16, and 20 MeV beams, respectively, and (2) the FWHM varied from the reference FWHM by 0.15, 0.32, 0.18, 0.07, 0.01, 0.22, and 0.43 MeV for the 7, 9, 10, 11, 13, 16, and 20 MeV beams, respectively.

- Correlation of R_{50} and R_{80-20} values with $\langle E \rangle^*_{m,o}$ and FWHM: R_{50} and R_{80-20} were measured and correlated with $\langle E \rangle^*_{m,o}$ and FWHM from the measured energy spectra. The 0.05 cm and 0.1 cm matching criteria for the R_{50} and R_{80-20}, respectively, led to a matching criteria of 0.12 MeV and 2.0 MeV for the $\langle E \rangle^*_{m,o}$ and FWHM, respectively.

6.2. Major conclusions

- Hypothesis: The hypothesis of this study was "Matched electron beams on MBPCC's six Elekta Infinity linear accelerators will have energy spectra that are sufficiently matched. Two spectra will be considered sufficiently matched if their $\langle E \rangle^*_{m,o}$ and FWHM agree to within 0.12 MeV and 2.0 MeV, respectively, which corresponds to 0.05 cm and 0.1 cm agreement in the R_{50} and R_{80-20} values of the %DD curves, respectively."

  Based on the results, the hypothesis is false. For the three Elekta Infinity accelerators matched to the Gonzales accelerator, at least one accelerator exceeded the 0.12 MeV matching criteria for $\langle E \rangle^*_{m,o}$ for all seven beam energies, whereas all beam energies on all three accelerators met the 2.0 MeV matching criteria for FWHM. For the one accelerator matched to the Houma accelerator, the

0.12 MeV matching criteria for the $\langle E \rangle^*_{m,o}$ was not met for six of the seven beam energies, whereas the 2.0 MeV matching criteria for the FWHM was met for all seven energies. It is likely that energy spectra metrics did not match due to (1) inadequacies in the Elekta Infinity accelerator beam tuning process, (2) subsequent drifting of the energy spectra, (3) systematic error in the placement of the CR strips in the magnet block slot, or a combination thereof.

- Sensitivity of energy spectra for beam matching: The energy spectra and their metrics, FWHM in particular, are significantly more sensitive for comparing beams than %DD curves and their metrics. Matched %DD curves do not necessarily result in matched energy spectra. Because unmatched energy spectra may impact beam stability, there could be some advantage to matching energy spectra when matching electron beams.
- Potential for a real-time, electron energy spectrometer: The apparatus and analysis techniques developed in this study offer the potential for an inexpensive, lightweight, real-time electron energy spectrometer.

6.3. Recommended future work

- Develop of real-time magnetic spectrometer: Every time the service engineer modifies accelerator parameters while tuning the beam, the clinical medical physicist must remeasure the %DD curve to determine if the result is acceptable. Since tuning a single beam may involve many modifications to the accelerator parameters, any measurement of the %DD curve must produce results within a couple seconds so as to not slow the tuning process. In lieu of %DD curve measurements, measurements of the energy spectra using this study's spectrometer could be used to observe the effect of modifying accelerator parameters. To do so, this study's spectrometer must produce results in real-time.

  For the magnetic spectrometer developed in this study to produce such immediate results, a real-time detection medium must be used to make measurements in lieu of CR strips. Most likely

this would involve permanently affixing a scintillating screen to the magnet block, which has the added benefit of eliminating the biggest sources of measurement error, the placement of the CR strips in the magnet block slot and the placement of the CR strips on the laser scanning carousel.

- Improvements to beam collimation and X-ray shielding: It is possible to improve the peak signal to X-ray background ratio by increasing the diameter of the Cerrobend® aperture at 95-cm SCD. MC simulations should be used to optimize the diameters of and distance between the Cerrobend® and spectrometer apertures. Additionally, it is possible to lower the mass of the collimation apparatus by reducing the size of the X-ray block. The majority of the X-ray block's mass, which composes most of the mass of the entire measurement device, does not contribute to blocking X-rays from reaching the CR strip.
- Enhancements to data analysis: The magnetic field model used in section 2.1.2 could be improved by including the positions of the magnetic field edges parallel to the CR strips in equation 2.7 as parameters. This would allow the position of those edges to be determined by the fit of equation 2.7 to the calibration data instead of assuming the edges are contiguous with the CR strips. Also, calibrating the magnetic spectrometer on one of MBPCC's Varian accelerators may improve the resulting calibration curve, as Varian energy spectra are more monochromatic and Gaussian-shaped than Elekta energy spectra (Wessels *et al* 1979).
- Methods for background subtraction: The bremsstrahlung X-ray background subtraction (section 3.1.1.2) and net dose profile smoothing (section 3.1.1.3) should be automated, as in the current implementation of the code those processes require operator intervention to produce a complete set of energy spectra for a single accelerator (5-6 minutes of manual curve fitting and smoothing per beam). Automating these processes would shorten the execution time and remove any variations in the results due to inconsistent operator performance. It might be possible to automate background subtraction using measured background subtraction. To perform measured background

subtraction, each energy spectrum could be measured normally and then measured again with all the same irradiation conditions except for the spectrometer aperture being blocked. The dose profile from the measurement with the aperture blocked would then be subtracted from the dose profile measurement with the aperture unblocked. The result would be the net dose profile.

6.4. Potential applications for real-time magnetic spectrometer

- Beam tuning and matching: A real-time version of this study's magnetic spectrometer would allow service engineers to match electron beam energy spectra instead of %DD curves. This would be advantageous because well-matched energy spectra should have well-matched %DD curves, whereas the inverse might not be true. This is because %DD curves are fairly insensitive to some spectral changes, particularly spectral width or shape. These details have no clinical relevance if the %DD curves match, but being able to examine the energy spectra directly adds a level of detail that might allow service engineers to gain a better understanding of what accelerator parameters must be modified to perfect the matching of the %DD curves. This insight might expedite a normally tedious, time-consuming process as well as improve the resulting match. Also, using a magnetic spectrometer for beam matching has the advantage of eliminating the error due to the placement of the physical center of the scanning ionization chamber at the surface of a water phantom prior to measuring %DD curves, meaning there would be less setup error in the data used to match accelerators. This is especially important when matching beams, as this setup error is systematic for a single setup but random from setup to setup.
- Quality assurance by medical physicist: A real-time version of this study's magnetic spectrometer could be used as a QA device, possibly replacing ionization measurements in water or Plastic Water® as the standard for monthly and yearly checks of electron beam energy. This would require new QA methods to be developed in tandem with the device to take advantage of the increased sensitivity

made available by measuring energy spectra. With this added sensitivity, it may be possible to detect spectral changes that impact the stability of %DD curves.

- Determination of electron beam energy spectra for radiation transport calculations: The resulting energy spectra measured at 95-cm SCD could be used in transport calculations to determine dose in a water phantom or patient. Also, the energy spectra at 95-cm SCD could be used to determine the energy spectra at the vacuum window of the accelerator.
- Determination of X-ray beam energy spectra for radiation transport calculations: It should be possible to configure this study's magnetic spectrometer to measure the energy spectra of Compton-scattered electrons, from which the incident X-ray spectra could be calculated. Such methods have been used previously with synchrotron keV X-ray beams (Dugas *et al* 2008) and MeV beams (Landry and Anderson, 1991). The advantage of this detector is that unlike electron-counting scintillating detectors, there is no detector dead time during an accelerator pulse.

References

Almond P R, Biggs P J, Coursey B M, Hanson W F, Huq M S, Nath R and Rogers D W 1999 AAPM's TG-51 protocol for clinical reference dosimetry of high-energy photon and electron beams *Med. Phys.* **26** 1847-70.

Andreo P, Brahme A, Nahum A and Mattsson O 1989 Influence of energy and angular spread on stopping-power ratios of electron beams *Phys. Med. Biol.* **34** 751-68.

Brahme A and Svensson H 1976 Specification of electron beam quality from the central-axis depth absorbed-dose distribution *Med. Phys.* **3** 95-102.

Deasy J O 1992 Electron Energy and Angular Distributions in Radiotherapy *PhD Dissertation* University of Kentucky.

Deasy J O, Almond P R and McEllistrem M T 1994 The spectral dependence of electron central-axis depth-dose curves *Med. Phys.* **21** 1369-76.

Deasy J O, Almond P R and McEllistrem M T 1996 Measured electron energy and angular distributions from clinical accelerators *Med. Phys.* **23** 675-84.

Deasy J O, Almond P R, McEllistrem M T and Ross C K 1994 A simple magnetic spectrometer for radiotherapy electron beams *Med. Phys.* **21** 1703-14.

Dugas J P, Oves S D, Sajo E, Matthews K L, Ham K and Hogstrom K R 2008 Monochromatic beam characterization for Auger electron dosimetry and radiotherapy *Eur. J. Radiol.* **68** (suppl) 137-41.

Elekta Limited 2007 *Digital Linear Accelerator Technical Training Guide - 1st Line* (Crawley, West Sussex: Elekta Limited).

Gerbi B J, Antolak J A, Deibel C F, Followill D S, Herman M G, Higgins P D, Huq M S, Mihailidis D N, Yorke E D, Hogstrom K R and Khan F M 2009 Recommendations for clinical electron beam dosimetry: Supplement to the recommendations of Task Group 25 *Med. Phys.* **36** 3239-79.

Harris G H 2012 Development and validation of an electron Monte Carlo model for the Elekta Infinity accelerator *MS Thesis* Louisiana State University and Agricultural and Mechanical College.

Hogstrom K R 1991 Treatment planning in electron-beam therapy *Frontiers of Radiation Therapy and Oncology: The Role of High Energy Electrons in the Treatment of Cancer* J M Vaeth and J L Meyer (Farmington, CT: Karger) pp 30-52.

Hogstrom K R 2004 Electron beam therapy: dosimetry, planning, and techniques *Principles and Practice of Radiation Oncology* C Perez *et al* (Baltimore, MD: Lippincott, Williams, and Wilkins) pp 252-82.

International Commission on Radiatioin Units and Measurements (ICRU) 1984 Radiation Dosimetry: Electron beams with energies between 1 and 50 MeV *ICRU Report 35* (Bethesda, MD: International Commission on Radiation Units and Measurements).

Johnsen S W, LaRiviere P D and Tanabe E 1983 Electron depth-dose dependence on energy spectral quality *Phys. Med. Biol.* **28** 1401-07.

Kainz K K, Hogstrom K R, Antolak J A, Almond P R, Bloch C D, Chiu C, Fomytskyi M, Raischel F, Downer M and Tajima T 2004 Dose properties of a laser accelerated electron beam and prospects for clinical application *Med. Phys.* **31** 2053-67.

Karzmark C J, Nunan C S and Tanabe E 1992 *Medical Electron Accelerators* (New York, NY: McGraw-Hill, Inc.).

Khan F M, Doppke K P, Hogstrom K R, Kutcher G J, Nath R, Prasad S C, Purdy J A, Rozenfeld M and Werner B L 1991 Clincal electron-beam dosimetry: Report of AAPM Radiation Therapy Committee Task Group No. 25 *Med. Phys.* **18** 73-109.

Kok J G and Welleweerd J 1999 Finding mechanisms responsible for the spectral distribution of electron beams produced by a linear accelerator *Med. Phys.* **26** 2589-96.

Landry D J and Anderson D W 1991 Measurement of accelerator bremsstrahlung spectra with a high-efficiency Ge detector *Med. Phys.* **18** 527-32.

O'Brien P, Michaels H B, Aldrich J E and Andrew J W 1985 Characteristics of electron beams from a new 25-MeV linear accelerator *Med. Phys.* **12** 799-805.

Pfalzner P M and Clarke H C 1981 Radiation parameters of 6 to 20 MeV scanning electron beams from the Saturne linear accelerator *Med. Phys.* **9** 117-20.

Rowlands J A 2002 The physics of computed radiography *Phys. Med. Biol.* **47** 123-66.

Tapley N D 1976 *Clinical Applications of the Electron Beam* (New York, NY: Wiley).

Udale M 1988 A Monte Carlo investigation of surface dose for broad electron beams *Phys. Med. Biol.* **33** 939-53.

Werner B L, Khan F M and Deibel F C 1982 A model for calculating electron beam scattering in treatment planning *Med. Phys.* **9** 180-87.

Wessels B W, Paliwal B R and Choi M C 1979 Characterization of Clinac-18 electron-beam energy using a magnetic analysis method *Med. Phys.* **6** 45-48.

Appendix A - Schematics of magnetic spectrometer and collimation apparatus

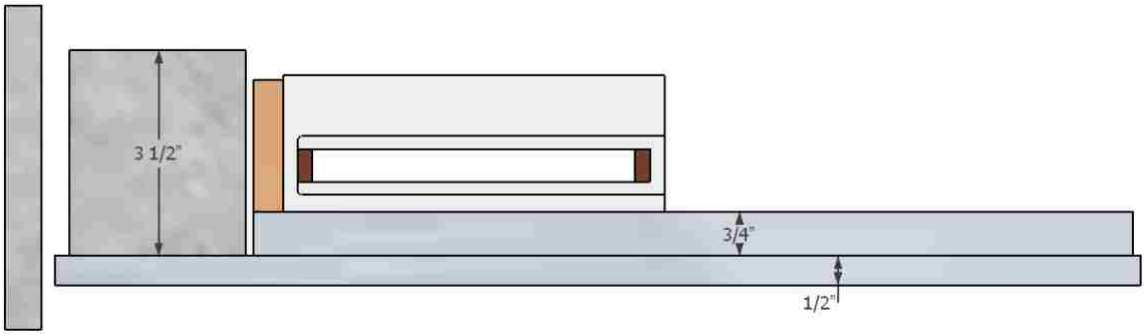

Figure A.1. Side view of combined spectrometer and collimation apparatus. The position of the aluminum baseplate relative to the Cerrobend® insert during irradiation is accurately depicted. The Cerrobend® insert and aluminum baseplate are shown unattached to reflect the fact that they are free to move relative to one another. All dimensions are to scale.

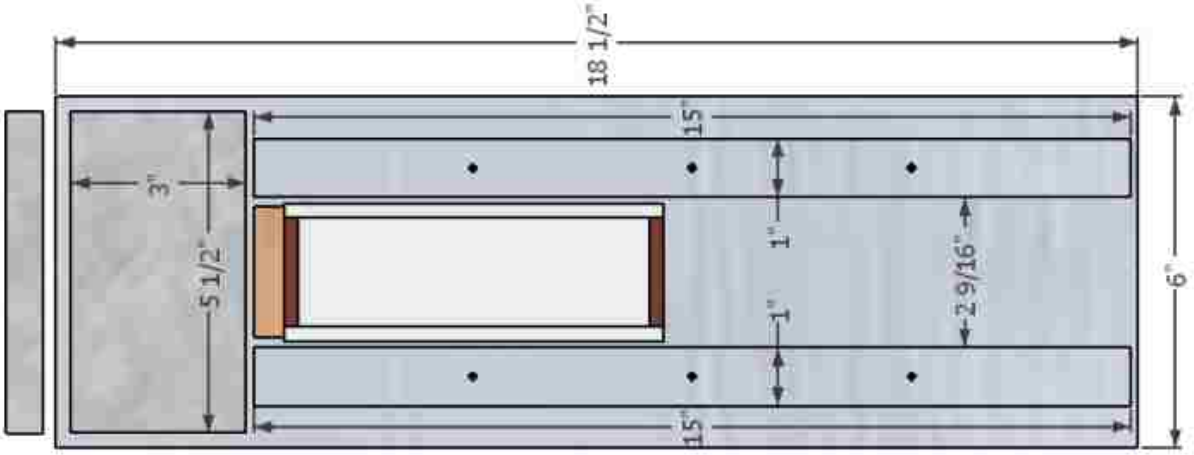

Figure A.2. Top view of combined spectrometer and collimation apparatus. The position of the aluminum baseplate relative to the Cerrobend® insert during irradiation is accurately depicted. The Cerrobend® insert and aluminum baseplate are shown unattached to reflect the fact that they are free to move relative to one another. All dimensions are to scale.

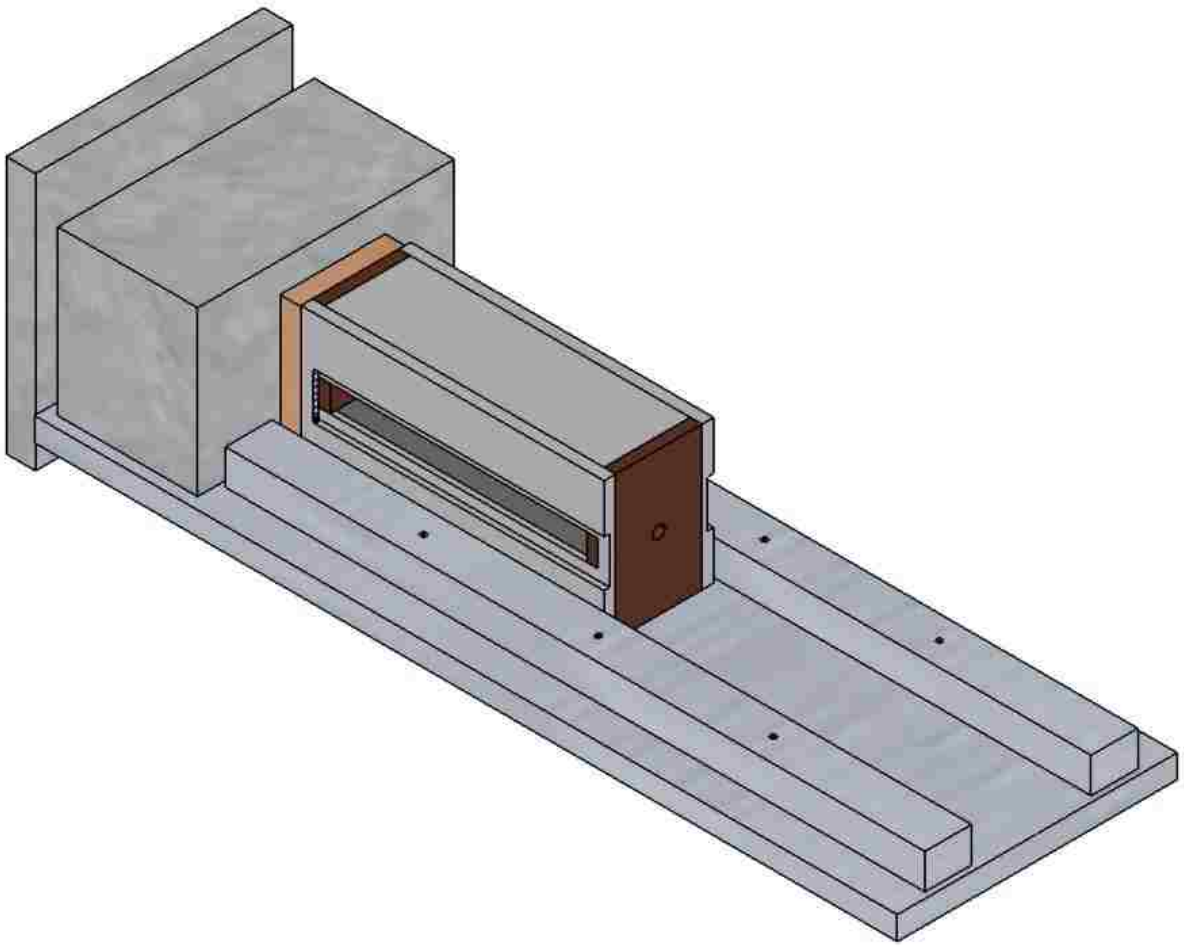

Figure A.3. Isometric view of spectrometer and collimation apparatus. The position of the aluminum baseplate relative to the Cerrobend® insert during irradiation is accurately depicted. The Cerrobend® insert and aluminum baseplate are shown unattached to reflect the fact that they are free to move relative to one another. All dimensions are to scale.

Appendix B - CR plates and CR plate readout device

To create a CR plate, phosphor grains are combined with a polymer binder and a solvent to create a slurry. This slurry is deposited onto a strong, flexible backing. After drying, the slurry hardens into the sensitive layer of the CR plate, titled "Phosphor layer" in Figure B.1. When irradiated, some electrons in the crystal lattice of the senstive layer's phosphor grains are excited into the conduction bands, leaving behind holes in the valence band. A single hole and electron pair created by this excitation creates a hydrogen-like psuedo-atom known as an exciton which is held together by the a mutual attraction between the hole and electron (Rowlands 2002).

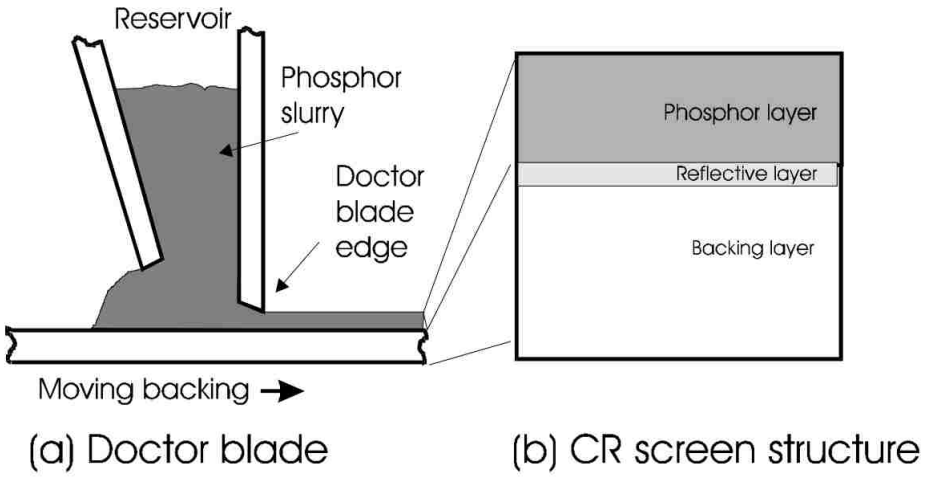

Figure B.1. CR Plate fabrication. Illustrated is the deposition of the sensitive phosphor layer onto the flexible backing layer of a CR plate (from Rowlands 2002).

This exciton moves freely through the crystal lattice until it is contained by one of the lattice's many traps. If trapped at one of the activator sites created by doping the crystal with activator elements, the electron-hole pair can be stimulated with a laser to recombine in a process known as photostimulable luminscence (PSL). An example activator site is illustrated in Figure B.2. During PSL, the exciton recombines and gives off energy in the form of photons of the activator element's characteristic wavelength. Hence, the trapping of excitons in phoshphor grains in the CR plate's sensitive layer forms a latent image that is readout with laser light.

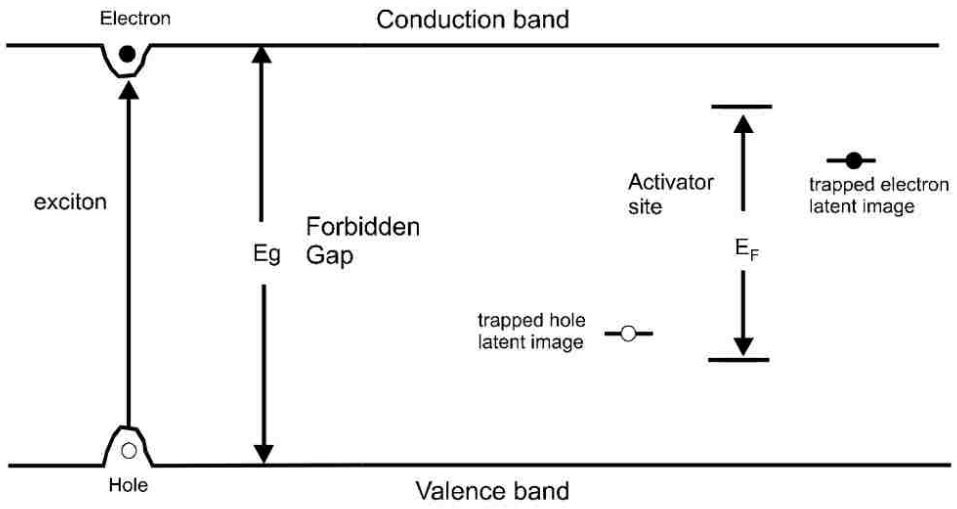

Figure B.2. Band structure and exciton trapping. Illustrated is the band structure of the crystal lattice of phosphor grains in the CR plate. Excitons traveling through the lattice are trapped at activator sites where they are stimulated to recombine with laser light (from Rowlands 2002).

To readout the latent image with laser light, a laser is scanned over the entire surface of the CR plate's sensitve layer. In this study, the readout device consisted of a rotating carousel and a laser focused into a spot beam that scans in the direction perpendicular to the carousel rotation direction. The CR plate is taped to this carousel and the scanning of the laser in combination with the carousel rotation results in a raster scan across the entire face of the CR strip. The resulting PSL photons are directed towards a light guide which transports them to a photomultipler tube (PMT) (Rowlands 2002). The PSL photons detected by the PMT are then mapped to the collection position, creating the CR plate image.

Vita

David McLaughlin was born in western Pennsylvania. He graduated from the Pennsylvania State University in 2010 with a B.S. in Electrical Engineering and a Minor in Physics. While at Penn State, he developed an interest in merging his technical education with the field of medicine, which led him to enter the Medical Physics program at the Louisiana State University in August 2010.